Sciencexpress Research Articles

Chelyabinsk Airburst, Damage Assessment, Meteorite Recovery, and Characterization

Olga P. Popova,[1] Peter Jenniskens,[2,3]* Vacheslav Emel'yanenko,[4] Anna Kartashova,[4] Eugeny Biryukov,[5] Sergey Khaibrakhmanov,[6] Valery Shuvalov,[1] Yurij Rybnov,[1] Alexandr Dudorov,[6] Victor I. Grokhovsky,[7] Dmitry D. Badyukov,[8] Qing-Zhu Yin,[9] Peter S. Gural,[2] Jim Albers,[2] Mikael Granvik,[10] Läslo G. Evers,[11,12] Jacob Kuiper,[11] Vladimir Kharlamov,[1] Andrey Solovyov,[13] Yuri S. Rusakov,[14] Stanislav Korotkiy,[15] Ilya Serdyuk,[16] Alexander V. Korochantsev,[8] Michail Yu Larionov,[7] Dmitry Glazachev,[1] Alexander E. Mayer,[6] Galen Gisler,[17] Sergei V. Gladkovsky,[18] Josh Wimpenny,[9] Matthew E. Sanborn,[9] Akane Yamakawa,[9] Kenneth L. Verosub,[9] Douglas J. Rowland,[19] Sarah Roeske,[9] Nicholas W. Botto,[9] Jon M. Friedrich,[20,21] Michael E. Zolensky,[22] Loan Le,[23,22] Daniel Ross,[23,22] Karen Ziegler,[24] Tomoki Nakamura,[25] Insu Ahn,[25] Jong Ik Lee,[26] Qin Zhou,[27,28] Xian-Hua Li,[28] Qiu-Li Li,[28] Yu Liu,[28] Guo-Qiang Tang,[28] Takahiro Hiroi,[29] Derek Sears,[3] Ilya A. Weinstein,[7] Alexander S. Vokhmintsev,[7] Alexei V. Ishchenko,[7] Phillipe Schmitt-Kopplin,[30,31] Norbert Hertkorn,[30] Keisuke Nagao,[32] Makiko K. Haba,[32] Mutsumi Komatsu,[33] Takashi Mikouchi[34] (the Chelyabinsk Airburst Consortium)

*Corresponding author. E-mail: Petrus.M.Jenniskens@nasa.gov

Author affiliatons are shown at the end of the text.

The asteroid impact near the Russian city of Chelyabinsk on 15 February 2013 was the largest airburst on Earth since the 1908 Tunguska event, causing a natural disaster in an area with a population exceeding one million. Because it occurred in an era with modern consumer electronics, field sensors, and laboratory techniques, unprecedented measurements were made of the impact event and the meteoroid that caused it. Here, we document the account of what happened, as understood now, using comprehensive data obtained from astronomy, planetary science, geophysics, meteorology, meteoritics, and cosmochemistry, and from social science surveys. A good understanding of the Chelyabinsk incident provides a unique opportunity to calibrate the event, with implications for the study of near-Earth objects and developing hazard mitigation strategies for planetary protection.

Chelyabinsk Oblast experienced an impact that was 100 times more energetic than the recent 4 kT of TNT equivalent Sutter's Mill (*1*). This was the biggest impact over land since the poorly observed Tunguska impact in 1908, for which kinetic energy estimates range from 3−5 (*2*) to 10−50 MT (*3*). From the measured period of infrasound waves circum traveling the globe (*4*), an early estimate of ~470 kT was derived for Chelyabinsk (*5*). Infrasound data from Russia and Kazakhstan provide 570 ± 150 kT; see supplementary materials (SM) Section 1.4 (*6*). Spaceborne visible and near-infrared observations (*7*) recorded a total irradiated energy of 90 kT (*5*, *8*), corresponding to a kinetic energy of 590 ± 50 kT using the calibration by Nemtchinov *et al*. (*9*). All values are uncertain by a factor of two because of a lack of calibration data at those high energies and altitudes.

The manner in which this kinetic energy was deposited in the atmosphere determined what shock wave reached the ground. Dash-cam and security camera videos of the fireball (Fig. 1) provide a lightcurve with peak brightness of -27.3 ± 0.5 magnitude (Fig. 2) (SM Sect. 1.2). The integrated lightcurve is consistent with other energy estimates if the panchromatic luminous efficiency was 7 ± 3%. Theoretical estimates under these conditions range from 5.6−13.2% (*10*).

Calibrated video observations provided a trajectory and pre-atmospheric orbit (Table 1) (SM Sect. 1.1). The fireball was first recorded at 97 km altitude, moving at 19.16 ± 0.15 km/s and entry angle 18.3 ± 0.2° with respect to the horizon, which is slightly faster than reported earlier (*11*). Combined with the best kinetic energy estimate, an entry mass of 1.3×10^7 kg (with a factor of two uncertainty) and a diameter of 19.8 ± 4.6 m is derived, assuming a spherical shape and the meteorite-derived density of 3.3 g/cm^3 based on x-ray computed tomography (SM Sect. 4.2, table S16).

Size and speed suggest that a shockwave first developed at 90 km. Observations show that dust formation and fragmentation started around 83 km and accelerated at 54 km (figs. S16 and S22). Peak radiation occurred at an altitude of 29.7 ± 0.7 km at 03:20:32.2 ± 0.1s UTC (SM Sect. 1.1-2), at which time spaceborne sensors measured a meteoroid speed of 18.6 km/s (*5*). Fragmentation left a thermally emitting debris cloud in this period, the final burst of which occurred at 27.0 km altitude (Fig. 1), with dust and gas settling at 26.2 km with distinctly higher billowing above that location (fig. S22). The dust cloud split in two due to buoyancy of the hot gas, leading to two cylindrical vortices (*12*).

Compared to the much larger Tunguska event (*2*, *3*), Chelyabinsk was only on the threshold of forming a common shock wave around the fragments when it broke at peak brightness (SM Sect. 1.2). Fragments were spatially isolated enough to be efficiently decelerated, avoiding the transfer of momentum to lower altitudes and resulting in less damage when the blast wave reached the ground.

Damage Assessment

In the weeks following the event, 50 villages were visited to verify the extent of glass damage. The resulting map (Fig. 3) demonstrates that the shockwave had a cylindrical component, extending furthest perpendicular to the trajectory. There was little coherence of the shockwave in the forward direction, where the disturbance was of long duration, shaking buildings and making people run outside, but causing no damage.

The strength of this shockwave on the ground was modeled (SM Sect. 2.4) assuming that an overpressure of $\Delta P > 500$ Pa was required (*13*). A 520 kT event, with detonations spread over altitudes ranging from 34−27 km and 24−19 km, would cause damage out to a distance of 120 km with the observed shape (Fig. 3). The fragments that penetrated

Downloaded from www.sciencemag.org on November 13, 2013

below 27 km must have contributed to the damage in order to match the shock wave arrival times (SM Sect. 2.4).

The number of houses damaged per 1,000 inhabitants (table S11) (SM Sect. 2.3) falls off with distance from the airburst source (r) as $r^{-2.6 \pm 1.2}$, with overpressure calculated to fall off as $r^{-2.4}$ (fig. S39). In Chelyabinsk itself, 3,613 apartment buildings (about 44%) had shattered and broken glass, but these were not evenly distributed in the city (fig. S37). Sharp sounds heard following the shockwave also point to the fragmentation causing a complicated distribution of pressure. Structural damage included the collapse of a zinc factory roof.

Directly below the fireball's path, the shock wave was strong enough to blow people off their feet. In Yemanzhelinsk, window frames facing the trajectory were pushed inwards, and suspended ceilings were sucked down above broken windows (fig. S36G). There was no structural damage to buildings, other than a statue of Pushkin inside the local library, cracked by a blown out window frame. Cracks in walls were documented in nearby Baturinsky and Kalachevo.

Electrophonic sounds were heard (SM Sect. 1.6), but there was no evidence of an Electromagnetic Pulse (EMP) under the track in neighboring Emanzhelinka. Due to shock wave induced vibrations, electricity and cell phone connectivity was briefly halted in the Kunashaksky district at the far northern end of the damage area. The gas supply was briefly interrupted in some districts due to valves reacting to the vibrations.

People found it painful to look at the bright fireball, but glancing away prevented lasting eye damage. Of 1,113 respondents to an internet survey who were outside at the time, 25 were sunburned (2.2%), 315 felt hot (28%) and 415 (37%) warm (SM Sect. 2.2). Mild sunburns were reported throughout the survey area (table S7), reflecting the fact that UV flux density falls off as $\sim r^{-2}$. In Korkino, 30 km from the point of peak brightness, one resident reported getting a mild sunburn on the face, followed by loss of skin flakes. Such effects occur at a minimum erythema dose of ~1,000 J/m^2 (*14*) of 290-320 nm radiation (mostly UV-B). Assuming 6,000 K radiation (*9*), the calculated dose would have been ~200 J/m^2 at Korkino. Ground-reflectance of UV light by snow may have further increased the dose.

Out of the total 1,674 collected internet queries, 374 mention 452 body injuries or inconveniences (SM Sect. 2.2). Of those, 5.3% reported sunburn, 48% eyes hurt, and 2.9% felt retinal burns. Because of the shock wave, 6.4% reported a concussion or mental confusion, upset, or exhaustion as a result of excessive stress. Flying glass and falling building debris affected a relatively small fraction of respondents: 4.8% reported cuts and 2.9% reported bruises, but no broken bones were reported.

The percentage of people asking for medical assistance (table S10) dropped with distance according to $r^{-3.2 \pm 0.5}$ (SM Sect. 2.1). The majority of injuries (1,210) took place in the densely populated Chelyabinsk city, but the highest fraction of people asking for assistance was near the trajectory track in the Korkinsky district (0.16%).

Meteorite Recovery

Shock radiation contributed to surface heating and ablation, but did not completely evaporate all fragments of Chelyabinsk, unlike in the case of Tunguska (*3*). Meteorites of ~0.1 g fell near Aleksandrovka close to the point of peak brightness, masses of ~100 g fell further along the trajectory near Deputatskiy, and at least one of 3.4 kg fell near Timiryazevskiy. One hit the roof of a house in Deputatskiy (fig. S46). Falling-sphere models suggest they originated at 32-26 km altitude (fig. S52), where the meteor model shows rapid fragmentation (fig. S18C). The location of the meteorites is consistent with prevailing NW winds of 5−15 m/s (fig. S24). An estimated 3,000−5,000 kg fell in this area (SM Sect. 3.1).

Two main fragments survived the disruption at 29.7 km. They flared around 24 km, with one falling apart at 18.5 km, and the other remaining luminous down to 13.6 km (Fig. 1 and fig. S15). Lightcurve modeling (SM Sect. 1.2) suggests that from this material another ~1 ton in larger fragments up to 100−400 kg in mass reached the ground. A 7-m sized hole was discovered in 70-cm thick ice on Lake Chebarkul (fig. S53A), in line with the trajectory (SM Sect. 1.1). A lakeshore video security camera, pointed to the site, recorded the impact (fig. S53B). Small meteorite fragments were recovered over an area up to 50 m from the impact location (Fig. 4C). Impact models (figs. S18 and S54) suggest a 200−1,000 kg meteorite would be required to create such a hole. A mass of ≥570 kg was recovered from the lakebed (fig. S53C).

The combined 4-6 t of surviving meteorites is only 0.03−0.05% of the initial mass. 76% of the meteoroid evaporated, with most of the remaining mass converted into dust (SM Sect. 1.3). Witnesses reported smelling "sulfur" and burning odors over a wide region concentrated near the fireball trajectory, starting about an hour after the fireball and lasting through much of the day (SM Sect. 1.5) (fig. S34).

Characterization of Recovered Meteorites

The unusually effective fragmentation and small surviving mass may have been caused by structural and material weakness. The asteroid had a lower compressive strength than the ~330 MPa measured for recovered, surviving meteorites (Section S4.1). The lightcurve (Fig. 2) is modeled with fragmentation starting at a low 0.2 MPa dynamic pressure, but tolerating higher pressure with decreasing fragment size. This is similar to other meteorite falls, where initial weakness was attributed to macroscopic cracks or microscopic porosity (*15*). For Chelyabinsk, however, the physical weakness is not microporosity related. X-ray computed tomography (SM Sect. 4.2) revealed a degree of compaction consistent with the lack of intragranular porosity typical of LL chondrites (*16*).

Some laboratory broken meteorites fragmented along shock veins (fig. S55), a possible weakness in the material that could have contributed to the abundant dust formation. The meteorite is composed of a breccia (*17*) of mildly shocked lighter clasts and moderately shocked darker clasts with abundant thin to cm-wide shock melt veins (Fig. 4A) (SM Sect. 4.4). A peculiar feature is that some shock veins exhibit a metal layer located ~20 microns inside the vein, which follows the outer contours of the vein (Fig. 4B), indicating that metal initially segregated from the most rapidly solidifying rims of the vein. This could contribute to weakness. Metal-rich tendrils also project outward from the vein.

The mineral compositional ranges (SM Sect. 4.4) are slightly larger than those reported before (*18*), but still compatible with a classification as LL5, shock stage S4 (*19*). The classification as LL chondrite is substantiated by oxygen and chromium isotope studies (SM Sect. 4.5−4.7), which put the meteorite near the L-end of the LL field (*20*, *21*) (Fig. 4D and fig. S68). Iron content and oxidation state also support the LL chondrite classification (Fig. 4E and fig. S58). Rare Earth element abundances are more similar to L chondrites (Fig. 4F and table S18), while one measured reflectance spectrum better matches that of H chondrites (fig. S72).

The Chelyabinsk (LL) parent body experienced a significant thermal and/or collision resetting event 115 ± 21 Ma after formation of the Solar System (*25*), not experienced by most other LL chondrites, possibly due to a significant impact event near its site of origin on the parent body. The phosphate U-Pb age is 4,452 ± 21 Ma (SM Sect. 4.8) (fig. S70), much younger than the majority of other ordinary chondrites phosphate ages dated by conventional TIMS methods (*22*, *23*). Perhaps one other piece of evidence for this is the 4.48 ± 0.12 Ga Pb-Pb isochron age of phosphates in a granite-like fragment found in the LL3-6 chondrite regolith breccia Adzhi-Bogdo (*24*), an observed fall in Mongolia in 1949.

Chelyabinsk shows a common orientation of metal grains indicating an impact-related petrofabric (fig. S59), stronger than that seen in any other ordinary chondrite of any shock stage (*26*) (fig. S60). This petro-

fabric probably reflects the most recent extraterrestrial shock event experienced by the Chelyabinsk meteoroid. The magnetic susceptibility value is at the upper end of the range for LL type (fig. S61) (*27*), closer to L type chondrites, suggestive of higher metal content in Chelyabinsk than a typical LL chondrite. However, detailed analysis of the remanent magnetization suggests that a shock event or the conditions of atmospheric entry led to significant resetting of the remanence (SM Sect. 4.3).

Recent meteoroid heating events are normally recorded by thermoluminescence (TL) (SM Sect. 4.10). In this case, the induced TL level of Chelyabinsk is lower than other petrographic type 5 or 6 chondrites, possibly because shock metamorphism to the level of S4 (30-35 GPa) (fig. S79) destroyed feldspar, the mineral phase responsible for the thermoluminescence signal (*28*). Atmospheric heating did not cause loss of natural TL signal, the steep thermal gradient being consistent with a very thin fusion crust on the measured samples (*29*). The natural TL value is consistent with the meteoroid having been heated at a perihelion distance of 0.6−0.8 AU (Table 1).

The shock did not remove all organic matter from the meteorite. Methanol-soluble polar organic compounds (Sect. S4.11) were detected in impact melt vein and chondrite fractions using electrospray ionization ion cyclotron resonance Fourier-Transform mass spectrometry (*30*). Out of more than 18,000 resolved mass peaks, 2,536 could be assigned to compounds containing C, H, N, O, S. The organic signature is typical of other shocked LL chondrites, showing a higher abundance of oxygen and nitrogen atoms in the impact melt (fig. S83). The presence of oxygenated sulfur is indicated by CHOS compounds containing on average 3 more oxygen atoms than CHO and CHNO compounds. The high abundance of CHOS compounds in a homologous series across the entire mass range testifies that most of these did not result from terrestrial contamination.

Impact shock induced fracturing on the Chelyabinsk parent body was followed by melting of metal and sulfides, which are pressure-driven through the meteorite. There are cases where this increased a meteorite's mechanical strength, the residual heat facilitating the process. However, in the case of Chelyabinsk, the production of cracks weakened the meteorite material more than shock melting increased its strength.

Source and Evolution of the Chelyabinsk Meteoroid

Chelyabinsk adds an LL5 type meteorite to a short list (SM Sect. 1.1) of 18 differently typed meteorites with known pre-atmospheric orbits (*1*). Only 8.2% of falls are LL chondrites (*31*). The Chelyabinsk meteorite is of particular interest because it is of the same type as asteroid Itokawa, from which samples were collected by the Hayabusa Mission (*32*). Indeed, both Itokawa and Chelyabinsk have similar low-inclined low-semi-major axis orbits (Table 1), which, according to one model (*33*), imply a 62%, 11%, and 25% probability for Chelyabinsk (and 71%, 0%, and 29% probability for Itokawa) of originating from the secular ν_6 resonance, the 3:1 mean-motion resonance, and the Intermediate Mars Crosser region, respectively. Multiplying these probabilities, assuming all LL chondrites enter the near Earth object region through the same escape route, there is now an 86% probability that they originated from ν_6. This supports the hypothesis (*34*) that they originated from the inner part of the LL-type (*35*) Flora asteroid family, which straddles the ν_6 resonance in 1.6−7.7° inclined orbits (*36*).

As a group, LL chondrites have a cosmic ray exposure age peaking at ~17 Ma (*34*). Chelyabinsk, on the other hand, was exposed only since ~1.2 Ma (SM Sect. 4.12). The responsible breakup that first exposed the Chelyabinsk meteoroid surface to cosmic rays was not likely part of the ongoing collision cascade in the asteroid main belt that followed the formation of the Flora family. Although fast pathways exist that can bring meteoroids from all three resonances into a Chelyabinsk-like orbit in about 0.2 Ma, such cases are rare (table S6). More likely, Chelyabinsk was exposed only since being ejected from the resonance, due to breakup from either thermal stresses, rotational spin-up, or from tidal forces in terrestrial planet encounters. The required structural weakness may have come from macroscopic cracks or from a weakly consolidated rubble pile morphology.

If tidal forces disrupted the Chelyabinsk meteoroid (*37*), events were set in motion 1.2 Ma ago during what was likely an earlier close encounter with Earth, when a 20-m sized chunk of subsurface Flora-family parent body rubble, rich in shock veins, separated from a larger object. The rest of that rubble could still be part of the near-Earth object population.

References and Notes

1. P. Jenniskens, M. D. Fries, Q. Z. Yin, M. Zolensky, A. N. Krot, S. A. Sandford, D. Sears, R. Beauford, D. S. Ebel, J. M. Friedrich, K. Nagashima, J. Wimpenny, A. Yamakawa, K. Nishiizumi, Y. Hamajima, M. W. Caffee, K. C. Welten, M. Laubenstein, A. M. Davis, S. B. Simon, P. R. Heck, E. D. Young, I. E. Kohl, M. H. Thiemens, M. H. Nunn, T. Mikouchi, K. Hagiya, K. Ohsumi, T. A. Cahill, J. A. Lawton, D. Barnes, A. Steele, P. Rochette, K. L. Verosub, J. Gattacceca, G. Cooper, D. P. Glavin, A. S. Burton, J. P. Dworkin, J. E. Elsila, S. Pizzarello, R. Ogliore, P. Schmitt-Kopplin, M. Harir, N. Hertkorn, A. Verchovsky, M. Grady, K. Nagao, R. Okazaki, H. Takechi, T. Hiroi, K. Smith, E. A. Silber, P. G. Brown, J. Albers, D. Klotz, M. Hankey, R. Matson, J. A. Fries, R. J. Walker, I. Puchtel, C. T. Lee, M. E. Erdman, G. R. Eppich, S. Roeske, Z. Gabelica, M. Lerche, M. Nuevo, B. Girten, S. P. Worden; Sutter's Mill Meteorite Consortium, Radar-enabled recovery of the Sutter's Mill meteorite, a carbonaceous chondrite regolith breccia. *Science* **338**, 1583–1587 (2012). doi:10.1126/science.1227163 Medline
2. M. B. E. Boslough, D. A. Crawford, Shoemaker-Levy 9 and Plume-forming collisions on Earth. *Ann. N. Y. Acad. Sci.* **822**, (1 Near-Earth Ob), 236–282 (1997). doi:10.1111/j.1749-6632.1997.tb48345.x
3. V. V. Svetsov, V. V. Shuvalov, Tunguska catastrophe of 30 June 1908, in *Catastrophic events Caused by Cosmic Objects*, V. Adushkin, I. Nemtchinov, Eds. (Springer, Dordrecht, 2008), pp. 227−267.
4. D. R. Christie, P. Campus, The IMS infrasound network: Design and establishment of infrasound stations, in *Infrasound Monitoring for Atmospheric Studies*, A. Le Pichon, E. Blanc, A. Hauchecorne, Eds. (Springer, Dordrecht 2010), pp. 29−75.
5. D. Yeomans, P. Chodas, Additional Details on the Large Fireball Event over Russia on Feb. 15, 2013. *NASA NEO Program Office Announcement, March 1, 2013* (NASA, Washington, 2013).
6. Materials and methods are available as supporting material on *Science* Online.
7. E. Tagliaferri, R. Spalding, C. Jacobs, S. P. Worden, A. Erlich, Detection of meteorite impacts by optical sensors in Earth orbit, in *Hazards Due to Comets and Asteroids, Space Science Series* (University of Arizona Press, Tucson, 1994), p. 199.
8. T. A. Ens, P. G. Brown, W. N. Edwards, E. A. Silber, Infrasound production of bolides: A global statistical study. *J. Atmos. Sol. Terr. Phys.* **80**, 208–229 (2012). doi:10.1016/j.jastp.2012.01.018
9. I. V. Nemtchinov, V. V. Svetsov, I. B. Kosarev, A. P. Golub', O. P. Popova, V. V. Shuvalov, R. E. Spalding, C. Jacobs, E. Tagliaferri, Assessment of kinetic energy of meteoroids detected by satellites-based light sensors. *Icarus* **130**, 259–274 (1997). doi:10.1006/icar.1997.5821
10. D. O. Revelle, Z. Ceplecha, Bolide physical theory with application to PN and EN fireballs. *ESA Special Publ.* **495**, 507–512 (2001).
11. J. Borovicka, P. Spurny, L. Shrbeny, Trajectory and orbit of the Chelyabinsk superbolide. CBET 3423, IAU Central Bureau for Astronomical Telegrams, D. W. E. Green, Ed., p. 1−1 (2013).
12. J. Zinn, J. Drummond, Observations of persistent Leonid meteor trails: 4. Buoyant rise/vortex formation as mechanism for creation of parallel meteor train pairs. *JGR Space Physics* **110**, (A4), A04306 (2005). doi:10.1029/2004JA010575
13. S. Glasstone, P. J. Dolan, *The Effects of Nuclear Weapons, Third edition* (U.S. Government Printing Office, Washington, D.C. (1977), 1−174.
14. M.-W. Huang, P.-Y. Lo, K.-S. Cheng, Objective assessment of sunburn and minimal erythema doses: Comparison of noninvasive in vitro measuring techniques after UVB irradiation. *EURASIP J. Adv. Signal Process.* **2010**, 483562 (2010). doi:10.1155/2010/483562

15. O. Popova, J. Borovicka, W. K. Hartmann, P. Spurny, E. Gnos, I. Nemtchinov, J. M. Trigo-Rodríguez, Very low strengths of interplanetary meteoroids and small asteroids. *Meteorit. Planet. Sci.* **46**, 1525–1550 (2011). doi:10.1111/j.1945-5100.2011.01247.x
16. G. J. Consolmagno, D. T. Britt, R. J. Macke, The significance of meteorite density and porosity. *Chem. Erde* **68**, 1–29 (2008). doi:10.1016/j.chemer.2008.01.003
17. A. Bischoff, E. R. D. Scott, K. Metzler, C. A. Goodrich, Nature and origins of meteoric breccias, in *Meteorites and the Early Solar System II*, D. S. Lauretta, H. Y. McSween Jr., Eds. (University of Arizona Press, Tucson, AZ, 2006), pp. 679−712.
18. M. A. Nazarov, D. D. Badyukov, N. N. Kononkova, I. V. Kubrakova, Chelyabinsk Meteoritical Bulletin: Entry for Chelyabinsk; http://www.lpi.usra.edu/meteor/metbull.php?code=57165 (2013).
19. D. Stöffler, K. Keil, E. R. D. Scott, Shock metamorphism of ordinary chondrites. *Geochim. Cosmochim. Acta* **55**, 3845–3867 (1991). doi:10.1016/0016-7037(91)90078-J
20. R. N. Clayton, T. K. Mayeda, J. N. Goswami, E. J. Olsen, Oxygen isotope studies of ordinary chondrites. *Geochim. Cosmochim. Acta* **55**, 2317–2337 (1991). doi:10.1016/0016-7037(91)90107-G
21. A. Trinquier, J.-L. Birck, C. J. Allègre, Widespread ^{54}Cr Heterogeneity in the Inner Solar System. *Astrophys. J.* **655**, 1179–1185 (2007). doi:10.1086/510360
22. C. Göpel, G. Manhès, C. J. Allègre, U-Pb systematics of phosphates from equilibrated ordinary chondrites. *Earth Planet. Sci. Lett.* **121**, 153–171 (1994). doi:10.1016/0012-821X(94)90038-8
23. Y. Amelin, Meteorite phosphates show constant ^{176}Lu decay rate since 4557 million years ago. *Science* **310**, 839–841 (2005). doi:10.1126/science.1117919 Medline
24. K. Terada, A. Bischoff, Asteroidal granite-like magmatism 4.53 Gyr ago. *Astrophys. J.* **699**, L68–L71 (2009). doi:10.1088/0004-637X/699/2/L68
25. J. N. Connelly, M. Bizzarro, A. N. Krot, Å. Nordlund, D. Wielandt, M. A. Ivanova, The absolute chronology and thermal processing of solids in the solar protoplanetary disk. *Science* **338**, 651–655 (2012). doi:10.1126/science.1226919 Medline
26. J. M. Friedrich, J. C. Bridges, M.-S. Wang, M. E. Lipschutz, Chemical studies of L chondrites. VI: Variations with petrographic type and shock-loading among equilibrated falls. *Geochim. Cosmochim. Acta* **68**, 2889–2904 (2004). doi:10.1016/j.gca.2004.01.010
27. P. Rochette, L. Sagnotti, M. Bourout-Denise, G. Consolmagno, L. Folco, J. Gattacceca, M. L. Osete, L. Pesonen, Magnetic classification of stony meteorites: 1. Ordinary chondrites. *Meteorit. Planet. Sci.* **38**, 251–268 (2003). doi:10.1111/j.1945-5100.2003.tb00263.x
28. C. P. Hartmetz, D. W. G. Sears, Thermoluminescence properties of shocked and annealed plagioclases with implications for meteorites. *Meteoritics* **22**, 400–401 (1988).
29. D. W. Sears, A. A. Mills, Temperature gradients and atmospheric ablation rates for the Barwell meteorite. *Nat. Phys. Sci (Lond.)* **242**, 25–26 (1973). doi:10.1038/physci242025a0
30. P. Schmitt-Kopplin, Z. Gabelica, R. D. Gougeon, A. Fekete, B. Kanawati, M. Harir, I. Gebefuegi, G. Eckel, N. Hertkorn, High molecular diversity of extraterrestrial organic matter in Murchison meteorite revealed 40 years after its fall. *Proc. Natl. Acad. Sci. U.S.A.* **107**, 2763–2768 (2010). doi:10.1073/pnas.0912157107 Medline
31. T. L. Dunn, T. H. Burbine, W. F. Bottke, Jr., J. P. Clark, Mineralogies and source regions of near Earth asteroids. *Icarus* **222**, 273–282 (2013). doi:10.1016/j.icarus.2012.11.007
32. T. Nakamura, T. Noguchi, M. Tanaka, M. E. Zolensky, M. Kimura, A. Tsuchiyama, A. Nakato, T. Ogami, H. Ishida, M. Uesugi, T. Yada, K. Shirai, A. Fujimura, R. Okazaki, S. A. Sandford, Y. Ishibashi, M. Abe, T. Okada, M. Ueno, T. Mukai, M. Yoshikawa, J. Kawaguchi, Itokawa dust particles: A direct link between S-type asteroids and ordinary chondrites. *Science* **333**, 1113–1116 (2011). doi:10.1126/science.1207758 Medline
33. W. F. Bottke, A. Morbidelli, R. Jedicke, J.-M. Petit, H. F. Levison, P. Michel, T. S. Metcalfe, De-biased orbital and absolute magnitude distributions of Near Earth Objects. *Icarus* **156**, 339–433 (2000).
34. P. Michel, M. Yoshikawa, Dynamical origin of the asteroid (25143) Itokawa: The target of the sample-return Hayabusa space mission. *Astron. Astrophys.* **449**, 817–820 (2006). doi:10.1051/0004-6361:20054319
35. V. Reddy, J. M. Carvano, D. Lazzaro, T. A. Michtchenko, M. J. Gaffey, M. S. Kelley, T. Mothé-Diniz, A. Alvarez-Candal, N. A. Moskovitz, E. A. Cloutis, E. L. Ryan, Mineralogical characterization of Baptistina Asteroid Family: Implications for K/T impactor source. *Icarus* **216**, 184–197 (2011). doi:10.1016/j.icarus.2011.08.027
36. D. Nesvorny, A. Morbidelli, D. Vokrouhlicky, W. F. Bottke, M. Broz, The Flora family: A case of the dynamically dispersed collisional swarm? *Icarus* **157**, 155–172 (2002). doi:10.1006/icar.2002.6830
37. E. Schunová, M. Granvik, R. Jedicke, G. Gronchi, R. Wainscoat, S. Abe, Searching for the first near-Earth object family. *Icarus* **220**, 1050–1063 (2012). doi:10.1016/j.icarus.2012.06.042
38. J. Troiano, D. Rumble, III, M. L. Rivers, J. M. Friedrich, Compositions of three low-FeO ordinary chondrites: indications of a common origin with the H chondrites. *Geochim. Cosmochim. Acta* **75**, 6511–6519 (2011). doi:10.1016/j.gca.2011.08.033
39. W. F. McDonough, Compositional model for the Earth's core, in *The Mantle and Core, Vol. 2. Treatise on Geochemistry*, R. W. Carlson, Ed. (Elsevier-Pergamon, Oxford, 2003), 547–568.
40. J. T. Wasson, G. W. Kallemeyn, Compositions of chondrites. *Phil. Trans. Roy. Soc. London A* **325**, 535–544 (1988). doi:10.1098/rsta.1988.0066
41. J. M. Friedrich, M.-S. Wang, M. E. Lipschutz, Chemical studies of L chondrites. V: Compositional patterns for 49 trace elements in 14 L4-6 and 7 LL4-6 Falls. *Geochim. Cosmochim. Acta* **67**, 2467–2479 (2003). doi:10.1016/S0016-7037(03)00024-3
42. J. I. Zuluaga, I. Ferrin, A preliminary reconstruction of the orbit of the Chelyabinsk meteoroid. 21 Feb 2013, arXiv:1302.5377v1 [astro-ph.ED] (2013).
43. P. Jenniskens, P. S. Gural, L. Dynneson, B. J. Grigsby, K. E. Newman, M. Borden, M. Koop, D. Holman, CAMS: Cameras for allsky meteor surveillance to establish minor meteor showers. *Icarus* **216**, 40–61 (2011). doi:10.1016/j.icarus.2011.08.012
44. P. S. Gural, A new method of meteor trajectory determination applied to mulitple unsynchronized video cameras. *Meteorit. Planet. Sci.* **47**, 1405–1418 (2012). doi:10.1111/j.1945-5100.2012.01402.x
45. F. L. Whipple, L. G. Jacchia, Reduction methods for photographic meteor trails. *Smiths. Contr. Astrophysics* **1**, 183–206 (1957). doi:10.5479/si.00810231.1-2.183
46. J. Borovicka, P. Spurny, L. Shrbeny, Trajectory and orbit of the Chelyabinsk superbolide. CBET 3423, D. W. E. Green, Ed., *Central Bureau for Astronomical Telegrams, International Astronomical Union*, p. 1–1 (2013).
47. D. Yeomans, P. Chodas, Additional details on the large fireball event over Russia on Feb. 15, 2013. NASA/JPL Near-Earth Object Program Office, March 1, 2013; http://neo.jpl.nasa.gov/news/fireball_130301.html (2013).
48. B. J. Gladman, F. Migliorini, A. Morbidelli, V. Zappala, P. Michel, A. Cellino, C. Froschle, H. F. Levison, M. Bailey, M. Duncan, Dynamical lifetimes of objects injected into asteroid belt. *Science* **277**, 197–201 (1997). doi:10.1126/science.277.5323.197
49. P. Jenniskens, Observations of the Stardust Sample Return Capsule entry with a slitless echelle spectrograph. *J. Spacecr. Rockets* **47**, 718–735 (2010). doi:10.2514/1.37518
50. O. Popova, Meteoroid ablation models. *Earth Moon Planets* **95**, 303–319 (2004). doi:10.1007/s11038-005-9026-x
51. V. V. Svetsov, I. V. Nemtchinov, A. V. Teterev, Disintegration of large meteoroids in Earth's atmosphere: Theoretical models. *Icarus* **116**, 131–153 (1995). doi:10.1006/icar.1995.1116
52. A. P. Golub', I. B. Kosarev, I. V. Nemtchinov, O. P. Popova, Emission spectra of bright bolides. *Sol. Syst. Res.* **31**, 85–98 (1997).
53. M. Boslough, D. Crawford, A. Robinson, T. Trucano, Mass and penetration depth of Shoemaker-Levy 9 fragments from time-resolved photometry. *Geophys. Res. Lett.* **21**, 1555–1558 (1994). doi:10.1029/94GL01582
54. V. V. Shuvalov, N. A. Artemieva, Numerical modeling of Tunguska-like impacts. *Planet. Space Sci.* **50**, 181–192 (2002). doi:10.1016/S0032-0633(01)00079-4
55. B. Baldwin, Y. Sheaffer, Ablation and breakup of large meteoroids during atmospheric entry. *J. Geophys. Res.* **76**, 4653–4668 (1971). doi:10.1029/JA076i019p04653
56. J. Borovička, O. P. Popova, I. V. Nemtchinov, P. Spurný, Z. Ceplecha, Bolides produced by impacts of large meteoroids into the Earth's atmosphere: Comparison of theory with observations. I. Benesov bolide dynamics and

fragmentation. *Astron. Astrophys.* **334**, 713–728 (1998).
57. P. A. Bland, N. A. Artemieva, The rate of small impacts on Earth. *Meteorit. Planet. Sci.* **41**, 607–631 (2006). doi:10.1111/j.1945-5100.2006.tb00485.x
58. Z. Ceplecha, P. Spurny, J. Borovička, J. Keclikova, Atmospheric fragmentation of meteoroids. *Astron. Astrophys.* **279**, 615–626 (1993).
59. Z. Ceplecha, D. O. Revelle, Fragmentation model of meteoroid motion, mass loss, and radiation in the atmosphere. *Meteorit. Planet. Sci.* **40**, 35–54 (2005). doi:10.1111/j.1945-5100.2005.tb00363.x
60. O. P. Popova, Passage of Bolides Through the Atmosphere. Meteoroids: The Smallest Solar System Bodies, Proc. Meteoroids Conference, Breckenridge, Colorado, USA, May 24–28, 2010, W. J. Cooke, D. E. Moser, B. F. Hardin, D. Janches, Eds. NASA/CP-2011-216469, p. 232 (2011).
61. V. I. Tsvetkov, A. Ya. Skripnik, Atmospheric fragmentation of meteorites according to strength theory. *Sol. Syst. Res.* **25**, 273–279 (1991).
62. O. Popova, J. Borovička, W. K. Hartmann, P. Spurný, E. Gnos, I. Nemtchinov, J. M. Trigo-Rodríguez, Very low strength of interplanetary meteoroids and small asteroids. *Meteorit. Planet. Sci.* **46**, 1525–1550 (2011). doi:10.1111/j.1945-5100.2011.01247.x
63. Z. Ceplecha, J. Borovička, W. G. Elford, D. O. ReVelle, R. L. Hawkes, V. Í. Porubčan, M. Šimek, Meteor phenomena and bodies. *Space Sci. Rev.* **84**, 327–471 (1998). doi:10.1023/A:1005069928850
64. A. P. Golub', I. B. Kosarev, I. V. Nemtchinov, V. V. Shuvalov, Emission and ablation of a large meteoroid in the course of its motion through the Earth's atmosphere. *Sol. Syst. Res.* **30**, 183–197 (1996).
65. I. V. Nemtchinov, V. V. Svetsov *et al*., Assessment of kinetic energy of meteoroids detected by satellite-based light sensors. *Icarus* **130**, 259–274 (1997). doi:10.1006/icar.1997.5821
66. A. R. Klekociuk, P. G. Brown, D. W. Pack, D. O. ReVelle, W. N. Edwards, R. E. Spalding, E. Tagliaferri, B. B. Yoo, J. Zagari, Meteoritic dust from the atmospheric disintegration of a large meteoroid. *Nature* **436**, 1132–1135 (2005). doi:10.1038/nature03881 Medline
67. J. Borovička, Z. Charavat, Meteosat observation of the atmospheric entry of 2008 TC3 over Sudan and associated dust cloud. *Astron. Astrophys.* **507**, 1015–1022 (2009). doi:10.1051/0004-6361/200912639
68. J. Zinn, J. Drummond, Observations of persistent Leonid meteor trails: 4. Buoyant model rise/vortex formation as mechanism for creation of parallel meteor train pairs. *JGR Space Physics* **110**, (A4), A04306 (2005). doi:10.1029/2004JA010575
69. Comprehensive Nuclear-Test-Ban Treaty organization (CTBTO) press release, 18.02.2013; http://www.ctbto.org/press-centre/press-releases/2013/russian-fireball-largest-ever-detected-by-ctbtos-infrasound-sensors/ (2013).
70. Y. Cansi, An automatic seismic event processing for detection and location: The P.M.C.C. method. *Geophys. Res. Lett.* **22**, 1021–1024 (1995). doi:10.1029/95GL00468
71. Yu. S. Rybnov, V. A. Kharlamov, V. F. Evmenov, Infrasound registration system of acoustic-gravitational waves, in *Dynamic Processes in a System of Inner and Outer Interacting Geospheres*, V. V. Adushkin, Ed., pp. 29–34 (2005).
72. M. A. Tsikulin, Shock waves during the movement of large meteorites in the atmosphere. Moscow, Nauka, 86 p. (1969). (English Translation: AD 715-537, National Technical Information Service, Springfield, Virginia, 1970)
73. D. O. ReVelle, Historical detection of atmospheric impacts by large bolides using acoustic-gravity waves, in Annals of the New York Academy of Sciences, Near- Earth Objects: The United Nations International Conference, J. L. Remo, Ed., New York Academy of Sciences, 822, 284–302 (1997).
74. W. N. Edwards, P. G. Brown, D. O. ReVelle, Estimates of meteoroid kinetic energies from observations of infrasonic airwaves. *J. Atmos. Sol. Terr. Phys.* **68**, 1136–1160 (2006). doi:10.1016/j.jastp.2006.02.010
75. W. N. Edwards, Meteor generated infrasound: Theory and observation, in *Infrasound Monitoring for Atmospheric Studies*, A. Le Pichon, E. Blanc, A. Hauchecorne, Eds., (Springer, Dordrecht, Netherlands, 2010), pp. 361–414.
76. E. Silber, D. O. ReVelle, P. G. Brown, W. N. Edwards, An estimate of the terrestrial influx of large meteoroids from infrasonic measurements. *J. Geophys. Res.* **114**, (E8), E08006 (2009). doi:10.1029/2009JE003334
77. J. L. Stevens, D. A. Adams, G. E. Baker, H. Xu, J. R. Murphy, I. Divnov, V. N. Bourchik, Infrasound Modeling Using Soviet Explosion Data and Instrument Design Criteria from Experiments and Simulations. Technical Report ADA446517S (2006).
78. P. Brown, A preliminary report on the Chelyabinsk fireball/airburst. *J. Int. Meteor Org.* **41**, 22–25 (2013).
79. J. P. Mutschlecner, R. W. Whitaker, L. H. Auer, An empirical study of infrasonic propagation, Los Alamos National Laboratory Technical Report, LA-13620-MS, Los Alamos, NM (1999).
80. J. P. Mutschlecner, R. W. Whitaker, Some atmospheric effects on infrasound signal amplitudes, in *Infrasound Monitoring for Atmospheric Studies*, A. Le Pichon, E. Blanc, A. Hauchecorne, Eds. (Springer, Dordrecht, Netherlands, 2010), pp. 455–474.
81. K. E. Gubkin, About similarity of explosions. *Физ. Земли Fizika Zemli* **N10**, 49–60 (1978).
82. J. Reed, Airblast overpressure decay at long ranges. *J. Geophys. Res.* **77**, 1623–1629 (1972). doi:10.1029/JC077i009p01623
83. V. N. Arkhipov *et al*., Mechanical Action of Nuclear Explosions. (Fizmatlit, Moscow, (2003), 384 p.
84. S. Glasstone, P. J. Dolan, *The Effects of Nuclear Weapons* (U.S. Department of Defense, U.S. Department of Energy, Washington, 1977).
85. J. Reed, Climatology of Airblast Propagations from Nevada Test Site Nuclear Airbursts. Sandia Laboratories Report SC-RR-69-572 (1969).
86. M. Lutzky, D. Lechto, Shock propagation in spherically symmetric exponential atmosphere. *Phys. Fluids* **11**, 1466–1472 (1968). doi:10.1063/1.1692129
87. S. Mannan, F. P. Lees, Lees' Loss Prevention in the Process Industries: Hazard Identification, Assessment and Control, vol. 1, 3rd edition (Elsevier Butterworth-Heinemann, 2005).
88. M. D. Brown, A. S. Loewe, Reference manual to mitigate potential terrorist attacks against buildings. USA, FEMA, p. 4–19 (2003).
89. V. V. Shuvalov, Multi-dimensional hydrodynamic code SOVA for interfacial flows: Application to thermal layer effect. *Shock Waves* **9**, 381–390 (1999). doi:10.1007/s001930050168
90. N. M. Kuznetsov, Thermodynamic Functions and Shock Adiabats for Air at high Temperatures (Mashinostroyenie, Moscow, 1965).
91. C. E. Needham, *Blast Waves: Shock Wave And High Pressure Phenomena* (Springer-Verlag, Berlin, 2010), 339 pp..
92. J. R. Blackford, Sintering and microstructure of ice: A review. *J. Phys. D.* **40**, R355–R385 (2007). doi:10.1088/0022-3727/40/21/R02
93. A. van Herwijnen, D. A. Miller, Experimental and numerical investigation of the sintering of snow. *J. Glaciol.* **59**, 269–274 (2013). doi:10.3189/2013JoG12J094
94. A. N. Kolmogorov, Selected Proceedings: Probability Theory and Mathematical Statistics, M. Nauka, Ed. (1986).
95. I. T. Zotkin, Stony meteorite shower Tsarev. *Meteoritika* **41**, 3–12 (1982).
96. P. Jenniskens, M. H. Shaddad, D. Numan, S. Elsir, A. M. Kudoda, M. E. Zolensky, L. Le, G. A. Robinson, J. M. Friedrich, D. Rumble, A. Steele, S. R. Chesley, A. Fitzsimmons, S. Duddy, H. H. Hsieh, G. Ramsay, P. G. Brown, W. N. Edwards, E. Tagliaferri, M. B. Boslough, R. E. Spalding, R. Dantowitz, M. Kozubal, P. Pravec, J. Borovicka, Z. Charvat, J. Vaubaillon, J. Kuiper, J. Albers, J. L. Bishop, R. L. Mancinelli, S. A. Sandford, S. N. Milam, M. Nuevo, S. P. Worden, The impact and recovery of asteroid 2008 TC(3). *Nature* **458**, 485–488 (2009). doi:10.1038/nature07920 Medline
97. Q. R. Passey, H. J. Melosh; Q. R. Passey H. J. Melosh, Effects of atmospheric breakup on crater field formation. *Icarus* **42**, 211–233 (1980). doi:10.1016/0019-1035(80)90072-X
98. E. D. Narkhov, V. A. Sapunov, A. Yu. Denisov, D. V. Savelyev, D. A. Galkin, D. S. Yakovenko, A. L. Fedorov, Magnetic prospecting and data interpretation of the Chebarkul meteorite. In: Proceedings of the International Workshop Asteroids and Comets: The Chelyabinsk event and the Chebarkul lake meteorite fall, Chebarkul, June 21–22, 2013, (Kray Ra, Chelyabinsk, 2013), pp. 72–75.
99. M. L. Gittings *et al*., The RAGE radiation-hydrodynamic code, Los Alamos National Laboratory Report LA-UR- 06-0027, Los Alamos, New Mexico. Published in: Computational Science and Discovery 1, 015005 (2008).
100. J. Kimberley, K. T. Ramesh, The dynamic strength of an ordinary chondrite. Meteoritics and Plan. *Sci.* **46**, 1653–1669 (2011).
101. R. V. Medvedev, F. Gorbachevich, I. Zotkin, Determination of physical properties of stone meteorites from the point of view of their disruption. *Meteoritika* **44**, 105–110 (1985).
102. I. T. Zotkin, P. V. Medvedev, F. F. Gorbatsevich, Strength properties of the Tsarev meteorite. *Meteoritika* **46**, 86–93 (1987).

103. E. N. Slyuta, S. M. Nikitin, A. V. Korochantsev, C. A. Lorents, A. Ya. Skripnik, Strong physical and mechanical anisotropy of ordinary chondrites. 40th Lunar and Planetary Science Conference, Abstr.1051 (2010).
104. J. M. Friedrich, Quantitative methods for three-dimensional comparison and petrographic description of chondrites. *Comput. Geosci.* **34**, 1926–1935 (2008). doi:10.1016/j.cageo.2008.05.001
105. J. M. Friedrich, D. P. Wignarajah, S. Chaudhary, M. L. Rivers, C. E. Nehru, D. S. Ebel, Three-dimensional petrography of metal phases in equilibrated L chondrites: Effects of shock loading and dynamic compaction. *Earth Planet. Sci. Lett.* **275**, 172–180 (2008). doi:10.1016/j.epsl.2008.08.024
106. E. Jarosewich, Chemical analyses of meteorites: A compilation of stony and iron meteorite analyses. *Meteoritics* **25**, 323–337 (1990). doi:10.1111/j.1945-5100.1990.tb00717.x
107. H. C. Urey, H. Craig, The composition of the stone meteorites and the origin of the meteorites. *Geochim. Cosmochim. Acta* **4**, 36–82 (1953). doi:10.1016/0016-7037(53)90064-7
108. A. J. Brearley, R. H. Jones, Chondritic meteorites, in *Planetary Materials*, J. J. Papike, Ed., Mineralogical Society of America, Reviews in Mineralogy 36, pp. 3-1–3-398 (1998).
109. A. N. Krot, K. Keil, E. R. D. Scott, C. A. Goodrich, M. K. Weisberg, Classification of meteorites and their genetic relationships, in *Meteorites, Comets and Planets*, A. M. Davis, Ed., Vol. 1, Treatise on Geochemistry (K. K. Turekian, H. D. Holland, Eds.) (Elsevier, Oxford, 2013).
110. J. M. Friedrich, A. Ruzicka, M. L. Rivers, D. S. Ebel, J. O. Thostenson, R. A. Rudolph, Metal veins in the Kernouve (H6 S1) chondrite: Evidence for pre- or syn-metamorphic shear deformation. *Geochim. Cosmochim. Acta* **116**, 71–83 (2013). doi:10.1016/j.gca.2013.01.009
111. N. H. Woodcock, Specification of fabric shapes using an eigenvalue method. *Geol. Soc. Am. Bull.* **88**, 1231–1236 (1977). doi:10.1130/0016-7606(1977)88<1231:SOFSUA>2.0.CO;2
112. N. H. Woodcock, M. A. Naylor, Randomness testing in three-dimensional orientation data. *J. Struct. Geol.* **5**, 539–548 (1983). doi:10.1016/0191-8141(83)90058-5
113. P. Rochette, L. Sagnotti, G. Consolmagno, L. Folco, A. Maras, F. Panzarino, L. Pesonen, R. Serra, M. Terho, A magnetic susceptibility database for stony meteorites. *Quaderni di Geofisica* **18**, 1–31 (2001).
114. S. J. Morden, The anomalous demagnetization behaviour of chondritic meteorites. *Phys. Earth Planet. Interiors* **71**, 189–204 (1992).
115. J. Gattacceca, P. Rochette, Toward a robust normalized magnetic paleointensity method applied to meteorites. *Earth Planet. Sci. Lett.* **227**, 377–393 (2004). doi:10.1016/j.epsl.2004.09.013
116. E. Jarosewich, R. S. Clarke, Jr., J. N. Barrows, Eds., The Allende meteorite reference sample. *Smithson. Contrib. Earth Sci.* **27**, 1–49 (1986).
117. P. G. Brown, A. R. Hildebrand, M. E. Zolensky, M. Grady, R. N. Clayton, T. K. Mayeda, E. Tagliaferri, R. Spalding, N. D. MacRae, E. L. Hoffman, D. W. Mittlefehldt, J. F. Wacker, J. A. Bird, M. D. Campbell, R. Carpenter, H. Gingerich, M. Glatiotis, E. Greiner, M. J. Mazur, P. J. McCausland, H. Plotkin, T. Rubak Mazur, The fall, recovery, orbit, and composition of the Tagish Lake meteorite: A new type of carbonaceous chondrite. *Science* **290**, 320–325 (2000). doi:10.1126/science.290.5490.320 Medline
118. J. M. Friedrich, M.-S. Wang, M. E. Lipschutz, Comparison of the trace element composition of Tagish Lake with other primitive carbonaceous chondrites. *Meteorit. Planet. Sci.* **37**, 677–686 (2002). doi:10.1111/j.1945-5100.2002.tb00847.x
119. K. Lodders, Solar system abundances and condensation temperatures of the elements. *Astrophys. J.* **591**, 1220–1247 (2003). doi:10.1086/375492
120. Metbase homepage; http://www.metbase.de/home.html (2013).
121. A. Yamakawa, K. Yamashita, A. Makishima, E. Nakamura, Chemical separation and mass spectrometry of Cr, Fe, Ni, Zn, and Cu in terrestrial and extraterrestrial materials using thermal ionization mass spectrometry. *Anal. Chem.* **81**, 9787–9794 (2009). doi:10.1021/ac901762a Medline
122. W. R. Shields, T. J. Murphy, E. J. Catanzaro, E. L. Garner, Absolute isotopic abundance ratios and the atomic weight of a reference sample of chromium. *J. Res. Natl. Bur. Stand.* **70A**, 193–197 (1966). doi:10.6028/jres.070A.016
123. A. Trinquier, J.-L. Birck, C. J. Allègre, C. Göpel, D. Ulfbeck, 53Mn–53Cr systematics of the early solar system revisited. *Geochim. Cosmochim. Acta* **72**, 5146–5163 (2008). doi:10.1016/j.gca.2008.03.023
124. P. H. Warren, Stable-isotopic anomalies and the accretionary assemblage of the Earth and Mars: A subordinate role for carbonaceous chondrites. *Earth Planet. Sci. Lett.* **311**, 93–100 (2011). doi:10.1016/j.epsl.2011.08.047
125. L. Qin, C. M. O. D. Alexander, R. W. Carlson, M. F. Horan, T. Yokoyama, Contributors to chromium isotope variation of meteorites. *Geochim. Cosmochim. Acta* **74**, 1122–1145 (2010). doi:10.1016/j.gca.2009.11.005
126. A. Yamakawa, K. Yamashita, A. Makishima, E. Nakamura, Chromium isotope systematics of achondrites: Chronology and isotopic heterogeneity of the inner solar system bodies. *Astrophys. J.* **720**, 150–154 (2010). doi:10.1088/0004-637X/720/1/150
127. I. Ahn, J. Lee, M. Kusakabe, B. Choi, Oxygen isotope measurements of terrestrial silicates using a CO2-laser BrF5 fluorination technique and the slope of terrestrial fractionation line. *Geosci. J.* **16**, 7–16 (2012). doi:10.1007/s12303-012-0011-x
128. Z. D. Sharp, A laser-based microanalytical method for the in situ determination of oxygen isotope ratios of silicates and oxides. *Geochim. Cosmochim. Acta* **54**, 1353–1357 (1990). doi:10.1016/0016-7037(90)90160-M
129. R. N. Clayton, T. K. Mayeda, Oxygen isotope studies of carbonaceous chondrites. *Geochim. Cosmochim. Acta* **63**, 2089–2104 (1999). doi:10.1016/S0016-7037(99)00090-3
130. E. D. Young, S. S. Russell, Oxygen reservoirs in the early solar nebula inferred from an Allende CAI. *Science* **282**, 452–455 (1998). doi:10.1126/science.282.5388.452
131. R. N. Clayton, T. K. Mayeda, A. E. Rubin, Oxygen isotopic compositions of enstatite chondrites and aubrites. *J. Geophys. Res.* **89**, (S01), C245–C249 (1984). doi:10.1029/JB089iS01p0C245
132. R. N. Clayton, T. K. Mayeda, Oxygen isotope studies of achondrites. *Geochim. Cosmochim. Acta* **60**, 1999–2017 (1996). doi:10.1016/0016-7037(96)00074-9
133. C. Gopel, J.-L. Birck, Mn/Cr systematics: A tool to discriminate the origin of primitive meteorites? Goldschmidt Conference Abstracts, A348 (2010).
134. A. J. Irving, R. Tanaka, A. Steele, S. M. Kuehner, T. E. Bunch, J. H. Wittke, G. M. Hupe, Northwest Africa 6704: A unique cumulate permafic achondrite containing sodic feldspar, awaruite and "fluid" inclusions, with an oxygen isotopic composition in the Acapulcoite-Lodranite field. Annual Meteoritical Society Meeting, #5231 (2011).
135. Q. L. Li, X. H. Li, F. Y. Wu, Q. Z. Yin, H. M. Ye, Y. Liu, G. Q. Tang, C. L. Zhang, In-situ SIMS U-Pb dating of phanerzoic apatite with low U and high common Pb. *Gondwana Res.* **21**, 745–756 (2012). doi:10.1016/j.gr.2011.07.008
136. T. Sano, S. M. Miyama, Magnetorotational instability in protoplanetary disks. I. On the global stability of weakly ionized disks with ohmic dissipiation. *Astrophys. J.* **515**, 776–786 (1999). doi:10.1086/307063
137. J. A. Trotter, S. M. Eggins, Chemical systematics of conodont apatite determined by laser ablation ICPMS. *Chem. Geol.* **233**, 196–216 (2006). doi:10.1016/j.chemgeo.2006.03.004
138. M. Tatsumoto, R. J. Knight, C. J. Allegre, Time differences in the formation of meteorites as determined from the ratio of lead-207 to lead-206. *Science* **180**, 1279–1283 (1973). doi:10.1126/science.180.4092.1279 Medline
139. K. R. Ludwig, User's manual for Isoplot, v. 3.0, a geochronological toolkit for Microsoft Excel. Berkeley Geochronological Center, Special Publication 4 (2003).
140. Y. Amelin, A. Kaltenbach, C. H. Stirling, The U-Pb systematics and cooling rate of plutonic angrite NWA 4590. 42nd Lunar and Planetary Science Conference 2011, Abstract 1682 (2011).
141. T. Mikouchi, K. Sugiyama, W. Satake, Y. Amelin, Mineralogy and Crystallography of Calcium Silico-Phosphate in Northwest Africa 4590 Angrite. 42nd Lunar and Planetary Science Conference 2011, Abstract 2026 (2011).
142. Y. Amelin, A. Ghosh, E. Rotenberg, Unraveling the evolution of chondrite parent asteroids by precise U-Pb dating and thermal modeling. *Geochim. Cosmochim. Acta* **69**, 505–518 (2005). doi:10.1016/j.gca.2004.05.047
143. T. Hiroi, S. Sasaki, S. K. Noble, C. M. Pieters, Space weathering of ordinary chondrite parent bodies, its impact on the method of distinguishing H, L, and LL types and implications for Itokawa samples returned by the Hayabusa mission. 42nd Lunar and Planetary Science Conference 2011, Abstract 1264 (2011).
144. T. Hiroi, M. Abe, K. Kitazato, S. Abe, B. E. Clark, S. Sasaki, M. Ishiguro, O. S. Barnouin-Jha, Developing space weathering on the asteroid 25143 Itokawa. *Nature* **443**, 56–58 (2006). doi:10.1038/nature05073 Medline

145. R. H. Biswas, P. Morthekai, R. K. Gartia, S. Chawla, A. K. Singhvi, Thermoluminescence of the meteorite interior: A possible tool for the estimation of cosmic ray exposure ages. *Earth Planet. Sci. Lett.* **304**, 36–44 (2011). doi:10.1016/j.epsl.2011.01.012
146. D. W. G. Sears, A. A. Mills, Temperature gradients and atmospheric ablation rates for the Barwell meteorite. *Nat. Phys. Sci (Lond.)* **242**, 25–26 (1973). doi:10.1038/physci242025a0
147. R. Chen, S. W. S. McKeever, Theory of thermoluminescence and related phenomena. (World Scientific, Singapore, 1997), 560 pp.
148. D. W. G. Sears, K. Ninagawa, A. Signhvi, Luminescence studies of extraterrestrial materials: Insights into their recent radiation and thermal histories and into their metamorphic history. *Chemie Erde Geochemistry* **73**, 1–37 (2013). http://dx.doi.org/10.1016/j.chemer.2012.12.001
149. M. Haq, F. A. Hasan, D. W. G. Sears, Thermoluminescence and the shock and reheating history of meteorites- IV: The induced TL properties of type 4-6 ordinary chondrites. *Geochim. Cosmochim. Acta* **52**, 1679–1689 (1988). doi:10.1016/0016-7037(88)90236-0
150. R. K. Guimon, K. S. Weeks, B. D. Keck, D. W. G. Sears, Thermoluminescence as a palaeothermometer. *Nature* **311**, 363–365 (1984). doi:10.1038/311363a0
151. W. R. Van Schmus, J. A. Wood, A chemical-petrologic classification for the chondritic meteorites. *Geochim. Cosmochim. Acta* **31**, 747–765 (1967). doi:10.1016/S0016-7037(67)80030-9
152. D. W. G. Sears, J. N. Grossman, C. L. Melcher, L. M. Ross, A. A. Mills, Measuring the metamorphic history of unequilibrated ordinary chondrites. *Nature* **287**, 791–795 (1980). doi:10.1038/287791a0
153. C. P. Hartmetz, R. Ostertag, D. W. G. Sears, A thermoluminescence study of experimentally shock-loaded oligoclase and bytownite. *J. Geophys. Res.* **91**, (B13), E263–E274 (1986). doi:10.1029/JB091iB13p0E263
154. P. H. Benoit, H. Sears, D. W. G. Sears, The natural thermoluminescence of meteorites- IV: Ordinary chondrites at the Lewis Cliff ice field. *J. Geophys. Res.* **97**, (B4), 4629–4647 (1992). doi:10.1029/91JB02982
155. P. Schmitt-Kopplin, Z. Gabelica, R. D. Gougeon, A. Fekete, B. Kanawati, M. Harir, I. Gebefuegi, G. Eckel, N. Hertkorn, High molecular diversity of extraterrestrial organic matter in Murchison meteorite revealed 40 years after its fall. *Proc. Natl. Acad. Sci. U.S.A.* **107**, 2763–2768 (2010). doi:10.1073/pnas.0912157107 Medline
156. D. Tziotis, N. Hertkorn, P. Schmitt-Kopplin, Kendrick-analogous network visualisation of ion cyclotron resonance Fourier transform mass spectra: Improved options for the assignment of elemental compositions and the classification of organic molecular complexity. *Eur. J. Mass Spectrom. (Chichester, Eng.)* **17**, 415–421 (2011). doi:10.1255/ejms.1135 Medline
157. C. M. Hohenberg, F. A. Podosek, J. R. Shirck, K. Arti, R. C. Reedy, Comparisons between observed and predicted cosmogenic noble gases in lunar samples. In: Proceedings 9th Lunar and Planetary Science Conference, Houston, TX, March 13–17, 1978, Vol. 2, New York, Pergamon Press, Inc., pp. 2311–2344 (1978).

Acknowledgments: The Russian Academy of Sciences field study of the Chelyabinsk airburst was supported by the Institute for Dynamics of Geospheres and grants of the Federal Targeted Program "Scientific and Educational Human Resources of Innovation-Driven Russia" and the RAS Presidium Program "Fundamental Problems of Investigation and Exploration of the Solar System". The office of Chelyabinsk Oblast Governor Mikhail Yurevich provided assistance. S. Petukhov and I. Talyukin from the Universe History Museum in Dedovsk contributed samples, as did M. Boslough of Sandia National Laboratories. U. Johann (Astrium Satellites GmbH) calculated the Chebarkul hole position from Pléiades 1A satellite observations. D. F. Blake provided use of a petrographic microscope. P.J. acknowledges support from the NASA Near Earth Object Observation Program, Q.Z.Y. and M.E.Z. from the NASA Cosmochemistry Program, and M.G. by the Academy of Finland.

Supplementary Materials
www.sciencemag.org/cgi/content/full/science.1242642/DC1
Supplementary Text
Figs. S1 to S87
Tables S1 to S24
References (*42–157*)

1 July 2013; accepted 28 October 2013
Published online 7 November 2013
10.1126/science.1242642

Author Affiliations
[1]Institute for Dynamics of Geospheres of the Russian Academy of Sciences, Leninsky Prospect 38, Building 1, Moscow, 119334, Russia. [2]SETI Institute, 189 Bernardo Ave, Mountain View, CA 94043, USA. [3]NASA Ames Research Center, Moffett Field, Mail Stop 245-1, CA 94035, USA. [4]Institute of Astronomy of the Russian Academy of Sciences, Pyatnitskaya 48, Moscow, 119017, Russia. [5]Department of Theoretical Mechanics, South Ural State University, Lenin Avenue 76, Chelyabinsk, 454080, Russia. [6]Chelyabinsk State University, Bratyev Kashirinyh Street 129, Chelyabinsk, 454001, Russia. [7]Institute of Physics and Technology, Ural Federal University, Mira Street 19, Yekaterinburg, 620002, Russia. [8]Vernadsky Institute of Geochemistry and Analytical Chemistry of the RAS, Kosygina Street 19, Moscow, 119991, Russia. [9]Department of Earth and Planetary Sciences, University of California at Davis, Davis, CA 95616, USA. [10]Department of Physics, University of Helsinki, P. O. Box 64, 00014 Helsinki, Finland. [11]Koninklijk Nederlands Meteorologisch Instituut, P. O. Box 201, 3730 AE De Bilt, Netherlands. [12]Department of Geoscience and Engineering, Faculty of Civil Engineering and Geosciences, Delft University of Technology, P.O. Box 5048, 2600 GA Delft, Netherlands. [13]Tomsk State University, Lenina Prospect 36, Tomsk, 634050 Russia. [14]Research and Production Association "Typhoon", fl. 2, 7 Engels Street, Obninsk, 249032, Russia. [15]Support Foundation for Astronomy "Ka-Dar", P.O. Box 82, Razvilka, 142717 Russia. [16]Science and Technology Center of the Social and Youth Initiatives Organization, 3-12-63 Udal'tsova Street, Moscow, 119415, Russia. [17]University of Oslo, Physics Building, Sem Saelands Vel 24, 0316 Oslo, Norway. [18]Institute of Engineering Sciences Urals Branch of the Russian Academy of Sciences, Komsomolskaya Street 34, Yekaterinburg, 620049, Russia. [19]Center for Molecular and Genomic Imaging, University of California, Davis, Davis, CA 95616, USA. [20]Department of Earth and Planetary Sciences, American Museum of Natural History, New York, NY 10024, USA. [21]Department of Chemistry, Fordham University, Bronx, NY 10458, USA. [22]Astromaterials Research and Exploration Science, NASA Johnson Space Center, Houston, TX 77058, USA. [23]Jacobs Technology, 2224 Bay Area Boulevard, Houston TX 77058, USA. [24]Institute of Meteoritics, University of New Mexico, Albuquerque, NM 87131–0001, USA. [25]Department of Earth and Planetary Materials Science, Tohoku University, Aramaki, Aoba, Sendai, Miyagi 980-8578, Japan. [26]Division of Polar Earth-System Sciences, Korea Polar Research Institute, 26 Songdomi rae, Yeonsu-gu, Incheon 406-840, Korea. [27]National Astronomical Observatories, Beijing, Chinese Academy of Sciences, Beijing 100012, China. [28]State Key Laboratory of Lithospheric Evolution, Institute of Geology and Geophysics, Chinese Academy of Sciences, Beijing 100029, China. [29]Department of Geological Sciences, Brown University, Providence, RI 02912, USA. [30]Analytical BioGeoChemistry, Helmoltz Zentrum Muenchen, Ingoldstäter Landstrasse 1, D-85764 Obeschleissheim, Germany. [31]Technical University Muenchen, Analytical Food Chemistry, Alte Akademie 10, 85354 Freising, Germany. [32]Geochemical Research Center, The University of Tokyo, 7-3-1 Hongo, Bunkyo-ku, Tokyo 113-0033, Japan. [33]Waseda Institute for Advanced Study, Waseda University, 1-6-1 Nishiwaseda, Shinjuku, Tokyo 169-8050, Japan. [34]Department of Earth and Planetary Science, The University of Tokyo, 7-3-1 Hongo, Bunkyo-ku, Tokyo 113-0033, Japan.

Table 1. Atmospheric trajectory and pre-atmospheric orbit for the Chelyabinsk meteoroid, with 2 standard deviation uncertainties. Angular elements are for equinox J2000.0.

Atmospheric trajectory	Chelyabinsk	Pre-atmospheric orbit	Chelyabinsk	Itokawa
H_b (beginning height, km)	97.1 ± 1.6	T_J (Tisserand's parameter)	3.87 ± 0.24	4.90
H_m (peak brightness, km)	29.7 ± 1.4	a (semimajor axis, AU)	1.76 ± 0.16	1.324
H_f (disruption, km)	27.0 ± 1.4	e (eccentricity)	0.581 ± 0.018	0.280
H_e (end height, km)	13.6 ± 1.4	q (perihelion distance, AU)	0.739 ± 0.020	0.953
V_∞ (entry speed, km/s)	19.16 ± 0.30	ω (argument of perihelion, °)	108.3 ± 3.8	162.8
h (entry elevation angle, °)	18.3 ± 0.4	Ω (longitude of ascending node, °)	326.4422 ± 0.0028	69.1
a_z (entry azimuth angle from South, °)	283.2 ± 0.4	i (inclination, °)	4.93 ± 0.48	1.6
V_g (geocentric entry speed, km/s)	15.3 ± 0.4	Q (aphelion distance, AU)	2.78 ± 0.20	1.70
Ra_g (geocentric right ascension of radiant, °)	333.2 ± 1.6	T_p (perihelion time)	2012-12-31.9 ± 2.0	2013-07-10.8
Dec_g (geocentric declination of radiant, °)	+0.3 ± 1.8	Epoch (ET)	2013-02-15.139	2013-04-18.0

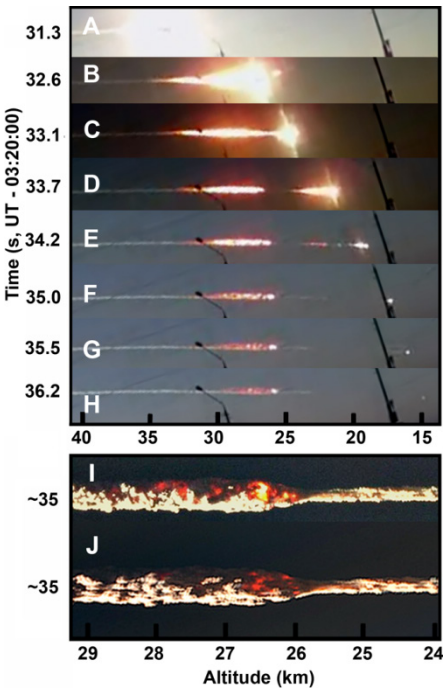

Fig. 1. Meteoroid fragmentation stages in video taken by Aleksandr Ivanov in Kamensk-Uralskiy. (**A**) Fireball just before peak brightness, at the moment when camera gain first adjusted. (**B**) End of main disruption. (**C**) Onset of secondary disruption. (**D**) End of secondary disruption, main debris cloud continues to move down. (**E**) Two main fragments remain. (**F**) Single fragment remains. (**G**) Thermally emitting debris cloud at rest with atmosphere. (**H**) Final fragment continues to penetrate. Meteor moved behind distant lamp posts. (**I** and **J**) Detail of the thermal emission from a photograph by Mr. Dudarev (I) and Marat Ahmatvaleev (J), after sky subtraction with high-pass filter and contrast enhancement. Altitude scale is uncertain by ±0.7 km.

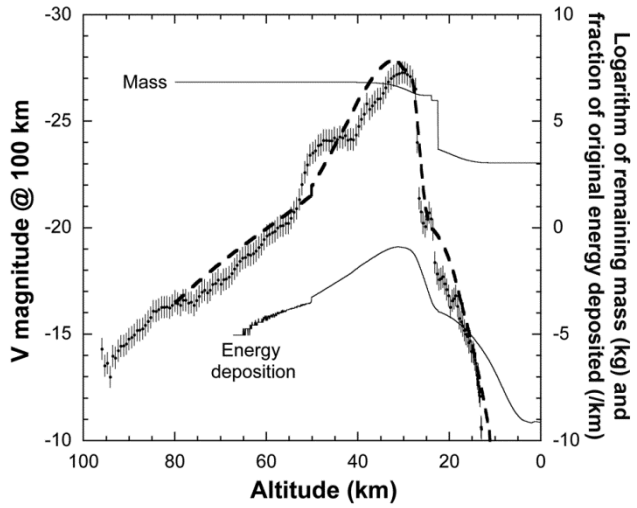

Fig. 2. Fireball visual magnitude irradiance lightcurve, normalized to 100 km distance. The bold dashed line shows the model fit to the lightcurve (SM Sect. 1.2), with thin lines showing total mass of all fragments passing a given altitude (kg) and the altitude dependent rate of energy deposition as a fraction of the original kinetic energy (km^{-1}).

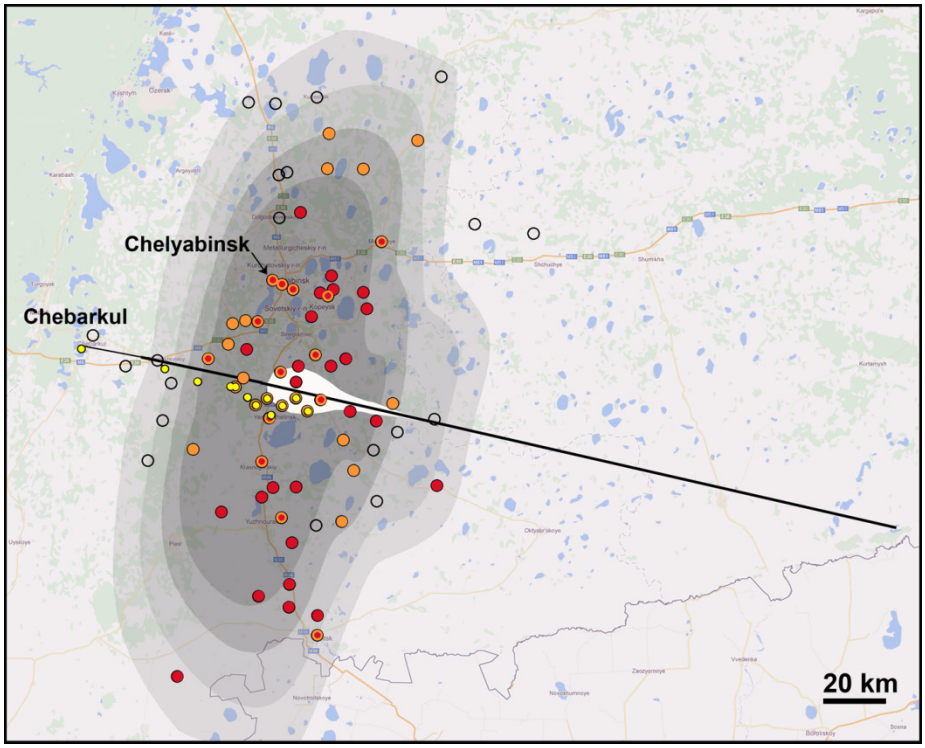

Fig. 3. Map of glass damage on the ground with models of overpressure. Field survey data are shown in solid orange circles for reported damage and open black circles for no damage, while solid red circles are the most damaged villages in each district reported by the government. Each point, irrespective of population density, represents one of many villages or city districts scattered throughout the area. Model contours (with progressive grey scale) represent kinetic energies and over pressures from inside out: 300 kT $\Delta p > 1{,}000$ Pa, 520 kT $\Delta p > 1{,}000$ Pa, 300 kT $\Delta p > 500$ Pa, and 520 kT $\Delta p > 500$ Pa, respectively. Also shown are the locations of meteorite finds (yellow points) and the ground-projected fireball trajectory (black line), moving from 97 km altitude right to 14 km altitude left. White shows the fireball brightness on a linear scale.

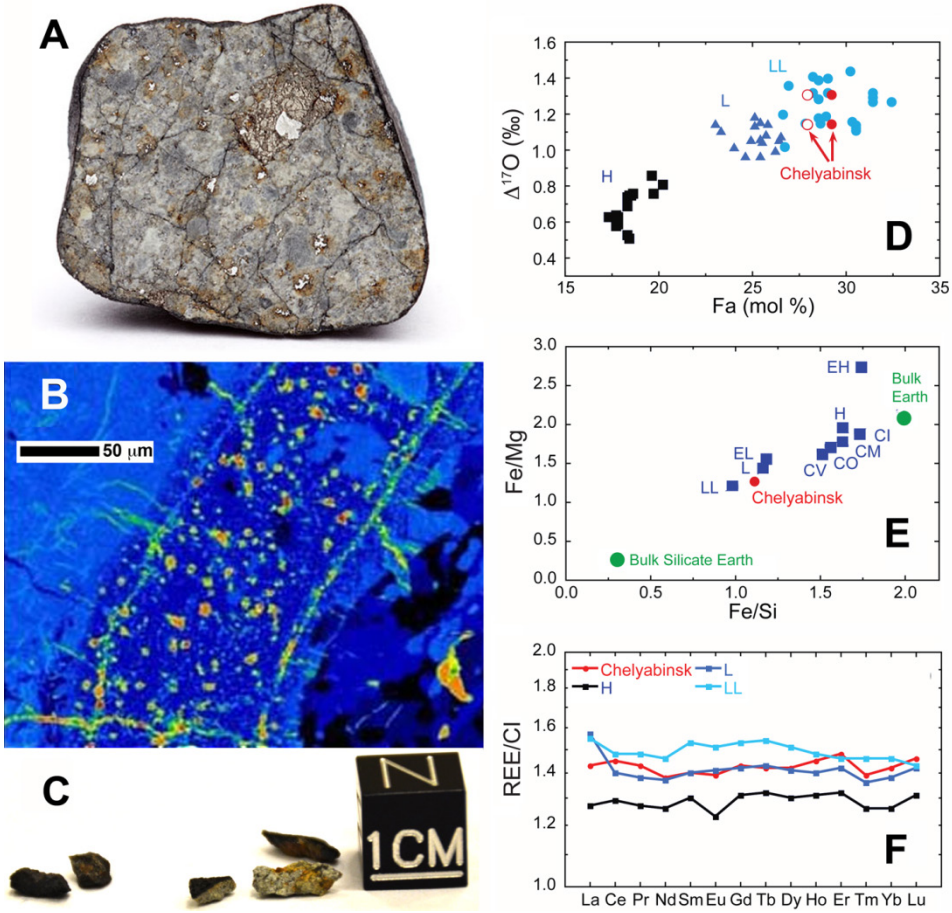

Fig. 4. Meteorite material properties, chemical and isotopic compositions. (**A**) Chelyabinsk meteorite (diameter ~4 cm) showing shock veins. (**B**) Fe element map of a shock vein. Note the metal layer (shown in green) located ~20 microns inside the vein. (**C**) Meteorite fragments recovered from the ice covered lake Chebarkul. (**D**) $\Delta^{17}O$ versus Fa mol% of olivine in Chelyabinsk, compared to other ordinary chondrites of type H, L, and LL (*38*). Fa is defined as mole ratio of Fe/(Fe+Mg) in olivine. Average $\Delta^{17}O$ values from UNM (1.15 ± 0.06‰) and from KOPRI (1.31 ± 0.04‰) for Chelyabinsk likely reflect indigenous heterogeneity in oxygen isotopes. Solid symbols are Fa number measured in this study (SM Sect. S4.3), while open symbols are from (*18*). (**E**) Ratio plots of the three major elements (Mg, Si, Fe; together with oxygen >90% of mass) for Chelyabinsk and the main chondrite groups. The bulk Earth and bulk silicate Earth compositions were taken from (*39*), chondrite compositions from (*40*). (**F**) CI chondrite normalized rare earth elemental pattern of Chelyabinsk compared to the average chondrite group compositions of (*38*, *41*).

www.sciencemag.org/cgi/content/full/science.1242642/DC1

Supplementary Materials for

Chelyabinsk Airburst, Damage Assessment, Meteorite Recovery, and Characterization

Olga P. Popova, Peter Jenniskens,* Vacheslav Emel'yanenko, Anna Kartashova, Eugeny Biryukov, Sergey Khaibrakhmanov, Valery Shuvalov, Yurij Rybnov, Alexandr Dudorov, Victor I. Grokhovsky, Dmitry D. Badyukov, Qing-Zhu Yin, Peter S. Gural, Jim Albers, Mikael Granvik, Läslo G. Evers, Jacob Kuiper, Vladimir Kharlamov, Andrey Solovyov, Yuri S. Rusakov, Stanislav Korotkiy, Ilya Serdyuk, Alexander V. Korochantsev, Michail Yu Larionov, Dmitry Glazachev, Alexander E. Mayer, Galen Gisler, Sergei V. Gladkovsky, Josh Wimpenny, Matthew E. Sanborn, Akane Yamakawa, Kenneth L. Verosub, Douglas J. Rowland, Sarah Roeske, Nicholas W. Botto, Jon M. Friedrich, Michael E. Zolensky, Loan Le, Daniel Ross, Karen Ziegler, Tomoki Nakamura, Insu Ahn, Jong Ik Lee, Qin Zhou, Xian-Hua Li, Qiu-Li Li, Yu Liu, Guo-Qiang Tang, Takahiro Hiroi, Derek Sears, Ilya A. Weinstein, Alexander S. Vokhmintsev, Alexei V. Ishchenko, Phillipe Schmitt-Kopplin, Norbert Hertkorn, Keisuke Nagao, Makiko K. Haba, Mutsumi Komatsu, Takashi Mikouchi (the Chelyabinsk Airburst Consortium)

*To whom correspondence should be addressed. E-mail: Petrus.M.Jenniskens@nasa.gov

Published 7 November 2013 on *Science* Express
DOI: 10.1126/science.1242642

This PDF file includes:

Supplementary Text
Figs. S1 to S87
Tables S1 to S24
References

Other Supplementary Material for this manuscript includes the following:
(available at www.sciencemag.org/cgi/content/full/science.1242642/DC1)

Movie S1

Table of Content

1. Asteroid Orbit and Atmospheric Entry

1.1. Trajectory and Orbit 3

Time of Entry 3

Astrometry of Video Records 4

Shadows in Video Records 11

Trajectory and Orbit 13

Preatmospheric Orbit 18

Final Fragments 19

Model of Meteoroid Orbital Dynamics 20

1.2. Lightcurve and Meteor Model 22

Lightcurve 22

Meteor Model 24

1.3. Thermal Radiation and the Smoke Cloud 30

Prevailing Winds and Train Drift 34

1.4. Infrasound Data 39

1.5. Witness Reports: Smells 45

1.6. EMP and Electrophonic Sounds 53

2. Damage Assessment

2.1. Injuries 55

2.2. Heat and Sunburn 57

2.3. Glass Damage 58

2.4. Model of the Shockwave 62

Blast Wave Arrival Times 69

2.5. Structures Hit by Falling Meteorites 74

3. Meteorite Recovery

3.1. Recovered Meteorites 75

Meteorite Recovery from Snow 80

Mass Distribution of Fallen Meteorites and Total Fallen Mass 81

Chebarkul Lake Meteorites 84

Model of Chebarkul Lake Impact 87

4. Meteorite Characterization

4.1. Mechanical Properties..... *89*

4.2. X-ray Computed Tomography..... *90*

Metal Grain Orientations..... *94*

4.3. Magnetic Susceptibility and Paleomagnetism..... *96*

4.4. Petrography and Mineralogy..... *98*

4.5. Major, Minor, and Trace Element Analyses..... *103*

4.6. Ultrahigh Precision Cr Isotope Analyses..... *106*

4.7. Oxygen Isotope Analyses..... *108*

4.8. U-Pb Age..... *110*

4.9. Reflection Spectroscopy..... *114*

4.10. Thermoluminescence..... *116*

4.11. Electrospray Ionization Ultra-High Resolution Mass Spectrometry..... *123*

4.12. Noble Gas Isotopes..... *128*

References and Notes only cited in Supporting Materials Section (42-157)..... *134*

Introduction to Supplementary Materials

This document contains supplementary material to the research article "Chelyabinsk Airburst, Damage Assessment, Meteorite Recovery and Characterization" (Popova et al., Science **342**, 2013), and is provided online as a Supporting Online Materials document (SOM). It contains collected data, methods of analysis, and a more in-depth interpretation of results. Individual sections address the asteroid orbit and atmospheric entry (SOM Sect. 1), damage assessment (Sect. 2), meteorite recovery (Sect. 3), and meteorite characterization (Sect. 4). The main contributors to each sub-section are identified.

1. Asteroid Orbit and Atmospheric Entry

1.1. Trajectory and Orbit

(Contributed by: P. Jenniskens, P. S. Gural, J. Albers, A. Kartashova, E. Biryukov, and V. Emel'yanenko)

Time of entry

Footage from 34 video security cameras in Chelyabinsk *Oblast* (the administrative term for the region) were recorded at 10 frames-per-second on a single time-calibrated server. Cameras were pointed downward on traffic and do not show the fireball itself. On February 15, 2013, sunrise in Chelyabinsk was at 03:17 Universal Time (UT). The landscape initially brightened to a peak at 03:20:29.8±0.1 UT, at which time the color temperature of the light lowered to a more yellow hue. Brightness continued to increase to a peak between 03:20:31.2 and 03:20:32.2 UT, different for different cameras because of gain adjustments. Brightness abruptly decreased at 03:20:32.65 UT, when the landscape became bathed in a reddish color. There was subsequently a brief increase of light with a more bluish tone peaking at 03:20:33.4 UT.

Table S1. Time and location of key events from the analyses of video records.

Event	Time (s, UT) (±0.1)	Latitude (º) (±0.018)	Longitude (º) (±0.030)	H (km) (±0.7)	V (km/s) (±0.16)
First detected	3:20:20.8	54.445	64.565	97.1	19.16
First peak	3:20:29.8	54.764	62.109	43.9	19.2
Main peak	3:20:32.2	54.845	61.412	29.7	19.2
End of thermal cloud formation	3:20:32.65	54.859	61.278	27.0	19.2
Secondary disruption	3:20:33.4	54.876	61.128	23.9	16.8
Tertiary disruption	3:20:34.7	54.905	60.865	18.5	12.1
Last detected	3:20:36.8	54.931	60.625	13.6	4.9
Thermal cloud comes to rest	~3:20:37	54.864	61.240	26.2	-.-

Astrometry of Video Records

Times were not synchronized in most of the other >400 videos posted on the internet, many from dashboard-mounted video cameras (dash-cam). Eight perspectives were calibrated during a two-week field investigation (March 9 - 24, 2013), by taking star background images at known times (Table S2). The Snezhinsk video was calibrated by local resident Gennadij Ionov on April 15th, and the Kamensk-Uralskiy video by Artem Burdanov of Ural Federal University on June 10th.

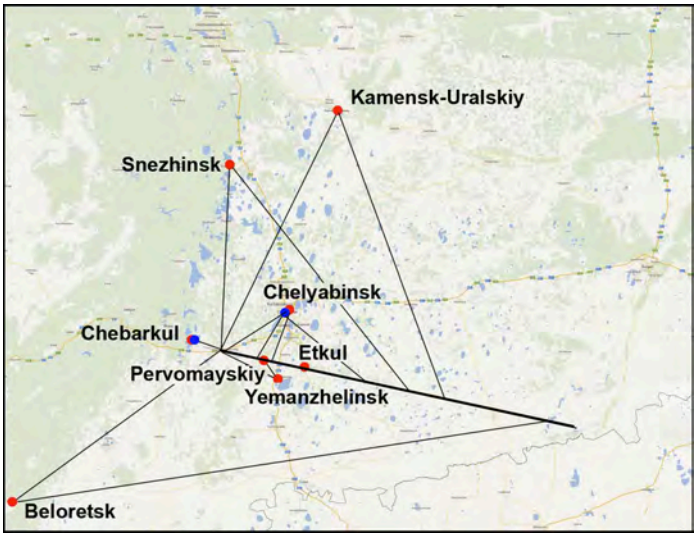

Fig. S1. Location of camera sites (meteor filmed - red; meteor shadow recorded - blue) used to reconstruct the trajectory.

Table S2. Star-background calibrated video camera sites. The video frame rate is in frames per second (fps). O-C is observed minus calculated dispersion in star positions for fitted coordinate frame.

#	Site		Latitude (ºN)	Longitude (ºE)	Alt. (m)	Type	Rate (fps)	O-C (')
	Early part:							
1	Pervomayskiy	PE	54.87060	61.17369	275	parked car	25	0.7
2	Korkino	KO	54.89089	61.39966	249	parked car	30	0.4
	All, but from a distance:							
3	Beloretsk	BE	53.95277	58.41020	537	car, stopped	30	1.2
4	Snezhinsk	SN	56.07940	60.74271	267	car, stopped	30	1.2
5	Kamensk-Uralskiy	KU	56.41500	61.91858	170	car, stopped	30	1.2
	Late part:							
6	Chelyabinsk Savina Street	CS	55.16633	61.44473	223	parked car	25	1.2
7	Chebarkul	CB	54.99510	60.40024	345	parked car	30	0.4
8	Yemanzhelinsk	YE	54.75664	61.30380	227	moving car	25	0.9
	Train (late part):							
9	Yemanzhelinsk bus depot	YB	54.75538	61.31534	240	hand-held	30	0.3
10	Etkul	ET	54.82193	61.58429	234	hand-held	30	0.3

Fig. S1 shows the location of these sites relative to the fireball trajectory. Calibration images were taken with a global positioning system (GPS) equipped Nikon D5100 camera with a wide angle 10-mm f3.5 lens, as well as a Canon EOS 40D camera, also with a 10-mm f3.5 lens. This provided a mean astrometric accuracy of <1.3' in observed minus calculated (O-C) star position (Table S2). The exposure time was 3-30s, depending on ambient light conditions, with star positions averaged over that time interval. The EXIF timestamp is the time of writing to disk.

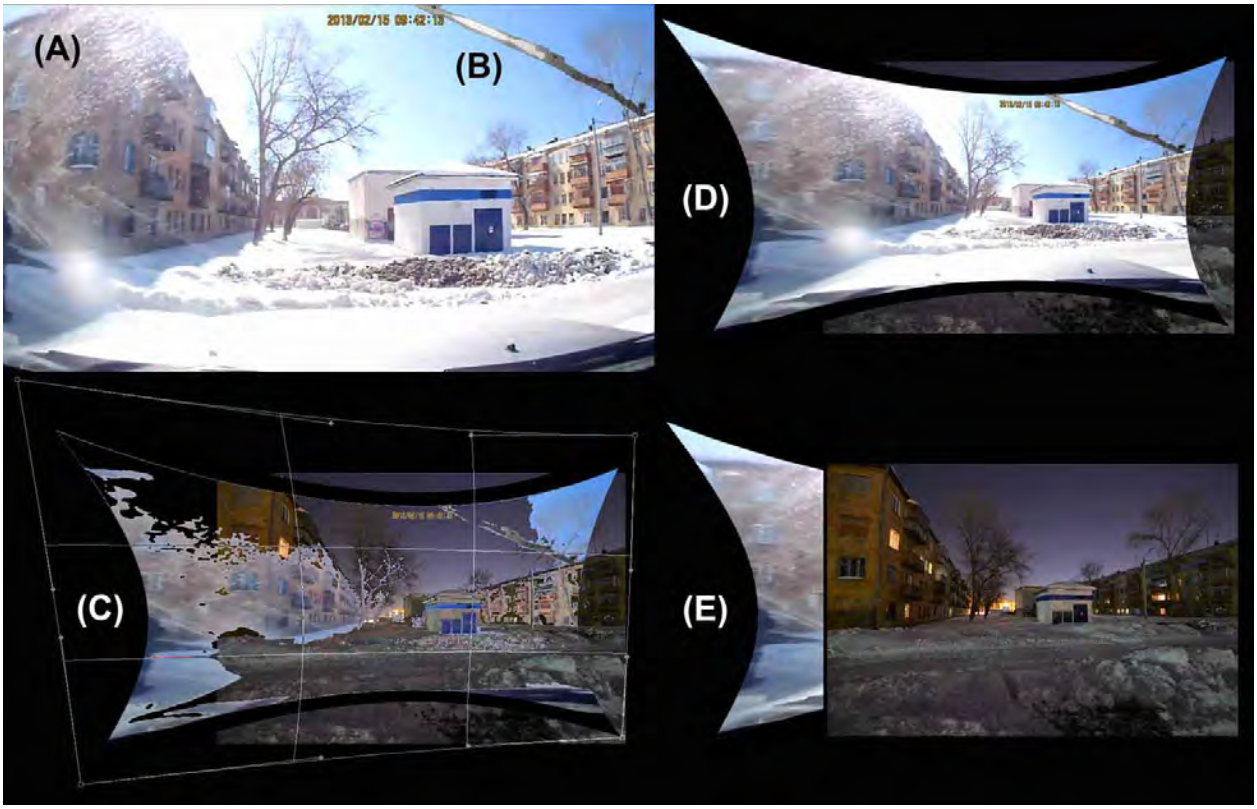

Fig. S2. Chelyabinsk Savina Street video by Alexandr Yakushenkov; **(A)** Frame at peak brightness, with position of the meteor inserted in all video frames **(B)**; Application of the Adobe Photoshop lens correction (at 3 x 100%) and 150% scaling, then slightly warped **(C)**, to match foreground features in star background image **(D, E)**.

The astrometric precision of the meteor trajectory is not determined by the astrometric accuracy of the star background images, but by how precisely foreground features can be matched. Matching was done by first projecting the centroid of the meteor in each frame onto a single video frame (when the scene is well illuminated). This image was then distorted to match the wide-angle star background image (Fig. S2). A near-perfect match was obtained for the

Chelyabinsk Savina Street recording, where many foreground features defined the lens distortion in this dash-cam. The image was matched within about 2 pixels at all positions in the image by applying three times the standard lens correction and a small warp to align the edges. This image was taken on March 15th, before leaves sprouted in springtime. The car was parked facing south and the meteor entered the top of the field of view, moving from left to right, well after the time of peak brightness at time stamp 9:42:13.20, which is the local time with some time offset.

Fig. S3. In Beloretsk, the directions are well aligned with the direction to the background mountains in this video by Pavel Gridnevskiy.

Beloretsk (Fig. S3) is a long distance south of the trajectory (Fig. S1). As such, the full length of the fireball is recorded. The car was in the process of stopping when the meteor appeared. The scene has a mountain range seen far in the distance. The composite video image was lens distortion corrected (no warp), rotated, and scaled to match the mountains in the star background image. Some stars are photographed below the meteor. The resulting alignment to foreground features is only approximate, but in reasonable agreement. Measurements were made every 1 second, starting at clock time 09:20:27 until 09:20:42, with peak brightness around 09:20:37.8.

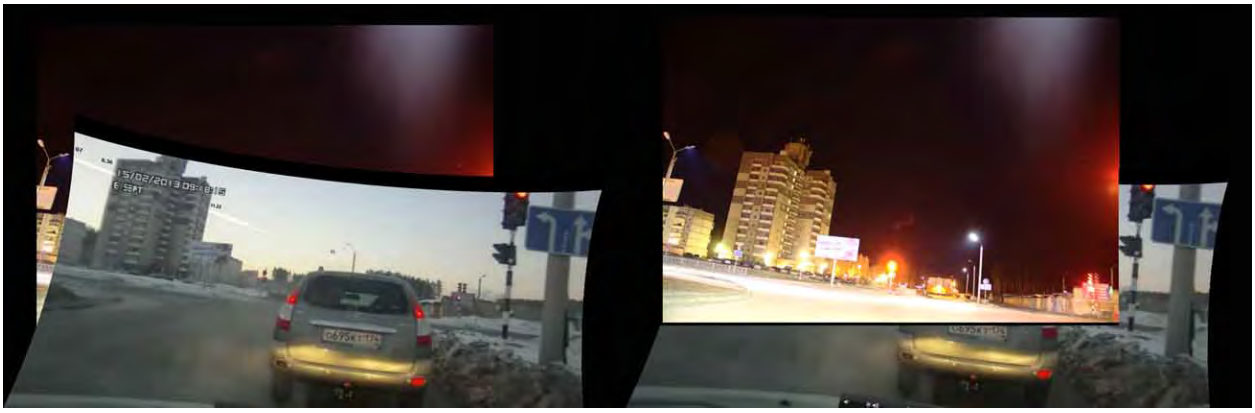

Fig. S4. Alignment of star background image to a frame from video by Nikita Sonin in Snezhinsk.

In Snezhinsk, located far north of the trajectory, the foreground is also at a relatively far distance and includes an apartment building and light fixtures (Fig. S4). The frame from a 25 fps video was lens corrected, rotated and scaled, and the perspective changed to match the foreground features. Stars were photographed below the meteor track. The meteor peak brightness was at about clock time 9:18:11.24. The fireball was recorded from 9:18:7.2-15.7.

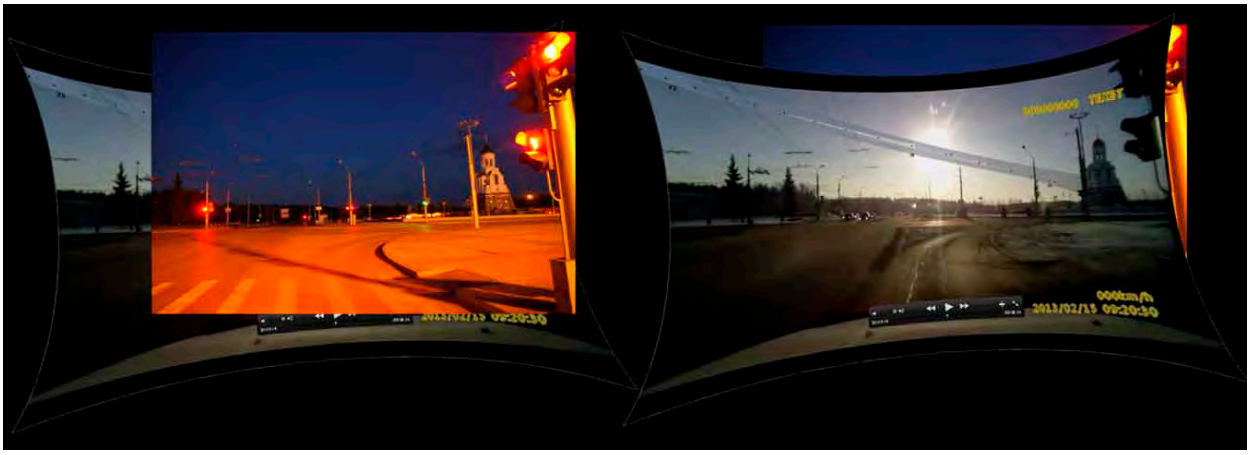

Fig. S5. In Kamensk-Uralskiy, the meteor moved behind several lamp posts in this video by Aleksandr Ivanov, with most foreground features in the far field.

In Kamensk-Uralskiy, Alexandr Ivanov obtained a spectacular video from a car stopped at a traffic light (Fig. S5). The traffic light is visible to the right, which accurately marks the car's position. The foreground features are all in the far field and include lantern poles behind which the meteor moved. These features accurately mark elevation. The image was lens corrected and slightly warped to match the azimuth directions to the far-field lantern poles and park's trees.

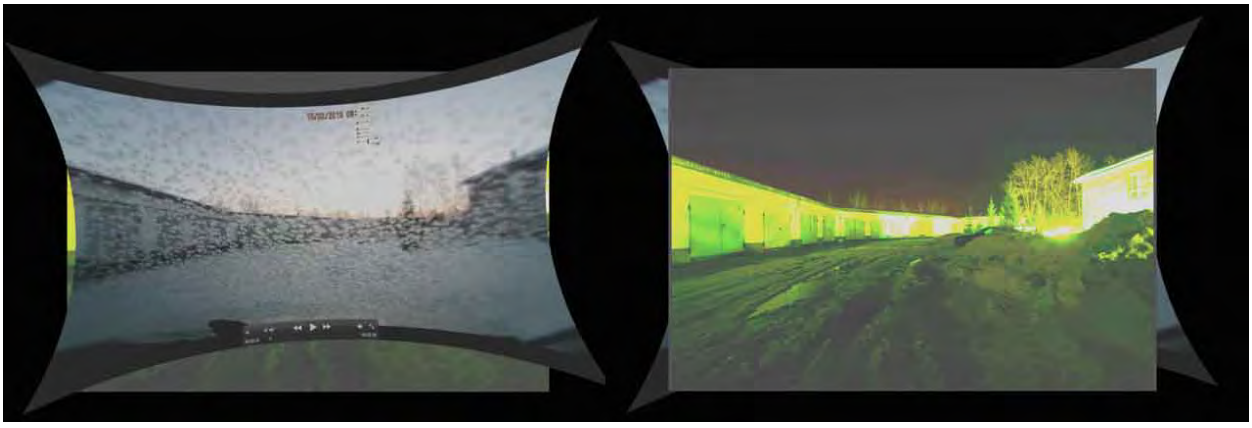

Fig. S6. Video in Pervomayskiy was taken by Nikolay Ivanov inside the courtyard of a hotel. The meteor appeared high right-of-center in the field, moving from bottom to top.

In Pervomayskiy, 25 fps video was rolling in a parked car with a scattering of ice crystals on the front window (Fig. S6). The camera was facing east and the early part of the meteor track is recorded. The meteor managed to avoid the ice crystals and is well tracked until the image becomes large from blooming. Unfortunately, all foreground features are in the near field. After lens correction, rotation and scaling, the buildings and trees are in alignment. The foreground fir trees are not matched, showing there is a small perspective problem. Useful data cover the video clock times from 9:13:23.76 to 9:13:32.0, with peak brightness at 9:13:36.40.

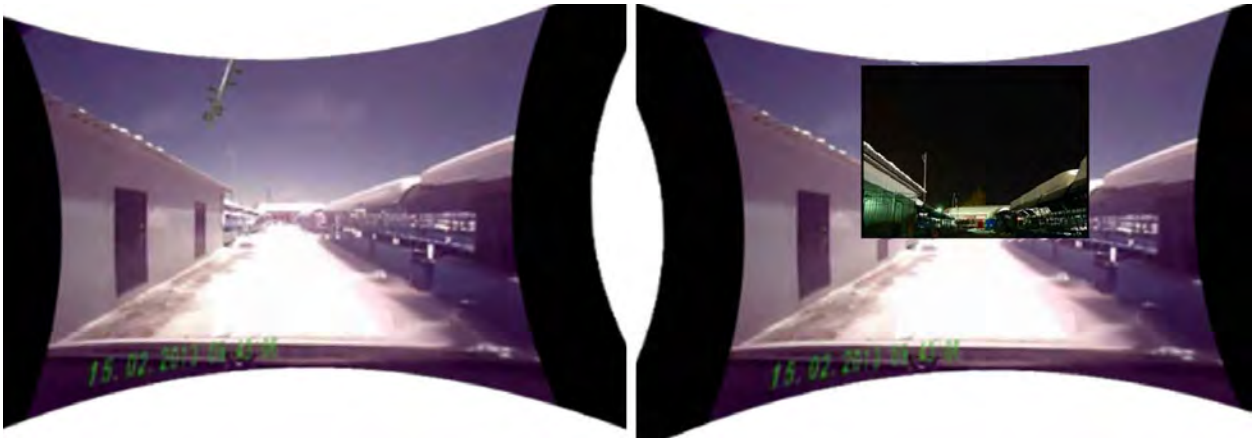

Fig. S7. Korkino's central market place, in YouTube video posted by a user Nek Rosato. Meteor started in the field and moved upwards.

In Korkino, a video recorded the onset and early part of the fireball, moving towards the observer with a low angular velocity (Fig. S7). Peak brightness occurred at clock setting 9:43:05.80. The video camera is of the same type as Yemanzhelinsk (see below), which needed twice the lens distortion correction of Chelyabinsk Savina Street. However, the near-field perspective is unreliable. The corrected image was linearly scaled and rotated to align with the house, telephone poles and tree in the distance near the center of the image.

In Chebarkul, the meteor emerged from a bright glow, passed through the point of peak brightness, then faded while leaving the field of view at the top (Fig. S8). The train of a second fragment is visible at a slight angle. The video shows relatively modest lens distortion. The image needed only a single Photoshop lens distortion correction and a perspective correction to provide a match with foreground features, but trees further back were not matched correctly, implying a small error in perspective. The corrected image was then shifted in azimuth to align with the furthest trees, which may not fully account for this error in perspective. Peak brightness was at 09:16:44.23 clock time and the meteor tracked every 1/15th s from 09:16:45 - 48.17.

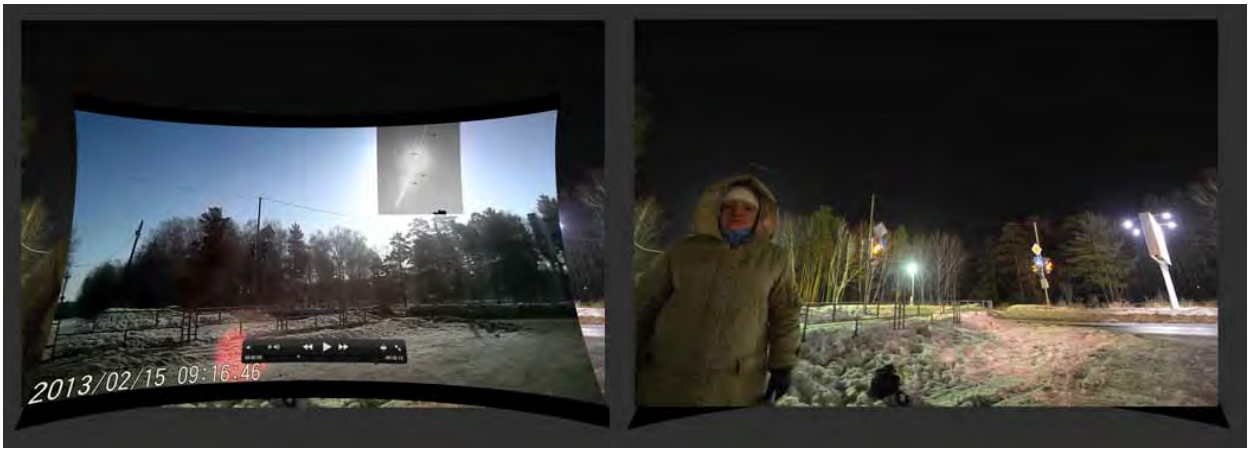

Fig. S8. In Chebarkul, a rich near-field foreground is matched well, but trees further from the camera are not. Right: Anna Kartashova shields the camera for one of the bright lights. YouTube video posted by user Julia Rizhaya.

Fig. S9. Alignment of star background image to video taken in Yemanzhelinsk by Alexandr Zakharov. The composite frame consists of the video frame taken at the site, plus a series of frames taken earlier when the car passed under a gas pipeline. Peter Jenniskens shields camera from foreground light.

Under the meteor trajectory in Yemanzhelinsk, the final part of the fireball was filmed from a moving car. Towards the end of the recording, the meteor initially faded abruptly, returned faintly for several frames before fading again and, finally, re-emerging in a single-frame terminal flare. All foreground features are in the far field. Two locations of the car were calibrated, 34m apart, one of which is shown in Fig. S9. As the direction in which the car was travelling did not change much during the recording, the position of the meteor was transposed by aligning the meteor train in each measured frame. The position of the fireball in every 5th frame was measured between 09:25.12 and 09:27.72 clock time. In addition, the car drove under a straight gas pipeline, creating a map of the lens distortion. Two times the normal lens correction (e.g., Fig. S2) straightened the meteor track and pipeline images transposed on the video frame (Fig.

S9). The perspective was adjusted to align the far field. No warping was applied. Small perspective errors are present near the edges.

Fig. S10. Alignment of foreground to star background image in Etkul. Video by Maxim Sevjukov.

In Etkul, the train appeared nearly overhead and was filmed by a hand-held camera (Fig. S10). Based on the filmed arrival time of the shock wave (which occurred 44.7 s later), this video frame was taken at 03:21:28 +/- 3s UT. The hand-held video did not have as wide angle a lens as the dashboard-mounted cameras in cars. Scaling, rotation, and a small perspective change were sufficient to reasonably align the image. Emphasis was given to aligning the distant towers.

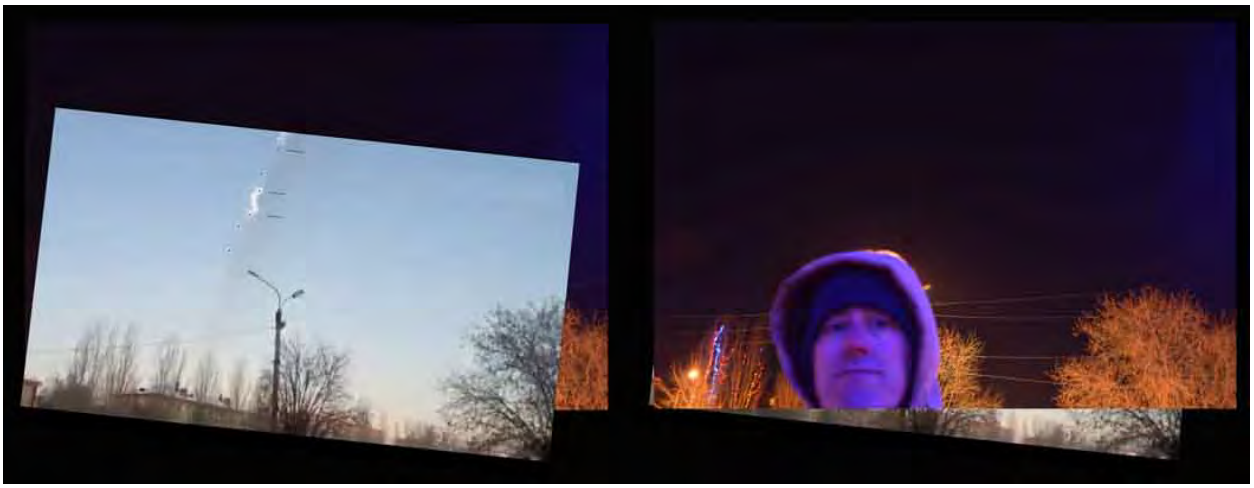

Fig. S11. Alignment to a star background of one frame in this hand-held YouTube video posted by Ekaterina Prokudina, taken at the Yemanzhelinsk bus station.

At the bus station in Yemanzhelinsk, the train was filmed by a hand-held camera. The background building chimneys were used to align the direction of the image. Rotation and

scaling were sufficient to achieve a reasonable alignment (Fig. S11). The filmed arrival of the shockwave (8.5s earlier) was used to time the image at 03:21:53.2 UT.

Shadows in Video Records

During peak brightness, the apparent fireball path was measured from shadows on the ground [42]. Of the 34 videos recorded on a single server in Chelyabinsk, fifteen show shadows crossing features on the ground that can be used to identify its position at selected times (Table S3). Four sites in Chelyabinsk and one site in Chebarkul were analyzed. Those include the two videos taken at the Revolution Square (#237) and the corner house at the Privokzalnaya Square (#30, not shown), which were posted on the internet shortly after the event.

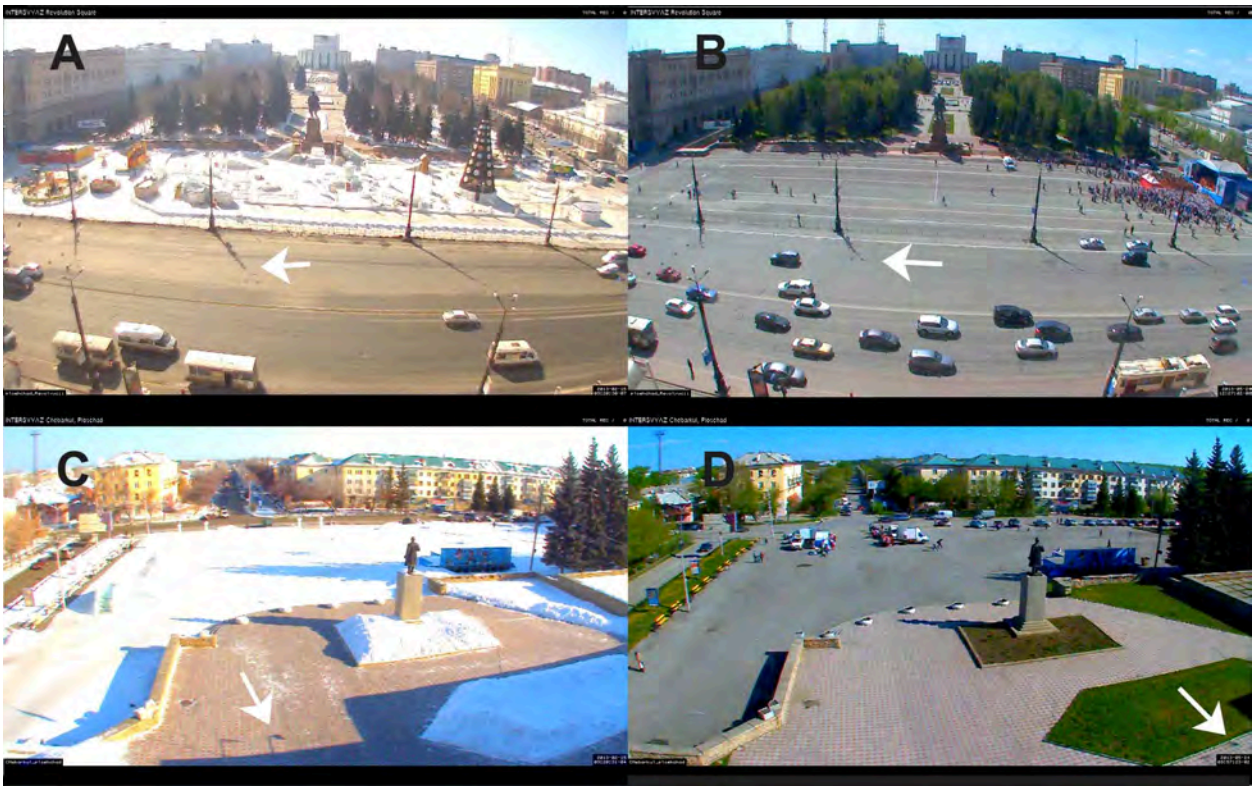

Fig. S12. Fireball (left) and Sun generated shadows (right) in video provided by Eduard Kalinin. **(A)** Fireball created shadows of lantern poles on the Revolution Square in Chelyabinsk (Site #237). **(B)** Corresponding calibration image of Sun shadow on 2013 May 24, at 3:27:11.3 UT; **(C)** Fireball shadow on square in front of the administration building in Chebarkul (site #105). **(D)** Calibration image showing same Sun generated light fixture shadows on 2013 May 24 at 3:57:23.2 UT. Arrow marks the shadow of the light fixture seen in Fig. S12C.

Tape measure, rope, an inclinometer and a Craftsman laser distance measuring tool were used to measure the height of obstacles and the length of shadows on the ground to determine the elevation of the meteor. The azimuthal directions are more uncertain and were determined by both using a compass and from the orientation of maps presented in Google Earth.

Table S3. Summary of video-analyzed shadow sites.

Video #	Site	Obstacle	Lat.(N)	Long. (E)	Alt. (m)
30	Chelyabinsk	Building	55.143436	61.414183	232
105	Chebarkul	Light fixture	54.977272	60.370341	338
160	Chelyabinsk	Sign	55.172211	61.453558	242
237	Chelyabinsk	Lanternpole	55.160144	61.402573	229
301	Chelyabinsk	Billboard	55.167406	61.443214	235

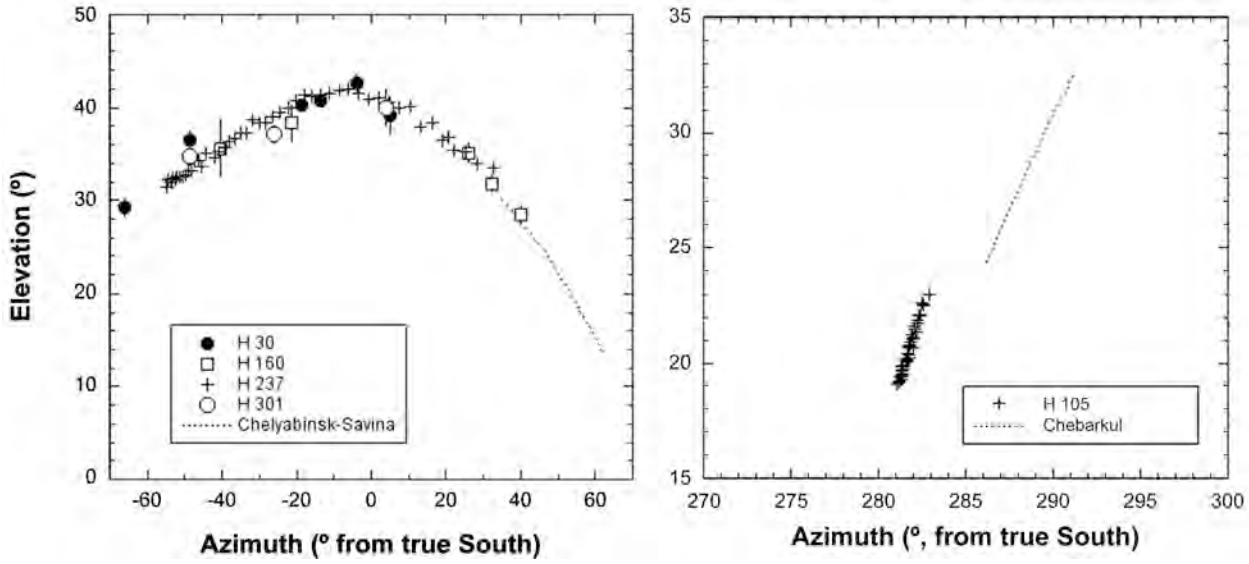

Fig. S13. Viewing angles from shadow length and direction at four nearby locations in Chelyabinsk (left, sites identified in Table S2) and one site (#105) in Chebarkul (+, right). Meteor moved from left to right. Dashed lines show the viewing directions derived from the video records of the fireball itself.

Sun shadows at different times in the day were also used to calibrate the Chelyabinsk Revolution Square and the Chebarkul administration building videos (Fig. S13). At Chelyabinsk, the Sun shadow azimuth was directly matched to the azimuth direction of fireball shadows. Elevation directions were derived from the sun shadow elevations after correcting for lens distortion and perspective of the camera. Azimuth and elevation directions for the Revolution Square and the Privokzalnaya Square (Fig. S13) are in good agreement with those determined by Zuluaga et al. [42]. Systematic errors in azimuth were decreased from about ±2.5º to ±1º. The

measured directions agree well with those derived from the Chelaybinsk Savina Street video (dashed line Fig. S13).

In Chebarkul, the Sun shadow was only briefly in the field of view. Using the measured height of the lamp fixture (14.5±0.3 m), the azimuth and elevation calculated for that point was transposed to other positions using the grid pattern of tiles in the square (each 0.3018±0.0005 m in width). The difference between the directions measured from the shadow and from the video record is partially due to the different locations in Chebarkul (dashed line Fig. S13).

Trajectory and Orbit

Astrometric data were combined using the CAMS software package [43,44], from which the trajectory data in Table S1 were calculated. In these calculations, the trajectory is assumed to be linear, with velocity decelerating with time (t) after reference time t_o described by two deceleration parameters a_1 and a_2 [45]:

$$V(t) = V_\infty + a_1 a_2 \exp(|a_2|*(t-t_o))) \quad \text{Eq. S1}$$

The method first calculates the intersection of the two planes through the meteor and two stations, with best results for a large convergence angle, the angle between the planes (Q). After that, individual lines of sight to the meteor in each video frame were used to optimize the trajectory fit, including by taking into account the equal time between the measurements [44]. The trajectories are derived by allowing a variable time offset to optimize the fit, as a result of which the trajectory is better defined as a function of altitude than as a function of time.

The result of the fit is sensitive to systematic errors. The measurements from Pervomayskiy and Korkino do not agree: both stations are located almost under the trajectory, but one sees the meteor arrive from an initial azimuth of 100.9º (after matching to the furthest features in the frame), the other from 102.8º. Only by combining many different solutions was it made clear that Pervomayskiy was slightly off, while the solution for Korkino was essentially correct.

Stations in Beloretsk, Snezhinsk and Kamensk-Uralskiy cover most of the meteor trajectory from a distance, providing solution V_∞ = 19.04 ± 0.09 km/s, a_1 = 0.0013±0.0004 km and a_2 = 0.97±0.07 s^{-1}. The apparent radiant is at R.A. = 328.39±0.12º, Dec. = 7.72±0.16º (here, the error bar gives the random errors from astrometry only, not the systematic errors). Eq. S1 does not accurately describe the deceleration. If we focus only on the >50 km part, Beloretsk, Kamensk-

Uralskiy, and Korkino, and assume no deceleration in this early part of the trajectory, then the radiant is at R.A. = 328.54±0.02º, Dec. = +7.17±0.02º, V_∞ = 19.13±0.01 km/s.

Table S4A. Constant velocity solutions for different station combinations that contribute data above 25 km altitude. Listed are apparent Right Ascension (R.A.) and Declination (Dec.) of the radiant and apparent entry speed (V∞), convergence angle (Q), as well as the altitude, latitude and longitude of the beginning and end point. Solutions for small values of Q are unreliable (shaded).

Stations	R.A. (º)	Dec. (º)	V∞ (km/s)	Q (º)	H b (km)	Lat. b (º)	Long. b (º)	H e (km)	Lat. e (º)	Long. e (º)
PE-BE	328.15	7.65	18.75	82.5	90.7	54.4867	64.2843	29.7	54.8436	61.4311
KO-KU	327.82	7.52	19.23	69.5	89.8	54.4738	64.2499	25.2	54.8596	61.2357
PE-SN	328.06	7.86	19.31	87.0	92.4	54.4808	64.3313	25.3	54.8658	61.2266
PE-KU	328.08	7.88	19.13	81.7	90.8	54.4876	64.2818	25.1	54.8636	61.2381
KO-SN	327.77	7.47	19.38	74.8	91.0	54.4675	64.2856	25.6	54.8609	61.2308
KO-BE	327.98	7.17	18.54	70.2	88.8	54.4776	64.2213	29.8	54.8409	61.4128
SN-CS	328.06	6.97	19.37	68.3	54.3	54.6806	62.6373	26.3	54.8518	61.2367
BE-CS	328.10	7.23	18.47	63.7	84.6	54.4978	64.0323	29.4	54.8336	61.3874
KU-CS	327.84	7.20	19.36	62.9	65.7	54.6106	63.1789	25.6	54.8543	61.2288
PE-LE	328.31	7.56	19.19	51.6	93.5	54.4749	64.3733	25.1	54.8752	61.1297
KO-LE	328.65	6.98	20.07	39.3	93.1	54.4565	64.3898	26.8	54.8621	61.1163
SN-LE	329.72	7.64	18.34	35.6	52.2	54.7311	62.5771	24.4	54.8789	61.1357
CS-LE	328.82	6.24	19.87	32.2	59.6	54.6511	62.8306	27.6	54.8571	61.1169
BE-LE	328.50	7.35	18.90	31.0	86.8	54.5127	64.1497	24.7	54.8804	61.1334
KU-LE	330.08	7.53	18.64	30.2	63.5	54.6656	63.1475	25.0	54.8723	61.1296
PE-CS	330.31	5.25	9.38	18.8	57.0	54.6353	63.1737	24.5	54.8579	61.2344
PE-KO	328.49	6.64	13.67	12.2	66.8	54.5821	63.5560	39.2	54.7585	62.1817
KU-SN	331.30	9.43	19.34	5.3	66.5	54.6210	63.1894	26.7	54.7797	61.2157
BE-SN	328.48	7.74	19.05	4.6	87.5	54.5139	64.1622	25.7	54.8660	61.2312
KO-CS	332.48	3.70	9.98	6.5	57.3	54.6268	63.2926	32.7	54.8167	61.5190
BE-KU	330.00	8.66	19.51	0.8	85.4	54.5103	64.0462	26.7	54.7937	61.2167

Seven stations provide data on the early part of the trajectory above 25 km altitude, leading up to and during the main disruption (Table S4A). Five video records are complemented by shadow measurements from Chelyabinsk and Chebarkul. Shadow measurements were sampled every 0.5s, video observations every 1.0s. The trajectory solutions (assuming no deceleration) of all combinations of two stations are listed in Table S4A. The divergence between solutions is a measure of the systematic errors from mismatching the foreground in video and star background images. Solutions are ordered in sequence of convergence angle (Q), the angle between the two planes from the station to the meteor trajectory. Ignoring the Q < 20º geometries that have

inaccurate results (shaded), the standard deviation is 0.68º in apparent Right Ascension (R.A.), 0.42º in Declination (Dec.), and 0.50 km/s in apparent entry speed (V∞). The standard errors in determining the mean are 0.18º, 0.11º and 0.13 km/s, respectively. Combining datasets should decrease these errors. Indeed, removing one of 7 stations (for a solution including deceleration) results in a scatter with standard deviation 0.22º, 0.30º and 0.18 km/s, respectively, with standard errors 0.08º, 0.11º and 0.07 km/s. Allowing deceleration in the solution still leads to constant velocity fits being more likely. Hence, no significant deceleration was measured above 25 km altitude. The mean values for radiant and speed at reference time 03:20:19.80 UT are:

	R.A. (º)	Dec. (º)	V_∞ (km/s)	a_1 (km)	a_2 (s^{-1})
V const., mean of 2-station	328.40±0.18	+7.35±0.10	19.10±0.13	-.-	-.-
all combined	328.64	+7.24	19.15	-.-	-.-
mean of all -1 combined	328.62±0.08	+7.27±0.11	19.18±0.07	-.-	-.-
>29 km, no KO,PE	328.39±0.01	+7.46±0.02	19.16±0.01	-.-	-.-
>25 km, no KO, PE	328.36±0.01	+7.49±0.01	19.07±0.01	0.0	N/A
shadow only (CS,LE)	328.55	+6.08	19.67	0.0	N/A
mean of all -1 combined	328.59±0.09	+7.26±0.10	19.24±0.05	$\sim 5\times10^{-4}$	~0.54
all combined	328.62±0.09	+7.26±0.10	19.11±0.05	1×10^{-6}	0.107

Table S4B. Same as Table S4A. Deceleration allowed solutions for different station combinations that contribute data below 25 km altitude

Stations	R.A. (º)	Dec. (º)	V∞ (km/s)	a_1 (km)	a_2 (/s)	t0 (s)	Q (º)	H b (km)	Lat. b (º)	Long. b (º)	H e (km)	Lat. e (º)	Long. e (º)
KU-YE	327.87	5.06	10.53	1e-6	3.269	33.50	79.3	23.4	54.8617	61.1268	13.8	54.9319	60.5705
YE-BE	327.74	8.07	14.51	3.906	0.513	34.16	78.9	24.2	54.9260	60.5918	13.4	54.9260	60.5918
SN-YE	327.29	7.98	9.53	9.5e-5	2.049	32.96	74.2	23.4	54.8672	61.1018	13.1	54.9234	60.6047
CY-YE	328.11	8.28	19.90	8.276	0.405	33.26	73.2	24.5	54.8684	61.1374	13.7	54.9239	60.6049
SN-CB	328.88	7.83	11.32	0.054	1.127	32.96	59.9	24.3	54.8799	61.1613	14.3	54.9323	60.6395
CB-KU	328.66	7.78	10.88	4.6e-4	1.598	32.80	54.7	23.6	54.8825	61.1448	13.7	54.9352	60.6312
CB-BE	328.50	7.81	11.13	2.1e-6	2.309	32.80	55.1	24.5	54.8781	61.1680	14.5	54.9313	60.6561
CB-YE	328.13	8.07	25.12	26.24	0.180	33.80	46.0	30.7	54.8478	61.3710	14.1	54.9355	60.5452
SN-CY	340.54	8.04	15.11	1.48e-3	2.336	32.96	32.6	22.9	54.9018	61.2622	15.9	54.9026	60.6453
CY-BE	341.83	7.39	15.96	0.726	1.030	33.26	27.8	20.9	54.9170	61.2323	15.0	54.9135	60.6271
CY-KU	339.35	7.42	17.32	4.08e-3	2.631	33.26	27.4	26.1	54.8605	61.2376	18.5	54.8700	60.5794
CB-CY	327.89	8.08	18.63	4.213	0.588	33.26	27.3	23.4	54.8822	61.1641	14.2	54.9313	60.7092
SN-KU	317.29	4.69	10.63	5.8e-4	0.012	32.96	5.2	25.4	54.7983	61.1269	13.7	54.9244	60.6173
SN-BE	321.41	4.69	9.65	0.0	0.0	32.96	4.8	24.3	54.8359	61.1029	14.1	54.9243	60.6346
KU-BE	293.04	-9.4	47.59	105.4	0.137	33.50	0.5	32.9	54.4297	61.0039	13.1	54.8324	60.4470

Similar data for the lines of sight covering data below 25 km are listed in Table S4B. Mean values for reference time 03:20:32.96 UT:

	R.A. (º)	Dec. (º)	V∞ (km/s)	a_1 (km)	a_2 (/s)
<25 km, mean of 2-station	328.12±0.17	+7.66±0.33	14.6± 1.8	0.70±0.05	(0.8)
<25 km, all comb., no CB	327.50±0.89	+8.97±0.89	14.46±1.38	0.35±0.28	0.81±0.05
<25 km, all comb., no YE	327.60±0.10	+8.17±0.15	15.58±1.33	0.643±2.77	0.975±0.185
<25 km, all combined	327.97	+8.05	12.58	0.027	1.31

The best-fit results to data in Tables S4A and S4B are shown in Fig. S14A. Above 25 km, the best-fit trajectory is constant velocity fit, while below 25 km the best-fit curve has deceleration with $a_1 = 0.35\pm0.03$ for $a_2 = 1.0$ (relative to time 03:20:32.96 UT).

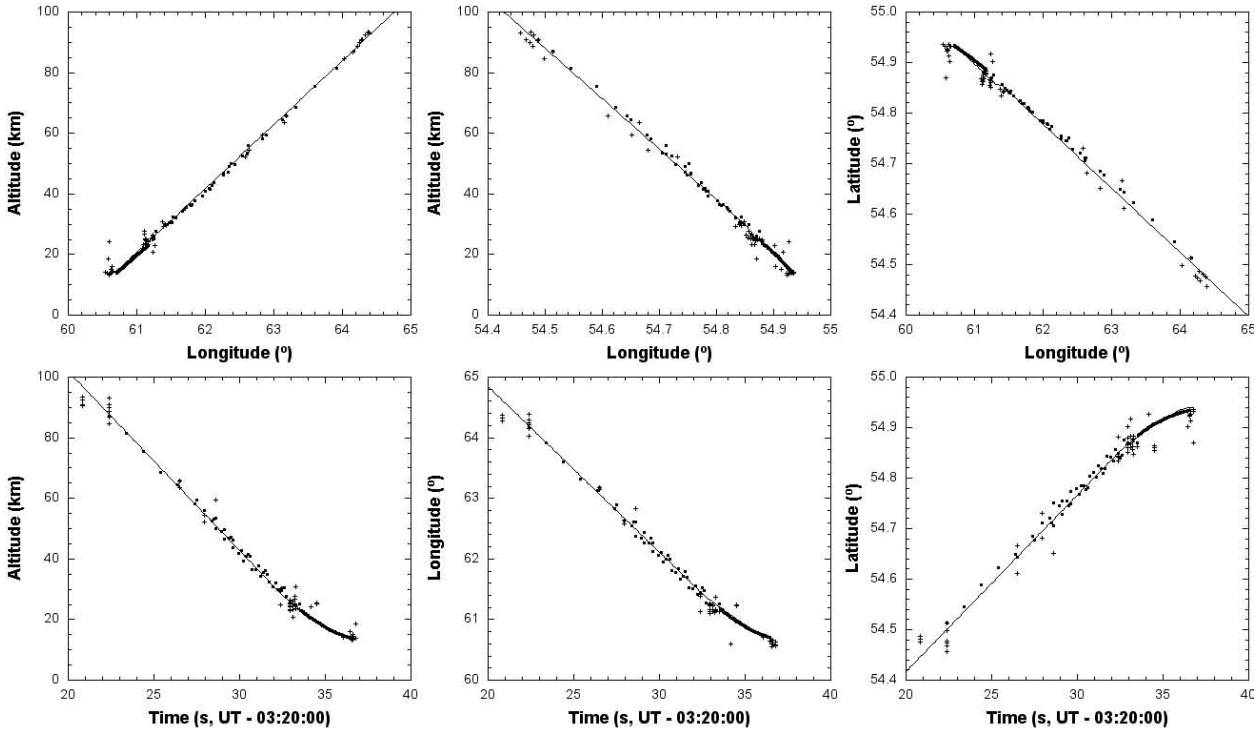

Fig. S14A. Fireball trajectory as a function of altitude and time. Points are model fit solutions for stations BE, KU, SN, LE and CS (> 25 km) and CY (< 25 km). Crosses are either begin or end points of individual 2-station solutions.

The initial speed is constrained by the individual data fits. In detail, the longitude at 03:20:32.65 UT from the trajectory fit above 25 km altitude is higher by about 0.055º than for the solution below 25 km. In the same way, the elevation is about 0.7 km higher. To align the

two solutions would demand an increase in the entry speed to at least 19.3 km/s. However, these differences are also approximately the range of systematic uncertainties in the longitude and altitude measurements.

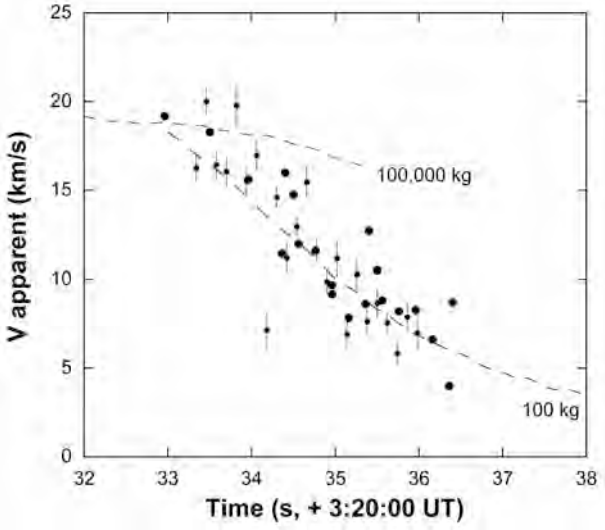

Fig. S14B. Deceleration of the main fragment below 25 km altitude: dots with error bars are averages over three 1/25 second frames from the perspective of the Chelyabinsk Savina Road video, while larger dots are 1-second averages as seen from Beloretsk, Snezinsk, Kamensk-Uralskiy and Yemanzhelinsk. The results are compared to falling 100 kg and 100,000 kg sphere models with density 3.3 g/cm^3 (dashed).

Details of the velocity profile in this part of the trajectory are not captured by applying Eq. S1. That would result in an abrupt drop of speed at 03:20:32.65 UT. The actual deceleration of the main fragment, which continued to fragment and ablate, is shown in Fig. S14B and is compared to that expected for a falling sphere of mass 100 kg or 100,000 kg (density 3.3 g/cm^3). A final mass up to 400 kg would also match the observed deceleration.

We adopt an apparent radiant at R.A. = 328.62±0.09º and Dec. = +7.26±0.10º. This trajectory has an elevation of 18.3±0.2º and azimuth of 283.2±0.2º at the entry point at 97.1 km altitude over 64.565ºE, 54.445ºN, where the meteoroid had a speed of 19.16±0.15 km/s. These values are for reference date and time: February 15, 2013 at 03:20:19.8 UT. A summary of positions and altitudes of key events is given in Table S1.

The apparent radiant corresponds to an Earth-gravity corrected geocentric radiant and speed: R.A.$_g$ = 333.2±1.0º, Decl.$_g$ = +0.3±1.1º, V_g = 15.3±0.2 km/s at solar longitude 326.4269±0.0001º (J2000). The trajectory direction and location is in good agreement with that derived by

Borovicka *et al.* [46], but we find an entry speed that is significantly higher (Table S5A). The speed at the time of peak brightness is sensitive to the deceleration model assumed.

Table S5A. Overview of trajectory data for the Chelyabinsk asteroid (Equinox J2000).

Source	Entry speed V_∞ (km/s)	R.A.$_\infty$ (º)	Decl.$_\infty$ (º)	Entry Angle (º)	Start Alt. (km)	Peak Alt. (km)	End of disr. Alt. (km)	Final Alt. (km)	Ref.
This work	19.16±0.15	328.62±0.09	+7.26±0.10	18.3±0.2	97.1	29.7	27.0±0.7	13.6	-.-
Y. & C.*	18.6**	328.9	+7.3	-.-	-.-	-.-	23.3	15	[47]
B. *et al.*	17.5±0.5	328.6±1.0	+8.0±1.0	16.5	91.8	31.7	-.-	14.9	[46]
Z. & F.	16.5±3.1	333.8±2.7	+12.4±2.7	18.1±1.7	~39.6	-.-	22.7±2.4	-.-	[42]

*) based on U.S. Government satellite sensor data, no error bars. **) velocity at peak brightness.

Our value of entry speed is slightly higher than the 18.6 km/s apparent speed (uncertainty in this value was not published) derived from satellite observations at the time of peak brightness [47], summarized in Table S5, perhaps suggesting that a small amount of deceleration occurred at the very end of the main disruption.

The radiant position and speed are significantly different, outside formal uncertainty intervals, from earlier determinations of the entry trajectory [42, 46-47]. These results, summarized in Table S5A, were derived from similar video observations, but using Google Earth to determine course astrometric directions to the fireball. The radiant position is in good agreement with [47], but our entry speed is significantly higher. Both radiant and speed are significantly different from [42]. These differences are important because the entry speed and entry angle affect the physical conditions of entry, and the direction (radiant) and magnitude of the entry speed determine the pre-atmospheric orbit of the meteoroid.

Preatmospheric Orbit

The pre-atmospheric orbit (Table S5B) was calculated from the observed apparent radiant and speed, by correcting for the Earth's rotation at the altitude of the meteor and applying Schiaparelli's equation to estimate the gravitational attraction of Earth [44]. Error bars were calculated from a Monte Carlo propagation of errors. Note that each orbital element is expressed in less significant digits than justified by the formal uncertainty in the solution, because the relative accuracy of the observed position of the meteoroid dictates a higher accuracy for any given orbit solution that fits the entry speed and direction at that point. Because of this, the orbit described by the elements as given in Table S5B passes by Earth. Expressed with additional digits, the nominal orbit has perihelion distance q = 0.738893 AU, semi-major axis a = 1.763270

AU, eccentricity e = 0.580953, inclination i = 4.928787º, argument of perihelion ω = 108.301927º and Node = 326.442018º (for Equinox J2000).

Table S5B. Overview of pre-atmospheric orbital data for the Chelyabinsk asteroid, with 1 standard deviation uncertainties (Equinox J2000).

Source	q (AU)	a (AU)	e	i (º)	ω (º)	Node (º)	Epoch (ET)	Ref.
This work	0.739 ±0.010	1.763	0.581 ±0.009	4.93 ±0.24	108.3 ±1.9	326.4422 ±0.0014	2013-02-15.139	-.-
Y. &C. *	0.750 ±-.-	1.764	0.57 ±-.-	4.2 ±-.-	109.90 ±-.-	326.46 ±-.-	-.-	[47]
B. *et al.*	0.768 ±0.011	1.55	0.50 ±0.02	3.6 ±0.7	109.7 ±1.8	326.410 ±0.005	2013-02-15.139	[47]
Z. & F.	0.828 ±0.03	1.73	0.51 ±0.08	3.45 ±2.02	120.6 ±2.8	326.70 ±0.79	2009-02-15	[42]

Final Fragments

After the main disruption, at least two large fragments emerged in the video at Chelyabinsk, causing two trains at a slight angle with respect to each other in the video from Chebarkul (Fig. S8). In later photographs (Fig. S15), both trains are seen to have developed the double billowing structure similar to the main train. The two trains are also seen in the train image by Marat Ahmetvaleev at 3:20:43 UT, immediately following the fireball (Fig. S15A). Only one of the trains (labeled "1" in Fig. S15) penetrated to low altitude.

The fragment that survived longest was discussed before, when examining the trajectory below 25 km. It initially trailed the second piece, only to overtake it just when that fragment faded at 18.0 km. The second fragment, as measured in Chebarkul and Chelyabinsk data (Fig. S15B and C), arrived from a radiant R.A. = 326.5±0.2º, Decl. = 8.3±0.1º, with <V> = 13.05 km/s assuming no deceleration. The fragment moved from 54.860±0.003ºN, 61.125±0.003ºE at 24.9 km to 54.899±0.001ºN, 60.806±0.001ºE at 18.0±0.1 km. The fading fragment moved slightly south of the deeper penetrating fragment and may have dropped meteorites just south of the city of Chebarkul.

The trajectory and speed are consistent with this fragment having created the hole in Chebarkul lake. The trajectory was manually iterated to match the trajectory of Fig. S14A. It was then propagated with no wind, assuming a spherical mass of 100 kg. The precision of the impact point (Long. = 60.2278ºE, Lat. = 54.9725ºN), about 5 km west of the Chebarkul Lake hole (Fig. S53 below), is limited by the accuracy of the astrometric data below 25 km (Figs. 14A and B),

ongoing ablation and fragmentation, and the unknown shape of the final mass, which limits the ability to accurately determine mass or ballistic coefficient. Due to the low entry angle, a 200 kg spherical mass would end up about 5.5 km further along the trajectory than a 100 kg mass. The uncertainty ellipse along the propagated trajectory is about 20 km long. The uncertainty ellipse perpendicular to the propagated trajectory is only about 1.6 km wide, with the Chebarkul Lake hole only 0.34 km south of the propagated trajectory. The expected wind drifts perpendicular to the trajectory for a 100 or 200 kg mass of reasonable shape and density are less than 0.1 km (see Sect. 3.1, Table S15).

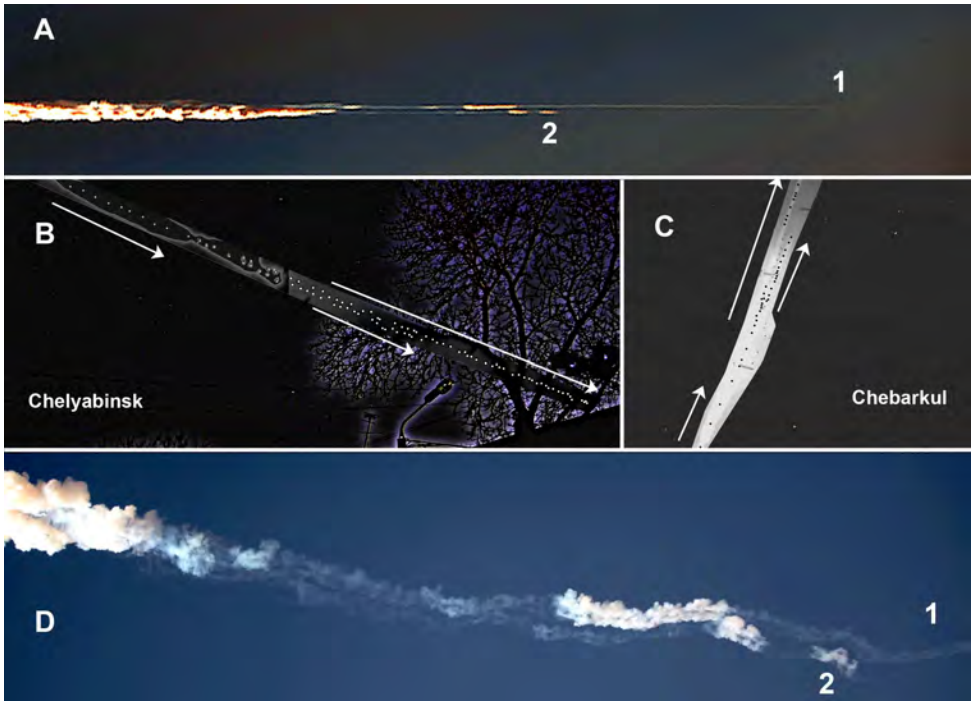

Fig. S15. Below 27 km, two fragments emerged from the main disruption. **(A)** Fragments are seen separately in this photo by Marat Ahmetvaleev, labeled "1" and "2". Points mark the position of each fragment in meteor video, projected on top of the star background images at **(B)** Chelyabinsk and **(C)** Chebarkul. **(D)** Each fragment's wake developed the double-train billows a short time later, documented in this photo by Evgueny Tvorogov from Chelyabinsk (55.03632ºN, 61.08503ºE) at 3:21:52 UT.

Model of Meteoroid Orbital Dynamics

(Contributed by: M. Granvik)

According to the Bottke *et al.* near-Earth object (NEO) model [33], Chelyabinsk has a 62 / 25 / 11 / 2 / 0 % probability of originating from the ν_6 secular resonance / the Intermediate Mars Crosser region / the 3:1 mean-motion resonance / the Outer main Belt / Jupiter Family Comets.

These numbers cover the one-sigma orbital uncertainty given in Table S5B, and are an average between adjacent bins in the semi-major axis, eccentricity, and inclination (a, e, i) space in order to accommodate the estimated uncertainty.

Given the measured orbit in Table S5B, dynamical modeling using forward integrations from realistic sources in the main asteroid belt was applied to calculate the time it takes for an object to evolve to a Chelyabinsk-like or Itokawa-like orbit after entering the NEO region (Table S6). Here, the 4:1 resonance is at ~2.06 AU, outside of the interval for Intermediate Mars Crossers (a > 2.1 AU). Hence, the 4:1 resonance probabilities are included in the ν_6 secular resonance source in the Bottke *et al.* model.

Table S6. Average time from first entering the NEO region until evolving to Chelyabinsk- or Itokawa-like orbit in My (in brackets: minimum/median/maximum values) and number of particles in the model that arrive in such orbits (N).

Source region	Chelyabinsk	N	Itokawa	N
ν_6 secular resonance	10.63±0.95 (0.19/3.5/430)	861	27.6±6.6 (1.5/14.3/350)	64
4:1 mean motion reson.	3.19±0.73 (0.10/1.2/125)	194	12.2±3.7 (1.5/6.3/67)	19
3:1 mean motion reson.	8.87±1.85 (0.10/1.9/191)	184	13.0±2.5 (2.3/13.5/32)	14
Hungaria or Phocaea	25.2±2.5 (0.14/2.6/695)	658	62.8±8.2 (0.4/28.4/543)	101

If the evolution time is used as a proxy for the last possible collision in the main belt, then one needs to add the ~1 My it takes to move from the post-collision orbit to the orbit bordering the NEO region [48].

The test particles analyzed do not necessarily spend all the time in the NEO region but may occasionally escape and then enter again. Particles escaping from the high-inclination Hungaria and Phocaea regions have multiple escape routes, which more or less mix together. The weighting for these regions is different, it typically being much more likely that the objects originate in the low-inclination part of the inner main belt than the high inclination Hungaria and Phocaea regions.

Note that the tail of the evolution time is probably dominated by objects that escape the NEO region and then enter again. Integrations were continued until a particle collided with the Sun or a planet, or escaped the (inner) Solar System. So, if the evolution time is used as a proxy for the last possible collision in the main belt, then the tail is probably misleading as is also the average evolution time. Hence, the median value listed in Table S6 (center value between brackets) is

more reliable than the average.

The three fastest transport routes for Chelyabinsk from the low-inclination region are through the 4:1 or 3:1 mean motion resonances (~0.1 Myr), while the three fastest transport routes from the high-inclination region originate in the Hungaria group (0.14, 0.20 and 0.22 Myr).

The results (Table S6) suggest that (1) Chelyabinsk may be younger than Itokawa on purely dynamical grounds and (2) both objects most likely originated in a low-inclination source region. However, a higher-inclination ($i > 7^{o}$) source region cannot be excluded.

1.2. Lightcurve and meteor model

Lightcurve

(Contributed by: P. Jenniskens)

The lightcurve of the meteor is the total radiated intensity of the fireball at optical wavelengths as a function of time or altitude. The lightcurves (Fig. S16) were derived from the fireball illumination of the ground and buildings in the video security cameras listed in Table S3. Different video cameras are gain-controlled in different ways, as a result of which some record a peak in brightness as early as 03:20:31.2 UT, others as late as 03:20:32.2 UT. By comparing the brightness of features in different cameras, it was possible to take these gain changes into account. Gain changes were least apparent (or had slowest response) in video #30 (Table S3). The camera saturates on directly illuminated features at peak brightness. However, the shape of the lightcurve during peak brightness was measured from the indirect illumination of shadowed tiles in video #30 (Table S3).

Before and after peak brightness, the meteor brightness was measured from two videos taken in Yekaterinburg (early part, Fig. S17A) and Yemanzhelinsk (late part, Fig. S9). The sum pixel intensity was corrected for saturation, using the method: F_corr = F_obs * exp (F_obs/F_scal) [49], where the scaling factor F_scal was determined by matching those parts of the lightcurve that overlapped with data derived from the shadow videos.

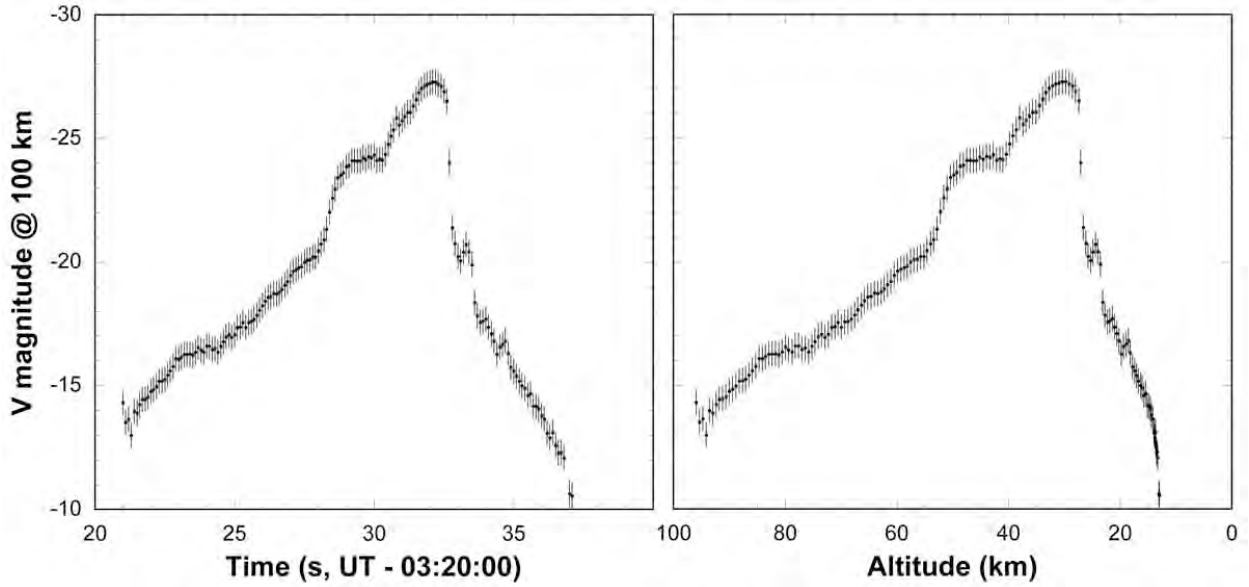

Fig. S16. (A) Lightcurve of the fireball. Error bars approximate the uncertainty from absolute calibration of the photometric data. **(B)** Lightcurve as a function of altitude.

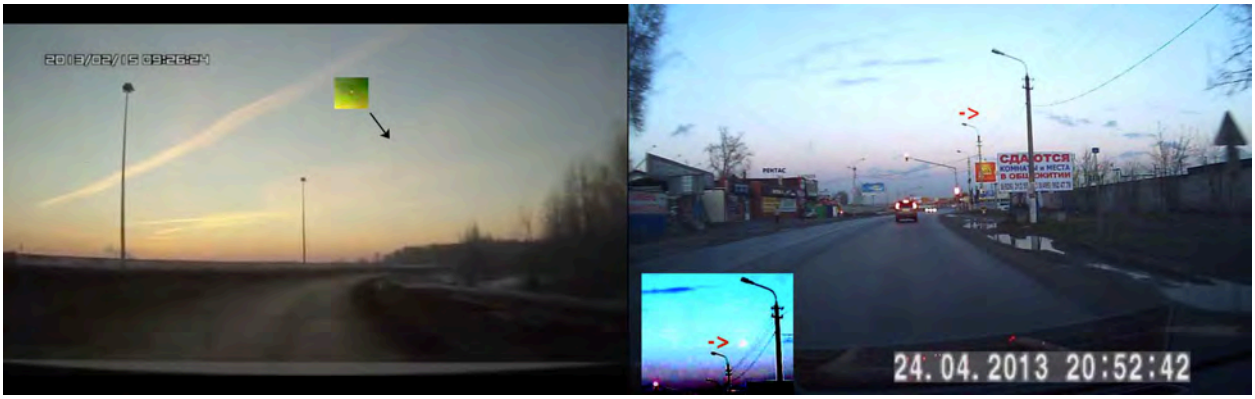

Fig. S17. (A) Left: first detection of the meteor in unaccredited video that went viral on the internet, taken near Yekaterinburg (Sverdlovsk Oblast - 56.7601N, 60.7639E). **(B)** Calibration image of wide-angle dash-board mounted camera taken in Moscow by Andrey Shugarov (Institute of Astronomy RAS). Inset: contrast enhanced area around the meteor and the moon.

Absolute calibration of the flux density was attempted by filming the near-full Moon in Moscow using a Mediox DVR100 model camera on April 24th, 3 minutes before sunset under similar lighting conditions as the fireball 2.5 minutes after sunrise (Fig. S17B). The camera adjusts the gain and offset depending on foreground features. The fraction of sky in the image was about the same as that in the videos used to calibrate the lightcurve. The resolved image of

the moon was detected. This corresponds to a -12.71 visual magnitude (98% of the moon's visible disk was illuminated). The image's peak intensity level was 253, while the bright sky background was 248 (0-255 full range).

The integrated luminosity between the calibration image and the first detection of the meteor (Fig. S17) corresponded to the meteor initially being 2.0 magnitude fainter than the moon. That means that the meteor, when it was first detected, was initially around -10.7 magnitude at a distance from Yekaterinburg of 378 km. Hence, the initial absolute brightness (that is, as seen from a distance of 100 km) was -13.6±0.5 magnitudes.

This calibration puts the peak visible brightness of the fireball at -27.3±0.5 magnitude as seen from 100 km distance (Fig. S16). In Chelyabinsk, the apparent visible brightness was -28.8 (±0.5) magnitude, brighter than the Sun at -26.0 magnitudes. Immediately under the track in Korkino, it peaked at about -29.6 magnitude. Indeed, of the respondents in an internet survey (see below), 3 put the peak brightness of the fireball as bright as the full Moon, 39 fainter than the Sun, 105 as bright as the Sun, and 1,155 brighter than the Sun.

The lightcurve has an integrated brightness equal to 1.42 seconds of emission at peak brightness. With an effective panchromatic passband width of 336 nm, this amounts to a total radiated energy of 28-69 kT in this band.

Meteor Model

(Contributed by: O. P. Popova)

The size of the Chelyabinsk meteoroid is large enough that its interaction with the atmosphere proceeds in the continuous flow regime. The Knudsen number (the ratio of the molecular mean free path to a characteristic body size) decreases to 0.1 at an altitude of 90 km, where a shock wave is formed around the meteoroid. Hydrodynamic models are able to describe the interaction of such large meteoroids with the atmosphere well - see review by Popova [50]. The ablation of the meteoroid is mainly governed by the radiation from the shock compressed air and from the ablation products [51,52]. Fragmentation adds more drastic effects than the relatively simple effects of deceleration and ablation. Meteor models are typically varied by how they handle fragmentation.

The hydrodynamical models that considered all effects, i.e., ablation, radiation and fragmentation, are sparse and have so far been applied only to several large $>10^8$ kg objects (e.g.,

[51, 53-54]). They assume that the fragments are closely packed and behave as a liquid, but these models cannot predict details of the fragmentation process, such as the simultaneous production of dust and fragments. The behavior of smaller meteoroids is typically described by standard equations based on the laws of conservation of mass, momentum, and kinetic energy [55-56].

The objective here is to fit in detail the observational data of the lightcurve (Fig. S16) and the deceleration (Fig. S14), in order to reproduce some aspects of, or the total picture of, the meteoroid interaction with the atmosphere [55-57] or to derive meteoroid parameters such as the ablation and shape-density coefficients [58,59].

The fragmentation may occur in different ways. One possibility is that a few large fragments are formed, which initially interact through their shock waves and then continue their flight independently and may be disrupted further (progressive fragmentation). This type of model usually incorporates a strength scaling law, assuming that the strength of fragments increases when the size decreases. Models differ by adopting different assumptions about the size distribution of fragments formed. The possibility to describe the fate of individual fragments makes it possible to describe the meteorite strewn field or the crater field.

A second approach is to assume that fragmentation occurs as a disruption into a cloud of small fragments and vapor, which initially are united by a common shock wave [51]. This approach is often applied to large bodies. These bodies (such as Tunguska, for example) may be essentially disrupted, but do not form separated fragments, all material continuing flight as a single strengthless body [54]. If the time between fragmentations is shorter than the time for fragment separation, all the fragments move as a unit, and a swarm of fragments and vapor penetrates deeper into the atmosphere, being deformed by the aerodynamical loading like a drop of liquid (called the "liquid-like" or “pancake” model). The smallest fragments fill the volume between the larger pieces and quickly evaporate. But large fragments may escape the cloud and continue the flight as independent fragments. Both fragmentation scenarios are realized in real events (much smaller than Tunguska), sometimes at different stages in the same meteor [56,60].

It is usually assumed that the destruction of a meteoric body begins at the moment when the aerodynamic pressure in the vicinity of a stagnation point becomes equal to some constant describing the strength of meteoroid material. There are different approaches to the choice of characteristic strength in the breakup criterion [51]. A compilation of data on stony meteorite strength [51, 61-62] provides an average compressive strength of 217 ± 134 MPa, and an average

tensile strength of 30 ± 17 MPa for gram-range samples recovered on the ground. In contrast, observational data from 13 meteorite falls with accurate tracking data on atmospheric entry resulted in estimated bulk strengths (meter-sized objects) in the range of 0.1 to 1 MPa on first breakup, while the maximal strength on breakup was no more than 1–10 MPa [62].

An initial meteoroid mass was assumed to be equal to $M = 7 \times 10^6$ kg, the entry velocity = 19 km/s, and the initial strength = 0.2 MPa. A heat transfer coefficient C_h~0.1 was adopted for the initial body and for all fragments, which corresponds to an ablation parameter of 0.016 s^2/km^2, similar to ~0.014 s^2/km^2 derived from other stony meteoroid falls [63]. The luminous efficiencies used were those derived for the satellite detector passband from radiative hydrodynamic numerical simulations [64,65]. The conversion factor to magnitudes was taken as 1.1×10^3 J/s per zero magnitude [63], or 2.6×10^{-11} $W/m^2/nm$ for a panchromatic band of 336 nm width and standard distance to the source of 100 km.

The adopted initial mass is lower than the estimated entry mass of 1.3×10^7 kg, but is chosen within the factor of two uncertainty. An increase of initial mass by a factor of two would lead to an increase of the meteor brightness by about +0.5 magnitude prior to fragmentation, and about +1.5 magnitudes at the peak. Both the luminous efficiencies and the conversion factor to visual magnitude are poorly known, which each can affect the brightness by up to a magnitude.

Our first attempts to model the lightcurve and deceleration was by using a progressive fragmentation model with a range of possible size-frequency distributions of fragments (power law, with two or a few surviving fragments) with a power law increase of strength with decreasing size (not shown). This approach resulted in too many pieces and too much mass of meteorites falling on the ground (about 300 tons in about 10^6 pieces), too bright radiation below 25 km altitude, and too small total irradiated energy (integral luminous efficiency ~6-8%).

The huge number of fragments formed at altitudes of 50-20 km during a short time suggests that the pure progressive fragmentation model fails because fragments cannot be considered independent. The formation and deceleration of the cloud of small fragments and dust was directly observed, emitting thermally at the final stages of evolution (Fig. S19, below). A hybrid model between the progressive fragmentation model and the pancake model [60] may provide a better representation. Unfortunately, the fraction of the initial mass that is converted into an expanding cloud of fragments is poorly determined from the observations.

The masses of daughter fragments in subsequent fragmentations are chosen randomly in every breakup. The fragment mass distribution of the surviving meteorites varied from one model run to another, with the largest surviving fragment about 100-400 kg and the majority of remaining fragments smaller than 10 kg.

This approach reproduces the main features of the light curve, but is based on a simplified description of the observed fragmentation process. The solution is not unique. For example, by assuming that a larger number of clouds of small fragments and dust are formed also reproduces the light curve, but requires even more free parameters.

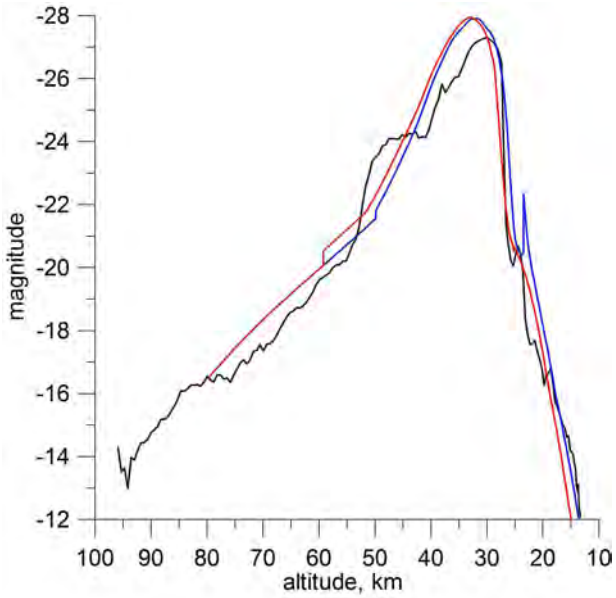

Fig. S18A. Two model lightcurves fitted to the data (red and blue; black is observed data). These represent two random realizations of fragmentation into three expanding clouds and a number of separated fragments.

Figure S18A shows the result for two arbitrary solutions that produce a reasonable fit to the observed lightcurve, albeit with small altitude discrepancies. For example, the narrow peak on the blue curve corresponds to a disruption of large fragments that survived the main fragmentation. There is a similar flare in the observed curve. The difference in peak intensity is simply caused by a different amount of mass involved in the breakup. Similarly, the higher observed intensity at 50-40 km altitude means that a higher amount of decelerated material was involved in the fragmentation at these altitudes.

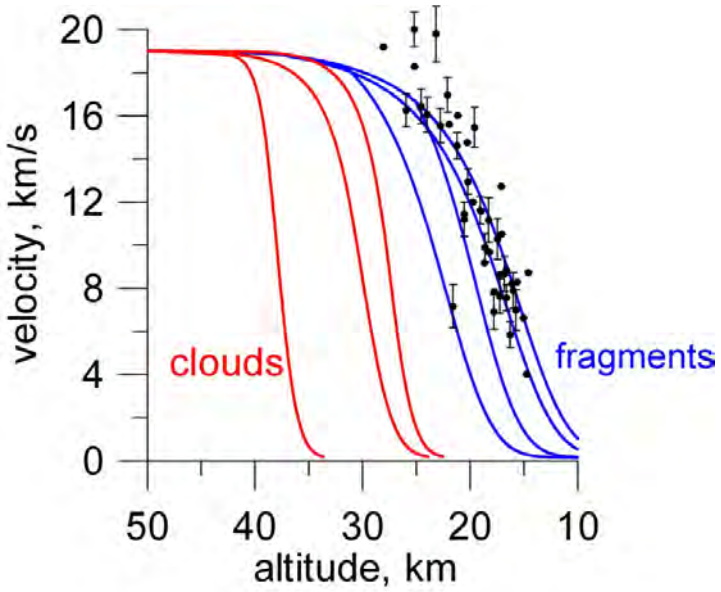

Fig. S18B. As Fig. 18A, showing deceleration data from Fig. S14B. Speed of some fragments for the blue scenario in Fig. S18A. Colors now refer to small debris and dust ("Clouds") formed prior to the 27-km event (red), while "fragments" are the surviving fragments (blue).

These models also describe the observed deceleration (Fig. 18B). The deceleration curve derived from the video records was nearly constant down to 27 km, followed by rapid deceleration below 27 km, with the possibility of some deceleration just before the 27-km altitude point (Sect. S1.1, Fig. S14B). The observed data is shown by black dots in Fig. S18B. The velocity profiles for fragments in the blue model of Fig. 18A are shown. Colors now refer to small fragments and dust ("Clouds") formed prior to the 27-km event (red), while a few of the surviving larger fragments are shown in blue. The final mass for the largest fragment is about 300 kg.

The number of fragments generated and the total amount of mass at any given altitude (including clouds of fragments and dust) are shown in Fig. S18C. The massive fragmentation at 32-29 km altitude created a rapid increase in the number of fragments. This corresponds to a peak in the energy loss at that altitude (Fig. S18E). Most of the mass and kinetic energy was deposited between 40 and 25 km altitude. The initial strength of the meteoroid was low, but the strength progressively increased during the fragmentation process. The loading pressure needed to continue the fragmentation process is shown in Fig. S18E-B.

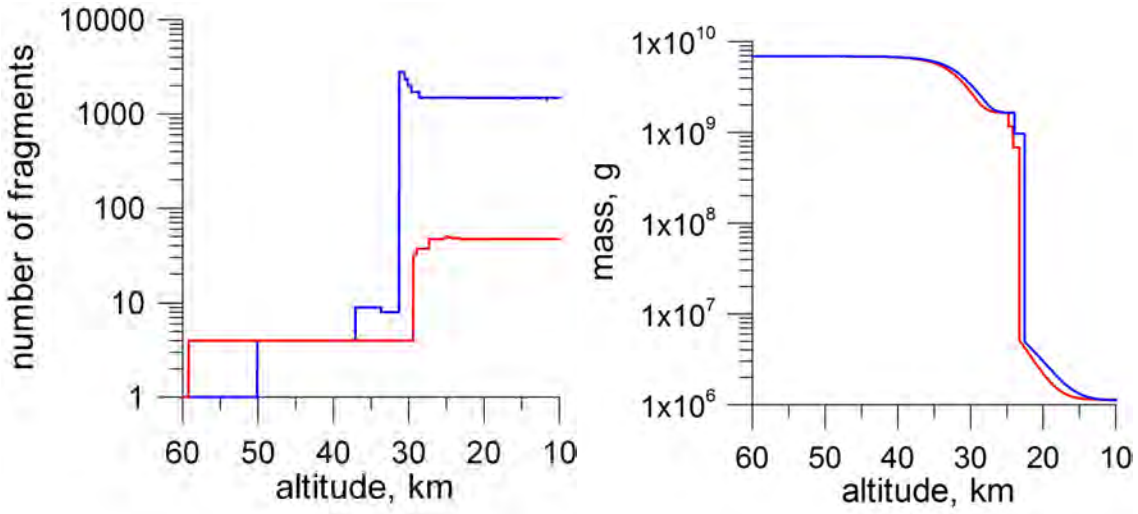

Fig. S18C. As Fig. 18A. **(A)** Number of fragments versus altitude. **(B)** Total mass of all surviving fragments as a function of altitude for the same two fragmentation model runs resulting into three expanding clouds of debris and a number of separate fragments.

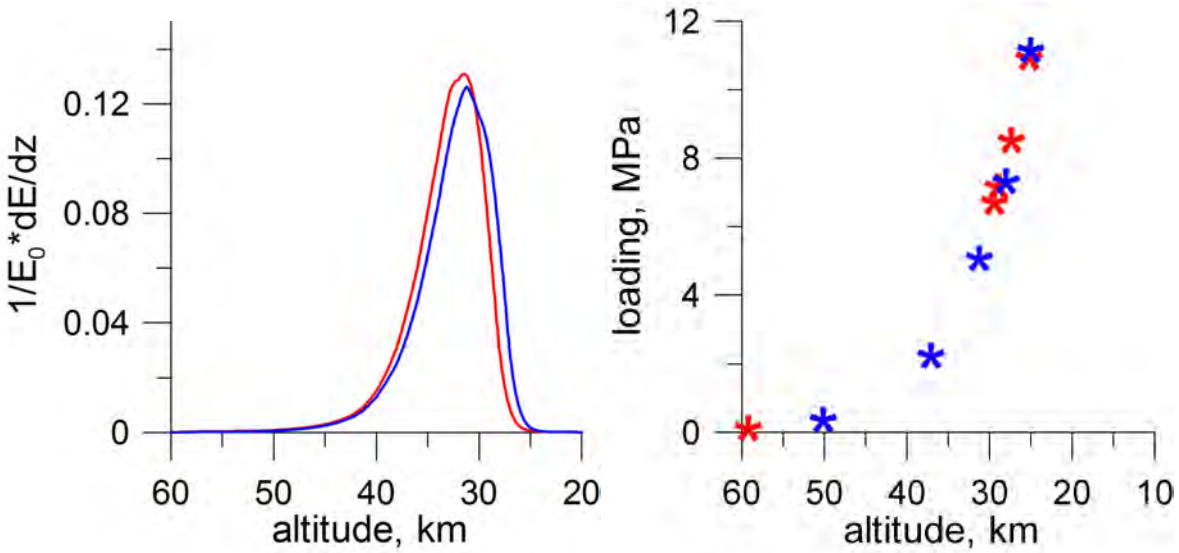

Fig. S18D. As Fig. 18A. **(A)** Energy loss as a function of altitude. **(B)** The strength of the fragments as a function of altitude, for the same two model runs.

The number and size of fragments, their precise location in the strewn field, etc., changes from one set of model assumptions to the next, but some aspects are well constrained. All need a

low fraction of fallen mass and a large energy/mass deposition above 20 km. The calculated integral luminous efficiency is 18-20%. The evaporated mass is about 76% of the initial mass, while 24% is converted into clouds of debris.

The cloud of fragments created in the 32-29 km breakup decelerated at altitudes of 27-23 km (observed: down to 26.2 km). This cloud of fragments resulted in the numerous small meteorites found in the area centered on Deputatskoye (see Sect.3.1). Based on the number density of recovered small meteorites, the total surviving mass from that cloud of small fragments adds up to about 3,000-5,000 kg (Sect.3.1).

The surviving fragments that stayed luminous below 25 km produced about 1,000 kg of surviving mass in the form of 20-2,000 individual meteorites in various model runs. These larger fragments form the leading part of the meteorite strewn field. The extent of this part of the strewn field varies from one run to another, but the largest fragment (mass 100-400 kg) is able to reach Chebarkul Lake for some model runs (see Sect. 3.1). The position of 3.4 kg meteorite (Sect. 3.1) is also in agreement with our modeling. Together with the surviving mass of smaller meteorites, the total fallen mass is about 4,000-6,000 kg, i.e. 0.03-0.05% of the initial mass.

More typical surviving fractions for other ordinary chondrite falls are in the range 0.1-3 %. Even lower fractions are known from fragile meteorites like the carbonaceous chondrite Tagish Lake and the polymict ureilite Almahata Sitta [62].

1.3. Thermal Radiation and the Smoke Cloud

(Contributed by: P. Jenniskens, O. P. Popova)

Thermal emission is responsible for yellow, orange, and red colors in the train just after the passing of the fireball in the video from Kamensk-Uralskiy and in the still images of Fig. S5 (also see Fig. 1 main manuscript), which were taken with short enough exposure (or far enough from the trajectory) to not saturate the color bands.

This cloud of thermally emitting debris came to rest between altitudes of 29 and 26 km (Fig S19). The color provides a record of the temperature: the red colors in Fig. S19B correspond to 700±100 K, about 5s after formation, if the smoke cloud is scattering sunlight with a color temperature of 5,780K. Assuming the initial temperature was that of evaporation (a lower limit) implies a cooling rate of ≥240 K/s. If the low elevation of the Sun at the time of the impact made

the smoke cloud look a little redder than unfiltered sunlight, then that would slightly raise the temperature estimate of the thermally emitting debris and decrease the cooling rate.

Fig. S19. Detail of the train's thermal emission. **(A)** Image posted by Mr. Dudarev on the Leprosorium website (http://img.leprosorium.com/) taken about 5.0s after passage of the meteor. Sky background was subtracted by applying a low-pass filter. **(B)** Image by Marat Ahmetvaleev, in an 0.6s exposure at 27 mm f/14 using a Canon 5D at ISO 50 and Cokin graduated filter, taken about 6.0s after the meteor. Sky subtracted in the same manner. Relative times derived from comparison with Kamensk-Uralskiy video.

The fireball smoke train exhibited most billowing between altitudes 80 and 27 km (Fig. S20). During this early part of the trajectory, the dust cloud split in two because of buoyancy and the development of two cylindrical vortices [68]. Below 27 km, the train suddenly showed less separation and less billowing (Fig. S20C). At this time, two main fragments emerged, each of which created a dust train that subsequently also split in two due to buoyancy (Fig. 15D).

The separation of the two cylindrical vortices shortly after formation (red lines in lower part of Fig. S21, showing a view from Yemanzhelinsk) is an indication of the amount of buoyancy of the hot air left in the meteor path, depending on air density and the amount of kinetic energy deposited per kilometer along the trajectory. Most energy was deposited between 50 and 27 km, in agreement with the general shape of the lightcurve (Fig. S16).

Above 40 km, the train showed a regular pattern of billows in an image taken from an aircraft (Fig. S22). A slight discoloration is visible between about 65 and 67 km altitude. This discoloration was seen both in airborne and ground-based observations and corresponds to a brief displacement of the train in Northern direction (e.g., Fig. S22D). Wind models do show a change in wind direction at this altitude (Fig. S24 below).

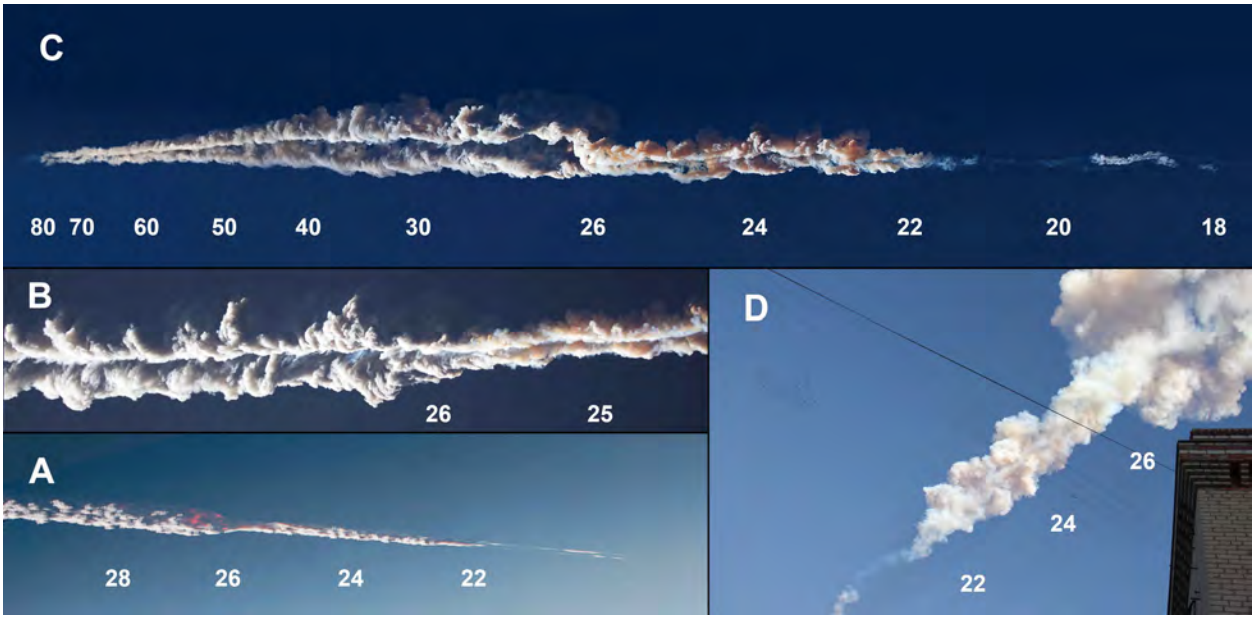

Fig. S20. (A) Smoke train ~ 5 s after formation, still glowing from orange and red thermal emission. Photo: Marat Ahmetvaleev. Approximate altitude markers in km. **(B)** Smoke train ~35 s after formation, view from Chelyabinsk by Evgueny Tvorogov. Orange colors may now be from NO emission. (**C)** Smoke train 46-73 s after formation, composite of several photographs by Tvorogov. (**D)** View ~1.5 min after formation below the train in Yemanzhelinsk, showing the high billow and wide train separation during the main flare. Photo: Victor I. Gubar.

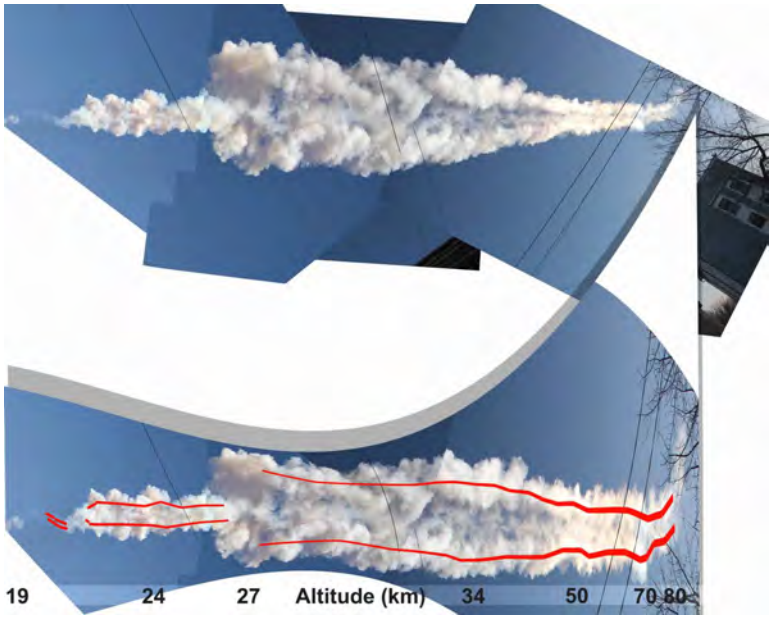

Fig. S21. Train as seen from below in Yemanzhelinsk about 1.5 minutes after formation, before (top) and after (bottom) an approximate correction for range, so vertical scale is the same for different altitude parts. Photo: Victor I. Gubar.

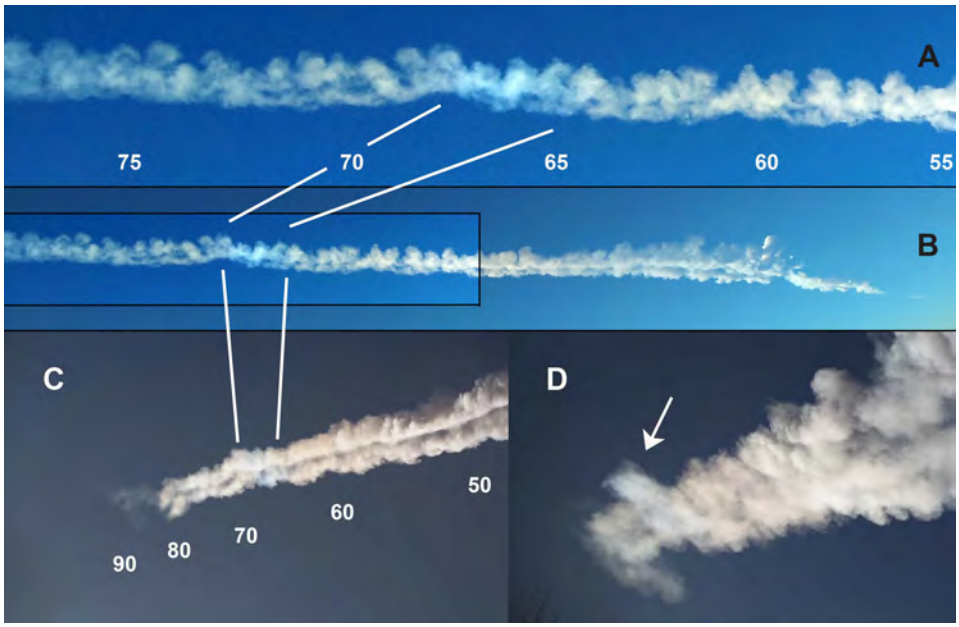

Fig. S22. (A) Discoloration in the smoke train ~20s after formation, along with a less cropped photo for context **(B)**, in an airborne photo taken by Sergey Valer'yanovich from the cockpit of flight Aeroflot 1639 from Omsk to Moscow. **(C)** Corresponding views from the ground in Chelyabinsk by Evgueny Tvorogov at 9:21:45 UT and **(D)** a short time later at 9:25:29 UT. Arrow marks the discolored train feature. Numbers refer to approximate altitudes in kilometer.

Our modeling (Sect. 1.2) suggests that this dust cloud contained a similar fraction (~ 24%) of the original mass of the meteoroid than measured for other falls. These clouds are formed more often at 60-30 km altitude, but data on particle size and mass fraction relative to that of the parent body are scarce [60]. Routine lidar observations detected such a dust cloud after the fragmentation of a 600 - 1,900 t meteoroid over the Antarctic [66]. Satellite observations showed that this meteoroid fragmented at 32 km altitude, with a second fragmentation at 25 km. The dust cloud was recorded 7.5 hours later. The total mass of dust in that dust cloud was estimated at ≥1,000 t (≥ 53% of the initial mass). Dust grain diameter and concentration were calculated as 0.4-0.98 µm and 2-6 10^6 particles per m^{-3}, respectively. Similarly, the mass of the dust cloud formed after the disruption of the 4-m sized 2008 TC_3 asteroid, observed by spaceborne mid-infrared sensors, was about 25% of the initial asteroid mass, and 5% of that was from recondensed vapor [67].

Prevailing Winds and Train Drift

(Contributed by: L. G. Evers, J. Kuiper, V. Kharlamov, O.P. Popova, and P. Jenniskens)

In the northern hemisphere winter, the wind in the stratosphere is directed to the east. This wind, known as the circumpolar vortex, can reach strengths of over 150 m/s around the stratopause at an altitude of 50 km, which is the top of the stratosphere. Its strength gradually decreases towards the lower stratosphere. In winter, the circumpolar directivity can be disturbed by planetary waves that propagate from the troposphere into the stratosphere and interact with the mean flow.

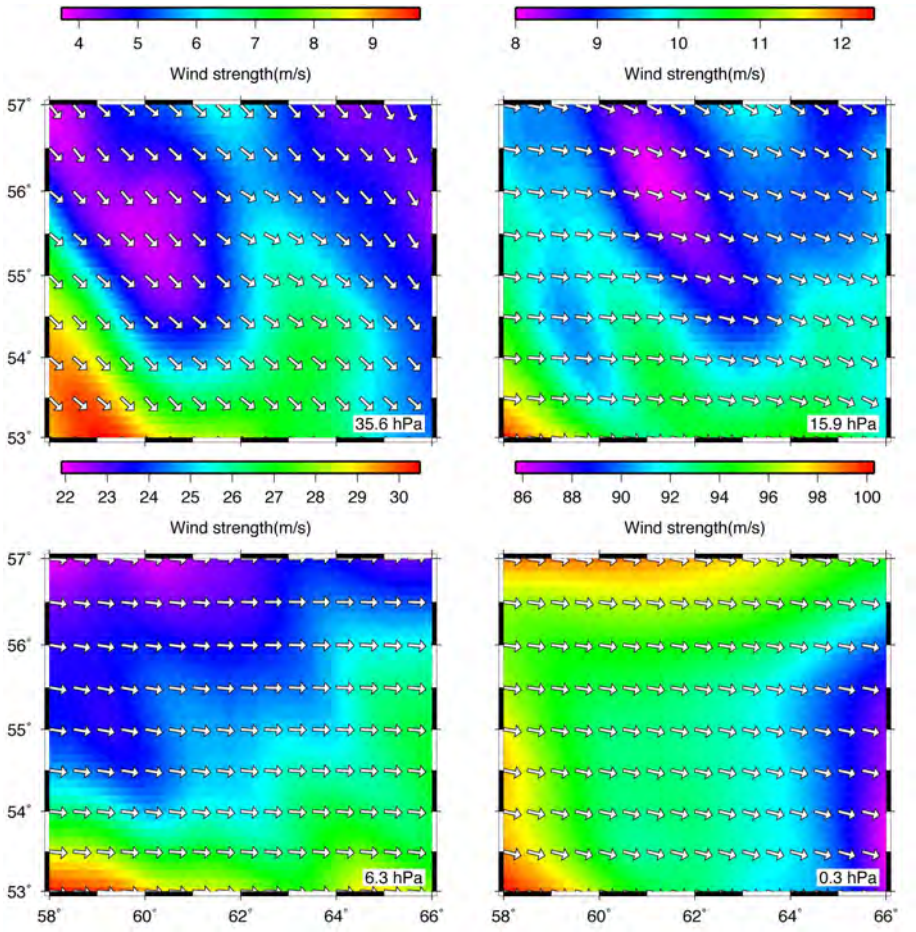

Fig. S23. Wind data from the ECMWF model at 06h UTC on February 15, 2013, in longitude and latitude coordinates. Various slices of altitude in the stratosphere are shown, each with a separate velocity-coded pattern of wind strength at particular atmospheric pressure in hectoPascal (corresponding altitude shown in parenthesis): 35.6 hPa (~22.2 km), 15.9 hPa (~27.0 km), 6.3 hPa (~32.7 km) and 0.3 hPa (~55.0 km). The wind direction is given by the white vectors.

Atmospheric specifications of these winds are provided by the European Centre for Medium-Range Weather Forecasts (ECMWF) every six hours (00:00, 06:00, 12:00 and 18:00 hour UTC) on a 0.5 by 0.5 degrees global spatial grid. The models consist of 91 levels with a decreasing vertical resolution, i.e., as a function of altitude, from tens of meters in the troposphere to several kilometers in the stratosphere. The top of the models lies in the mesosphere at a level of around 78 km. The non-forecast models are validated with actual measurements of atmospheric parameters like wind and temperature.

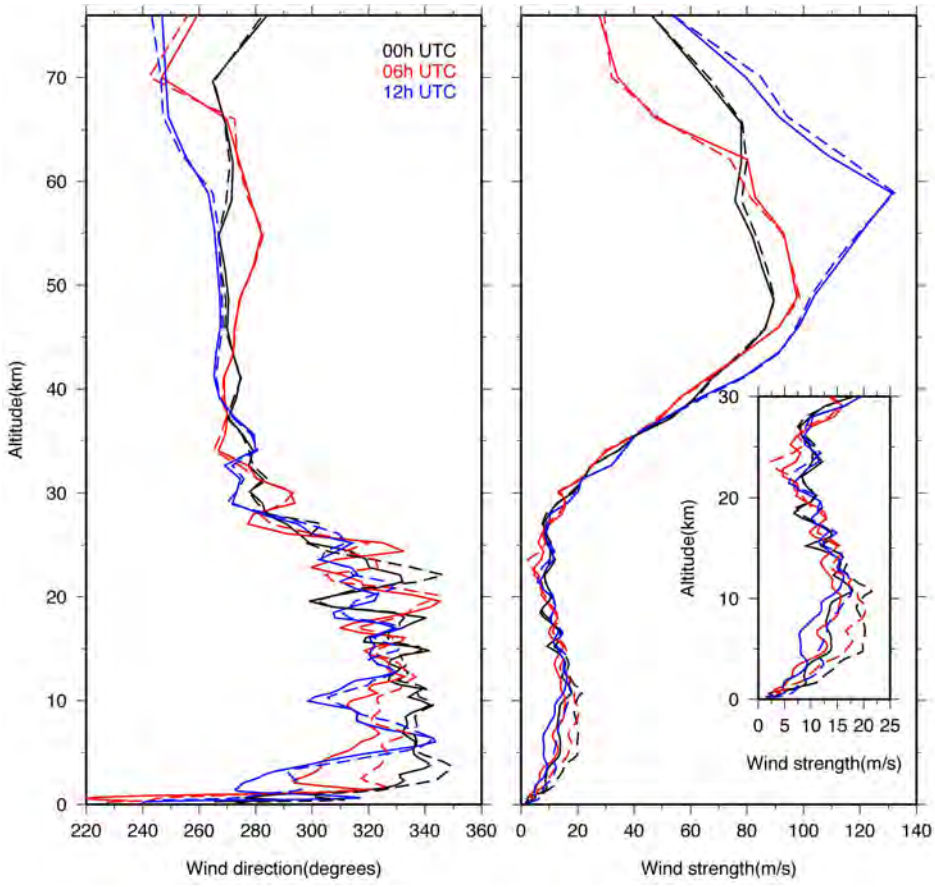

Fig. S24. The wind direction and strength from ECMWF specifications at 00h (black), 06:00 (red) and 12:00 UTC (blue) for 54.5ºN, 61.0ºE (solid lines) and 54.5ºN, 62.5ºE (dashed lines). The inset in the wind strength frame zooms into the lower stratosphere and troposphere.

Fig. S23 shows the wind strength and direction over the area of interest for 06:00 UTC for several levels in the stratosphere. A well-developed circumpolar vortex is present over the area, which is predominantly directed from the west to the east. At lower levels the vortex points towards a more southeastern direction. The strength varies from a couple of meters per second in

the lower stratosphere to over 100 m/s around the stratopause. The lateral variations in the wind strength increase with altitude from 6.1 m/s at 35.6 hPa to 14.6 m/s at 0.28 hPa. The wind strength is lowest at 15.9 hPa with a value of 4.4 m/s.

In order to assess the variation in the wind as a function of time, the 00:00, 06:00 and 12:00 UTC model outputs are plotted in Fig. S24. The profiles are valid for 54.5ºN, 61.0ºE near Deputatskiy (point t1 in Fig. S26 below) and for 54.5ºN, 62.5ºE, close to point t6 in Fig. S26. Data from local meteorological stations measured the wind at ground-level to be of about 1-3 m/s in agreement with the model. The ECMWF wind profile below 30 km is also in good agreement with that derived from atmospheric sounding at the Verkhneye Dubrovo station (56.73ºN, 61.06ºE), the nearest station to Chelyabinsk (Fig. S25).

During the day, there is an increase in the wind velocity in the (upper) stratosphere, while the wind direction varies around an average value of 270 degrees, i.e., a wind to the east. In the lower stratosphere and troposphere, there seems to be a larger variation in the wind direction, while the strength is much less variable. The wind strength in the lower stratosphere is about 10 m/s (see the inset of Fig. S24). The average direction is towards the southeast. These observations are consistent for both location t1 and t6. However, it should be noted in the above that the resolution decreases with altitude, which does not allow fine scale structure to be resolved in the upper stratosphere in as much detail as in the lower stratosphere and troposphere.

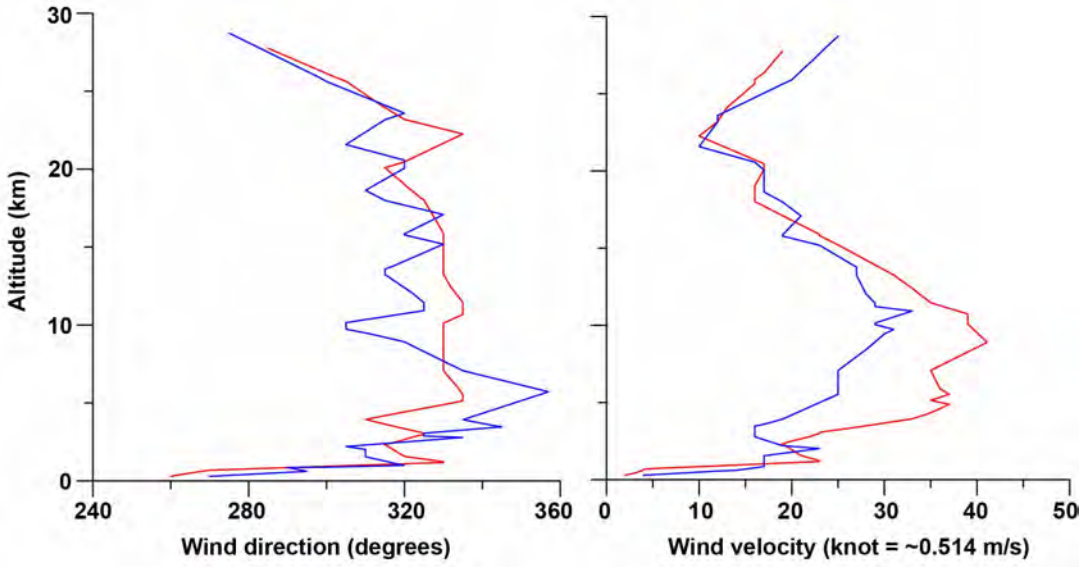

Fig. S25. Wind profile from atmospheric sounding at the Verkhneye Dubrovo station (56.73ºN, 61.06ºE), the nearest station to Chelyabinsk, at 0:00 UT (red line) and 12:00 UT (blue line) on February 15, 2013.

Based on the above analysis, the higher part of the smoke train is expected to move to the east as a function of time (opposite to the direction of the meteor and slightly to the north), while the lower part, i.e., lower than 27 km, should exhibit a displacement to the southeast. Due to the stronger winds in the upper atmosphere, the higher part is expected to disperse faster than the lower part. Unresolved fine scale structure in the stratosphere, for example due to gravity wave activity, may lead to additional wind shear, which can extend over several kilometers in altitude.

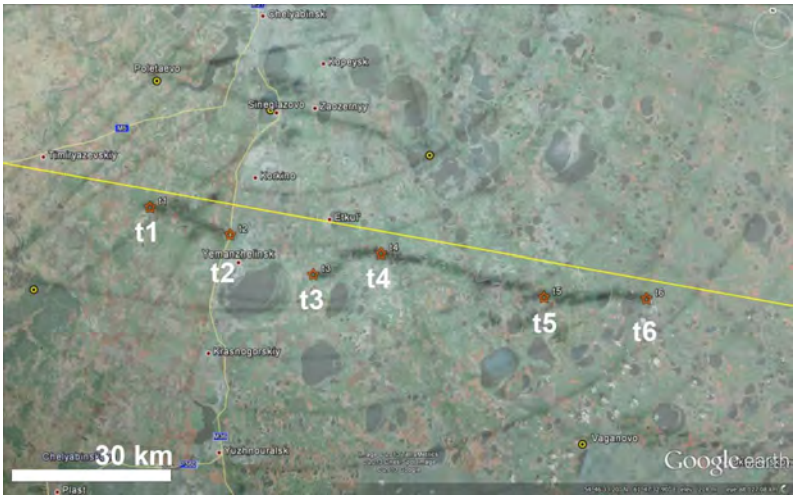

Fig. S26. Chelyabinsk airport radar detection of the smoke train shortly after the fireball (black band below yellow line, the video-derived fireball trajectory). Points labeled t1 through t6 are discussed in the text.

The dust cloud was detected by the airport radar in Chelyabinsk, which scans around at a rate of 12 rotations per minute. A slightly blurred photograph of the radar screen was taken a short time (time unknown) after the event (Fig. S26). The map shows 10-km spaced concentric circles and 10^{o} radial lines, as well as a number of identified locations. Those locations were aligned using Google Earth and reflections identified as possibly from the train are highlighted in black.

The approximate altitudes corresponding to the six points in Fig. S26 correspond to t1 ~ 22.7 km, t2 ~ 27.3 km, t3 ~ 30.3 km, t4 ~ 36.7, t5 ~ 46.6 and t6 ~ 52.8 km altitude, assuming only southward drift, and correspondingly lower altitudes if the drift was also towards the east. The wind direction-change around 29 km is responsible for the break in the train in Fig. S26. Mild winds between 22 and 27 came from about 310^{o}. The train is indeed located slightly south of the fireball trajectory. Above 30 km, the curvature in the train is that expected from wind strength changes as a function of altitude (Fig. S24). The much stronger winds between 30 and 58 km were from 270^{o}, and the train would be expected to have moved slightly north of the fireball

path, rather than slightly south. Hence, local winds around 03:20 UT appear to have been slightly more north of due east.

Fig. S27 shows the lower part of the train at 24-18 km altitude as observed from Yemanzhelinsk 81±1 seconds after peak brightness of the fireball, and from Etkul 56±3 s after the fireball. Both images were calibrated against background stars (Fig. S10-S11). The train at 18.5 km altitude was calculated to have drifted south perpendicular to the line of sight at a rate of 5.5±0.1 m/s in Yemanzhelinsk and 4.2±0.2 m/s in Etkul. The ECMWF model (Fig. S24) and the atmospheric sounding measurements at Verkhneye Dubrovo station (Fig. S25) have a southern component to the wind speed perpendicular to the line of sight of ~8 m/s.

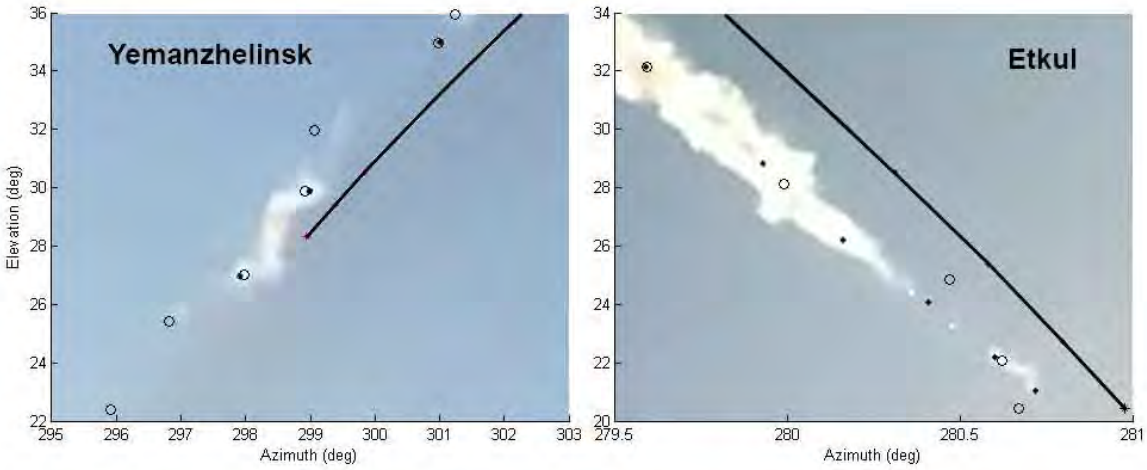

Fig. S27. Train drift relative to the best-fit fireball trajectory (solid line), as filmed in Yemanzhelinsk and Etkul. Black dots are modeled directions, open circles are the actual measurement points. At both sites below the track, the train had drifted in southern direction by the time these images were taken.

1.4. Infrasound Data

(Contributed by: Y. S. Rybnov, V. A. Kharlamov, O. P. Popova, A. Solovyov, Y. S. Rusakov, V. V. Shuvalov)

Infrasound waves are low-frequency (< 20 Hz) acoustic waves above the 10^{-3} Hz Brunt-Vaisala frequency of the atmosphere. They attenuate slowly and can travel on global scales. The Chelyabinsk meteoroid generated infrasound waves that were recorded by 11 Comprehensive Nuclear-Test-Ban Treaty Organization stations (CTBTO), as well as other stations all over the globe [69].

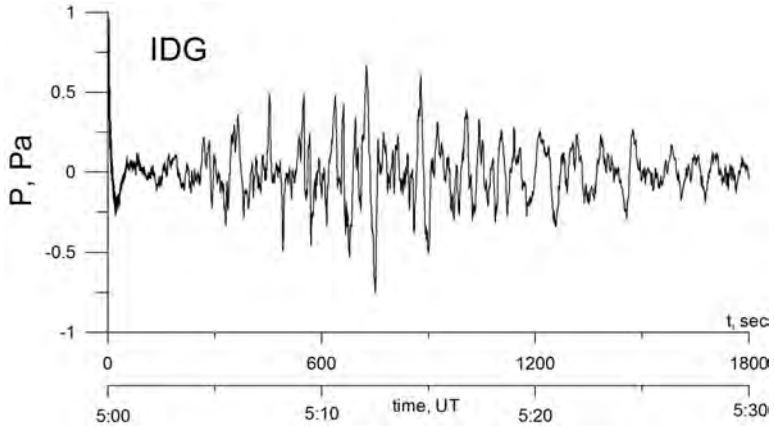

Fig. S28. The infrasound signals from the Chelyabinsk event recorded at IDG, Moscow. Shown signals are filtered in the range 0.01 - 1 Hz.

In this section, signals are discussed that were obtained in four locations nearest to the impact: (1) at a ~1,500 km distance in Moscow at the Institute for Dynamics of Geospheres (IDG), shown in Fig. S28; (2) at a ~1,500 km distance in Mikhnevo at the Institute for Dynamics of Geospheres' Geophysical Observatory; (3) at a ~1,520 km distance in Obninsk at the Research and Production Association "Typhoon" (Fig. S29), and (4) at a ~1,600 km distance in Tomsk at the Tomsk State University (Fig. S29). In addition, another relatively close range infrasound record was obtained by one of the CTBTO station in Kazakhstan is discussed (IS31, Aktyubinsk), located ~520 km from the impact (Fig. S29). Microbarometers with a frequency range 0.001-10 Hz were used at IDG and Mikhnevo, while those in Obninsk and Tomsk were sensitive over the range 0.003-10 Hz. Aktyubinsk (IS31) is equipped with absolute pressure microbarometers (MB2000, France), sensitive from 0.001 to 4 Hz.

The propagation of infrasound waves, and their interpretation as a source of information about the kinetic energy of the Chelyabinsk impact, is sensitive to local atmospheric conditions. To verify that these signals originated from the Chelyabinsk impact, the bearing angles were determined by Progressive Multi-Channel Correlation (PMCC; [70]) and by the correlation function method [71] to a precision of about $\pm 0.5^0$, which corresponds to about ± 13 km in Chelyabinsk area. At the first approximation winds were ignored. All bearing angles passed within 15 km from Karataban, about 20 km east from Yemanzhelinsk. The infrasound signal arrived in Tomsk earlier than in Moscow/Obninsk, suggesting western winds of about 23.5 m/s on average in the stratospheric waveguide where the signal was propagating.

The influence of wind on the propagation was calculated based on the wind data from weather stations along the trajectory of propagation (Fig. S25). Based on the available data, the measured average wind speed was 23.3 m/s, in agreement with the estimate above. By taking these wind speeds into account, the source position shifts about 30 km westward and is now centered between Korkino and Yemanzhelinsk, close to the position of peak brightness based on the video data (Sect.1.1).

At distances larger than a few hundred kilometers, the infrasound waves from meteoroid entries are very similar to those from chemical explosions with the same kinetic energy released [72]. Estimating the source energy for infrasound sources generally relies on empirical scaling relations derived from known sources. These relations use either the period at the maximum amplitude of the signal or the peak-to-peak amplitude [73-76].

Ens *et al.* [8] have examined a data set consisting of 71 bolides detected by satellite sensors, which provided energy and location estimates, with simultaneous measurements of the same events by infrasound detectors. The energy of these bolides was about 0.02–20 kt TNT equivalent yield. Based on a mean amplitude-yield relationship, the predicted amplitudes for a 1 kt event varied by nearly two orders of magnitude at a distance of 1,000 km. The Chelyabinsk event would result in an extremely low energy of less than a few kilotons, based on the amplitude of 2 Pa at 1,500 km.

Infrasound signals from 30 Soviet air nuclear explosions at altitude not exceeding 4,000 m, with energy yields from 10 to 2,400 kt TNT, were recorded at distances from 500 to 3,000 km [77]. The amplitude of the infrasound signal varied by a factor of 4-8, depending on the wind velocity and direction at stratospheric heights (40–60 km), the direction to the source, and the

weather conditions at the registration point. Again, the amplitude-yield relations are not very precise at these long ranges.

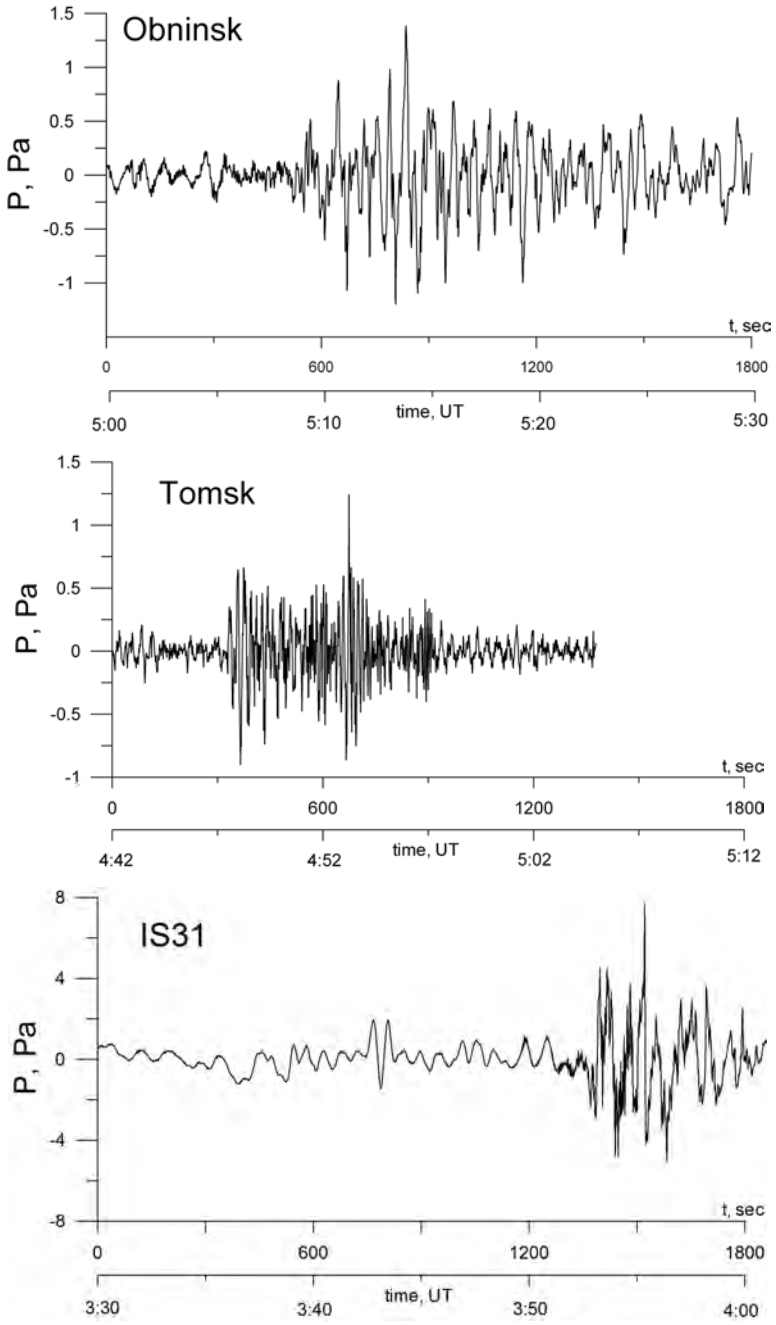

Fig. S29. The infrasound signals from Chelyabinsk event recorded at Obninsk, Tomsk, and Aktyubinsk (IS31). Shown signals are filtered in the range 0.01 - 1 Hz.

The period at maximum amplitude is generally more insensitive to propagation effects than the amplitude of the signal. From the period-yield relation derived by Ens *et al.* [8], a yield of

~470 kt TNT was previously reported for the periods observed at international locations of the CTBTO network [78]. To better understand the uncertainty in this number, we analyzed the data from Russia and Kazakhstan.

Based on the Stevens et al. [77] infrasound data, the frequency at maximal amplitude f_m changed only a few percent when the distance was doubled. The dependence of yield (E) on the frequency f_m can be approximated as follows:

$$f_m \approx \frac{\hat{E}_f}{2\pi\sqrt[3]{E}}, \qquad \text{Eq. S2}$$

where E is the energy yield and K_f is the proportionality coefficient. The probability distribution of K_f as well as their dependency on the propagation direction are shown in Fig. S30. Application of the χ^2 criterion shows that these distributions are log-normal to good approximation, with mean values $K_f \approx 1{,}65^{+0{,}113}_{-0{,}113}$ for the signal propagating in an east-west direction, and $K_f \approx 1{,}21^{+0{,}195}_{-0{,}195}$ for the propagation in the north-south direction.

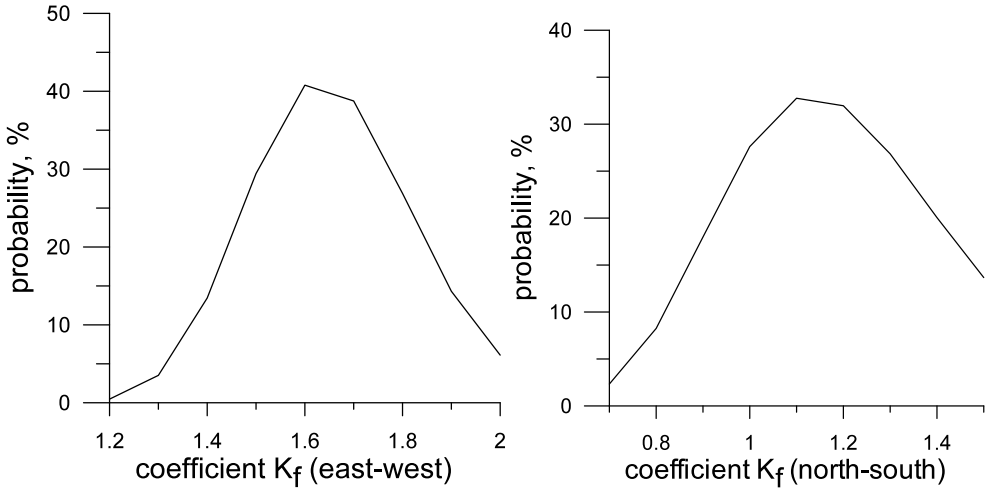

Fig. S30. The probability distribution of coefficients K_f in the direction east-west (a), and north-south (b) derived from experimental data.

The frequency spectra of the Chelyabinsk event are shown in Fig. S31. The characteristic frequencies (at maximum amplitude) are about f_m ~0.039 Hz for Tomsk, 0.032 Hz for Obninsk, 0.0285 for Aktyubinsk and 0.0326 Hz for Moscow. The early peak at even lower frequency in the Moscow spectra (~0.014 Hz) may be due to turbulence, but that remains uncertain. From these frequencies, the yield was calculated.

Energy estimates, summarized in Fig. S32, vary by about a factor of 2.5. The mean is 433±127 kt TNT. If the lowest frequency value would be taken as representative, the estimated energy would increase a few times, which would put the Chelyabinsk event into the Mt energy range.

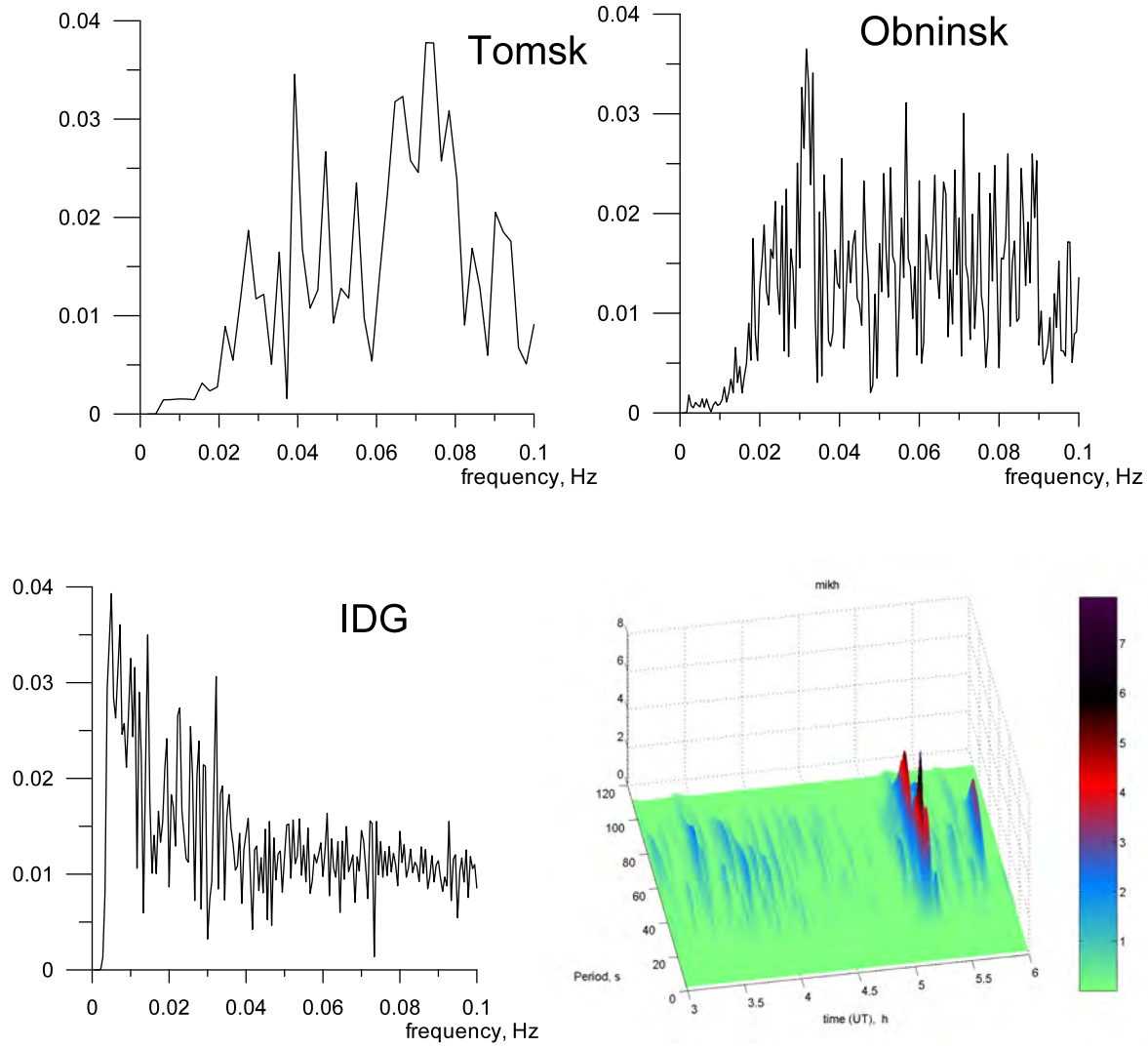

Fig. S31. Spectra of infrasound signals (Pressure in Pa versus frequency in Hz) at different locations (Tomsk, Obninsk, IDG) and a wavelet representation of the spectrum recorded at the Mikhnevo IDG station shown in 3D color. Spectral power (in arbitrary units) is plotted as a function of time and frequency period.

The scatter is caused by the influence of stratospheric winds on signal propagation. The wind velocity at stratospheric heights may exceed 50 m/s. It is possible to take the effects of winds into account by considering how stratospheric winds vary seasonably [74-76, 79-80]. Based on

the Stevens *et al.* [77] dataset, the frequency at maximum amplitude varies as a function of the distance from the energy source:

$$\lg E \approx a - b \cdot \lg f_m - c \cdot \lg R + d\,, \qquad \text{Eq. S3}$$

where E is the energy yield in kt TNT, f_m is the characteristic frequency and R is the distance from the source in km, d is the azimuth and season correction factor (see below). Coefficients in the equation are as follows: a~0.65, b~2.3 and c~0.49.

The factor d may be expressed as $d = K_s * K_a$, where K_s is the seasonal coefficient and K_a is the azimuth coefficient. K_s takes into account the seasonal variation of wind velocity, and K_a incorporates the azimuth from the source to the registration point. The values of these coefficients, based on the Stevens *et al.* [77] data, are given in Fig. S33.

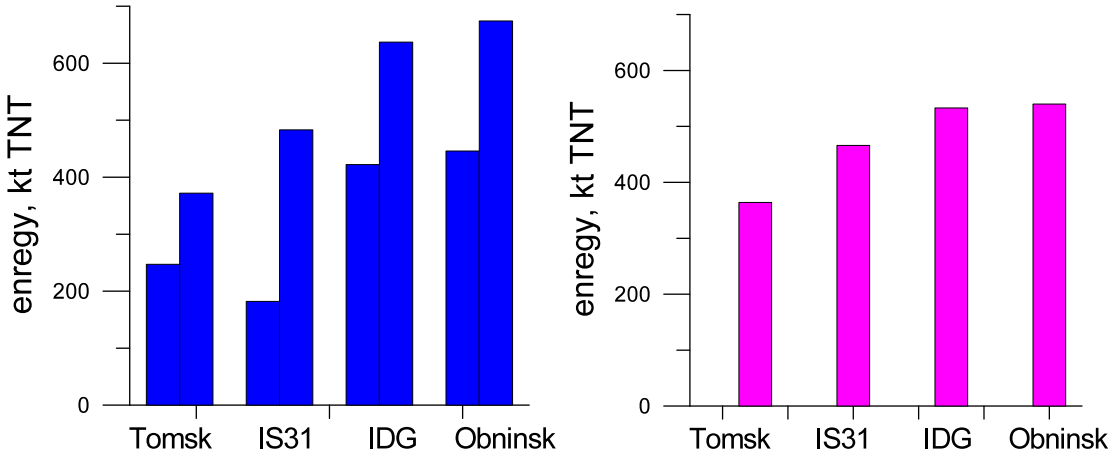

Fig. S32. Energy estimated **(A)** based on Eq. S2 (left), showing a range of solutions, and **(B)** based on Eq. S3 (right), taking stratospheric winds into account.

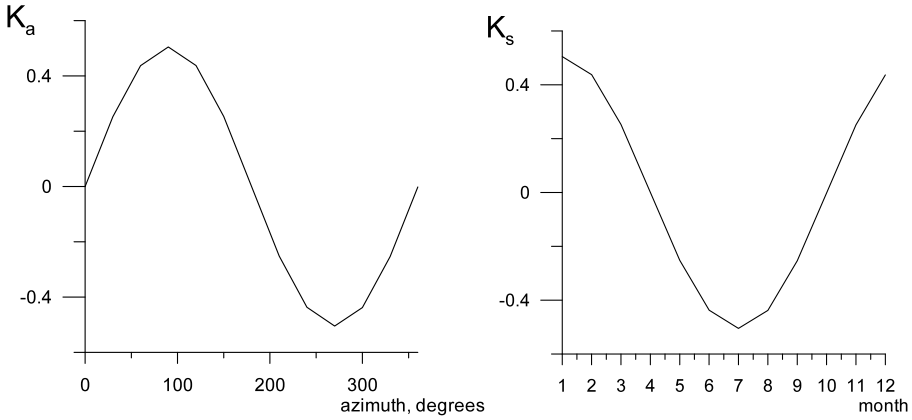

Fig. S33. Azimuth correction coefficient K_a (left) and seasonal correction coefficient K_s.

The yield estimates based on Eq. S3 are shown in Fig. S32. The average energy estimate now is 432±60 kt TNT. The results from one station to the next are now in better agreement.

This is not the full story. Eqs. S2 and S3 are obtained based on analysis of infrasound records from nuclear explosions at altitudes below 4 km. The corresponding yield of a chemical explosion, for example, is two times smaller due to a different partitioning of energy going into the blast wave [81-84]. The height of the burst may increase the effective energy yield as the partitioning of the energy changes with altitude [84-85]. In addition, free air explosions tend to have about a two times higher yield due to the absence of a surface reflection [86]. At the altitude of about 30 km, the correction factor is thought to be about 1.33±0.30 [84-85]. There is no calibration data, however, for such high altitudes and such high energies. The influence of the height of the burst on the infrasound signal at long distances is unclear [79]. With these caveats, the most probable kinetic energy of the Chelyabinsk meteoroid impact is 570±150 kt TNT.

1.5. Witness Reports: Smells

(Contributed by: S. Korotkiy, I. Serdyuk, A. Kartashova, S. Khaibrakhmanov)

In the immediate aftermath of the fireball, various smells were reported in a wide area around the fireball trajectory. Most distinct smells were reported while under the trajectory and starting about one hour after the event.

Data on smells can only be collected by interviewing witnesses. Two approaches were taken to collect a variety of data from witness interviews, results of which are summarized in Table 7A and 7B. In this section, data on smells are discussed.

First, a total of 1,674 witness accounts were collected via a questionnaire on the internet, a great example of crowd sourcing. Unfortunately, the responses are mostly from highly populated areas centered on Chelyabinsk, the Miass / Chebarkul area, and the highway M36 corridor (Fig. S34). Questions asked included requesting information about the eye witness location, sounds heard (yes, no, or observer was inside at the time of the event and therefore could not hear sounds from the meteor), temperature effects (observer became hot, felt some heat, did not feel heat, was inside, provide own description), smells (smell of burning, no smell, own description of smell), ashes (yes ashes, no ashes, did not notice), blast wave arrival (time difference estimated, yes, did not hear, was inside), and whether there were any injuries (Table S7B).

Fig. S34A. Eye witness reports on smells collected by internet query. Red = "burning smell", blue "no smell", yellow points are "other", mostly also reporting smells of various kind. The black line is the fireball trajectory.

Secondly, to cover the smaller villages in the area as well, some 50 villages and towns were visited between 3 and 5 weeks after the event, during which time about 150 locals were questioned (Table S7A). These offer natural sampling points for information, because the population is concentrated in villages and small towns, with no houses in between. In most cases, several people in the each village were questioned (the number given in the first column of Table 7A), often starting from those operating the local grocery stores and including random observers encountered on the street, until reports of damage were confirmed. In addition, several telephone interviews were made to cover further outlaying villages (labeled "*" in Table 7A) and data from official reports were collected for a few major population centers (labeled "**" in Table 7A).

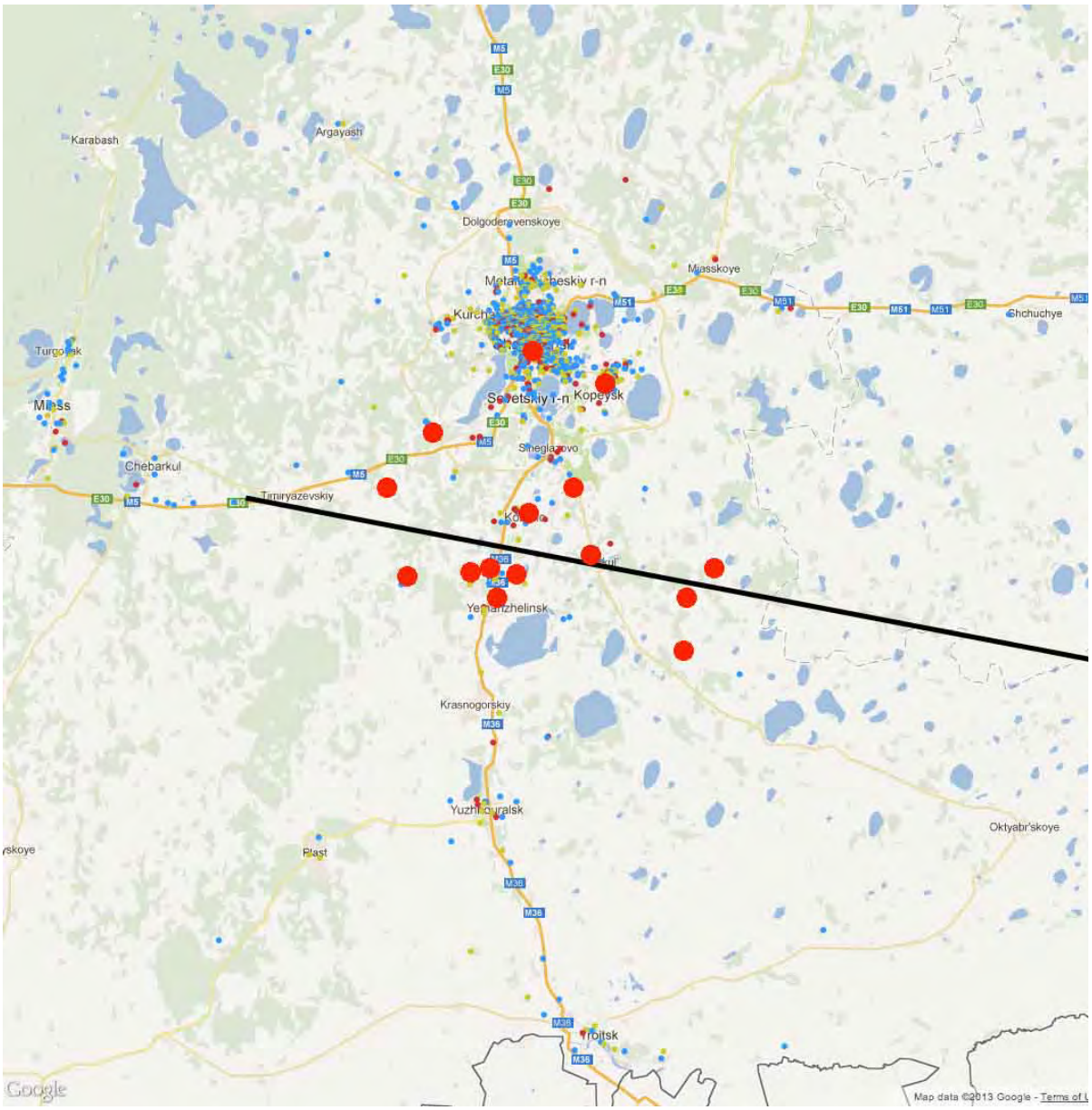

Fig. 34B. As Fig. 34A, wider area with reports of smells (large red dots) from eye witness interviews. The strongest smells were from locations under the trajectory.

The witnesses were asked whether the fireball was seen (was the light blinding, did they have pain in their eyes, was heat felt, did sunburn occur?), how the impact of the shockwave was experienced (level of shaking, was dust generated?), whether damages or injuries occurred (structural damage, flying glass?), whether unusual scents were smelled, and whether meteorites were found locally.

Field survey reports of smells were concentrated in the area surrounding the fireball trajectory, with scents starting about an hour after the event (Fig. S34B). Fourteen villages where scents were reported are marked using red labels on the map of Fig. S34. The eastern edge of the area coincides with the eastern edge of the glass damaged area (Fig. 3). Similarly, Arkhangel'skoe is the most western village where smells were reported, which is situated near the western edge of the glass damaged area.

Nearly all respondents reported similar scents, described either as a sulfur smell, a burning smell, or a smell similar to that of gunpowder. After an initial strong burst, the scents continued for a few hours. These smells may have originated from the decomposition of troilite (FeS), which is one of the main component of this meteorite. Alternatively, some burning scents may have been caused locally when the shockwave dispersed soot from flues and stoves.

Respondents in Emanzhelinka, immediately under the fireball trajectory, also reported an ozone smell, similar to that smelled after a thunderstorm. Ozone may have been produced in the immediate surroundings of the fireball from UVB radiation of the meteor with λ= 200-300 nm wavelengths. This fact supports reports about the prevalence of sunburns, also caused by UV radiation.

Table S7A. Summary of eye witness reports ordered per village/city (-.- = no data; ">" = followed by). # is number of persons interviewed. D is the ground projected distance from the village center to the point below peak brightness at Lat. = 54.845ºN, Long. = 61.412ºE.

#	Location	D (km)	Heat	Smell	Sound	Shaking	Dust	Glass damage	Aggrieved person	Injuries
4	Aleksandrovka	10	-.-	no	yes	-.-	-.-	yes	-.-	no
3	Arkhangel'skoe	30	-.-	sulfur	faint	-.-	no	some old windows	headaches	no
1	Bashakul'	95	-.-	-.-	noise	-.-	-.-	no	-.-	no
4	Baturinskiy	8	yes	strong	yes	-.-	no	severe, house cracked	headaches	-.-
3	Belonosovo	4	yes	-.-	-.-	-.-	ashes	yes	-.-	no
2	Beloretsk	219	no	no	no	no	no	no	no	no
3	Belousovo	35	no	yes	3 plops	-.-	-.-	one	-.-	no
1*	Beloyarskoye	79	-.-	-.-	-.-	faint	-.-	no	-.-	-.-
1*	Bereznyaki	15	-.-	-.-	-.-	yes	-.-	-.-	-.-	-.-
5	Brodokalmak	92	yes	no	-.-	faint	-.-	some	-.-	no
1	Butaki	27	-.-	-.-	-.-	-.-	-.-	some	-.-	no
6	Chebarkul	68	-.-	no	strong+ few faint	-.-	-.-	no	no	no
30	Chelyabinsk center	34	yes	yes	yes	yes	yes	some, roof	yes	yes

								collapse		
20	Chelyabinsk State University	38	-.-	-.-	yes	yes	-.-	some	-.-	yes
20	Chelyabinsk South Ural State University	35	-.-	-.-	yes	yes	-.-	severe	-.-	-.-
1*	Chumlyak	96	-.-	-.-	-.-	-.-	-.-	no	-.-	-.-
7	Deputatskiy	18	yes	-.-	yes	yes	-.-	some	no	no
2	Dolgoderevens-koe	57	-.-	-.-	-.-	yes	-.-	no	-.-	no
2	Emanzhelinka	9	heat felt	ozone	-.-	-.-	-.-	severe	-.-	yes
8	Etkul	11	no	sufur and burned wire	2 strong >few faint	a few minutes	soot	severe	-.-	yes
3	Kalachevo	13	yes	burned wire	3 plops	-.-	-.-	sever, house cracked	2 men-cuts	yes
5	Karataban	26	yes	no	-.-	sharp shock	-.-	only old windows	-.-	no
2	Kazbaevo	39	-.-	no	yes	long shaking	no	no	no	no
1*	Koelga	39	-.-	-.-	-.-	-.-	-.-	Some	-.-	-.-
3	Kolobanovo	40	-.-	no	strong+ few faint	no	no	no	no	no
4	Kopeysk	38	yes	yes	-.-	yes	-.-	severe	-.-	yes
3	Korkino	6	sunburn, peeling	yes	yes	-.-	-.-	yes	yes	yes
6	Kunashak	96	no	no	no	faint	-.-	no	-.-	no
1	Lebedevka	39	-.-	no	-.-	-.-	-.-	no	-.-	no
4	Lesnoy	55	-.-	yes	no	-.-	-.-	some	-.-	no
1	Markovo	49	-.-	no	-.-	faint	-.-	no	-.-	no
3	Miasskoye	58	-.-	no	-.-	-.-	-.-	significant	-.-	yes
1	Muslyumovo	85	-.-	-.-	-.-	-.-	-.-	some	-.-	no
5	Nikolaevka	36	no	burning	1> few faint	-.-	-.-	no	-.-	no
4	Novobalandino	35	yes	-.-	faint	-.-	ashe s	hospital	headaches, eyes hurt	yes
2	Novotroitskiy	25	-.-	no	3 plops	-.-	-.-	some	-.-	no
**	Nugumanova	76	-.-	-.-	-.-	-.-	-.-	school	-.-	no
2	Pervomayskiy	15	yes	-.-	yes	-.-	-.-	yes	-.-	-.-
3	Petrovskoe	48	no	no	1>few faint	-.-	-.-	some	-.-	no
1	Pogudino	40	no	-.-	yes	-.-	-.-	no	-.-	no
4	Poletaevo	28	yes	yes	3 plops	-.-	-.-	some	-.-	no
2	Polevskoy	196	no	no	no	no	no	no	no	no
2	Potapovo	22	-.-	no	no	-.-	-.-	some	-.-	no
1	Preobrazhenka	50	-.-	-.-	-.-	-.-	-.-	no	no	no
2	Priozerniy	9	-.-	-.-	-.-	-.-	-.-	yes	-.-	-.-
1	Rozhdestvenka	49	no	no	1 strong	-.-	-.-	some	-.-	no
3	Russkaya Techa	110	yes	-.-	1 strong > thundr	-.-	-.-	no	-.-	no
2	Sakkulovo	71	-.-	-.-	-.-	-.-	-.-	no	-.-	no
1	Sary	7	-.-	-.-	-.-	-.-	-.-	some	-.-	no

2	Smolino	24	-.-	-.-	-.-	-.-	-.-	school	-.-	no
2	Sultaevo	70	-.-	-.-	3 crashes	yes	-.-	no	-.-	no
**	Surakovo	73	-.-	-.-	-.-	-.-	-.-	school	-.-	no
1	Taendy	24	yes	sulfur gun-powder	1 strong> 3-4 faint	yes	-.-	yes	-.-	no
5	Timiryazevskiy	42	-.-	no	yes	5 min	no	no	no	no
5	Travniki	55	sunburn	no	1>5 faint	no	no	no	no	no
**	Troitsk	86	-.-	-.-	-.-	-.-	-.-	some	-.-	no
2	Uchaly	142	no	no	no	no	no	no	no	no
3	Uvel'skiy	45	-.-	-.-	-.-	yes	-.-	some	-.-	yes
2	Varlamovo	53	-.-	-.-	yes	yes	-.-	no	-.-	-.-
5	Verkhnyaya Pyshma	242	no	no	no	no	no	no	no	no
1*	Yaroslavka	50	-.-	-.-	-.-	-.-	-.-	no	-.-	-.-
15	Yekaterinburg	226	no	no	no	no	no	no	no	no
6	Yemanzhelinsk	11	sunburn	sulfur, bitter taste	yes	yes	soot, ashes	severe, statue cracked	headaches	yes
**	Yuzhnouralsk	45	-.-	-.-	yes	yes	-.-	yes	-.-	-.-
3	Zaural'skiy	13	yes	yes	yes	yes	ashes	severe	-.-	-.-
5	Zvyagino	44	yes	no	1 strong> few faint	5 min.	no	no	no	no

* based on telephone interviews; ** reported by authorities.

Table S7B. As Table S7A, giving summary of eye witness reports collected by internet query, ordered per village/city (-.- = no data; ">" = followed by).

#	Location	D (km)	Heat	Smell	Sound	Sha-king	Dust	Damage	Aggrieved person	Meteo-rites
1	Akbasheva	62	-.-	no	no	-.-	no	-.-	-.-	-.-
2	Aleksandrovka	10	-.-	no	yes	-.-	-.-	yes	-.-	yes
2	Argayash	80	yes	no	no	-.-	no	-.-	-.-	-.-
12	Asbest	240	no	no	no	-.-	no	-.-	no	-.-
1	Barachinskiy	385	no	no	no	-.-	no	-.-	no	-.-
1	Baturinskiy	8	yes	yes	yes	-.-	no	-.-	yes	yes
1	Belonosovo	4	yes	-.-	-.-	-.-	yes	yes	-.-	yes
1	Beloretsk	219	no	no	no	-.-	no	no	no	no
1	Belozery	83	yes	no	no	-.-	no	-.-	-.-	-.-
1	Bishkil'	44	no	no	yes	-.-	no	-.-	no	-.-
2	Bobrovka	92	yes	yes	yes	-.-	no	-.-	yes	-.-
1	Bogdanivich	219	no	no	no	-.-	no	-.-	no	-.-
1	Bolshoye Balandino	58	-.-	yes	-.-	-.-	-.-	-.-	-.-	-.-
1	Bolshoye Kharlushi	50	yes	no	no	-.-	no	-.-	-.-	-.-
2	Borisovka	15	no	no	yes	-.-	no	-.-	no	-.-
1	Celinnoe	151	no	yes	no	-.-	no	-.-	no	-.-
6	Chebarkul	71	no	no	no	-.-	-.-	no	no	yes

1301	Chelyabinsk	37	yes	yes	no	yes	no	-.-	yes	-.-
1	Cheremushki	56	no	no	yes	-.-	no	-.-	-.-	-.-
1	Cherkasovo	52	yes	yes	yes	-.-	yes	-.-	yes - ears	-.-
2	Churilovo	43	yes	yes	no	-.-	no	-.-	no	-.-
2	Dolgoderevenskoe	57	-.-	no	no	no	no	no	-.-	-.-
4	Emanzhelinka	9	yes	yes	no	-.-	no	yes	no	yes
3	Etkul	11	yes	yes	no	yes	yes	yes	-.-	-.-
1	Il'ino	54	no	no	no	-.-	no	-.-	no	-.-
1	Ishalino	66	no	no	no	-.-	no	-.-	yes	-.-
4	Kamensk-Ural'skiy	175	no	no	no	-.-	no	-.-	no	-.-
3	Kanashevo	56	no	no	no	-.-	no	-.-	no	-.-
2	Kasargi	57	yes	no	yes	yes	no	-.-	-.-	-.-
1	Kashino	192	no	no	no	-.-	no	-.-	no	-.-
1	Kasli	120	no	no	no	-.-	no	-.-	no	-.-
2	Kataysk	176	yes	yes	no	-.-	no	-.-	no	-.-
1	Kazantsevo	48	yes	yes	yes	-.-	no	-.-	-.-	-.-
2	Khomutinino	35	yes	yes	no	-.-	no	-.-	-.-	-.-
3	Klenovka	17	-.-	no	yes	-.-	no	-.-	-.-	-.-
1	Kluchevka	57	yes	no	yes	-.-	no	-.-	no	-.-
1	Kluchi	48	-.-	yes	yes	-.-	yes	-.-	-.-	-.-
32	Kopeysk	38	yes	yes	yes	yes	no	yes	yes - eyes, ears	yes
1	Korablevo	21	no	no	no	-.-	no	-.-	no	-.-
20	Korkino	6	yes	yes	yes	-.-	no	yes	yes	yes
2	Kostanay	233	yes	no	no	-.-	no	-.-	no	-.-
1	Krasnoe Pole	43	yes	no	no	-.-	no	-.-	no	-.-
3	Krasnogorskiy	30	yes	yes	no	-.-	no	-.-	-.-	-.-
1	Krasnoufimsk	295	no	no	no	-.-	no	-.-	-.-	-.-
1	Krasny Partizan	287	no	no	no	-.-	no	-.-	no	-.-
12	Kremenkul'	40	yes	yes	yes	-.-	no	-.-	yes - eyes	-.-
1	Krugloe Lake	44	yes	no	yes	-.-	no	-.-	-.-	-.-
3	Kurgan	261	no	no	no	-.-	no	-.-	no	-.-
6	Kurochkino Lake	22	yes	yes	no	-.-	no	-.-	no	-.-
1	Kusa	134	yes	yes	no	-.-	no	-.-	no	-.-
2	Lazurny	60	no	no	yes	-.-	no	-.-	no	-.-
1	Lebedevka	39	-.-	no	-.-	-.-	-.-	-.-	-.-	-.-
1	Lesnoy	55	-.-	yes	no	-.-	-.-	yes	-.-	-.-
2	Lubimovo/ Uksyankoe	161	no	no	no	-.-	no	-.-	no	-.-
1	Magnitny	220	no	no	no	-.-	no	-.-	-.-	no
5	Magnitogorsk	220	no	no	no	-.-	no	-.-	yes - eyes	no
1	Malaya Sosnovka	25	-.-	yes	yes	-.-	no	-.-	-.-	-.-
1	Malysheva	36	no	no	no	-.-	no	-.-	no	-.-
1	Medvedevo	43	-.-	no	yes	-.-	no	-.-	-.-	-.-
1	Medvedskoe	110	no	no	no	-.-	no	-.-	no	-.-
1	Metlino	105	no	no	no	-.-	no	-.-	no	-.-

20	Miass	87	no	yes	no	-.-	no	-.-	yes - eyes	-.-
2	Miasskoye	57	no	yes	no	-.-	no	yes	no	-.-
1	Mirniy	48	-.-	yes	yes	-.-	-.-	-.-	-.-	-.-
1	Nikolaevka	36	no	yes	no	-.-	-.-	no	yes	no
1	Nizhniy Tagil	355	yes	no	no	-.-	no	-.-	no	-.-
1	Novy Mir	79	no	no	no	-.-	no	-.-	no	-.-
1	Novobaturino	4	no	yes	no	-.-	yes	-.-	no	-.-
1	Novogorniy	96	yes	no	no	-.-	no	-.-	no	-.-
1	Novoural'sk	281	no	yes	no	-.-	no	-.-	no	-.-
1	Novoye Pole	50	no	no	yes	-.-	no	-.-	-.-	-.-
5	Novyy Kremenkul'	41	yes	yes	yes	yes	no	-.-	yes - eyes	-.-
1	Nyazepetrovsk	175	yes	no	no	-.-	no	-.-	no	-.-
2	Oktyabr'skiy	35	yes	yes	yes	-.-	yes	-.-	-.-	-.-
1	Ozerniy	43	-.-	no	no	-.-	-.-	-.-	-.-	-.-
1	Ozersk	107	yes	no	no	-.-	no	-.-	-.-	-.-
1	Pechenkino	15	yes	yes	no	-.-	yes	-.-	-.-	-.-
3	Petrovskiy	44	yes	no	yes	-.-	no	-.-	yes - eyes	-.-
3	Plast	69	yes	yes	no	-.-	no	-.-	yes - eyes	-.-
3	Poletaevo	28	yes	no	yes	-.-	no	yes	yes - eyes	-.-
1	Polevoy	17	yes	no	-.-	-.-	-.-	-.-	-.-	-.-
1	Polevskoy	190	no	no	no	-.-	no	no	no	no
2	Polovinka	200	yes	no	no	-.-	no	-.-	no	-.-
1	Pristantsionniy	141	no	no	no	-.-	no	-.-	no	-.-
1	Rodniki	73	no	no	no	-.-	no	-.-	no	-.-
1	Roza	7	yes	no	no	-.-	no	-.-	-.-	-.-
1	Sadoviy	47	yes	yes	yes	yes	no	-.-	yes - eyes, ears	-.-
2	Sargazy	22	yes	yes	no	-.-	no	-.-	yes - eyes	-.-
4	Satka	154	no	no	no	-.-	no	-.-	yes - eyes	-.-
1	Severnyy	32	yes	-.-	yes	-.-	-.-	-.-	yes - eyes, ears	-.-
1	Shadrinsk	192	no	no	no	-.-	no	-.-	no	-.-
8	Shagol	45	yes	yes	no	-.-	no	-.-	no	-.-
1	Shuch'e	95	no	no	no	-.-	no	-.-	no	-.-
8	Sineglazovo	16	yes	yes	no	-.-	no	-.-	yes - eyes, ears	-.-
1	Siniy Bor	35	yes	yes	no	-.-	no	-.-	-.-	-.-
2	Snezhinsk	145	no	no	no	-.-	no	-.-	no	-.-
2	Sokolovo	17	yes	no	no	-.-	no	-.-	no	-.-
1	Sosnovka	171	yes	yes	yes	-.-	no	-.-	-.-	-.-
1	Talica	281	no	no	-.-	-.-	no	-.-	no	-.-
4	Talovka	328	yes	yes	no	-.-	no	-.-	no	-.-
1	Tayandy	24	yes	no	no	-.-	no	-.-	no	-.-
2	Tominskiy	19	-.-	yes	yes	-.-	no	-.-	-.-	-.-
1	Travniki	55	no	no	no	no	no	no	no	no
1	Travyanoe	150	no	no	no	-.-	no	-.-	no	-.-
2	Trekhgorny	191	no	no	no	-.-	no	-.-	no	no
8	Troisk	89	yes	no	no	-.-	no	-.-	no	no

17	Tujmen'	365	no	no	no	-.-	no	-.-	no	-.-
1	Tuktubaevo	44	no	no	yes	-.-	no	-.-	no	-.-
11	Turgoyak	92	no	no	no	-.-	no	-.-	no	-.-
1	Uchaly	142	yes	yes	yes	-.-	no	-.-	yes	-.-
1	Ust'-Katav	209	no	no	no	-.-	no	-.-	no	no
1	Verkhnyaya Samarka	33	no	no	no	-.-	no	-.-	no	-.-
2	Yalutorovsk	366	no	no	no	-.-	no	-.-	no	-.-
1	Yasnye Polyany	153	yes	no	yes	-.-	no	-.-	no	-.-
10	Yekaterinburg	227	no	no	no	-.-	no	-.-	no	no
9	Yemanzhelinsk	11	yes	yes	yes	yes	no	yes	yes	yes
3	Zauralskiy	13	yes	yes	no	-.-	no	-.-	-.-	no
9	Zlatoust	118	no	no	no	-.-	no	-.-	yes - eyes	no

1.6. EMP and Electrophonic sounds

(Contributed by: S. Khaibrakhmanov, A. Kartashova, S. Korotkiy, I. Serdyuk)

Bright fireballs may produce significant extremely low frequency (ELF) and very low frequency (VLF) radio emissions. If so, these electromagnetic signals would induce voltage changes across power lines, called an electro-magnetic pulse (EMP), and be audible by coupling to dielectric materials in the immediate surroundings of the witnesses, called electrophonic sound.

Two local electricity companies in Yemanzhelinsk district, AES Invest and the Inter-Regional Distributive Grid Company of the Urals, reported that there were no significant voltage surges across power lines at the time of the bolide. The electricity supply did not switch off.

Information on electrophonic noises was not gathered in a systematic fashion during the field study, but some detailed reports were obtained (Table S8). While in his office in Yemanzhelinsk, Evgeny Svetlov, the head of the Yemanzhelinsk administration and an electrical engineer by training, heard a noise like the buzz of the electrical transformer during the main bolide flash. Alexander Polonsky, a car driver, heard a noise like the roar of two fighter planes even before he saw the bolide, while standing on a street in Yemanzhelinsk. Finally, Vladimir Bychkov, a police programmer and physicist by training, heard a noise like the sizzle of oil in a frying pan, during the bright stage of the bolide while he stood on a square in Chelyabinsk. The noise appeared to be from the direction of the bolide. The noise stopped at the main bolide flash, but there was a short sound like a clap during the flash. None of these witnesses were wearing glasses.

Table S8. Summary of eye witness reports of electrophonic noises (compiled by Sergey N. Zamozdra).

Name	Age (yr)	Profession	Location	Sound	Time	Environment, dielectrics
Evgeny Svetlov	39	electrical engineer	Yemanzhelinsk: administration office	like a buzz of an electrical transformer	during the main bolide flash	office furniture, big wooden tables, paper, cabinets
Alexander Polonsky	~45	car driver	Yemanzhelinsk street	like the roar of two fighter planes	during the approach of the bolide	no data
Vladimir Bychkov	~43	physicist	Chelyabinsk open area near regional hospital	sizzle of oil in frying pan, and clap like a fluorescent bulb burning out	bright stage of bolide (the clap during main flash)	Cars (distance ~5 m), trees (distance ~30 m)

From the 1,674 people interviewed during the internet survey, 198 reported hearing sounds. The sound effects were described as hissing, as if you run fireworks noise interference, the sound of bengal light, crackle, sparking, crackling, rustle, rustling, like a whistle, squeaking, rumble, and the sound of a passing plane (Table S9).

Table S9. Summary of electrophonic noises reported in internet survey.

Description of sound	#
Hiss or hissing, as if you run fireworks noise interference	76
Like sound of bengal light	13
Whistle sound	26
Squeak	2
Crackle or sparking or crackling	25
Rustle or rustling	6
Rumble	19
Like passing plane	31

2. Damage Assessment

2.1. Injuries

(Contributed by: P. Jenniskens, A. Kartashova, O. P. Popova, S. Korotkiy, I. Serdyuk, V. Emel'yanenko, S. Khaibrakhmanov)

According to tallies compiled by hospitals and communicated to us by the Headquarters of the Russian Ministry of Emergencies in the Chelyabinsk area (Table S10), 1,613 people asked for medical assistance at hospitals, 112 people were hospitalized, 2 in serious condition. Media reported that a 52-year old woman had a broken spine and was flown to Moscow for treatment. There were no fatalities. All people were released from the hospital after four weeks.

Table S10. Number of people asking for medical assistance for each district as a function of range to the airburst source (Data provided by Russian Ministry of Emergencies). Range is the distance from the meteoroid's 29.7-km point at altitude (Table S1) to the main population center in the district (in brackets).

District	Latitude (N)	Longitude (E)	range (km)	# inhabitants (2013 Census)	# injured	%
Korkinsky (Korkino)	54.8956	61.3832	28	63,400	102	0.161
Yemanzhelinsky (Yemanzhelinsk)	54.7536	61.3097	29	53,781	50	0.093
Etkulsky (Etkul)	54.8230	61.5857	34	30,697	32	0.104
Chelyabinsk	55.1692	61.4045	45	1,156,471	1,210	0.105
Kopeysky	55.1020	61.6159	48	142,029	159	0.112
Yuzhnouralsky	54.4436	61.2617	54	37,877	36	0.095
Uvel'sky (Uvel'skiy)	54.4429	61.3640	57	31,627	7	0.022
Sosnovsky (Dolgoderevenskoye)	55.3460	61.3408	59	63,308	6	0.009
Krasnoarmeysky (Miasskoye)	55.2841	61.8903	72	43,100	7	0.016
Troitsky M.R.	54.0860	61.5565	96	27,400	0	<0.004
Troitsky T.R.	54.0860	61.5565	96	77,700	0	<0.002

Most people asking for medical attention had cuts and bruises from broken glass shattered by the shock wave. No injuries came directly from structural damage or from traffic accidents. The blast wave shattered windows in a wide area, both inward and outward depending on location. Ceiling tiles and support structures in suspended ceilings were sucked down after nearby windows broke, suggesting the action of both positive and negative pressure. Near the epicenter,

structurally old window frames were also blown in or out. Structural damage was rare. One aging roof collapsed at a zinc factory in Chelyabinsk and took along part of a supporting wall. A few other older walls cracked, a confirmed case was in a private residence in Baturinskiy (part of Yemanzhelinsk), but also as far out as the village of Russkaya Techa (administration building).

The percentage of people asking for medical assistance dropped rapidly as a function of distance from the airburst source (Table S10), according to a range (r) power-law dependence of $r^{-3.2\pm0.5}$, or an exponential decay with range having exponent -0.059±0.009 /km (providing a better fit). Note that most districts fall along a north-south line perpendicular to the trajectory and it is insensitive whether the range to the 27-km altitude point is considered, or that perpendicular to the trajectory, except for Etkul, Korkino and Yemanzhelinsk. The majority of injuries (1,210) took place in Chelyabinsk city (population density is about 1,130 km^{-2}), as the city is the most populated part of Chelyabinsk *Oblast*. The highest fraction of people asking for assistance was near the trajectory in the Korkino (0.16%).

The district boundaries within Chelyabinsk Oblast distort the record somewhat. Even though Dolgoderevenskoye did not have any injuries (Table S7), 6 were reported injured in the district (Table S10). The main hospital for the Sosnovsky municipal district is there. The most damaged areas in this district are at Tominsky, Archangelskoye, Mirny, Sargazy, and Solnechny. So, it is likely that the injured came from those villages instead. Miasskoye, too, is the center of the Krasnoarmejsky municipal district. Again, no injuries were reported in Miasskoye itself, despite significant damage, but injured could have come from Berezova and Oktyabrsky, elsewhere in the district.

Of the 1,754 internet questionnaires filled out, 1109 reported no injuries and 271 left the injury section blank. The remaining 374 reports (21.3%) mentioned 452 types of injuries or inconveniences. Most of those who responded probably did not request medical assistance. Of the 374 people affected, 20 (5.3%) reported sunburn, 70 (19%) were temporarily blinded, 180 (48%) felt eyes hurt, and 11 (2.9%) sensed retinal burns. The shock wave arrival had a significant effect also: 24 (6.4%) had a concussion or were mentally confused, upset, or exhausted as a result of excessive stress, and 118 (32%) of those affected were temporarily deaf. Video records exist that show the shock wave was strong enough at places to blow people off their feet. Flying glass and falling building debris affected a relatively small fraction of

respondents: 18 (4.8%) had cuts and 11 (2.9%) had bruises, but no respondent reported having had broken bones.

2.2. Heat and Sunburn

(Contributed by: A. Kartashova, P. Jenniskens, O. P. Popova, S. Khaibrakhmanov, S. Korotkiy, I. Serdyuk)

People who looked directly at the fireball had painful eyes (Table S7) and all of them closed their eyes or turned in the opposite direction. There were no reports of lasting eye damage (lens or retina) from watching the fireball.

Throughout the survey area, there were reports of mild sunburns following the fireball sighting (Table S7). Of 1,113 respondents in the internet survey who were outside at the time of the fireball, 25 were sunburned (2.2%), 315 felt hot (28%), and 415 (37%) felt warm. In Kokino (r = 30 km), resident Vladimir Petrov reported sunburn as severe as causing his skin to peel off some time after the event. Korkino is almost directly underneat, ~33 km from the point in the trajectory where peak radiation occurred. Many reports mentioned feeling heat in the neck, when the fireball was behind the observer.

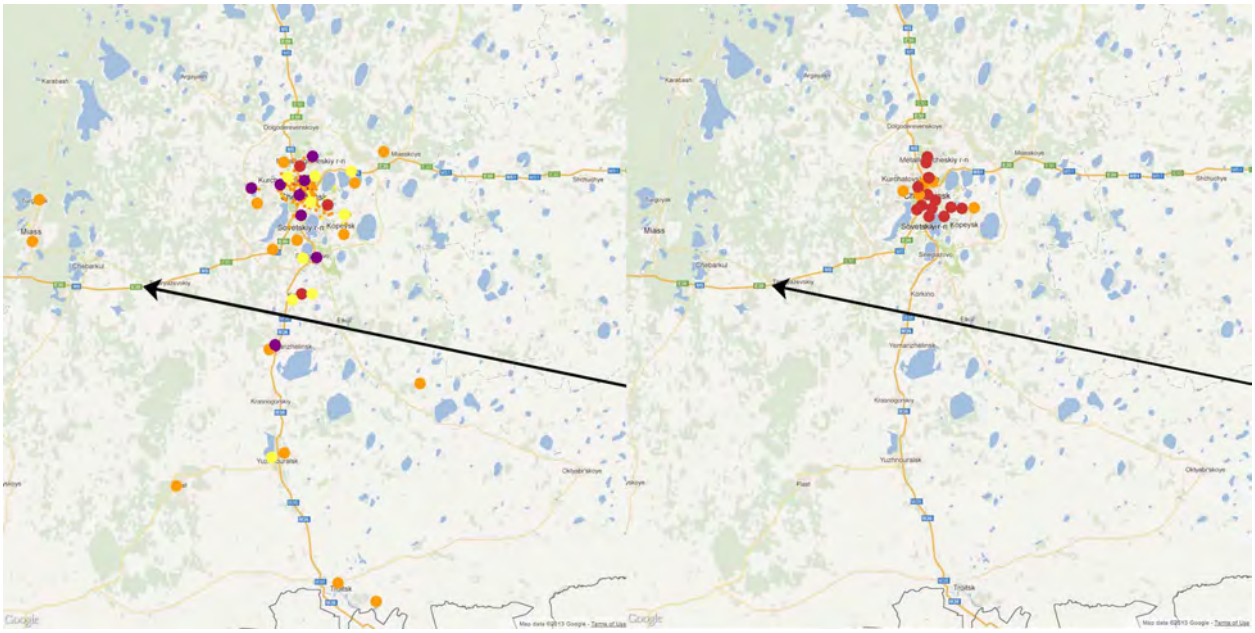

Fig S35. Left: Reports of sunburn (purple), burning retina (red), blinded for some time (yellow), and having irritated eyes (orange). **Right:** Reports of being cut by glass (red) and unspecified injuries (orange).

The villages where heat sensations were reported were distributed throughout the surveyed area (Fig. S35), but did not extent as far as Yekaterinburg (range r = 223 km) or Verkhnyaya Pyshma (r = 238 km) in the north and Uchaly (r = 127 km) or Beloretsk (r = 204 km) in the south. This reflects the fact that the light's flux density falls off with the inverse square of the distance to the brightest point of the fireball (r^{-2}). At those distant sites, the radiation flux density was a factor of 18 (Uchaly) to 63 (Verkhnyaya Pyshma) lower.

2.3. Glass damage

(Contributed by: P. Jenniskens, O. P. Popova, S. Khaibrakhmanov, A. Kartashova, E. Biryukov, V. Emel'yanenko, A. Dudorov)

One set of data on the extent of glass damage was provided by the Chelyabinsk Regional administration and the regional office of the Emergency Department. These data were collected by officials in the weeks after the event to address the need for government-supported primary window replacement. Each listed building was inspected. That did not include secondary ones such as balcony glazing, damage of which was still observed weeks after the event.

Damage took place in eleven municipal districts of Chelyabinsk *Oblast*. Data are grouped per district in Table S11. In total, 7,320 buildings were affected, amongst which were 740 schools and universities, 296 medical facilities, 110 cultural organizations, 48 sport facilities and 6,097 apartments and houses.

Fig S36. Examples of glass damage in pictures from Yemanzhelinsk. **(A)** Broken window glass. **(B)** Initial protection against wind. **(C)** Window frames blown in. **(D)** Clean up. **(E), (F)** and **(H)** Lost window frames in school. **(G)** Suspended ceiling sucked down. Photos by Victor I. Gubar of Yemanzhelinsk.

Table S11. Number of damaged buildings per district and number of buildings damaged per 1000 inhabitants (fr). Range is distance from meteoroid's 29.7-km point at altitude (Table S1) to center of municial (M.R.) or city (T.R.) district. *

District	Medi-cal	Social	Cultu-ral	Educa-tional	Sports	Houses	Total	Range (km)	Total inhab.	fr.
Korkinsky	21	2	9	59	1	502	594	28	63,400	9.4
Yemanzhelinsky	13	3	6	32	0	322	376	29	53,781	7.0
Etkulskiy	14	1	14	33	0	241	303	34	30,697	9.9
Chelyabinsk	184	16	43	423	34	3613	4,313	45	1,156,471	3.7
Kopeysky	40	3	14	109	8	903	1,077	48	137,601	7.8
Yuzhnouralsky	2	2	4	25	3	210	246	54	37,877	6.5
Uvel'skiy	8	1	12	28	1	154	204	57	31,627	6.5
Sosnovsky	1	0	0	5	0	42	48	59	63,308	0.8
Krasnoarmeysky	11	1	8	20	1	92	133	72	43,100	3.1
Troitsky M.R.	1	0	0	6	0	7	14	96	27,400	0.5
Troitsky T.R.	1	0	0	0	0	11	12	96	77,700	0.2

*) No damage reported from these other districts in Chelyabinsk Oblast: Agapovsky (225 km), Argayashsky (76), Ashinsky (248), Bredinsky (280), Chebarkulsky (58), Chesmensky (131), Kartalinsky (212), Kaslinsky (140), Katav-Ivanovsky (212), Kizilsky (272), Kunashaksky (106), Kusinsky (132), Nagaybaksky (180), Nyazepetrovsky (174), Oktyabrsky (99), Plastovsky (71), Satkinsky (155), Uysky (105), Varnensky (173), and Verkhneuralsky (179), with the distance from the center of the district to the point below the main explosion at Lat. = 54.845º, Long. = 61.412º given in brackets.

The number of houses damaged per 1,000 inhabitants (fraction, Table S11) shows an $r^{-2.6\pm1.2}$ dependency on distance from the airburst source (r), or an exponential decay with exponent -0.050±0.009 /km. Due to a high number and density of buildings, and a large number of high-rise buildings, 3,613 apartment buildings (about 44% of the total amount) were damaged in Chelyabinsk, mainly from shattered and broken glass in windows and doors.

The most damaged districts included the most populated, Chelyabinsk and Kopeysk, and districts close to the trajectory (Korkino and Yemanzhelinsk). In the Korkino municipal district, 594 buildings were damaged. 7,938 wooden windows and 1,077 double pane windows were broken in multi-apartment living houses. In Yemanzhelinsk municipal district, 376 buildings were damaged and 2,776 windows were broken in 322 inhabited multi-apartment houses.

In the Chelyabinsk/Kopeysk area, the damage was not evenly distributed in the city. Certain areas were damaged more than others. Also, the side of buildings damaged was not always in the shock wave arrival direction. Fig. S37 shows some examples from some areas throughout the city, in which sides of buildings with known glass damage are marked red, those that did not suffer damage are marked blue.

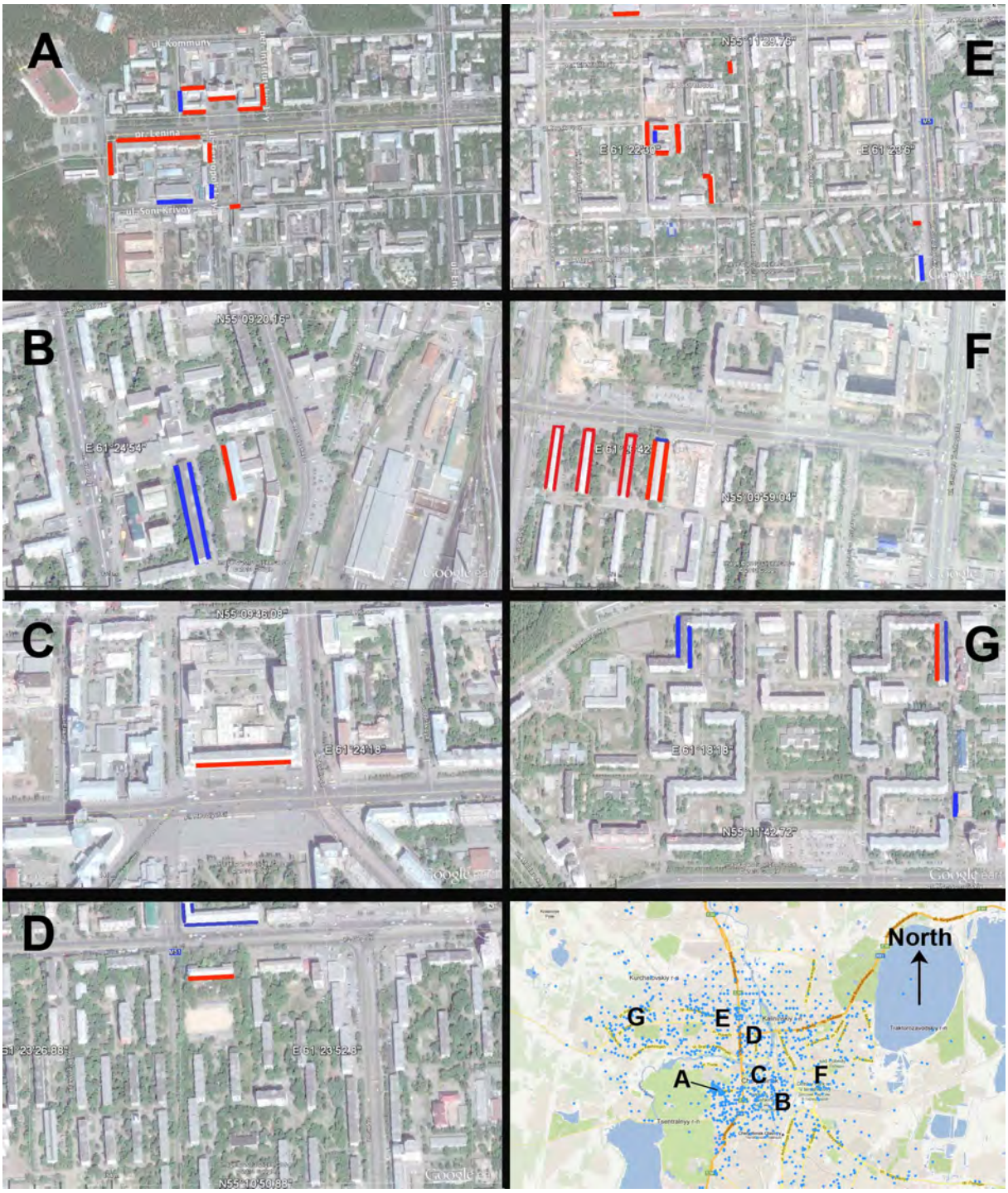

Fig S37 (A-G). Example areas in the city of Chelyabinsk with red marking glass damage, blue no damage. North is up. Shock wave arrived from the South. No reliable data exist for other buildings on the maps. Sites are identified in bottom right map, which also shows the distribution of internet responses (blue dots). This distribution reflects to some extent the distribution of homes and internet access, but may also reflect the level of damage in the city. Note, for example, the clustering of responses in the heavily impacted area around South Ural State University ("A").

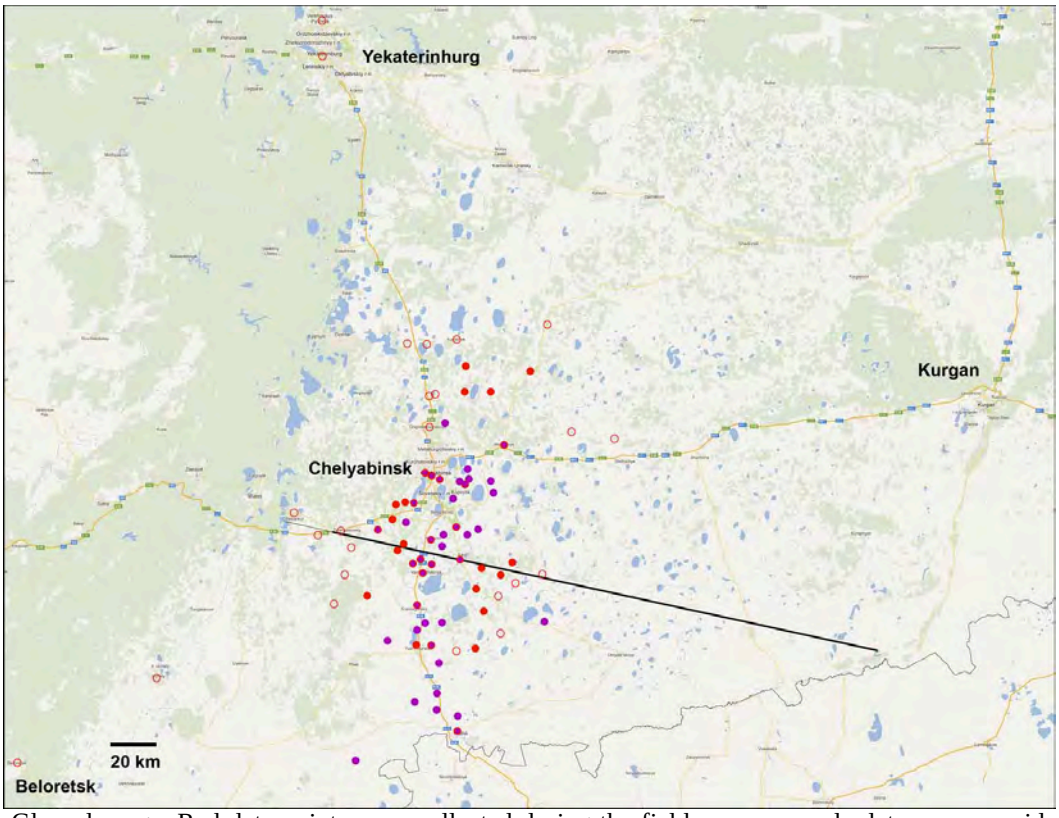

Fig S38. Glass damage. Red data points were collected during the field survey, purple data were provided by the Emergency Department. Open circles indicate that no glass damage occurred.

The most damaged settlements according to official data are shown by purple symbols in Fig. S38. The damage area has an extent of about 180 km from north to south and 80 km from east to west, but is shaped along a curved arc centered on Yemanzelinsk, extending from the northern parts of Chelyabinsk as far south as Troitsk.

Red data points in Figure S38 are collected during the field survey, purple data points are villages that reported damage through the Ministry of Emergencies at Chelyabinsk. Open circles are sites where no damage occurred. The red points include many villages that had only a few windows damaged (usually in school buildings). Hence, the inner contour of the purple points may represent a higher overpressure than the outer contour of the red sites.

The value of overpressure, Δp, needed to break window glass is dependent on the glass thickness and surface area. These values are not different between windows in Russia (most affected buildings being from the 20th century) and other locations in the world. Glasstone and Dolan [84] estimated the overpressure which caused essential glass damage at about Δp~3,500-5,000 Pa. According to Mannan and Lees [87], an overpressure of about Δp~700 Pa is able to

shatter 5% of glass windows, Δp~1,400 Pa would break 50%, and Δp~3,500 causes damage to about 90% of glass windows. This suggests that a value of Δp~500 Pa would describe the extent of the damage area where just a few windows were broken (Table S7A), while Δp~1,000 Pa would result in significant window damage as in the central core of Fig. S38 [88].

2.4. Model of the shockwave

(Contributed by: V. V. Shuvalov, O. P. Popova, Y. S. Rybnov)

To model the damage on the ground, numerical modeling of explosions with different energies, and at different altitudes in the atmosphere, were conducted. The gasdynamical code SOVA (SOlid Vapor Air, [89]) was applied, with a numerical grid density of 1000×500 points. Realistic atmospheric densities, pressures, and temperatures were used as input to the model. The standard atmosphere model CIRA (COSPAR International Rerence Atmosphere) was used to include the variation of atmospheric density and temperature with altitude. The Kuznetsov [90] table giving the equation of state of air was used. The maximum pressure at different points on the ground was calculated, which took into account the reflection of the shock wave by the surface.

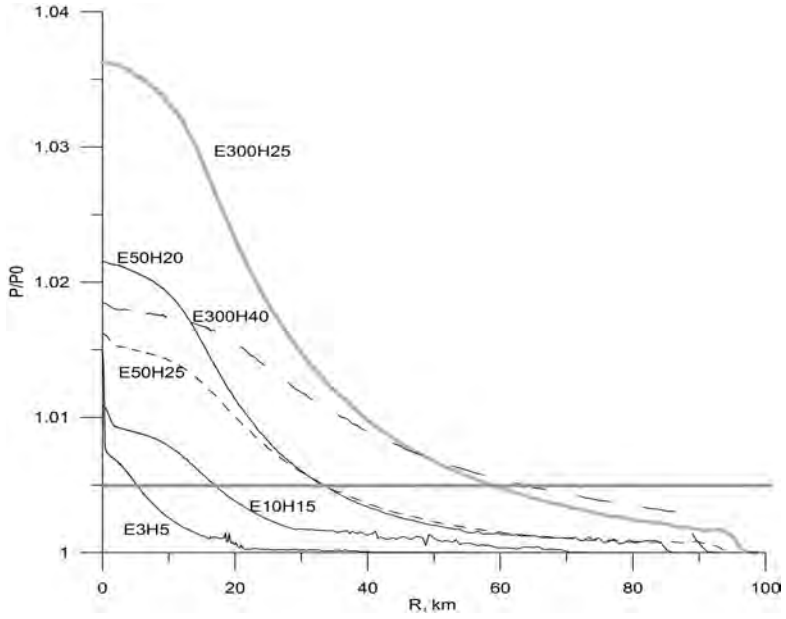

Fig. S39. The relative pressure versus distance R from the ground-projected position of the point source explosion, normalized to 1 atmosphere pressure, that would be caused by explosions with different energy energy (E) ranging from 3 to 300 kT TNT and altitudes (H) ranging from 5 to 25 km. The horizontal line corresponds to an overpressure of Δp~500 Pa.

A point-source explosion at 25 km altitude with energy of 300 kT equivalent TNT is able to cause an overpressure of $\Delta p \sim 500$ Pa over an area with diameter of ~60 km (Fig. S39).

In practice, the energy is not released in a single explosion during flight and fragmentation of the meteoroid through the atmosphere. A number of numerical simulations were conducted that attempted a more realistic release of energy along the trajectory. In each model, the total kinetic energy of the entering asteroid was fixed at 300 kT TNT. An entry angle of 16.5 degree with respect to the horizon was assumed (observed: 18.3º). The observed fireball had three main moments of fragmentation and corresponding flares (Fig. S16), hence three principal moments of energy release were considered. The last part of the trajectory below 21 km was not taken into account, because the radiation was fainter in this part of trajectory and the meteoroid mass and velocity had decreased significantly.

Three different cases were considered. In all cases the energy was released along the trajectory with a time delay corresponding to the meteoroid motion. For these models, the numerical grid has 500×250×250 points along the X, Y and Z axes. The X axis was taken along the trajectory in a direction opposite to the meteoroid motion, Y was taken perpendicular to the trajectory, while Z was vertical in upward direction.

In case I, all energy was released in one point X,Y = (+20, 0) km at Z = 31.7 km altitude, which corresponded to the main flare.

In case II, all energy was released along the trajectory between points (+100, 0) at 55 km altitude and (-16, 0) at 21 km altitude, and this energy release was taken to be proportional to the air density. Such energy release corresponded to a meteoroid flight with constant cross section, no disruption and negligible ablation, and without deceleration.

In case III, half of the energy (150 kt TNT) was released along the trajectory as in case II, 30% of energy (90 kt) was released in the first flare at (+20, 0) at 31.7 km altitude, 15% of energy (i.e. 45 kt) during the middle flare at (0, 0) at 25.8 km altitude and the final 5% (i.e. 15 kt) was released during the small flare at the end of the considered trajectory (-16, 0) at 21 km altitude. These altitudes correspond to early estimates of the entry trajectory [46].

The relative pressure distribution in the plane (X, Z) is given in Fig. S40 for case III at three different time steps. Time t=0 corresponds to the end of energy release. At all times, the

spherical shock waves from the three individual flares and the ballistic shock wave caused by the meteoroid's subsonic flight are well distinguishable.

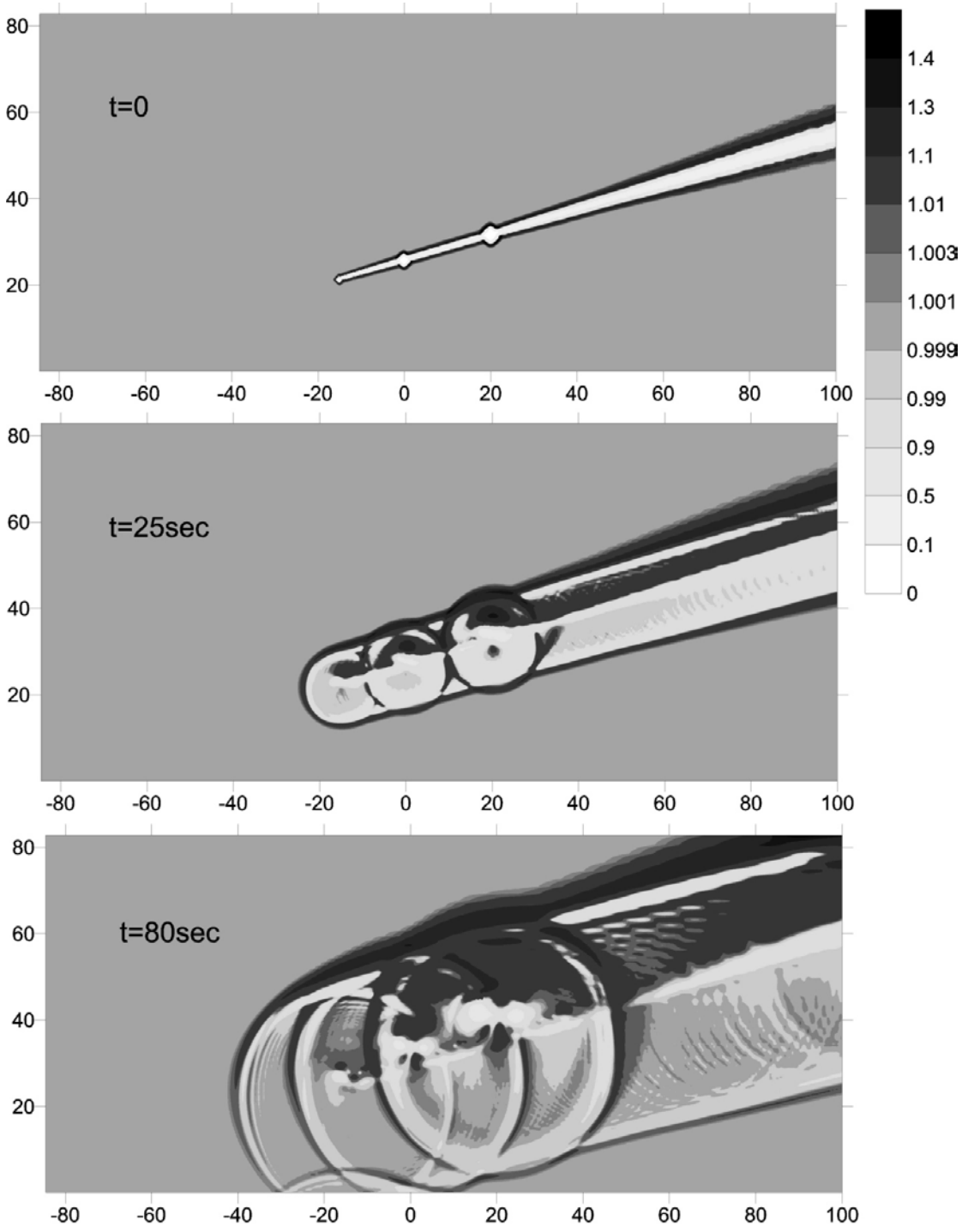

Fig. S40. The relative pressure P/P_0 distribution (P_0 is the pressure at the surface) for case III, case of 300 kt TNT continuous energy release with three flares (see text).

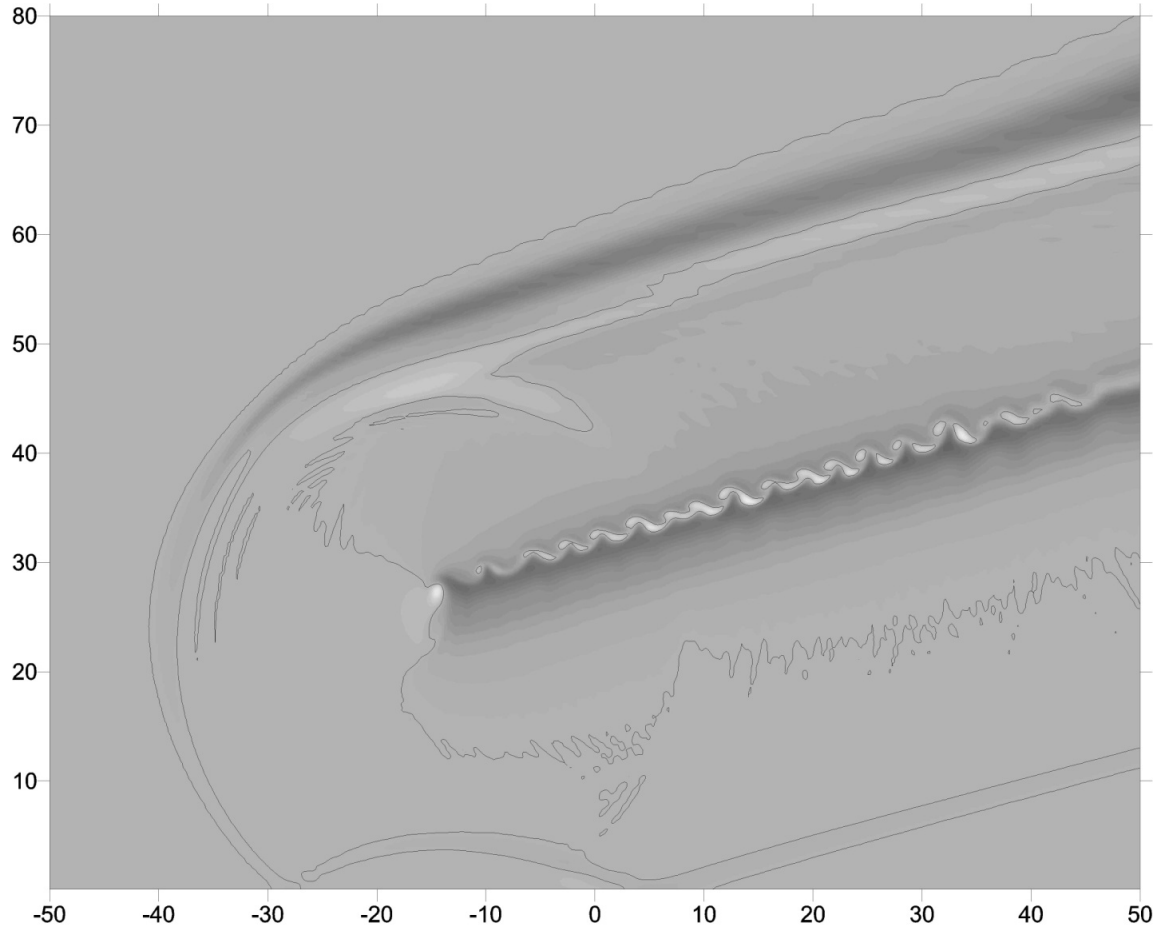

Fig. S41. The relative density ρ/ρ_o distribtuion (ρ_o being the density at the Earth surface) at the moment when the shock wave reaches the surface. The contour line corresponds to 0.1% compression. Case II – 300 kt TNT energy is released continuously along the trajectory (proportionally to the air density).

The ballistic shock wave has a conical shape with a small opening angle due to the high meteoroid velocity (taken at 18-19 km/s) compared to the sound velocity (0.3 km/s), at which speed the quickly decaying shock wave is spreading. It is important to note that the moment of the shock wave arrival at some point on the ground does not depend on the position of the main flare along the trajectory. To a good approximation, sound arrives at a location from the nearest point to the trajectory (but see below).

The relative density distribution in the plane (X, Z) is given in Fig. S41 for case II at the moment when the shock wave reaches the surface. At this time, the meteoroid wake already started to show billowing due to the development of instabilities.

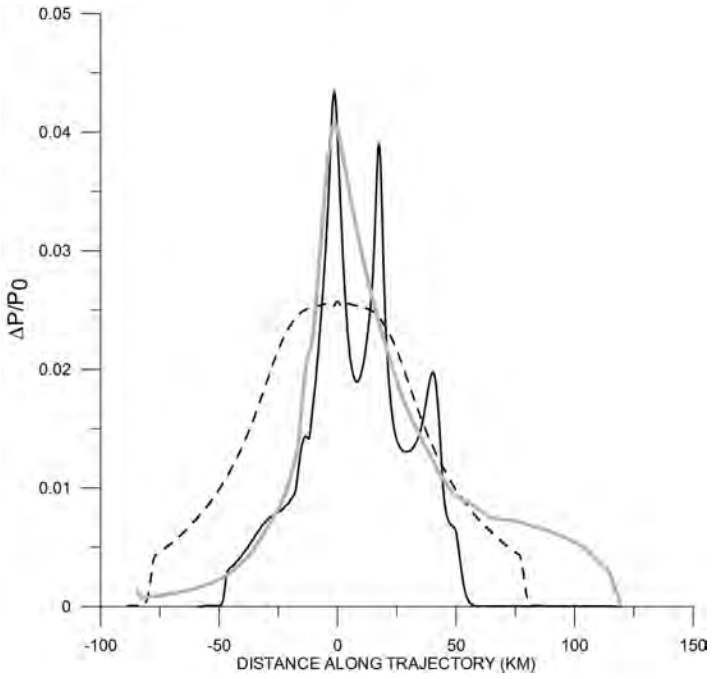

Fig. S42. The relative overpressure on the ground along the trajectory for case I (black dashed curve), case II (grey curve), and case III (black solid curve). Forward direction is towards the left.

The relative overpressure on the ground along the trajectory is given in Fig. S42. Projected to the Earth surface (X, Y plane), the overpressure contours of Δp>500 Pa and Δp>1000 Pa are shown in Fig. S43A. This pattern should reflect the observed area of broken windows.

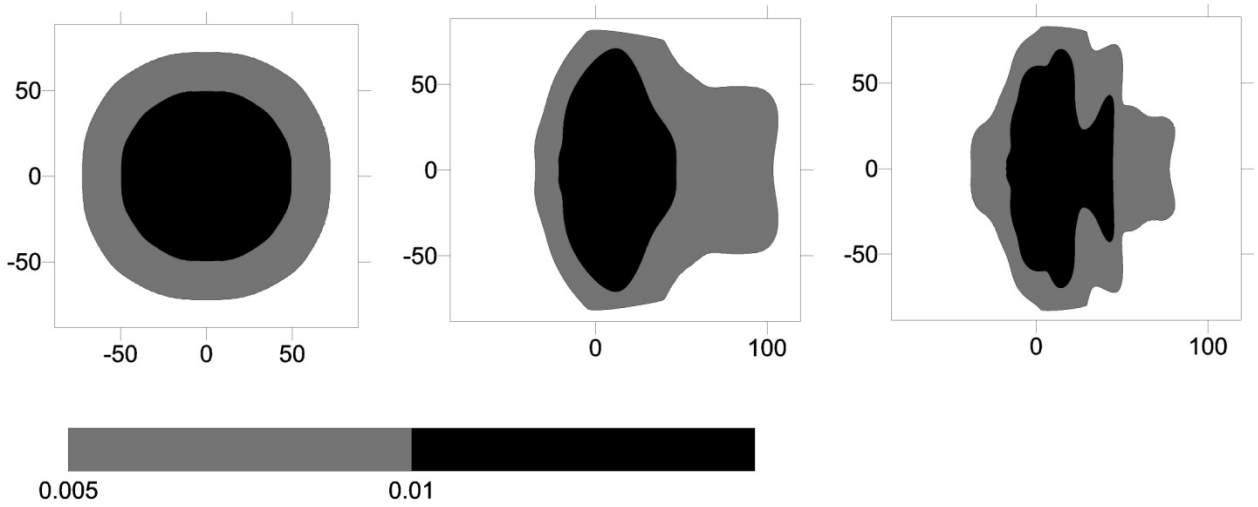

Fig. S43A. For three considered cases, shown is the surface area corresponding to overpressures of Δp>500 Pa (relative overpressure >0.005; colored grey) and Δp>1000 Pa (relative overpressure >0.01, colored black). Case I: left panel; Case II: middle panel; Case III: right panel.

In all three considered cases, the surface area on the ground that was affected by the shockwave is very similar, determined mainly by the total amount of energy released. The shape of the overpressure distribution is determined by the details of the energy release along the trajectory. This may be explained by the fact that in all cases the main part of energy is released at a similar high altitude and the size of the energy source is comparable (or even smaller) than the distance to it. In the case of a point energy source (case I) the damaged area has a circular geometry. In both cases considered where the energy source is stretched along the trajectory (cases II and III) the area of damage is elongated in the direction perpendicular to the trajectory. Non-constant energy release (case III) is needed to match the observed pattern in Fig. S38.

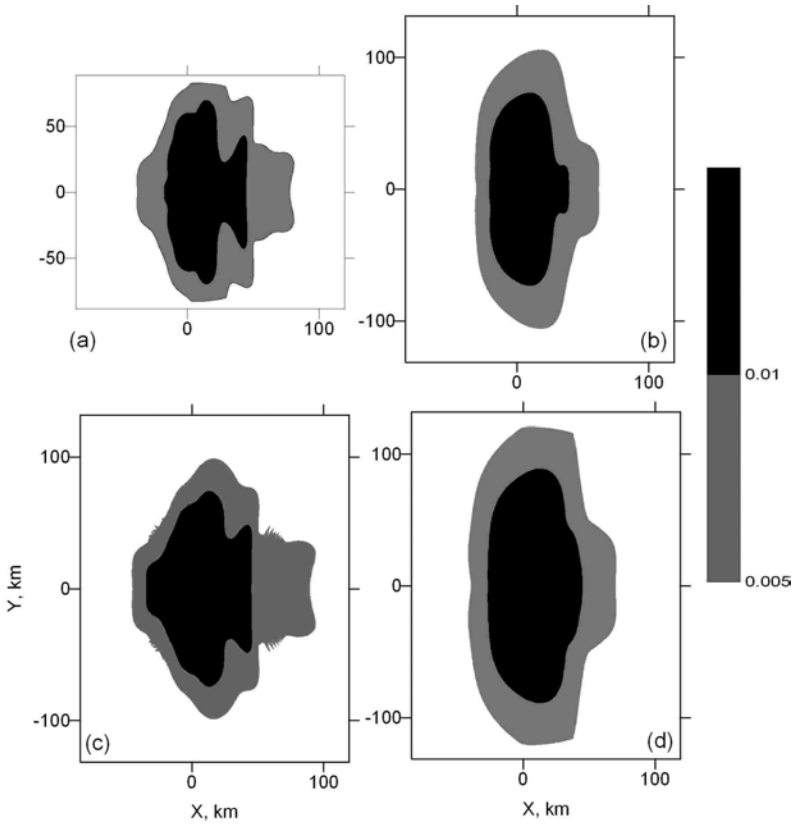

Fig. S43B. Surface overpressures from total initial energy 300 kT (a, b) and 520 kT (c, d) of TNT. Left panels (a, c) are deposition Case III and Case IV (see below), while right panels (b, d) are Case V. Gray is overpressure Δp>500 Pa (relative overpressure >0.005), black corresponds to Δp>1000 Pa (relative overpressure >0.01).

In case III, which has the continuous energy release with three flares, the peaks of overpressure are evident in the places where the shock waves from individual flares intersect

(Fig. S42). In case II (continuous energy release along limited trajectory), there is only one pronounced peak, which corresponds to the transition from cylindrical explosion to the spherical one. In case I, the peak is not sharp and its thickness has about the radius of curvature of the arriving shock wave. Case III also best describes the rapid decrease of overpressure in forward direction and the long tail of overpressure observed towards the back of the trajectory during eye witness interviews (Fig. S38). The Δp = 500 Pa contour for the 300 kT impact reaches to ~75 km. Using the scaling law distance $D \sim E^{1/3}$ [84], implies that an energy of E ~ 520 kT would cause an airburst that reaches to 90 km from the trajectory.

In order to check this scaling law, we calculated the overpressure on the surface for 520 kt TNT total meteoroid energy (Fig.S43B). The altitudes of energy deposition were now based on the trajectory determined in this work (Case IV). Similar to Case III, half of the energy (260 kt TNT) was released along the trajectory, 30% of energy (156 kt) was released in the first flare at (+18.6) at 29.7 km altitude, 15% of energy (i.e., 78 kt) during the middle flare at (0, 0) at 23.9 km altitude and the final 5% (i.e., 26 kt) was released during the small flare at the end of the considered trajectory (-17.2km) at 18.5 km altitude.

One more case (Case V) was modeled under the assumption that all energy was released in accordance with the bolide light curve (Fig. S16, S18A). Results are shown in Fig. S43B. This results in a more extended area perpendicular to the trajectory. At 520 kt TNT, the overpressure contour (P>500 Pa) reaches 120 km in this direction, compared to 102 km for 300 kt TNT Case III. So far, case V is our best effort in matching the observed damage area (Fig. 3, main text).

The results confirm that the total affected area is roughly scaled with the total energy and the shape of the area is dependent on features of assumed energy release. An energy release in proportion to the observed lightcurve results in a more narrow overpressure zone along the trajectory and a more extended zone in perpendicular directions.

However, the manner of energy release affects not only the pressure pattern on the ground (Fig. S43A, 43B), but also the structure of disturbances in the air and the observed structure of the meteor wake (Fig. S41). The relative pressure P/P_0 distribution for Case V (520 kt TNT) is shown in Fig. S43C. Compared to Fig. S40 (Case III, 300 kt TNT), there are noticeable differences in the pressure pattern.

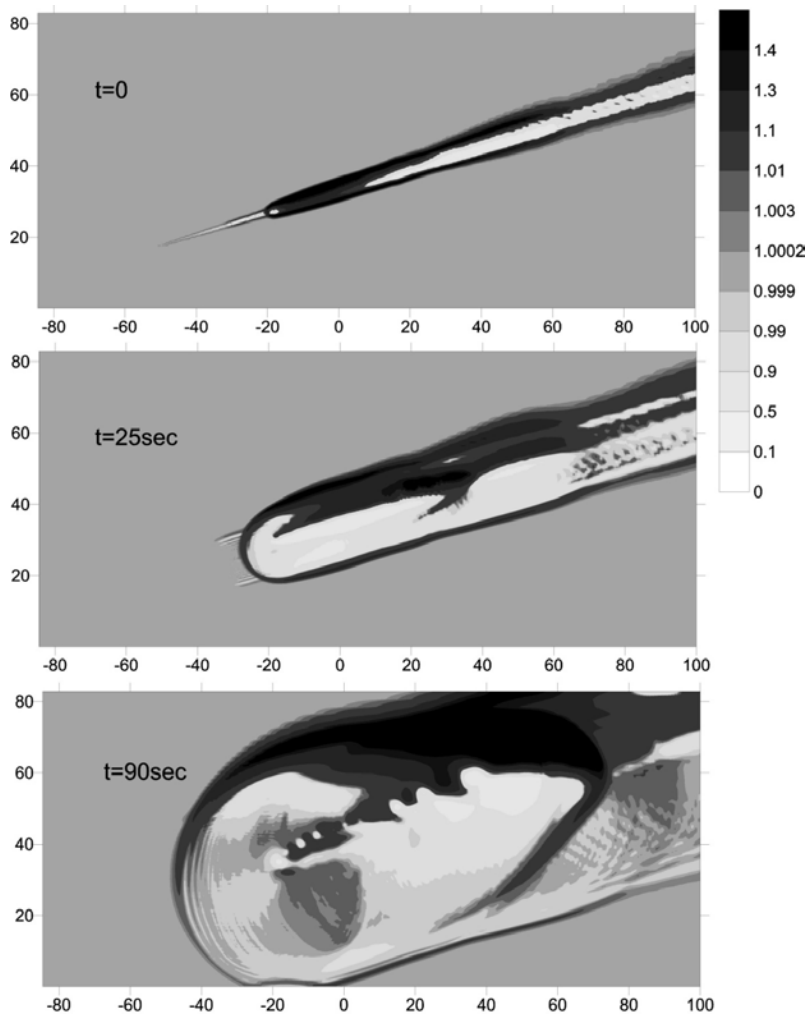

Fig. S43C. The relative pressure P/P_0 distribution (P_0 is the pressure at the surface) for Case V (520 kt TNT released in proportion to the light curve).

Blast Wave Arrival Times

(Contributed by: V. V. Shuvalov, O. P. Popova, Y. S. Rybnov, and P. Jenniskens)

A blast wave is a particular type of shock wave caused by the deposition of a large amount of energy in a small very localized volume, a propagating disturbance characterized by an extremely rapid rise in temperature, pressure, and density [91]. Blast wave arrival times can be estimated assuming that the wave expands with a constant velocity equal to the sound speed. Our numerical simulations show that this is a good assumption for the blast wave when an airburst occurs at high altitude [91]:

$$t_0(x,y) = \frac{1}{c_0}\left[(x + z_0 \tan^{-1}\alpha)^2 (\sin\alpha)^2 + y^2 \right]^{1/2} \quad \text{if } x > z_0 \tan\alpha \qquad \text{Eq. S4}$$

$$t_0(x,y) = \frac{1}{c_0}\left[(x^2 + z_0^2 \quad + y^2 \right]^{1/2} \quad \text{if } x \le z_0 \tan\alpha \qquad \text{Eq. S5}$$

Here t_0 is counted from the time when the meteoroid reaches the terminal point, c_0 is the sound speed, shock angle $\alpha = \beta$ - *arcsin* (c_o/U), where U is the meteoroid velocity, and β is the trajectory entry angle (to the horizon). The meteoroid moves from right to left in the plane Z0X, whereby $(0,0,z_0)$ are the coordinates of the terminal point. Terminal point here means the end of the main energy release by the meteoroid, in the case of Chelyabinsk this corresponds to the brightest part of the meteoroid lightcurve. The comparison of arrival time determined based on Eqs. S4-S5 and gasdynamical numerical modeling demonstrates satisfactory agreement (Fig. S44). By comparing these results to observed arrival times, it is possible to determine the altitude where most meteoroid energy was deposited.

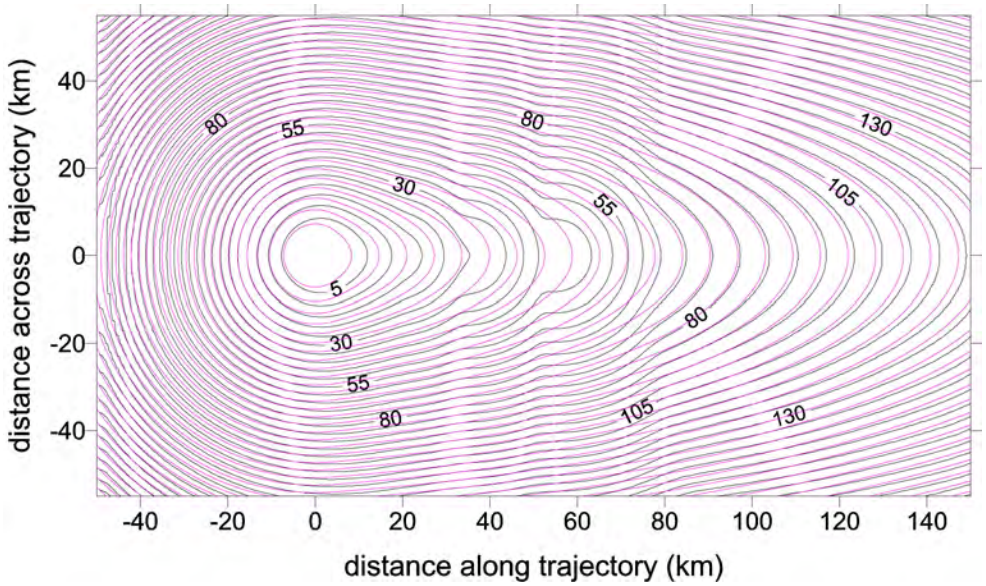

Fig. S44. The comparison of arrival time estimates based on Eqs.S4-S5 (grey lines, assuming a terminal altitude of 15 km), compared to results from gasdynamical numerical modeling (magenta lines). Time is counted from the moment when the blast wave reaches the ground just under the terminal point.

Eighteen time-calibrated video records (at 10 frames per second) provide a record of the arrival times of the shockwave in the Chelyabinsk/Kopeysk area (Table S12). Most reliable are those where the shockwave shakes the camera, or moves smoke, car exhaust, or cables in the

field of view. Less reliable are those that show car alarms go off, because they tend to have a variable delay of a few tenths of seconds (or much more).

Table S12. Summary of shock wave arrival times from video records. Range is distance from site to the approximate 23.9-km point (Table S1) at altitude.

Video #	Site	Lat. (N)	Long. (E)	Alt (m)	Range (km)	Time UT (±0.1s)	Detection
90	Chelyabinsk	55.17098	61.29611	226	42	03:22:52.8	car alarms
30	Chelyabinsk	55.14344	61.41418	232	43	03:22:53.1	car alarm
97	Kopeysk	55.11727	61.60240	213	48	03:22:54.8	swinging cable
171	Kopeysk	55.11686	61.61304	211	48	03:22:55.4	cable, billboard
177	Chelyabinsk	55.15866	61.39614	230	44	03:22:56.2	car alarm
31	Chelyabinsk	55.16260	61.38184	229	44	03:22:56.8	car alarms
237	Chelyabinsk	55.16014	61.40257	229	44	03:22:57.0	camera shakes
417	Chelyabinsk	55.16818	61.43558	223	46	03:23:00.4	car exhaust, cables
258	Chelyabinsk	55.17832	61.35922	215	44	03:23:00.6	cable
160	Chelyabinsk	55.17221	61.45356	234	46	03:23:02.0	cable cam. shake
329	Chelyabinsk	55.19525	61.32239	258	46	03:23:02.1	waving banner
452	Chelyabinsk	55.18404	61.39359	228	46	03:23:02.8	balloons waving
30a	Chelyabinsk	55.19009	61.35732	252	45	03:23:03.1	camera shakes
216	Chelyabinsk	55.18320	61.38599	229	46	03:23:03.3	cable
60	Chelyabinsk	55.19177	61.38485	223	46	03:23:05.9	waving banner
35	Chelyabinsk	55.25174	61.40274	251	52	03:23:24.8	car exhaust, cable
105	Kurgan	55.46484	65.26888	82	272	03:28:01.7	swinging cable
2	Pervomayskiy	54.87060	61.17369	275	23	03:21:47.8*	car shaking
6	Korkino	54.89089	61.39966	249	30	03:22:00.8*	car shaking
7	Yemanzhelinsk	54.75664	61.30380	227	30	03:22:01.7*	car shaking

*) relative to peak luminosity at 03:20:32.2 UT.

We use this simplified approach to compare blast wave arrival time with data from Table S12. An entry velocity of 18.6 km/s and an entry angle of 18 degrees to the horizon were assumed, but a 19.15 km/s entry speed give very similar results. The wind and dependence of sound velocity on atmospheric profile were neglected, as well as the difference between the sound speed and the shock wave velocity near the source (blast radius). The difference between real and model arrival times may reach 2-5 s dependent on the atmospheric conditions. For most video cameras located in Chelyabinsk and Kopeysk, the time delay Δt between maximum brightness and blast wave arrival is about 140-151 s (Table S12, Fig. S45A). In Kurgan, about 270 km from the chosen trajectory point, Δt ~450 s (Fig. S45C). The smallest values of Δt are obtained for Pervomayskiy, Korkino and Yemanzhelinsk: Δt ~ 76-90 s.

For a given entry velocity and angle, the blast wave arrival time is dependent on the assumed terminal altitude of energy release (z_0). Fig. S45A shows the arrival times corresponding to z_0 = 29.7 km, at the peak of the lightcurve profile (Fig. S16). It is reasonable to suggest that most energy is deposited here, but that does not appear to be the case. The wave arrives too late in Chelyabinsk (Δt ~ 160 s) and the sites of Pervomayskiy, Korkino and Yemanzhelinsk near the trajectory (Δt>100-110 s). Also, the wave arrived earlier in Korkino than Pervomayskiy, opposite to observations (Table S12).

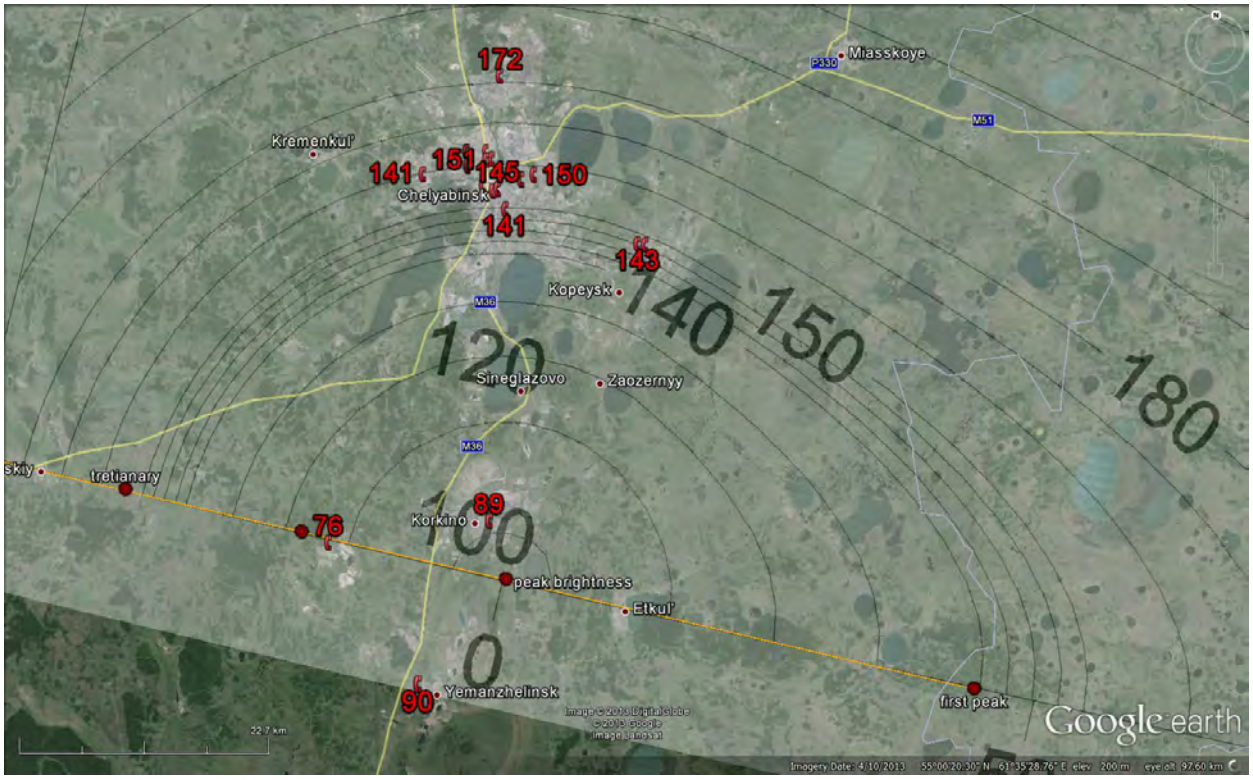

Fig. S45A. Blast wave arrival times from a conical source with 29.7 km terminal altitude, comparing those calculated (black lines) and observed (red markers). The yellow line is the meteoroid trajectory.

It appears that energy release down to lower altitude is important. With the source at 23.9 km altitude at the peak of the third flare (Fig. S45B), and after increasing the arrival times by 1.2 s to account for the relative time that the meteoroid arrived at this altitude (Table S1), the calculated arrival times are in good agreement in the Chelyabinsk-Kopeysk area, but the arrival times in Pervomayskiy and Korkino are 4 s late. That is well within the range of our estimated uncertainty. Hence, the energy deposition past peak brightness and down to 23 km significantly contributed to setting the arrival times for the shock wave.

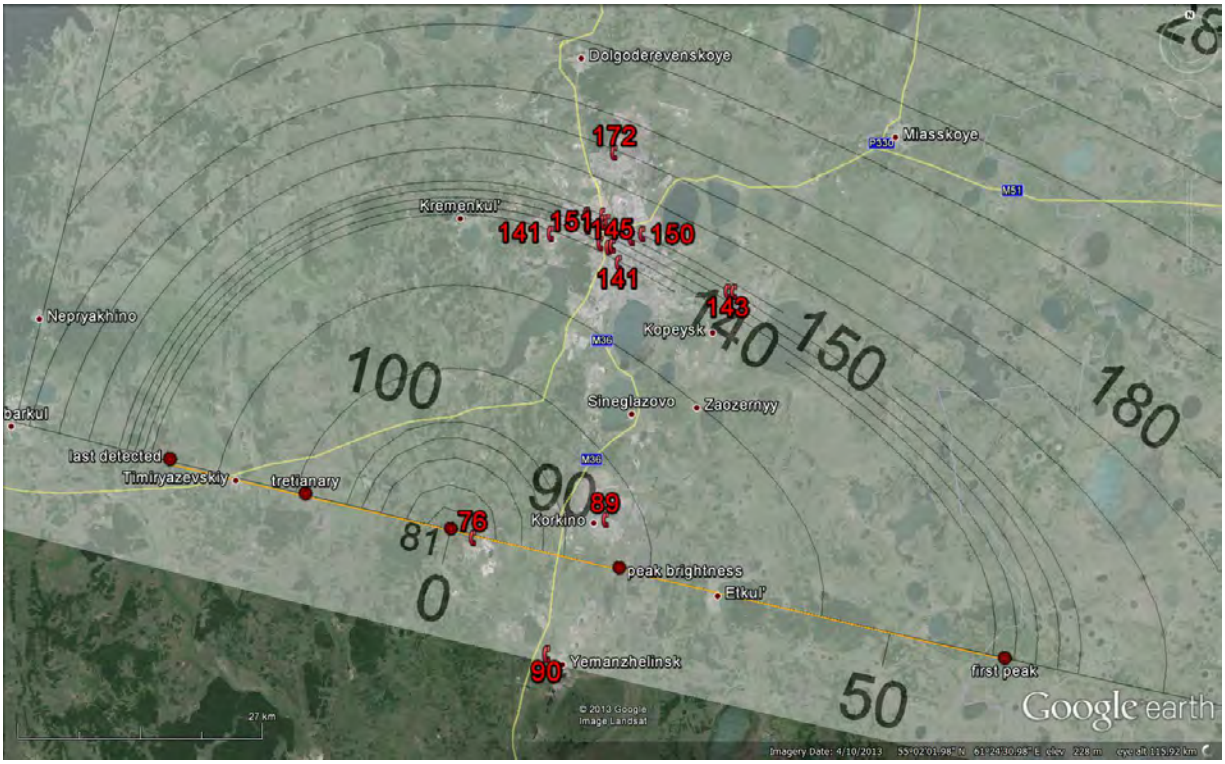

Fig. S45B. Same as Fig. S45A, for a conical source with 23.9 km terminal altitude.

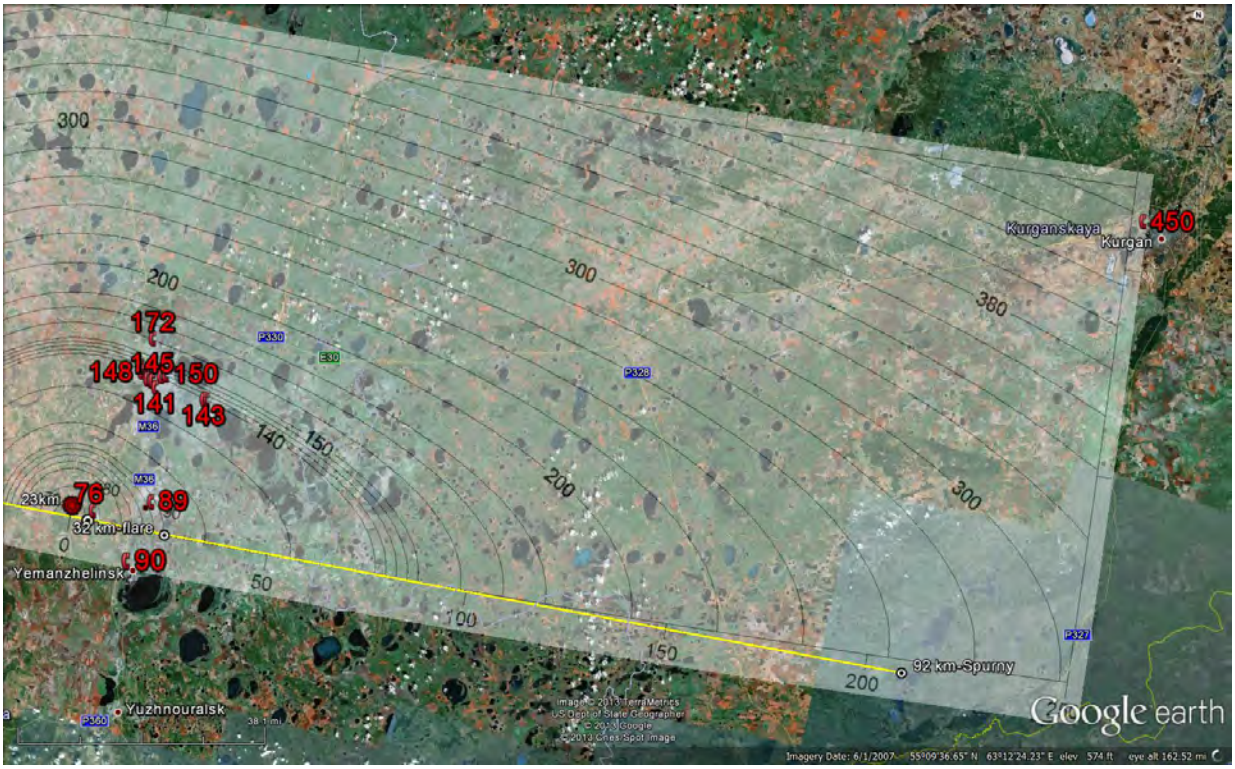

Fig. S45C. Expanded view of Fig. S45B, for a conical source with 23.9 km terminal altitude.

A lower terminal height of 18 km (after adding 2.5s to account for flight time) would also result in reasonable agreement with arrival times at observing locations, because those are determined by earlier parts of the trajectory. There are no data further forward along the trajectory that could measure the contribution from this altitude. In Chebarkul, even a smoke cloud in video #105 (Table S3) did not react to the shockwave.

A conically shaped blast wave (see for example Fig. S40) provides agreement with the blast arrival time in Kurgan (Δt = 450 s, Fig. S45C), whereas a spherical energy source essentially overestimates the propagation time. Kurgan is located 272 km from the source region and the shock wave arrival was measured by the response of a swinging cable right in front of the video security camera (Table S12).

In conclusion, comparing the arrival times from conical sources with different terminal altitudes to those observed at different locations demonstrated that a conical source can satisfactory describe the observed blast wave arrival times, but only if the energy deposition continued down to 23 km altitude. The deposition of the energy, which is responsible for the formation of the blast wave, occurred spread along the trajectory. Only a negligible fraction of the initial kinetic energy (and mass) was probably deposited below 23 km.

2.5. Structures hit by Falling Meteorites
(Contribution by P. Jenniskens, O. P. Popova)

Small meteorites were found on the roof of a building in Emanzhelinka. Only one structure, a secondary building owned by the Biryukovy family in Deputatskiy, was damaged by a falling meteorite. The meteorite created a gap at the edge of a corrugated plate (arrow in Fig. S46) and was found in fragments at the foot of the building. No injuries occurred.

Fig. S46. The owners of the property in Deputatskiy (left) show the meteorite responsible for the structural damage (arrow) to one of us (O.P., center).

3. Recovered Meteorites

3.1. Meteorite Recovery.

(Contributed by: S. Khaibrakhmanov, A. V. Korochantsev, M. Yu. Larionov, V. Grokhovsky, P. Jenniskens, A. Kartashova, O. Popova, D. Glazachev)

A series of dedicated searches for meteorites were organized by the Chelyabinsk State University, the Ural Federal University in Yekaterinburg, and by the Vernadsky Institute of Geochemistry and Analytical Chemistry of the Russian Academy of Sciences in Moscow between February 19th and 25th. In these early searches, the exact (< 10 m) location of most meteorite finds was not documented. The meteorites with exact find locations are listed in Table S13. The searches were continued after the snow melt on April 12th, resulting in many more finds with known locations. Meteorites studied in this work are identified in Fig. S47.

Fig. S47. Fragments of Chelyabinsk (C2 - C6) analyzed in this study. Find locations are marked. C2 is an oriented meteorite, backside shown.

Fig. S48. Confirmed locations of meteorite finds. Numbers indicate meteor altitude in km.

Table S13. Chelyabinsk meteorites with known masses and find locations. They are listed in the order that the information was provided. Those labeled with an asterisk are studied in this work (Fig. S47).

C#	Mass (g)	Latitude (N)	Longitude (W)	Altitude (m)	Date Find	Finder
1	-.-	54.8388	61.1241	280	2/15/2013	Biryukovy (house hit)
2*	5.83	54.8273	61.1594	282	2/19/2013	V. Kubrin
3*	4.46	54.8022	61.2756	256	2/19/2013	A. Dudorov
4*	4.84	54.8022	61.2756	256	2/19/2013	student CSU
5*	1.58	54.8022	61.2756	256	2/19/2013	S. Khaibrakhmanov
6*	0.46	54.8022	61.2756	256	2/19/2013	S. Khaibrakhmanov
7	1,060	54.8698	60.9672	281	4/15/2013	V. Bogdanovsky
8	430	54.8752	60.9551	306	4/16/2013	V. Bogdanovsky
9	150	54.8427	61.0828	308	2/26/2013	E. Tvorogov
10	470	54.8514	61.0209	302	2/28/2013	E. Tvorogov
11	11.41	54.8711	60.8533	298	4/13/2013	S. Khaibrakhanov
12	18.41	54.8720	60.8555	314	4/13/2013	A. Bukhalov
13	6.9	54.8742	60.8233	317	4/13/2013	A. Zhilkin
14	1,800	54.8598	60.9348	298	4/23/2013	M. Pen'kova
15	3.6	54.8420	61.1036	297	2/22/2013	S. Petukhov
16	2.8	54.8463	61.1084	297	2/22/2013	I. Talyukin
17	382	54.8502	61.1054	300	2/21/2013	S. Petukhov/I. Tayukin
18	125	54.8448	61.1066	300	2/22/2013	S. Petukhov/I. Tayukin
19	50	54.8376	61.0925	300	2/23/2013	S. Petukhov/I. Tayukin
20	56	54.8347	61.0968	300	2/23/2013	S. Petukhov/I. Tayukin
21	126	54.8428	61.1029	300	2/23/2013	S. Petukhov/I. Tayukin
22	200	54.8428	61.1029	300	2/23/2013	S. Petukhov/I. Tayukin
23	156	54.8617	61.1356	300	2/24/2013	S. Petukhov/I. Tayukin
24	420	54.8331	61.0879	300	2/24/2013	S. Petukhov/I. Tayukin
25	15	54.8610	60.9909	300	4/15/2013	S. Petukhov/I. Tayukin
26	141	54.8760	60.9782	300	4/15/2013	S. Petukhov/I. Tayukin
27	142	54.8748	60.9844	300	4/15/2013	S. Petukhov/I. Tayukin
28	151	54.8620	60.9978	300	4/15/2013	S. Petukhov/I. Tayukin
29	320	54.8741	60.9775	300	4/16/2013	S. Petukhov/I. Tayukin
30	760	54.8745	60.9801	300	4/16/2013	S. Petukhov/I. Tayukin
31	122	54.8732	61.1017	300	4/17/2013	S. Petukhov/I. Tayukin
32	190	54.8503	61.0892	300	4/19/2013	S. Petukhov/I. Tayukin
33	1,748	54.8845	60.8176	300	4/20/2013	S. Petukhov/I. Tayukin
34	10	54.8440	61.0664	300	4/22/2013	S. Petukhov/I. Tayukin
35	256	54.8789	60.8601	300	4/22/2013	S. Petukhov/I. Tayukin
36	980	54.8850	60.8660	300	4/22/2013	S. Petukhov/I. Tayukin
37	198	54.8828	60.8755	300	4/23/2013	S. Petukhov/I. Tayukin
38	1,000	54.8776	60.9210	300	4/23/2013	S. Petukhov/I. Tayukin
39	252	54.8885	60.8948	300	4/23/2013	S. Petukhov/I. Tayukin
40	201	54.8805	60.9810	300	4/24/2013	S. Petukhov/I. Tayukin
41	450	54.8734	60.9893	300	4/24/2013	S. Petukhov/I. Tayukin
42	715	54.8592	61.0308	300	4/25/2013	S. Petukhov/I. Tayukin
43	45	54.8589	61.0297	300	4/25/2013	S. Petukhov/I. Tayukin
44	133	54.8550	61.0575	300	4/26/2013	S. Petukhov/I. Tayukin
45	95	54.8533	61.0816	300	4/26/2013	S. Petukhov/I. Tayukin
46	25	54.8588	61.0234	300	4/28/2013	S. Petukhov/I. Tayukin
47	1,050	54.8744	60.9002	300	4/30/2013	S. Petukhov/I. Tayukin
48	290	54.8724	60.9068	300	4/30/2013	S. Petukhov/I. Tayukin
49	170	54.8807	60.9931	300	5/2/2013	S. Petukhov/I. Tayukin
50	501	54.8761	60.8972	300	5/3/2013	S. Petukhov/I. Tayukin

51	40	54.8371	61.1701	300	2/25/2013	Vernadsky Institute
52	6.0	54.8372	61.1699	300	2/25/2013	Vernadsky Institute
53	5.9	54.8372	61.1687	300	2/25/2013	Vernadsky Institute
54	18	54.8372	61.1684	300	2/25/2013	Vernadsky Institute
55	50	54.8719	60.9666	300	4/14/2013	locals
56	23	54.8704	60.9565	300	4/14/2013	locals
57	503	54.8718	60.9677	300	4/14/2013	locals
58	1,786	54.9041	60.7867	300	5/15/2013	V. Bogdanovsky
59	186	54.8705	60.9769	300	4/15/2013	locals
60	3,400	54.9011	60.7575	300	4/26/2013	A. Usenkov
61	21.7	54.8731	60.9668	300	4/15/2013	locals
62	300	54.8732	60.9557	300	4/15/2013	locals
63	102.5	54.8765	60.9543	300	4/15/2013	locals
64	354	54.8754	60.9528	300	4/15/2013	locals
65	164.2	54.8741	60.9676	300	4/15/2013	locals
66	147.5	54.8689	60.9778	300	4/19/2013	locals
67	4.2	54.8629	60.9514	300	4/19/2013	locals
68	30.0	54.8520	60.9893	300	4/19/2013	V. Bogdanovsky
69	22.1	54.8648	60.9522	300	4/19/2013	locals
70	36.9	54.8696	60.9607	300	4/19/2013	locals
71	439	54.8688	60.9679	300	4/19/2013	locals
72	35	54.8710	60.9307	300	4/20/2013	locals
73	198	54.8708	60.9307	300	4/20/2013	locals
74	14.9	54.8693	60.9342	300	4/20/2013	locals
75	30	54.8687	60.9348	300	4/20/2013	locals
76	107	54.8687	60.9421	300	4/20/2013	locals
77	14.9	54.8676	60.9412	300	4/20/2013	locals
78	439	54.8697	60.9275	300	4/20/2013	locals
79	27	54.8691	60.9266	300	4/20/2013	locals
80	1,220	54.8701	60.9144	300	4/20/2013	locals
81	361	54.8722	60.9262	300	4/20/2013	locals
82	593	54.8716	60.8875	300	4/21/2013	locals
83	84	54.8706	60.8939	300	4/22/2013	locals
84	448	54.8699	60.9520	300	4/22/2013	locals
85	200	54.8652	60.9627	300	4/22/2013	locals
86	76	54.8670	60.9482	300	4/23/2013	locals
87	55	54.8686	60.9296	300	4/23/2013	locals
88	150	54.8747	60.9496	300	4/23/2013	locals
89	97.9	54.8823	60.9642	300	4/24/2013	locals
90	82.5	54.8799	60.9649	300	4/24/2013	locals
91	24.5	54.8792	60.9528	300	4/24/2013	locals
92	963	54.8740	60.9542	300	4/24/2013	locals
93	23.7	54.8718	60.9562	300	4/24/2013	locals
94	136	54.8724	60.9170	300	4/24/2013	locals
95	1,845	54.8784	60.7943	300	4/24/2013	locals
96	60	54.8653	60.9905	300	4/24/2013	V. Bogdanovsky
97	117	54.8625	61.0031	300	4/24/2013	locals
98	150	54.8638	61.0193	300	4/24/2013	locals
99	110	54.8797	60.9368	300	4/29/2013	locals
100	356	54.8772	60.9351	300	4/29/2013	locals
101	52	54.8772	60.9322	300	4/29/2013	locals
102	290	54.8772	60.9304	300	4/29/2013	locals
103	502	54.8818	60.9152	300	4/29/2013	locals
104	201	54.8777	60.9143	300	4/29/2013	locals
105	560	54.8853	60.9027	300	4/30/2013	locals
106	200	54.8863	60.8981	300	4/30/2013	locals

107	133	54.8395	61.1188	300	4/30/2013	locals
108	53	54.8592	61.0746	300	4/30/2013	locals
109	150	54.8760	60.9873	300	5/3/2013	locals
110	250	54.8780	60.9529	300	5/3/2013	V. Bogdanovsky
111	175	54.8763	60.9777	300	5/3/2013	locals
112	150	54.8445	61.1540	300	5/3/2013	locals
113	590	54.8798	61.0213	300	5/7/2013	locals
114	303	54.8719	60.9675	300	4/15/2013	locals
115	902	54.8803	60.9365	300	5/9/2013	locals
116	190	54.8830	60.9288	300	5/9/2013	locals
117	600	54.8836	60.9267	300	5/9/2013	locals
118	515	54.8877	60.9158	300	5/10/2013	locals
119	490	54.8849	60.9221	300	5/10/2013	locals
120	125	54.8746	60.9523	300	4/14/2013	locals
121	1,430	54.9071	60.8158	300	5/12/2013	locals
122	3,070	54.9037	60.8088	300	5/13/2013	V. Bogdanovsky
123	520	54.8855	60.8134	300	5/13/2013	V. Bogdanovsky
124	41	54.8393	61.1459	298	5/29/2013	A. Filimonov
125	360	54.8694	61.0919	300	5/29/2013	A. Prokopenko
126	420	54.8844	61.0857	300	5/29/2013	A. Prokopenko
127	200	54.8854	61.0676	300	5/29/2013	A. Prokopenko
128	548	54.9007	61.0625	300	5/29/2013	A. Prokopenko
129	25	54.8355	61.1088	300	4/12/2013	locals
130	5.8	54.8355	61.1088	300	4/12/2013	locals
131	82.9	54.8567	61.1212	300	4/13/2013	locals
132	219.6	54.8586	61.0938	300	4/13/2013	locals
133	76	54.8539	61.1246	300	4/13/2013	locals
134	29.6	54.8639	61.1246	300	4/13/2013	locals
135	16.1	54.8551	61.1008	300	4/13/2013	locals
136	75.8	54.8559	61.1016	300	4/13/2013	locals
137	32.4	54.8594	61.1222	300	4/13/2013	locals
138	49	54.8585	61.1076	300	4/13/2013	locals
139	57.9	54.8556	61.1026	300	4/13/2013	locals
140	153.5	54.8379	61.1084	300	4/14/2013	locals
141	5	54.8473	61.1103	300	4/14/2013	locals
142	49.7	54.8503	61.0988	300	4/16/2013	locals
143	16.2	54.8503	61.0988	300	4/16/2013	locals
144	1.9	54.8503	61.0988	300	4/16/2013	locals
145	11.4	54.8304	61.0988	300	4/16/2013	locals
146	13.9	54.8452	61.0989	300	4/16/2013	locals
147	303	54.8659	61.0171	300	4/17/2013	locals
148	10.2	54.8659	61.0035	300	4/17/2013	locals
149	12.2	54.8677	61.0120	300	4/17/2013	locals
150	163	54.8676	61.0129	300	4/17/2013	locals
151	86.6	54.8683	61.0138	300	4/17/2013	locals
152	14.1	54.8685	61.0133	300	4/17/2013	locals
153	100	54.8632	61.0053	300	4/17/2013	locals
154	152.9	54.8822	60.9744	300	4/18/2013	locals
155	1,410	54.8722	60.9736	300	4/19/2013	locals
156	493	54.8848	60.9683	300	4/19/2013	locals
157	19.4	54.8585	61.0194	300	4/20/2013	locals
158	376	54.8565	61.0174	300	4/20/2013	locals
159	68.8	54.8956	61.0107	300	4/20/2013	locals
160	38.1	54.8613	61.0174	300	4/20/2013	locals
161	28.8	54.8652	61.0343	300	4/22/2013	locals
162	63.8	54.8628	61.0302	300	4/22/2013	locals

163	24.9	54.8559	61.0170	300	4/22/2013	locals
164	68.7	54.8821	60.8874	300	4/23/2013	locals
165	358.5	54.8861	60.9124	300	4/23/2013	locals
166	350.2	54.8861	60.9124	300	4/23/2013	locals
167	52.5	54.8744	60.8939	300	4/23/2013	locals
168	278	54.8758	60.8946	300	4/23/2013	locals
169	2,180	54.8797	60.9099	300	4/23/2013	locals
170	1,889	54.8560	60.9107	300	4/23/2013	locals
171	125.2	54.8786	60.8930	300	4/23/2013	locals
172	1,510	54.8766	60.9094	300	4/23/2013	locals
173	118	54.8841	60.8578	300	5/23/2013	locals
174	3.6	54.8866	60.9092	300	5/29/2013	locals
175	129	54.8774	60.9082	300	5/29/2013	locals
176	28	54.8890	60.8241	300	6/15/2013	K. Ryazantsev
177	148	54.8856	60.8541	300	6/20/2013	K. Ryazantsev
178	10	54.8809	60.8635	300	6/21/2013	K. Ryazantsev

Table S14. Chelyabinsk meteorite collections with approximate find locations.

#	Total mass (g)	Mean (g)	Range (g)	N	Latitude (N)	Longitude (W)	Altitude (m)	Date Find	Finder
A	1.99	0.039	0.06-0.95	51	54.9594	60.3221	318	2/17	UrFU - Larionov
B	166	5.9	0.7-20.6	28	54.8022	61.2756	256	2/19-25	CSU - Dudorov
C	1,300	5.2	-.-	~250	54.8273	61.1594	282	2/19-25	V. Kubrin
D	780.0	120	20-300	9	54.8022	61.2756	256	2/19-25	A. Khaibrakhmanov
E	169	3.68	0.04-100	46	54.8271	61.1502	279	2/19-25	E. Chayko
F	5,000	30.9	1.4-120.5	>9	54.8022	61.2756	256	2/19-25	T. Iljin
G	15.45	0.4	0.04-1	41	54.8129	61.2814	245	2/19-25	L. Kuznetsova
H	-.-	-.-	0.5-5	50	54.7852	61.3703	230	2/19-25	Mrs. Pivovarova
I	133	133	133	1	54.8402	61.1020	291	2/23	S. Zamozdra
J	483	12.0	0.4-37	40	54.8461	61.1029	295	2/23	S. Buchkov / D. Rakhmankulov
K	235.0	2.6	0.2-35	90	54.8222	61.1667	276	2/23-24	A. Wahl
L	2.2	1.1	1-1.2	2	54.7604	61.3519	225	2/19-25	O. Panova
M	7	2.3	0.5-5	3	54.7604	61.3519	225	2/19-25	local children
N	4	0.4	0.2-3	9	54.8138	61.4622	230	2/19-25	local
O	10	<0.1	0.1-3	100+	54.7702	61.4980	225	2/19-25	local
P	>86	-.-	0.04-86	many	54.7965	61.2514	262	2/19-25	locals
Q	495.7	1.72	0.58-11.1	288	54.804	61.251	251	2/22-23	R. Kolunin
R	2,989.3	44.6	0.39-1806	67	54.858	60.935	291	2/22-23	L. Alexandrov:
S	309.7	1.35	0.23-20.25	229	54.816	61.303		2/22-23	S. Malagamba
T	647.6	27.0	0.53-29.70	24	54.843	61.127	286	2/19	M. Larionov
U	556.5	92.8	7.52-299.5	6	54.860	60.977	286	4/21	N. Kruglikov

Other information about the distribution of meteorite falls comes from the approximate location (±0.5-1 km) of meteorite finds in collections (Table S14). Photographs of meteorite collections were taken with a scale and the finder was asked to identify the approximate find location. Unless specified otherwise, only meteorite collections that could be photographed are included in the list.

In examining the large Kubrin collection (Table S14), it became clear that half of the larger 3-5 cm sized meteorites found near Bereznyaki were oriented in shape. One example is meteorite C2, shown in Figure S47, which is a thin, flat, meteorite that travelled with its flat side forward.

Meteorite Recovery from Snow

(Contributed by: P. Jenniskens, A. V. Korochantsev)

Meteorites fell in snow and were found several days after the fall by looking for holes and digging in search of 10-15 cm long ice cones that encapsulated the meteorites (Figs. S49-S50). Snow fall on February 25 prevented further meteorite searches until later in the season.

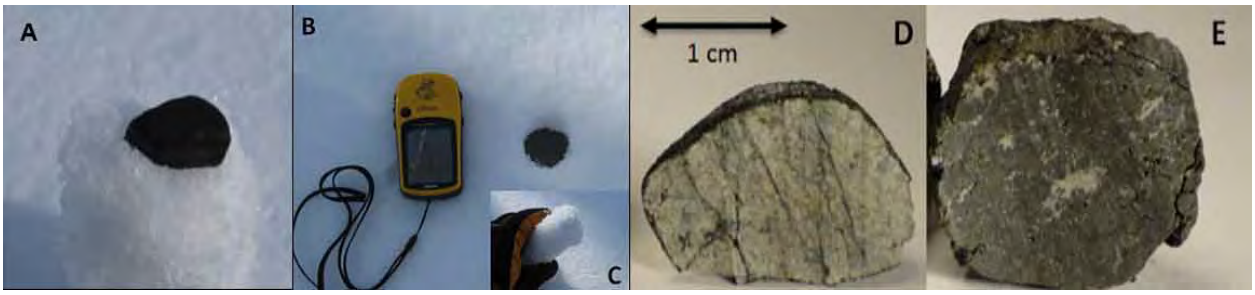

Fig. S49. (A) Meteorite found during the Vernadsky Institute, RAS, field campaign; **(B-C)** Hole in snow layer and ice cone attached to meteorite; **(D)** Chondritic meteorite; **(E)** Impact melt.

Fig. S50. (A) Hole from falling meteorite in snow layer with ice cone exposed; **(B)** The meteorite is recovered at the bottom tip of the ice cone. Photo's from a video by V. Kubrin.

The exact mechanism generating the observed ice cones is not readily understood; however, they may be created by the following process. Competing processes make a freshly fallen snow layer more powdery over time, closely related to the bond-to-grain ratio in snow [92]. At

temperatures below freezing, larger and more dendritic grains in low density dendritic snow morphologies undergo a growing metamorphosis and form stronger bonds over time by sintering, but at the same time result in the formation of unbounded small rounded particles. On the surface, on the other hand, the temperature fluctuations by exposure to sunlight cause snow crystals to undergo a disintegrating metamorphosis, by becoming rounder in shape to minimize free energy, which sinter to form stronger bonds. This process is responsible for forming an icy crust [92, 93]. We found layers of icy crust at different levels in the snow pack.

In the days following the fall, wind swept powdery snow filled the lower half of the holes, which tended to be 3-4 times wider than the meteorite. Winds could have rounded the snowflakes by loosing their points. Temperature fluctuations then made them susceptible to the type of disintegrating metamorphosis found near the surface by sintering into larger rounded grains. Moreover, vapor diffusion is the main mechanism leading to sintering [92] and perhaps sintering was intensified by a higher humidity in the tunnels. This turned the snow into ice popsicles, isolated from the surrounding powdery snow.

Mass Distribution of Fallen Meteorites and Total Fallen Mass

(Contributed by: A. E. Dudorov, S. A. Khaibrakhmanov, A. E. Mayer, D. D. Badyukov, and P. Jenniskens)

Here, we consider a total of 939 meteorites with known recovery masses, totaling 7,767 g, with individual samples ranging from 0.04 to 300 g. Most of these meteorites were found near Emanzhelinka and Deputatsky and collected during the field search by the Vernadsky Institute RAS and Chelyabinsk State University.

The mass distribution, normalized to unity (Fig. S51), is close to a log-normal mass distribution function:

$$f(m) = A \exp\left(-\frac{(\log m - \mu)}{\sigma^2} \right), \qquad \text{(Eq. S6)}$$

where A, μ and σ are the distribution parameters. A least-squares fit to the histogram gives: A = 0.60 ± 0.02, μ = 0.27 ± 0.02, σ = 0.67 ± 0.02. (dashed line in Fig. S51). The log-normal distribution implies that the process leading to the production of these fragments happened randomly and in a cascading way [94]. In some cases too, the strewn-field mass distribution was well described by a log-normal distribution [95].

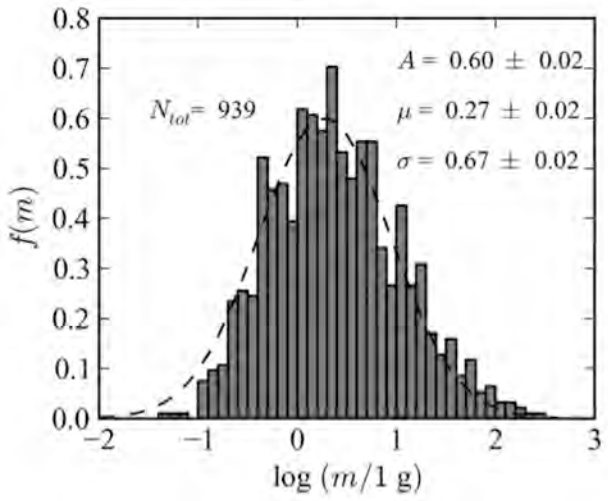

Fig. S51. Meteorite mass distribution, histogram with a log-normal fit (dashed line).

Atmospheric drag causes size-sorting along the trajectory and the distribution does not include the >300 g fragments found further west. On the other hand, if this same log-normal distribution extends to masses as large as 1.8 kg, the largest fragment found just west of Deputatskiy (Table S13), then the total fallen mass comes out to >789 kg. This is a lower limit because larger masses may have fallen as part of this population of fragments.

Table S13 and S14 lists a total mass of just over 69 kg, representing a meteorite line density (mass per kilometer along the trajectory) of about 2 kg/km. This is a lower limit. An estimate of the actual value can be made from the large collection of Vyacheslav Kubrin (Table S14), who estimated his finds represented only 10% of the total amount of meteorites recovered from a triangular area of 0.23 km^2 centered on longitude 61.1636ºE. This translates to a meteorite density of 57 kg/km^2 at that location. If the meteorite strewn field has an effective width of 2 km [96], then the line density is 114 kg/km, assuming that the search area is near the center of the strewn field. Previous falls found a constant line density along the trajectory [96] which, for a 40-km long confirmed fall area out to the location of the 1.8-kg fragment, translates to a total fallen mass of approximately 4,600 kg between Aleksandrovka and the location west of Deputatskiy where the 1.8-kg fragment was found (Fig. S48). The accuracy of this number depends on the accuracy of the recovery efficiency, the effective width of the field, and to some extent if Kubrin's finds were made at the center of the strewn field.

This does not include material surviving from disruptions below 29.7 km altitude. Light curve modeling (Sect. 1.2) suggested that larger fragments survived down to the ground, the

largest about 100-400 kg (recovered: 600-650 kg). The fragment mass distribution varied from one model to another, but there could be about 1,000 kg more in 20-2000 fragments in the area up to 70 km west along trajectory from the point of maximum brightness (line density ~14 kg/m). The number density of these fragments is lower than that for the gram-sized fragments. If so, the total fallen mass is about 4,000-6,000 kg (i.e., 0.03-0.05% of the initial mass).

Table S15. Ground-projected displacement and the time it takes meteorites of different mass to fall to the ground from 29.7 km altitude, assuming a spherical shape with density 3.3 g/cm^3 (Sect. S4.2), drag coefficient C_d = 0.43 if Mach number Ma < 0.5, C_d = 1.0 if Ma > 1.4, and otherwise C_d = 0.715 + 0.285 *sin* [3.1415 (Ma/0.9 - 1.05)], and prevailing winds (Sect. S1.4). Lateral velocity from fragment interaction after disruption [97], responsible for the lateral spreading of the strewnfield, was not taken into account.

Mass (kg)	Time (s)	Measured Time (s)	Impact Speed (m/s)	Perpendicular Displacement (km)*	Along Track Displacement (km)**	Measured Along Track Displacement (km)***
0.0001	758	-.-	17	-12.4	-9.0	-6
0.001	514	-.-	25	-8.3	-1.3	6
0.01	347	-.-	37	-6.2	10.7	18
0.1	235	-.-	55	-3.8	20.4	33
1.0	158	-.-	82	-2.6	32.4	43
10	107	-.-	124	-1.8	45.6	-.-
100	73	-.-	184	-1.4	59.4	-.-
600	53	62.5	225	-1.0	70.7	67

) Negative is south of track; **) If no further ablation; *) Relative to 29.7 km altitude point.*

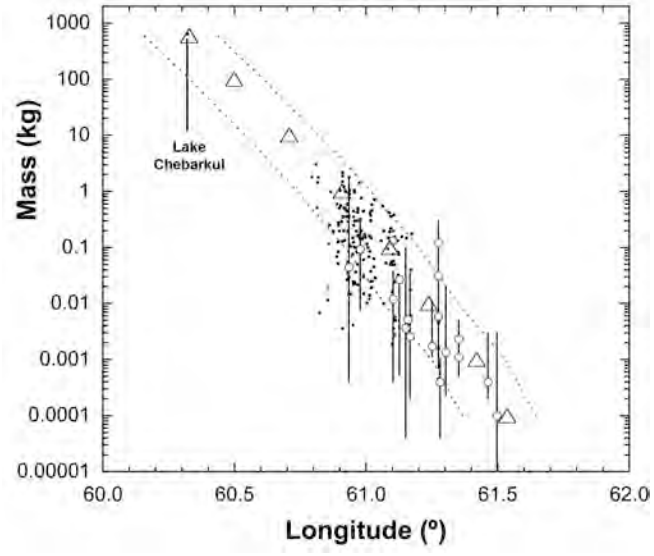

Fig. S52. Observed and calculated position of meteorites on the ground, for an origin longitude of 61.40ºE (=29.5 km altitude, triangle), 61.51ºE (=31.8 km altitude, upper dashed line) and 61.23ºE (=26.1 km altitude, lower dashed line). Black dots are single finds, open circles are group finds.

Table S15 lists the calculated and measured displacements along the trajectory for release at 29.7 km altitude. Size sorting due to small fragments being more efficiently stopped than bigger ones by friction with the atmosphere resulted in a mass (m), in kg, falling on average at a longitude λ = 60.906 - 0.188

$\log^{10}(m)$ - 0.0073 $(\log^{10}(m))^2$, but a range of masses is found at each location (see below). Comparing the mass-dependent behavior to the observed distribution of meteorites (Fig. S52), calculated from the point that no further ablation occurred, shows that meteorites were mostly broken into their final form between 31.8 km and 26.1 km (±0.6 km) altitude, in good agreement with an episode of rapid fragmentation in our meteor model (Fig. S18C).

Chebarkul Lake Meteorites

(contributions by: V. Grokhovsky and P. Jenniskens)

Shortly after the fall, a circular hole was found in Chebarkul Lake with a scattering of ice fragments surrounding it (Fig. S53A). During investigation by Ural Federal University (UrFU) researchers on February 17th, 51 small rocks were found scattered 5-50 m from the hole (Fig. S53A, and #1 in Table S14). A police guard did not permit searches within 5 m of the hole.

Fig. S53A: Small meteorite fragments recovered by a UrFU research team from Chebarkul Lake near the hole in the ice layer, shown right in an airborne photograph taken by Eduard Kalinin from a Diamond C2 aircraft shortly after the hole's discovery on February 16th at 11:05:34 UT.

The position of the hole was measured at Lat. = 54.959377 ±0.0003ºN, Long. = 60.322107±0.0005ºE at about 01:00 UT that day, by placing two people at opposite sides of the hole with the center of the hole on the viewing line, in two configurations forming a cross, and measure their position using a handheld GPS. The hole dimensions were estimated at a slightly asymmetric ~7x8 m. The ice layer thickness was about 70 cm. Subsequent measurements suggest that the GPS systems used that day were not well calibrated.

Many recovered meteorite fragments show fusion crust with strong curvature (Fig. S53A). The abundance of fusion crust may be a selection effect, as darker rocks were easier to find, or it may indicate that these fragments came from the surface of the impacting meteorite, which then must have been irregularly shaped by ablation.

At the time, the origin of these fragments was uncertain. Alternatively, they might have come from smaller meteorites that fragmented deep in the atmosphere and low enough to not cause further fusion crust. In that case, however, fragments ought to have fallen over a wider area along the trajectory, but no other such fragments were found.

Fig. S53B: Meteorite impact on Lake Chebarkul, captured in video by Nikolaj Mel'nikov. From top to bottom: at 03:20:32.20 UT, the landscape is lit by the fireball; at 03:21:34.68 UT, the landscape is unremarkable, reddish illuminated by the rising sun; one frame later, a cloud of ice or snow is detected (dot just below the arrow); in later frames that cloud is observed to be blown in the wind out of the frame to the right. Video courtesy of Gennadiy Ionov.

The meteorite impact on the lake's icy cover was captured on video by a 25 fps video security camera owned by Nikolaj Mel'nikov in Chebarkul (Long. = 60.34461ºE, Lat. = 54.976852ºN). The video shows that 62.52 seconds after the fireball lit up the landscape, a white spot emerged suddenly from one frame to the next, in the direction where the hole in the lake was later found (Fig. S53B). Counting frames from the time of peak brightness, assumed to be at 3:20:32.2±0.1 UT (Sect. 1.1), the impact occurred at 03:21:34.72±0.1 UT. What is presumably a cloud of ice or snow is seen to rise and expand in subsequent frames, creating a dark shadow in the landscape behind. The cloud is then elongated by wind, which blows stronger higher above the ice. In the next 7 minutes, the cloud drifts towards the right side of the frame, seen in projection against the dark forested shore in the background (Fig. S53B).

In an effort to locate a possible surviving meteorite, a team of the UrFU Quantum Magnetometry Laboratory conducted a magnetometer survey of the site using a MMPOS-2

magnetometer-gradiometer and standard GPS navigator Garmin-60cx on February 28th and March 11th [98]. 6,000 points of the Earth magnetic field were measured in a grid separated by 1 m, covering an area of 60 x 100 meters around the hole (Fig. 53C). An anomaly was found at Long. = 60.3206725ºE, Lat. = 54.9593669ºN, indicative of what may be an iron-containing object, just South-East from the center of the hole at the time of the measurement [98]. The absolute accuracy of that position was 15 meters. Subsequent dives only found depressions in the mud at the bottom of the lake. The position of the hole was 98m further west than measured on February 17, at Long. = 60.32058±0.00013ºE and Lat. = 54.95940±0.00013ºN (Fig. S53C).

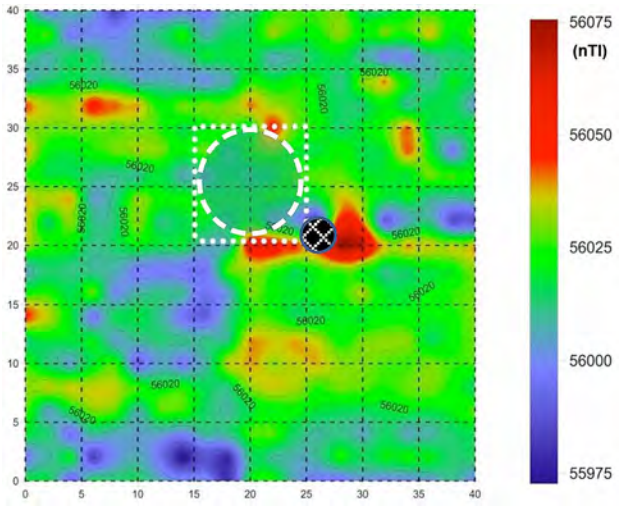

Fig. S53C: Map of magnetic anomalies with a resolution of 1 nT [98]. The dashed circle marks the position of the hole on March 11. The solid black circle marks the suspected location of the meteorite. North is up, and the center of hole (affected by ice drift) is displaced by X = +20m and Y = +25m.

A similar, but again slightly different, location and a further hole diameter estimate as well as sun illumination data were derived upon request from a calibrated satellite image (© CNES 2013, Distribution Astrium Services /Spot Image S.A., France, all rights reserved) taken at 50 cm/pixel resolution by the French Pléiades 1A satellite at 7:30:41.6 UTC on February 22. The published picture can be found on the website: http://www.astrium-geo.com/en/4687-russian-meteorite-impact-viewed-by-pleiades. The hole was viewed in a direction 10.3ºW and 32.1ºN, while the Sun elevation was 24.52º and azimuth 168.54º (SSE). Shadows of people standing close to the hole are seen. The diameter and the center of the hole were measured from the calibrated full resolution satellite image data by Ulrich Johann, Astrium Satellites GmbH. The values determined here are 6.3±0.5m, with Long. = 60.32087±0.00006ºE, Lat. = 54.95976 ±0.00006ºN with respect to the GPS reference frame WGS 84 geoid, respectively. This is 19m east and 40m north of the magnetometer survey position. Drift in the ice sheet from winds and tides, or measurement errors, could account for these smaller differences.

At the time of writing, news came that the search of meteorite fragments in the lake based on the magnetometer results was successful. The first probable meteorite fragment with a mass of 1.5 kg was recovered from the bottom of the lake by diver Alexey Lyahov in the morning of 2013 September 24th. The main mass was recovered on October 16th and found to weigh ≥570 kg, part of which is shown in Fig. S53D. The impacting mass may have been 600-650 kg.

Fig. S53D: Main mass of the Chelyabinsk fall at the Chelyabinsk State Museum of Local History shortly after recovery from Chebarkul Lake. Photo courtesy of Andrey Yarantsev.

Model of Chebarkul Lake Impact

(Contributed by: G. Gisler)

In order to investigate whether the hole could indeed have been created by a falling meteorite, 2-D dynamical simulations in axisymmetry were run to investigate the size of the expected hole in a 70-cm thick ice layer at -25 ºC ground temperature (-20ºC air temperature) for different sized masses (spheres of 3.3 g/cm^3) impacting the ice. The simulations were done with RAGE [99], a finite-volume adaptive-mesh hydrocode. Time steps of ~300 ns are required to resolve pressure waves across the finest 0.25cm mesh size. The water depth used in the simulations was 7 m with a reflective bottom boundary. Three conditions were investigated: a 10 kg meteorite falling at the expected 140 m/s (Table S15), a 100 kg meteorite falling at a high 600 m/s, and a 200 kg meteorite falling at 1,300 m/s. In this initial investigation, vertical impact trajectories were assumed (the calculated impact angles are 3º, 45º, and 47º from the vertical, respectively).

The 10 kg meteorite (Fig. S54A) punched through the ice intact, but did not carry enough momentum to create a water rebound powerful enough to increase the hole size to 6 meter

diameter. The ice refroze rapidly. The 100 kg meteorite (Fig. S54B) just barely punched through the ice. The meteorite shattered and the remains smeared around the bottom of the crater. The water was heated enough to not have frozen over at the end of the simulation.

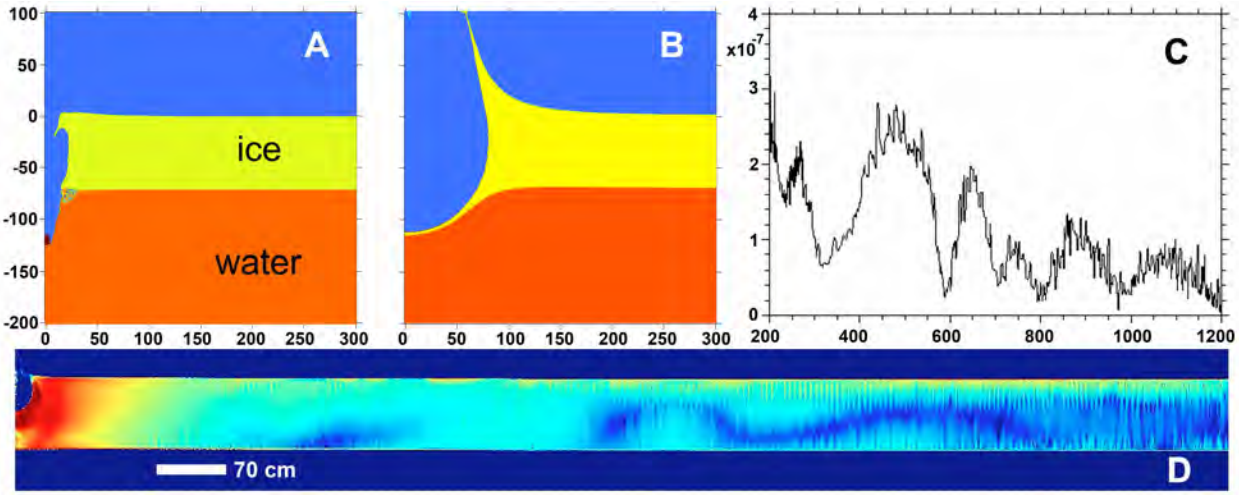

Fig. S54: A 2-D model of meteorites falling on ice (yellow) covering the lake water (orange). Vertical and horizontal scales are in cm, while the color scale depicts density, ranging from 0.0 to 1.0 g/cm^3 (blue to red). **(A)** 10 kg meteorite falling at 140 m/s; **(B)** A 100 kg meteorite falling at 600 m/s; **(C)** A 200 kg meteorite falling at 1,300 m/s, plot now showing the second invariant of the deviatoric stress tensor in the ice at 15 ms after contact, plotted in a linear scale ranging from 0 to 4.0 × 10^7 dyn/cm^2; **(D)** A color representation of the deviatoric stress tensor values in two dimensions as a slice through in the ice layer. Color scale is logarithmic, ranging from 1.0 × 10^6 (blue) to 3.0 × 10^9 dyn/cm^2 (red).

The 200 kg meteorite (Fig. S54C) impact shakes the ice out to at least 12 m from the impact site (edge of numerical grid), but these oscillations are insufficient to break the ice, which has a tensile strength of 3 × 10^9 dyn/cm^2. Because of the shaking, there is some cavitation occurring in the water below. These low-density voids limit the time step of the calculations, which made this a slow run. These pockets are small and ice breakup is not expected from these cavitations. Instead, this would result in some pock marking of the ice layer's bottom surface. Hence, inspection of the bottom ice surface may have revealed whether the impact energy was as high as the value assumed here.

The calculations suggest that the ice is so thick and cold that it would prove a robust shield preventing fragments of under 100 kg getting through. On the other hand, a large enough fragment (200-1,000 kg) could have made a hole in the ice.

4. Meteorite Characterization

4.1. Mechanical Properties

(Contributed by: V. Grokhovsky, S. Gladkovsky, P. Jenniskens, and D. Sears)

Mechanical properties of the Chelyabinsk meteorite were determined at NASA Ames, using a SouthWark-Emery Tensil Machine to measure the load at which small, uncut meteorites developed the first crack. Three meteorites broke at a load of 1.16 (C3), 1.11 (C4), and 0.49 kN (C5), respectively (Fig. S47). The effective surface area to which the pressure was applied was measured by placing aluminum foil between meteorite and press. From the smallest area of the indent on the top and bottom of the meteorite (measured: 0.027, 0.034, and 0.012 cm^2), the quasistatic compression strength is determined to be 330 MPa (C3: 4.46 g), 327 MPa (C4: 4.84 g) and 408 MPa (C5: 1.58 g), similar to other ordinary chondrites [100]. The uncertainty is mostly that in the surface area, nominally ~20%, but perhaps as high as a factor of two.

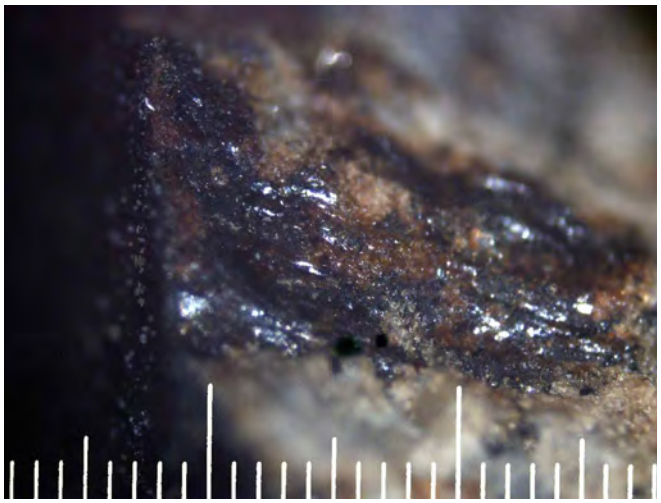

Fig. S55: Optical image of Chelyabinsk C4, broken along a shock vein that terminated at the fusion crust on the left. The shock vein surface is warped like that of a shatter cone. Scale bar is in mm (main markers: cm).

At the Ural Federal University (UrFU), compression strength measurements were made using the universal servo-hydraulic INSTRON 8801 tensil machine (grip displacement 0.5 mm/min) at room temperature. For this measurement, the meteorite was cut to have a squared area of approximately 10 × 10 mm and height 20 mm. Similarly cut Tsarev (type L5) meteorite samples [95] were used for comparison. The minimum rupture load for Tsarev samples was 16.26 kN, while Chelyabinsk samples broke at 6.18 kN. This translates to a compressive strength of 132.5 MPa for Tsarev and 64.0 MPa for Chelyabinsk. Literature values for Tsarev [101-103] are in the range 150-500 MPa (median value: 320 MPa). Hence, it is possible that this compression strength is underestimated by a

factor of 2-3 in both cases. Alternatively, the Chelyabinsk sample measured at UrFU was weaker than the Chelyabinsk meteorites measured at Ames due to fractures or other type of weakness along shock veins.

Meteorite C4 developed a crack along one of the shock veins (Fig. S55). This is a potentially important weakness in the structural strength of this particular ordinary chondrite that could have contributed to the manner of fragmentation during descent. The exposed surface of the shock vein, photographed at the CheMin laboratory at NASA Ames Research Center (Fig. S55), shows the same surface features as typically seen in shatter cones.

The melt in the cracks that underlay melt veins can act either to strengthen the material by welding clasts together, or leave clasts only weakly consolidated. Veins in the Chelyabinsk meteoroid were created by an impact event in space, probably the one that produced the brecciated structure of mildly shocked lighter clasts and moderately shocked darker clasts [17]. Moderate shocks can fracture the rock. Strong shocks can cause the melting of metal and sulfides, which are then pressure-driven through the cracked meteorite, increasing its mechanical strength, the residual heat facilitating the process. This can make the material harder than the original rock. In this case, however, the laboratory experiments suggest that the production of cracks weakened the meteorite more than shock melting increased its strength. Indeed, bolide observations show that there is no clear correlation between shock level (S1-S6) and fragmentation behavior in ordinary chondrite bolides [15].

4.2. X-ray Computed Tomography

(Contributions by: D. J. Rowland, J. Friedrich, Q.-Z. Yin, N. W. Botto, and S. Roeske)

A 0.53g fragment of Chelyabinsk, C3-3-4, was imaged at the Center for Molecular and Genomic Imaging at University of California (UC), Davis, for X-ray Computed Tomography (CT). X-ray tomographic images were obtained on the Center’s MicroXCT-200 specimen CT scanner (Xradia Inc.). The CT scanner has a variable X-ray source capable of a voltage range of 20-90kV with 1-8W of power. Samples were mounted on the scanners sample stage, which has submicron level of position adjustments. The sample was secured in place using a custom plastic holder such that the samples did not come in contact with any adhesive material. Scan parameters were adjusted based on the manufacturer's recommended guidelines. First, the source and detector

distances were adjusted based on sample size and the optimal field of view for the given region of interest. Once the source and detector settings were established, the optimal X-ray filtration was determined by selecting among one of 12 proprietary filters, in this case the Xradia LE5 filter was used. Following this procedure, the optimal voltage and power settings were determined for optimal contrast (85kV and 8W (94microAmp)).

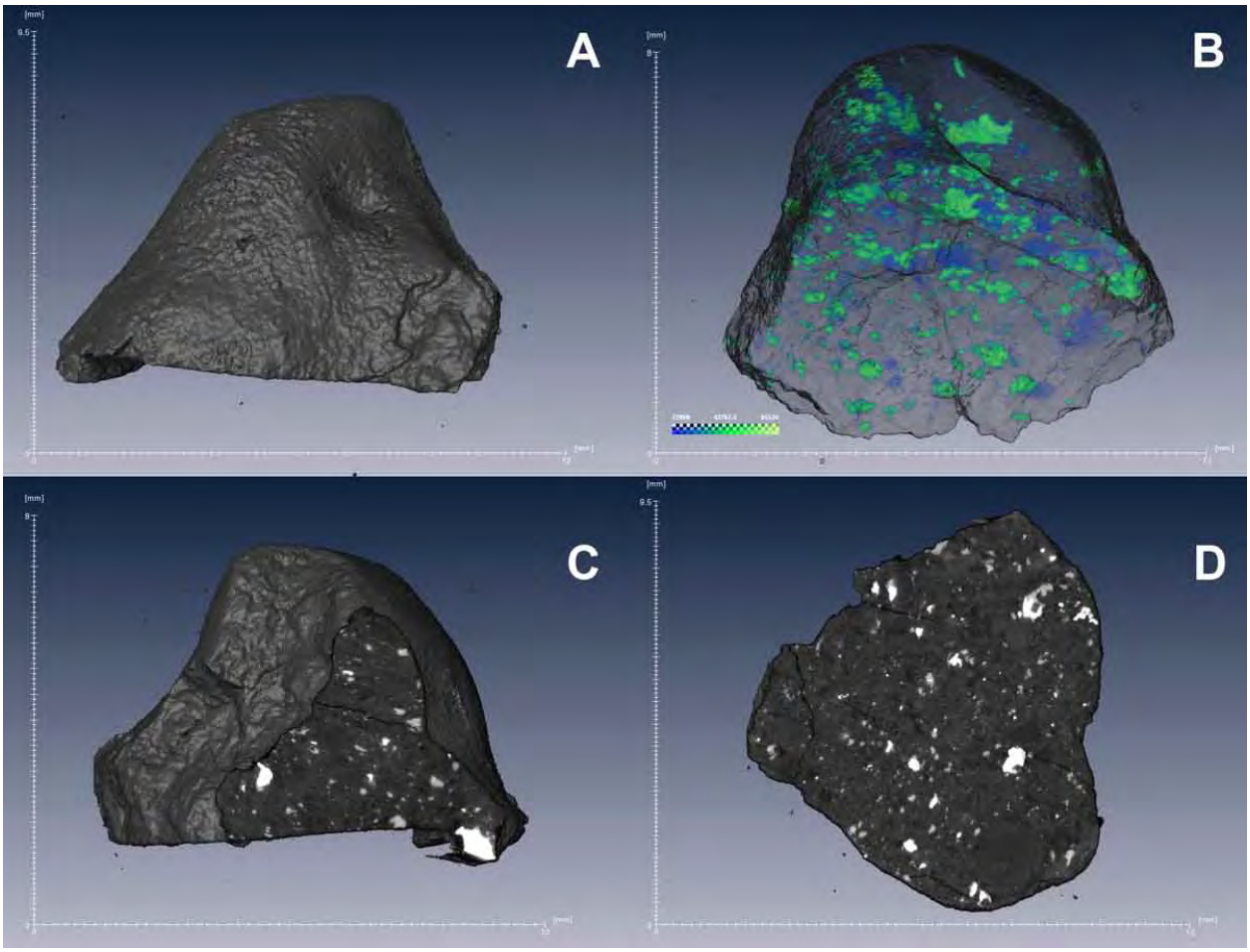

Fig. S56. X-ray CT imagery of Chelyabinsk, fragment C-3-3-4. **(A)** Surface shape model rendering of X-ray CT data showing external structure of the stone with fusion crust. **(B)** Shows a volume rendering of internal components. The internal components were rendered in a blue-green color scale with a threshold of 22000-65535 over the nominal full scale of 0-65535, thus making the surface and matrix materials transparent for the solid object imaged. The green components are FeNi and FeS and the light blue components are finely disseminated FeNi and FeSi grains intermingled with silicates. **(C)** Single slice view of the interior (1 of 1155 X-ray CT slices in this view direction with a pixel size of 5.4618 micron). **(D)** Full section of the X-ray CT image (one of 2600 scans with a pixel size of 5.4618 microns).

Table S16. X-ray CT imaging of Chelyabinsk (fragment C3-3-4). Sample mass, CT resolution, number of image stacks, measured volume, and computed density (g/cm3) are listed.

Scan ID	Mass (g)	Resolution (µm/vxl)	Tiles	Volume (cm3)	Density (g/cm3)	Lab
C3-3-4	0.53277	5.4618	1	0.16147	3.30	UCD-CMGI

A total of 2600 projections over 360 degrees were obtained with 8 seconds per projection. The camera pixels were not binned and the source-detector configuration resulted in a voxel size of 5.4618 micron. The tomographic image was reconstructed with a center shift (0.355 pixels) and beam hardening parameter value of 0.25 to obtain optimized images. A smoothing filter of kernel size 0.7 was applied during reconstruction. Images were reconstructed into 16-bit values.

With a precisely computed volume of 0.16147 cm^3 for the imaged fragment mass of 0.53277 gram, we obtain a bulk density of 3.30 g/cm^3 for Chelyabinsk (Table S16). This bulk density is in reasonable agreement when compared with the Consolmagno *et al.* [16] data for LL chondrites, which reports 3.22±0.22 g/cm^3.

Fig. S56 shows the exterior surface model of Chelyabinsk (C3-3-4) as determined by X-ray CT imaging (panel a), interior high atomic number (Z) elements shown in green (FeNi metal, FeS) and blue (silicates intermingled with finely disseminated FeNi and FeS grains) (panel b) as well as the slices of X-ray absorption maps (panels c, d). Fusion crust on the exterior, fractures and void spaces, and chondritic texture in the interior with abundant chondrules, metal and sulfide grains are obvious. Full X-ray CT data and 3D rendition of the fragment C3-3-4 are available as part of the Supplementary Materials (Movie S1) and from the UC Davis website at http://www.youtube.com/user/YinLabatUCDavis.

In addition to the 3D morphological description of chondritic components, we have used X-ray CT data to precisely quantify the fraction of Fe metal (1.11 ± 0.13%) and FeS (troilite, 4.54 ± 0.54%) in Chelyabinsk (C3-3-4), following methodologies described by Friedrich [104, 105]. A 2D X-ray map of K-alpha lines from the electron microprobe results (Fig. S64 below) gives a troilite fraction of 4.6%. While the troilite fractions for H, L, and LL chondrites do not vary significantly (Fig. S57A), the metal fractions vary significantly among the ordinary chondrite groups (Fig. S57B). Chelyabinsk's metal fraction of 1.11±0.13% is most consistent with those of the average LL chondrite group [106].

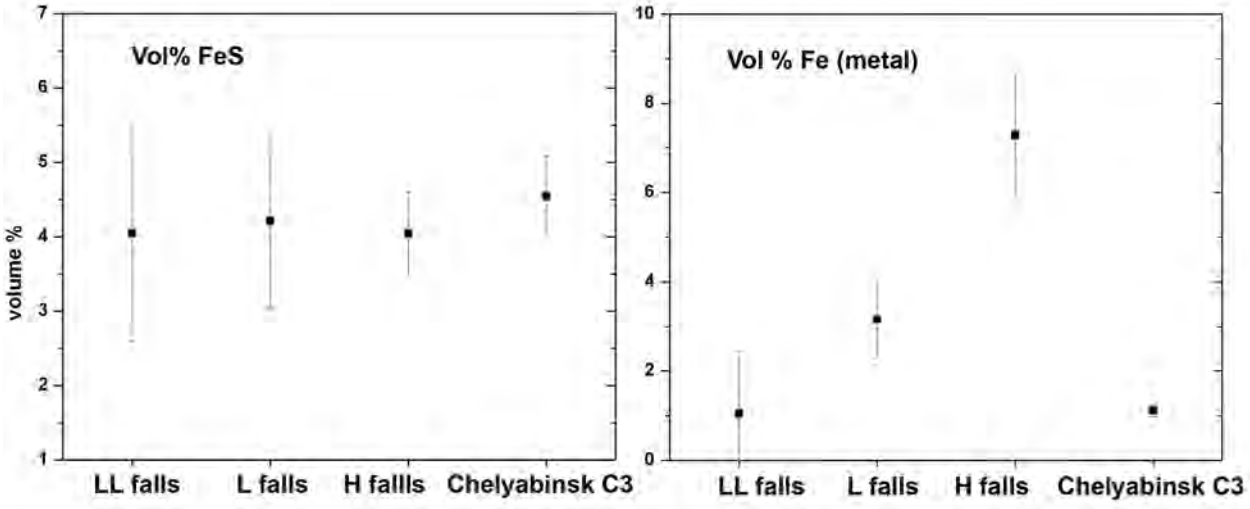

Fig. S57. (A) Troilite (FeS) and **(B)** metal fractions in Chelyabinsk deduced from the X-ray CT data of C-3-3-4. Data source for LL, L and H falls [106].

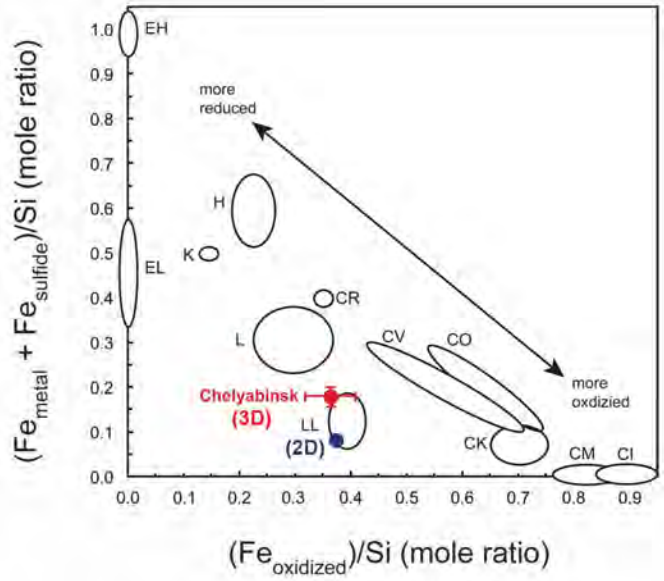

Fig. S58. Urey-Craig diagram [107] showing the position of Chelyabinsk relative to other major chondrite groups of relative iron contents and oxidation states of the chondritic groups, where iron present in metal and sulfide phases is plotted versus iron present in silicate and oxide phases, for bulk chondrite composition. Red point represents 3D data obtained from the X-ray CT, blue point represents K-alpha line X-ray map from a 2D section by electron microprobe. Bias between the 2D and 3D approaches are apparent. The plot is adapted and modified after Brearley and Jones [108] and Krot et al. [109].

The estimated metal and sulfide fraction shown in Fig. S57, together with whole rock major elemental composition of Fe and Si (see Section S4.5), allow the data to plot in the classic Urey-Craig diagram [107-109] for chondrite classification to delineate their respective oxidation states. As shown in Fig. S58, Chelyabinsk plots closest to the LL field.

Metal grain orientations

(Contributed by: J. Friedrich)

Nearly all chondrites have experienced several episodes of impact-related processing and Cheylabinsk is no exception. Cheylabinsk is a breccia consisting of at least two distinct light and dark lithologies. This brecciation is impact related: an impact into the Cheylabinsk parent body broke up the material and redeposited it. This material later experienced at least one significant consolidating shock event, which produced the current S4 shock stage and petrofabric alignment seen in the material.

Petrofabric investigations, including orientation and intensity of foliation, within the Chelyabinsk C3-3-4 stone was accomplished by methods found in Friedrich et al. [104-105, 110]. In short, metal grains within tomographic volumes are digitally isolated and best-fit ellipsoids are drawn around each. Orientation of the foliation can then be displayed by drawing a line through the long axis of each ellipsoid and collectively projecting points of intersection on a hypothetical sphere surrounding a sample on a stereoplot (Fig. S59).

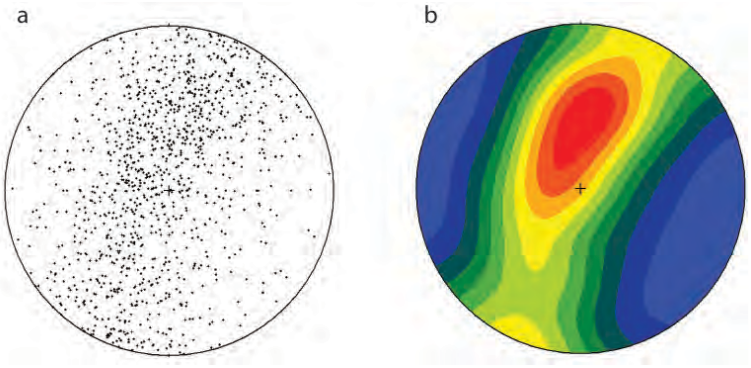

Fig. S59. (A) Equal area, lower hemisphere stereoplot of major axis orientation of all individual metal grains in the Chelyabinsk C3-3-4 stone. **(B)** Density distribution for the metal grain orientations. The petrofabric is the result of a significant impact or compaction event on the Chelyabinsk (LL) parent body sometime prior to atmospheric entry (see [105]).

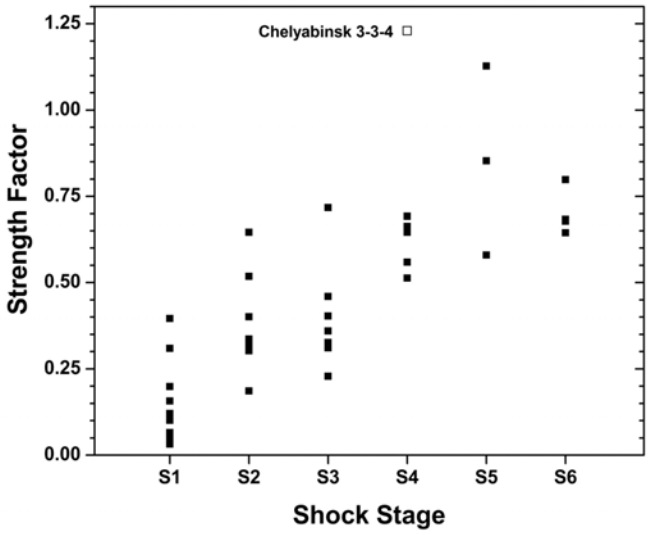

Fig. S60. Degree of compaction or collective preferred orientation of metal grains (given by the Strength Factor, C) versus shock stage in equilibrated ordinary chondrites.

Chelyabinsk has significant common orientation of metal grains indicating an extraordinary impact-related petrofabric in the analyzed sample (Fig. S59B). To obtain a quantitative value for the intensity of foliation, we used a variation of the orientation tensor method: the natural logarithm of the ratio of major over minor eigenvalues of the ellipsoids are computed to yield a strength factor C [111,112]. The higher the strength factor, the greater the common orientation of the metal grains in the sample and the greater the compaction/shock loading apparent in the material volume under investigation (Fig. S60). Strength of the petrofabric correlates well with degree of shock loading and related compaction.

The Chelyabinsk C3-3-4 sample has an exceptionally well developed petrofabric, stronger than those seen to date for ordinary chondrites of any shock stage (Fig. S60). Other data in Fig. S60 include results from LL, L, and H chondrites [105, 110]. The petrofabric reflects the most recent extraterrestrial shock event experienced by the Chelyabinsk sample. The degree of compaction is consistent with the lack of intragranular porosity present in X-ray microtomography volumes (Fig. S56 and [110]).

4.3. Magnetic Susceptibility and Paleomagnetic Signature
(Contributed by K.L. Verosub, Q.-Z. Yin, and M. Sanborn)

Magnetic susceptibility was measured with a Bartington MS-2 magnetic susceptibility meter using an MS-2B probe in the Department of Earth and Planetary Sciences at the UC Davis. Sample 3-3-4 had a magnetic susceptibility value of $\log^{10}\chi = 4.49$ (where χ is measured in units of 10^{-9} m^3/kg). Values of $\log^{10}\chi$ for all LL type meteorites range from about 3.5 to 4.7 with LL5 meteorites falling in the slightly narrower range of 3.7 to 4.6 [27, 113]. Thus Sample 3-3-4 falls at the upper end of the normal range for LL5 meteorites (Figure S61A).

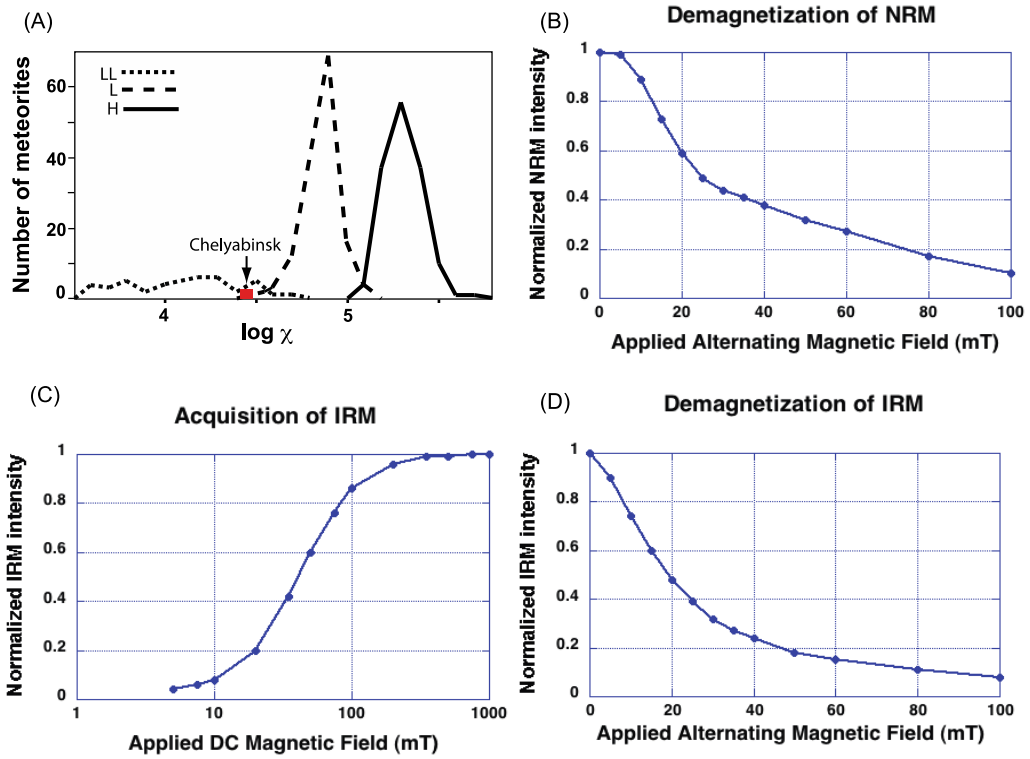

Fig. S61. (A) Magnetic susceptibilities of Chelyabinsk (C3-3-4) compared to those of ordinary chondrite groups [27,113]. **(B)** Alternating field demagnetization of natural remanent magnetization (NRM) of sample C3-3-4. The intensity of magnetization is normalized by the initial intensity of magnetization, which was 3.41×10^{-3} Am^2/kg. **(C)** Acquisition of isothermal remanent magnetization (IRM) in d.c. magnetic field. The intensity of magnetization is normalized by the final intensity of the IRM, which was 1.11×10^{-2} Am^2/kg. **(D)** Alternating field demagnetization of isothermal remanent magnetization (IRM). The intensity of magnetization is normalized by the intensity of magnetization achieved during the acquisition of the IRM.

Some other LL5 meteorites with high values of $\log^{10}\chi$ are Richmond (4.45), Aldsworth (4.54) and Paragould (4.54) [27,113]. Because LL5 meteorites have experienced some degree of thermal metamorphism, it is unlikely that magnetite is the primary magnetic mineral and hence it is not possible to estimate the iron concentration from the magnetic susceptibility.

The magnetization of Sample 3-3-4 was measured with a 2-G Enterprises Model 755 automated cryogenic magnetometer in the Paleomagnetism Laboratory at UC Davis. The sample responded well to progressive alternating field demagnetization of the natural remanent magnetization (NRM). The initial intensity was 3.41×10^{-3} Am^2/kg with a median destructive field of 25 mT (Figure S61B). The initial (arbitrary) direction of magnetization was I = -36° D = 314°, but during demagnetization the inclination moved smoothly to I = 43° while the declination remained unchanged, indicating the presence of two components of magnetization.

The sample was resistant to attempts to create a laboratory-induced anhysteretic remanent magnetization (ARM). The ARM experiment was done twice, and in both cases, there was only a modest (factor of 2) increase in the intensity of magnetization and almost no change in the magnetic direction. When subjected to alternating field demagnetization, ARM reverted back to the intensity observed at the end of the demagnetization of the NRM. This mode of behavior is unusual for terrestrial samples. One possible interpretation is that the thermal metamorphism that the sample experienced created an array of strongly-interacting magnetic grains. Studies of other meteorites have also found various types of anomalous ARM behavior [114].

An attempt to induce an isothermal remanent magnetization (IRM) in the sample using progressively higher d.c magnetic fields up to 1T was more successful. Most of the IRM was acquired with applied fields between 20 and 75 mT (Figure S61C). The saturation IRM was 1.11×10^{-2} Am^2/kg; the direction of the induced magnetization quickly became parallel to the applied field. Alternating field demagnetization of the IRM showed roughly the same behavior as demagnetization of the NRM (Figure S61D).

In some instances, the NRM and IRM demagnetization behavior of a meteorite can be used to estimate the magnetic field(s) in which the NRM was acquired. The basic principle of the method, known as REM′, is that one finds the demagnetization interval over which the NRM/IRM ratio is constant [115]. That ratio times 3000 gives the magnetic field intensity in μT. For Sample 3-3-4, the NRM/IRM ratio is essentially constant at 0.38 over the

demagnetization interval of 10 to 25 mT, which yields a magnetic field estimate of 1138 μT. However, the demagnetization interval corresponds to the interval over which one of the two components of the NRM was being removed, and hence may not be appropriate for the REM′ method. Over the demagnetization interval from 35 mT to 80 mT, the NRM/IRM ratio ranges from 0.47 to 0.56 with a mean of 0.52, which yields a magnetic field estimate of 1545 μT. Both of these estimates of the magnetic field are two orders of magnitude higher than magnetic field estimates obtained from other meteorites using the REM′ method. The most likely explanation for this result is that the conditions of entry into the Earth's atmosphere led to resetting of whatever previous remanent magnetization might have been present in the meteorite.

4.4. Petrography and Mineralogy

(Contributions by: M. Zolensky, Q.-Z. Yin, S. Roeske, N. W. Botto, Loan Le, Daniel Ross)

Electron microprobe studies of Chelyabinsk C3 and C4 at NASA Johnson Space Flight Center indicate that the petrography and mineral chemistry of Chelyabinsk is basically very similar to what was already reported by Nazarov *et al.* [18]. The meteorite is a breccia of less-shocked white clasts and moderately-shocked black clasts with abundant thin to cm-wide shock melt veins. Chondrules exhibit clear boundaries in some instances and in others are significantly recrystallized. Olivine exhibits mosaicism, planar deformation features, and local melting. There is no primary glass, having been devitrified to plagioclase (Ab79-85), which is partially isotropic. Accessory phases include troilite, diopside, endiopside, chromite and kamacite. Olivine and low-calcium pyroxene compositions average at Fa = 28.65 and Fs = 23.50, with percent mean deviations of 0.54 and 4.70%, respectively. Olivine contains up to 0.05wt% CaO, but is generally less than 0.02 wt%. These mineral compositional ranges are slightly larger than those reported by [18], but still compatible with a classification as LL5, shock stage S4 as discussed in the next section [19].

The shock melt veins (Fig. S62) show metal layers located about 20 micron inside the vein, but which follow the outer contours of the vein, shown as white in the BSE image of Fig. S62A, and clearly in the Fe and Ni maps. Metal veins also project outward from the vein. It appears that this layer is more Fe-rich, whereas the dispersed individual metal grains inside the vein are more Ni rich (Fig. 62D and F).

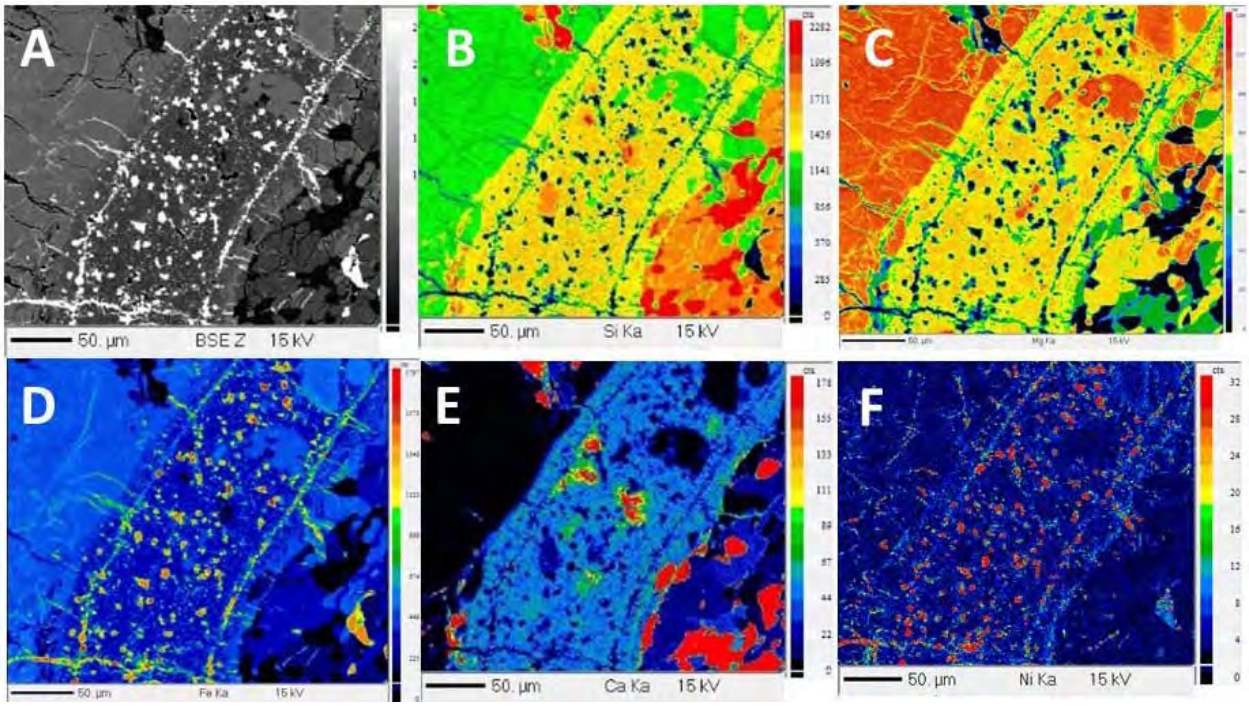

Fig. S62. A shock melt vein in Chelyabinsk. **(A)** Backscattered electron (BSE) image, **(B)** Si element map, **(C)** Mg element map, **(D)** Fe element map, **(E)** Ca element map, **(F)** Ni element map.

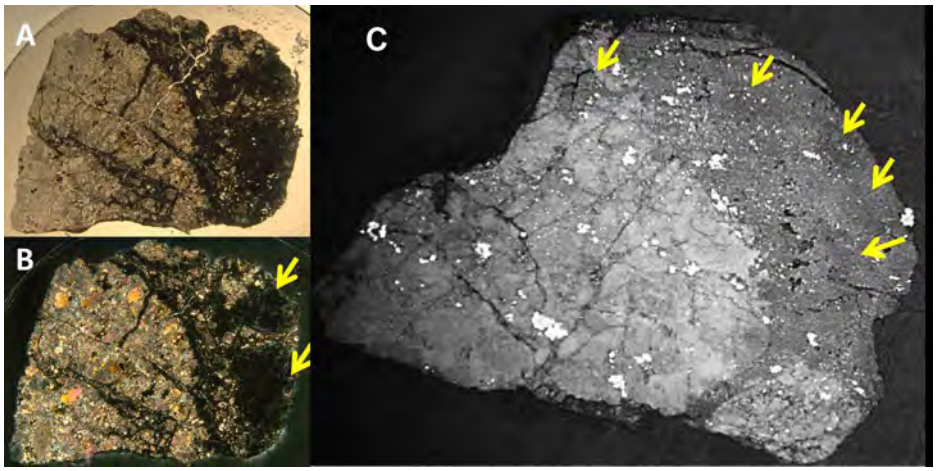

Fig S63. Chelyabinsk C4 in optical light: comparison on a thin section in **(A)** plane polarized light, and **(B)** crossed polars. The shock-darkened lithology is indicated by arrows. The section measures 1.5 cm across. **(C)** Light optical image of a polished surface, metal is white.

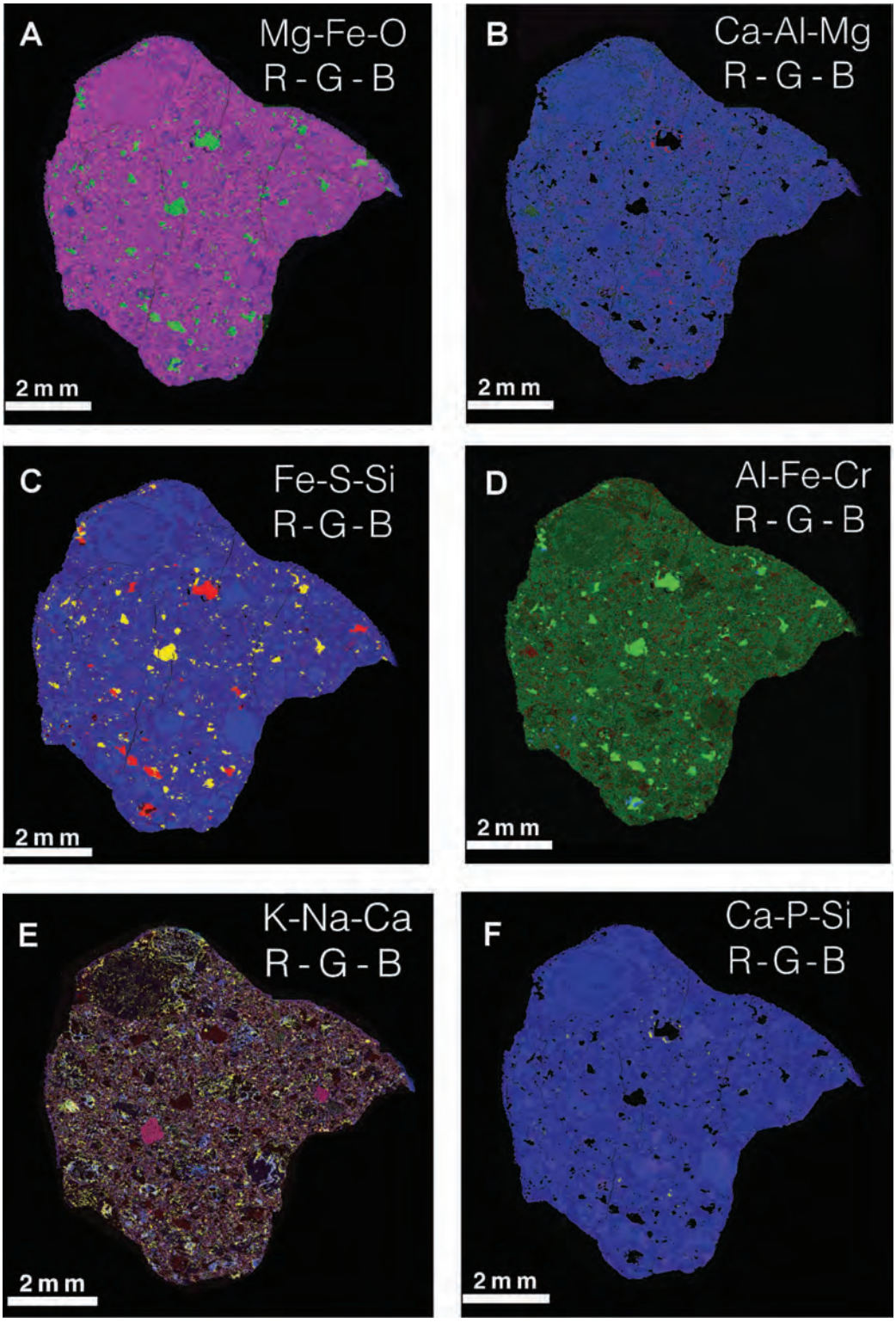

Figure S64. Three elements, false color composite images, arranged in red-green-blue sequence, for Chelyabinsk polished section C3-3-4a.

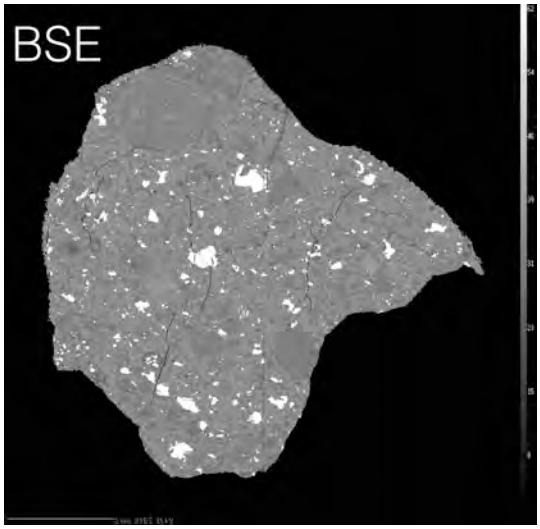

Fig. S65. Backscattered electron (BSE) mosaic map of Chelyabinsk C3-3-4a, showing many chondrules, including one bared olivine chondrule, metal and sulfide (troilite) grains, and fine grained matrix material.

The lower left 2/3 of the sample C4 is dominated by the white, less shocked lithology (Fig. S63). The upper right 1/3 consists of dark gray shock melt materials with black, highly-shocked pieces (Fig. 63C, arrowed).

At UC Davis, simultaneous elemental X-ray maps from the main characteristic peak (K-alpha) of major elements (O, Na, Mg, Al, Si, P, S, K, Ca, Ti, Cr, Mn, and Fe) (Fig. S64) and a high-resolution back-scattered electron (BSE) image (Fig. S65) were collected from a polished thin section of Chelyabinsk C3-3-2, and C3-3-4a, respectively. A Cameca SX-100 was used, a 5-spectrometer wavelength dispersive electron microscope, which is housed in the Department of Earth and Planetary Sciences. The instrument settings were 15 keV, 80 nA current, 5 micron wide beam. The resulting stage scan is a merged file of numerous ~ 1600 micron wide cells, with X-rays being recorded for 5 milliseconds every 4 microns as the stage moves. The false color imagery records increasing intensity of X-ray counts for each element. A series of three elements composite images (in RGB, i.e. red-green-blue sequence) are shown in Fig. S64 to highlight elemental and mineral compositions.

BSE imagery combined with energy-dispersive spectrum (EDS) shows that the major silicate phases in the sample are olivine, orthopyroxene, and plagioclase. The troilite (FeS) occurs both as coarse crystals and as very fine (<3 micron across) grains aligned within pyroxene and olivine. FeNi metal is variable in composition and locally contains minor Co. Minor phases include chromite, ilmenite, apatite, and an FeZnS compound.

Table S17A. Chemical composition (Wt%) of olivine in a polished section of Chelyabinsk C3-3-2. Trace elements are listed with the detection limits.

Comment	Mg	Si	Ca (120 ppm)	Mn	Fe	Ni (525 ppm)	Cr (170 ppm)	O	Total
olivine 1	21.19	17.49	0.011	0.32	20.38	0.013	0.011	39.83	99.25
olivine 2	21.57	17.63	0.015	0.36	20.45	0.007	0.018	40.27	100.32
olivine 3	21.33	17.44	0.025	0.35	20.32	0.021	0.002	39.86	99.35
olivine 6	21.51	17.55	0.038	0.35	20.15	-0.012	0.005	40.04	99.65
olivine 7	21.49	17.55	0.015	0.34	20.38	0.005	0.029	40.10	99.90
olivine 8	21.39	17.49	0.029	0.33	20.44	0.022	0.058	40.01	99.77
olivine 9	21.47	17.49	0.016	0.35	20.35	0.010	0.003	40.00	99.69
olivine 10	21.42	17.35	0.007	0.35	20.28	0.013	0.227	39.89	99.54
olivine 11	21.47	17.45	0.013	0.37	20.11	-0.009	0.027	39.90	99.34
olivine 12	21.39	17.49	0.013	0.37	20.34	-0.010	0.008	39.94	99.55

Olivine composition was determined quantitatively by wavelength dispersive analysis. Instrument set-up conditions were 15 keV, 30 nA current, 1 micron beam. Standards for the major elements are as follows: Si, Mg: Olivine 174.1, from lherzolite nodule, Kamooloa stream Kauai; Ni, Fe: synthetic olivine; Mn – Rhodonite. Ca – Cr-augite; Cr – Chromite. Ni is below the detection limit on all points. The data are presented in Table S17, from which we calculate average Fa = 29.2±0.3 for olivine (compared to Fa = 28.65 measured at NASA JSC). Fa of olivine vs. $\Delta^{17}O$ shows Chelyabinsk is an LL chondrite (Fig. 4D, main text).

Table S17B. Same in Wt% oxide.

Comment	MgO	CaO	MnO	FeO	NiO	Cr2O3	SiO2	Total
olivine 1	35.14	0.015	0.416	26.22	0.017	0.017	37.43	99.25
olivine 2	35.77	0.021	0.467	26.31	0.008	0.027	37.72	100.32
olivine 3	35.37	0.035	0.457	26.14	0.026	0.002	37.32	99.35
olivine 6	35.67	0.054	0.450	25.92	-0.015	0.007	37.54	99.65
olivine 7	35.63	0.021	0.437	26.22	0.006	0.042	37.55	99.90
olivine 8	35.48	0.041	0.425	26.30	0.027	0.085	37.42	99.77
olivine 9	35.61	0.022	0.448	26.18	0.013	0.004	37.42	99.69
olivine 10	35.52	0.010	0.454	26.09	0.016	0.332	37.13	99.54
olivine 11	35.61	0.019	0.481	25.87	-0.011	0.039	37.32	99.34
olivine 12	35.47	0.018	0.475	26.17	-0.012	0.011	37.41	99.55

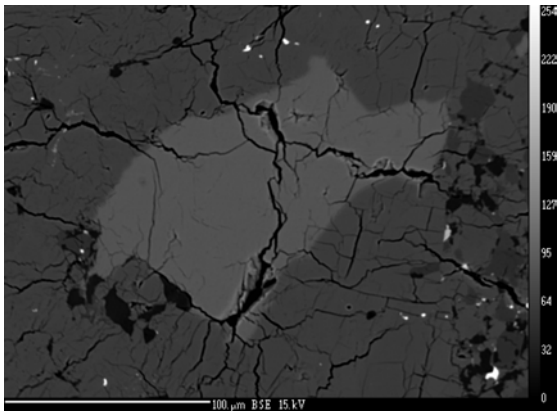

Fig. S66. Back-scattered electron image of apatite grain in Chelyabinsk C3-3-2 polished section.

The Ca-P-Si composite map (Fig. S64F) shows the locations of phosphate. The larger of these regions of P concentration were selected for imaging to document shape and size of the phosphate grains (Fig. S66) as target materials for U-Pb isotopic dating (see Section 4.8). The composition of the grains were confirmed with energy-dispersive spectrum (EDS), which show all of the possible major and minor elements in one display acquired over 5-second time intervals. Most that were imaged are Ca-phosphate with minor Mg. Some of the Ca-phosphate (assumed to be apatite) contains significant Cl (Cl-Apatite). Apatite, known to contain significant amount of U and Th, are suitable for in-situ U-Pb dating to determine its absolute age and thermal history of the Chelyabinsk parent asteroid (see Section 4.8).

4.5. Major, Minor, and Trace Element Analyses

(Contributed by: Q.-Z. Yin, J. Wimpenny, A. Yamakawa, and M. E. Sanborn)

Major, minor and trace element concentrations were determined using a high resolution magnetic sector inductively coupled plasma mass spectrometer (Thermo Fisher *Element XR* ICP-MS) at UC Davis. A sample slice (C3-3-1: 108.85 mg) was crushed by mortar and pestle to obtain a homogenized powder. An aliquot of the whole rock powder (35.95 mg) was dissolved by concentrated HF-HNO_3 mixture in Teflon Parr bomb and heated in the oven at 200°C for 60 hours to ensure complete dissolution of all refractory phases. Once dissolved, small aliquots of each sample were taken, weighed using a 5-digit balance, and diluted to factors of ~ 5000 and 500,000 for trace and major element analyses respectively. All samples were diluted using 2% twice distilled HNO_3. An internal standard comprising In, Re and Bi was added to each sample at a level of 10ppb in order to correct drift within each analytical session.

Samples were introduced to the *Element XR* using a dual cyclonic glass spray chamber and a Teflon nebulizer with a flow rate of 50µl/min. The system was initially tuned for maximum signal intensity using a 1 ppb solution of In, which gives a signal of ~1,000,000 cps at low resolution. The Element XR has a range of resolving capabilities; low resolution (m/Δm ~400), medium resolution (m/Δm ~4000) and high resolution (m/Δm ~10,000). Elements that have interferences at low resolution such as the transition elements and K can be analyzed using MR or HR in order to avoid isobaric interferences. Prior to the analyses mass calibrations were performed at each resolution, and the crossover threshold between counting, analogue and Faraday mode was also calibrated.

During each analytical session unknowns were calibrated using reference data for terrestrial standards. Five standards were used with a range of chemical compositions; two basalts (BCR-2 and BHVO-2); two andesites (AGV-2 and JA-1) and one peridotite standard (JP-1). The accuracy of our measurements were assessed by analyzing a series of well characterized meteorite samples (Allende CV3, Murchison CM2, Orgueil CI1, Tagish Lake and Lance CO3) and comparing our measured values with published data. In general our measurements reproduced published values for these meteorites to within ~5%. There are some exceptions to this and larger uncertainties are associated with Na, K, Sn, Cs and W measurements. Certain elements such as the PGE's could not be successfully calibrated using the terrestrial standards either because their concentrations in these standards are too low, or reference values are not well known. Instead, we used Allende, Murchison, Orgueil and Tagish Lake to calibrate these elements and treated Lance as an unknown to assess accuracy.

Table S18. Major, minor and trace element composition of the Chelyabinsk and other chondritic meteorites

	Units	Chelyabinsk	Allende		Murchison		Orgueil		Tagish Lake			Lance	
			Meas.	Ref.[a]	Meas.	Ref.[b,c]	Meas.	Ref.[d]	Meas.	Ref.[b,c]		Meas.	Ref.[e]
Li	ppm	1.60	1.44	1.89	1.58	1.50	1.47	1.47	1.28	1.20			
Be	ppm	0.039	0.046	0.030	0.040	0.040	0.036	0.025	0.030	0.052			
Mg	Wt%	15.96	14.44	14.77	11.81	11.50	9.29	9.58	10.60	10.80		14.12	14.10
Al	Wt%	1.18	1.72	1.70	1.09	1.13	0.80	0.85	0.95	0.99	**	1.31	1.42
P	Wt%	0.153	0.104	0.100	0.113	0.103	0.131	0.095	0.105	0.090		0.115	0.114
Ca	Wt%	1.70	1.78	1.86	1.28	1.29	0.98	0.92	1.25	0.98		1.86	1.64
Sc	ppm	9.54	11.73	11.50	8.24	8.20	5.96	5.90	6.84	7.20		10.69	9.36
Ti	Wt%	0.072	0.088	0.090	0.069	0.055	0.052	0.045	0.059	0.052		0.076	0.078

V	ppm	63.59	89.23	91.50	65.16	75.00	48.50	54.30	57.66	59.00		79.04	89.00
Cr	ppm	3482	3802	3626	3146	3050	2657	2650	2854	2840			
Mn	Wt%	0.300	0.143	0.155	0.176	0.165	0.183	0.193	0.164	0.153		0.17	0.15
Co	ppm	401.9	634.4	580.0	561.4	560.0	475.6	506.0	519.3	485.0			
Fe	Wt%	20.3	22.6	23.5	21.0	21.3	18.4	18.5	19.7	19.3	**	25.40	24.37
Ni	Wt%	1.17	1.31	1.270	1.21	1.230	1.00	1.080	1.15	1.110		1.38	1.40
Cu	ppm	73.9	113	120	133	130	133	131	125	120			
Zn	ppm	49.9	115	113	174	180	308	312	217	207			
Ga	ppm	4.52	5.77	5.40	7.56	7.60	9.55	9.80	7.97	8.40			
As	ppm	2.17	n/a	1.9	n/a	1.8	n/a	1.85	n/a	1.74	*	1.79	1.80
Se	ppm	9.47	n/a	10.5	n/a	12	n/a	21	n/a	14.3	*	7.87	7.50
Rb	ppm	2.90	1.25	1.29	1.64	1.60	2.37	2.31	1.80	1.55			
Sr	ppm	10.56	15.93	14.70	10.07	10.00	7.40	7.81	7.88	8.30			
Y	ppm	2.09	2.94	3.20	2.09	2.00	1.59	1.53	1.91	2.13			
Nb	ppm	0.362	0.574	0.559	0.398	0.400	0.296	0.279	0.348	0.410			
Ru	ppm	0.696	n/a	1.007	n/a	0.87	n/a	0.655	n/a	1.08	*	1.01	1.10
Sb	ppm	0.100	0.096	0.088	0.133	0.130	0.169	0.130	0.172	0.170			
Ba	ppm	3.41	n/a	4.00	n/a	3.10	2.56	2.46	2.98	2.77	*		
La	ppm	0.363	0.512	0.510	0.315	0.320	0.258	0.246	0.341	0.310			
Ce	ppm	0.947	1.280	1.330	0.818	0.940	0.659	0.600	0.872	0.745			
Pr	ppm	0.140	0.198	0.210	0.120	0.137	0.098	0.091	0.125	0.114			
Nd	ppm	0.697	1.012	1.009	0.612	0.626	0.501	0.464	0.622	0.531			
Sm	ppm	0.231	0.325	0.328	0.193	0.204	0.169	0.152	0.203	0.185			
Eu	ppm	0.081	0.103	0.113	0.072	0.078	0.058	0.058	0.073	0.066			
Gd	ppm	0.285	0.399	0.409	0.251	0.290	0.213	0.205	0.243	0.247			
Tb	ppm	0.058	0.075	0.081	0.050	0.051	0.041	0.038	0.049	0.048			
Dy	ppm	0.381	0.481	0.440	0.331	0.332	0.267	0.255	0.302	0.260			
Ho	ppm	0.083	0.096	0.113	0.068	0.077	0.054	0.057	0.067	0.066			
Er	ppm	0.242	0.294	0.300	0.213	0.221	0.167	0.163	0.201	0.188			
Tm	ppm	0.039	0.052	0.055	0.033	0.035	0.026	0.026	0.033	0.032			
Yb	ppm	0.258	0.308	0.300	0.223	0.215	0.172	0.169	0.211	0.185			
Lu	ppm	0.040	0.043	0.049	0.032	0.033	0.027	0.025	0.031	0.033			
Hf	ppm	0.154	0.203	0.197	0.148	0.180	0.106	0.106	0.135	0.134			
Ta	ppm	0.019	0.036	0.035	0.022	0.019	0.015	0.015	0.018	0.022			
Ir	ppm	0.417	n/a	0.684	n/a	0.58	n/a	0.435	n/a	0.547	*	0.663	0.720
Tl	ppm	0.002	0.054	0.053	0.081	0.092	0.116	0.142	0.109	0.090			
Pb	ppm	0.256	1.28	1.26	1.69	1.60	3.05	2.63	2.40	2.90			
Th	ppm	0.044	0.064	0.059	0.046	0.041	0.034	0.031	0.042	0.039			
U	ppm	0.014	0.017	0.015	0.012	0.012	0.009	0.008	0.011	0.009			

Notes: Major, minor and trace element concentrations in Chelyabinsk, alongside measured values for 5 previously characterized 'standard' meteorites with published values for comparison. Reference values have been taken from the following publications; [a]Jarosewich *et al.* [116], [b]Brown *et al.* [117],

[c]Friedrich *et al.* [118], [d]Lodders [119], and [e]Metbase [120]. Element concentrations are calculated by calibrating to a series of terrestrial standards; BCR-2, BHVO-2, AGV-2, JA-1 and JP-1. Elements marked * have been calibrated using the meteorites Allende, Murchison, Orgueil and Tagish Lake and consequently no concentration data can be provided for these meteorites. Accuracy of these analyses can be assessed by comparing our measured values with reference data for Lance. Elements marked ** have also been calibrated using the meteorites Allende, Murchison, Orgueil and Tagish Lake, however these meteorites were also separately measured as unknowns during the sample run and the results of these analyses are presented in italics for comparison with reference data.

4.6. Ultrahigh Precision Cr Isotope Analysis
(Contributed by: Q.-Z. Yin, , A. Yamakawa, and M. E. Sanborn)

A fragment of Chelyabinsk, C3-3, was sliced using a BUEHLER IsoMet Low Speed Saw and Diamond Wafering Blade. A sample slice (C3-3-1: 108.85 mg) was crushed using an agate mortar and pestle to obtain a homogenized powder. An aliquot of the homogenized whole rock powder (35.95 mg) was dissolved using concentrated HF-HNO_3 in a 3:1 mixture in Parr acid digestion vessel by heating in an oven at 200°C for 60 hours to ensure complete dissolution of all phases, including Cr-rich refractory phases such as spinel and chromite. The resulting clear sample solution was evaporated, dissolved in 6 M HCl, heated at 90 °C overnight and evaporated again. The sample was then re-dissolved in 6 M HCl and a 40 % aliquot of the dissolved sample was taken for Cr isotope measurements.

Following a three step column chemistry as described in Yamakawa *et al.* [121], the Cr isotope ratios were measured using ThermoFisher *TRITON-Plus* at the Department of Earth and Planetary Sciences at UC Davis. The purified Cr fraction collected after the column chemistry separation procedure was mixed with a silica gel-boric acid-Al type activator and loaded onto a single outgassed W filament. The Cr fraction was split among four filaments with equal loading amounts (i.e., 3 µg Cr per filament). Standard filaments, with Cr standard SRM 979, were analyzed both before and after the four filaments with the sample. The instrumental mass fractionation effect was corrected according to an exponential law using a $^{50}Cr/^{52}Cr$ ratio = 0.051859 [122]. Interferences on ^{50}Cr and ^{54}Cr from ^{50}V and ^{54}Fe, respectively, were corrected by monitoring ^{51}V and ^{56}Fe. The beam intensity of ^{52}Cr was set at 1×10^{-10} A (± 15 %). A gain calibration was performed before each analysis. Each filament measurement consisted of 48

blocks of 25 cycles (8 s integration time per cycle) for a total of 1200 ratios per filament. A 60 s baseline was measured and the amplifiers were rotated at the beginning of each block.

Table S19. Cr isotopic data of Chelyabinsk from this study. For comparison, the ε^{53}Cr and ε^{54}Cr data for other ordinary chondrites from literature [21,123] are also shown in this table.

	ε^{53}Cr	ε^{54}Cr
Chelyabinsk	0.23 ± 0.03	-0.38 ± 0.08
Ste.-Marguerite (H4)	0.13 ± 0.06	-0.39 ± 0.07
Knyahinya (L5)	0.15 ± 0.06	-0.38 ± 0.08
Chainpur (LL3.4)	0.24 ± 0.06	-0.47 ± 0.07
Olivenza (LL5)	0.23 ± 0.06	no data
St-Séverin (LL6)	0.28 ± 0.06	-0.41 ± 0.10

ε^{53}Cr and ε^{54}Cr values of the sample were calculated relative to the Cr standards, defined as $\varepsilon^{53,54}\text{Cr} = [(^{53,54}\text{Cr}/^{52}\text{Cr})_{\text{sample}}/(^{53,54}\text{Cr}/^{52}\text{Cr})_{\text{standard}} -1] \times 10^4$. Our result shows both ε^{53}Cr and ε^{54}Cr values of Chelyabinsk are identical within error to those of other LL chondrites (Table S19 and Fig. S67). ε^{54}Cr values are becoming an increasingly useful tool to identify meteorite groups and provenances (e.g. [21, 124]). Here we show that Chelyabinsk (ε^{54}Cr = -0.38 ± 0.08) is identical to those of other ordinary chondrites (~-0.4), suggesting that Chelyabinsk is derived from the precursor material in the solar nebula where LL type ordinary chondrites formed.

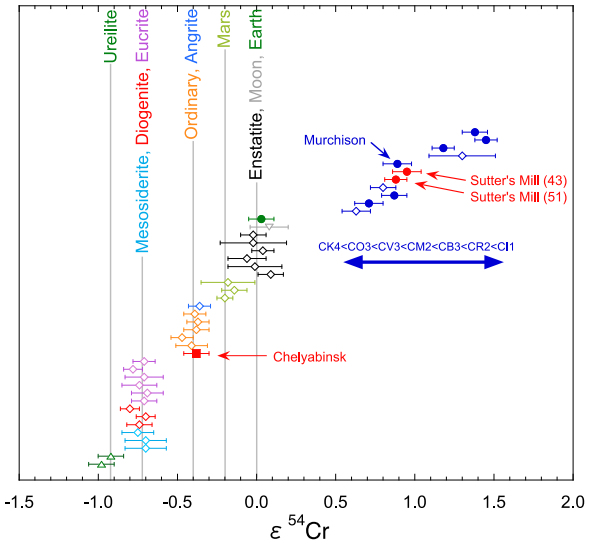

Fig. S67. Variation of ε^{54}Cr values among various terrestrial and extraterrestrial materials. Our ε^{54}Cr data of Chelyabinsk is identical to those of reported values for ordinary chondrites. Filled symbols represent data acquired at University of California, Davis (two data points for Sutter's Mill are reported in Jenniskens *et al.* [1]). The ε^{54}Cr data of Earth and Moon are represented by JP-1 and 70017, respectively. Open symbols are literature data: diamonds, inverted triangle and regular triangles from Trinquier *et al.* [21], Qin *et al.* [125], and Yamakawa *et al.* [126], respectively.

4.7. Oxygen Isotope Analyses

(Contributed by: K. Ziegler, T. Nakamura, I. Ahn, J. I. Lee, Q.-Z. Yin, M. E. Sanborn, and A. Yamakawa)

Bulk oxygen isotope compositions of many ordinary chondrites are summarized and reported by Clayton *et al.* [20]. The three ordinary chondrite groups have oxygen isotope compositions that fall in similar ranges but are resolvable from each other. Thus, the measurement of oxygen isotope ratios is a useful tool to identify different ordinary chondrite groups.

Four Chelyabinsk meteorites, an 0.6 g sample C3-3 (Fig. S47) provided by Chelyabinsk State University to the Consortium, TJI (~1g) acquired by Korea Polar Research Institute, and Samples 001 and 002 (~0.5 g) provided to the University of New Mexico, were gently crushed with mortar and pestle. Fresh fragments of interior materials were selected under a stereoscopic microscope to avoid any possible contamination from fusion crust. Oxygen isotope analyses were performed using the CO_2 laser-based BrF_5 fluorination system following procedures of Ahn *et al.* [127] at the Korea Polar Research Institute (KOPRI), Korea, and following modified procedures of Sharp [128] at the Institute of Meteoritics (IOM) at the University of New Mexico in Albuquerque, U.S.A.

Table S20. Oxygen isotope compositions of Chelyabinsk bulk rock samples.*

Stone	Mass (mg)	$\delta^{17}O'$ (‰)	$\delta^{18}O'$ (‰)	$\Delta^{17}O'$ (‰)	Lithology	Laboratory
TJI	2.87	3.89 ± 0.01	5.05 ± 0.01	1.22 ± 0.01	light	KOPRI
TJI	1.85	3.84 ± 0.01	4.79 ± 0.01	1.31 ± 0.01	light	KOPRI
TJI	2.04	3.76 ± 0.01	4.69 ± 0.01	1.28 ± 0.01	light	KOPRI
001-A	1.0	3.62 ± 0.01	4.67 ± 0.01	1.15 ± 0.01	grey	IOM
002-A	1.1	3.77 ± 0.01	4.99 ± 0.01	1.14 ± 0.01	grey	IOM
002-B	1.4	3.73 ± 0.01	4.86 ± 0.01	1.17 ± 0.01	melt	IOM
C3-3-3	1.0	3.89 ± 0.03	5.03 ± 0.01	1.23 ± 0.03	greyish	IOM
C3-3-3	1.2	3.53 ± 0.01	4.76 ± 0.01	1.02 ± 0.02	greyish	IOM
C3-3-3	1.3	3.58 ± 0.02	4.58 ± 0.01	1.16 ± 0.02	greyish	IOM
C3-3-3	1.8	3.67 ± 0.01	4.40 ± 0.01	1.13 ± 0.01	greyish	IOM
C3-3-3	1.8	3.62 ± 0.01	4.63 ± 0.01	1.17 ± 0.01	greyish	IOM

*) The analytical uncertainty is the 1-standard-error obtained by 20 cycles of sample-standard comparison in the mass spectrometer.

Oxygen isotopic ratios were calculated using the following procedure: the $\delta^{17,18}O$ values refer to the per-mil deviation of a sample's ($^{17}O/^{16}O$) and ($^{18}O/^{16}O$) ratios from the V-SMOW standard values, expressed as $\delta^{17,18}O = [(^{17,18}O/^{16}O)_{sample}/(^{17,18}O/^{16}O)_{V\text{-}SMOW} - 1] * 10^3$. The delta-values were then converted to linearized values by calculating: $\delta^{17,18}O' = \ln[(\delta^{17,18}O + 10^3)/10^3] * 10^3$ in order to create a straight mass-fractionation line in the three oxygen isotope plot such as Fig. S68 (A). The $\Delta^{17}O'$ values were obtained from the linear δ values by the following relationship: $\Delta^{17}O' = \delta^{17}O' - 0.528 * \delta^{18}O'$. $\Delta^{17}O'$ values of zero define the terrestrial mass-fractionation line, and $\Delta^{17}O'$ values deviating from zero indicate mass-independent isotope fractionation. Typical analytical precision of the laser-fluorination technique is better than ± 0.02‰ for $\Delta^{17}O'$.

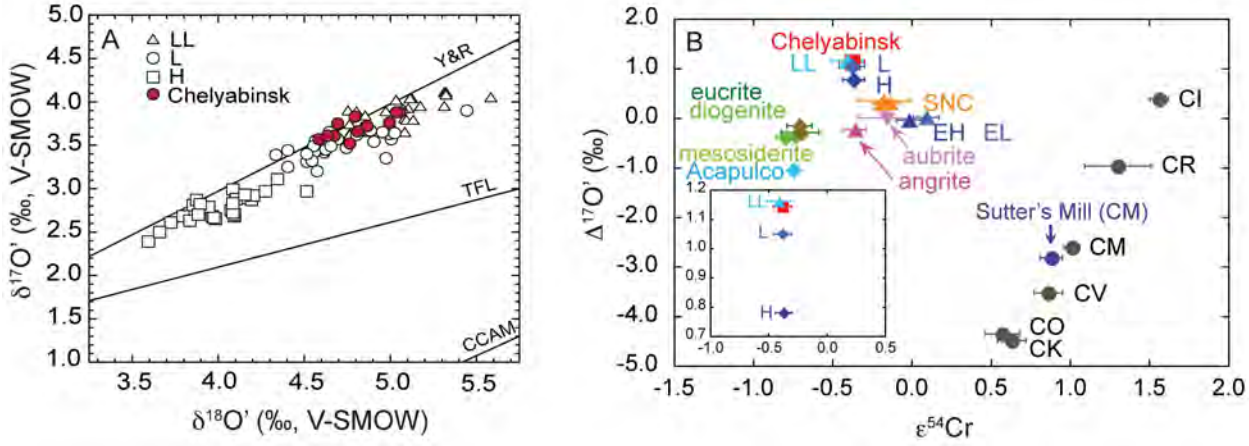

Fig. S68. (A) Oxygen isotope diagram, plotting Chelyabinsk (red circles) and H, L and LL chondrites [20]. TFL refers to terrestrial fractionation line as defined above. CCAM refers to carbonaceous chondrite anhydrous mineral line [129]; Y&R refers to a line defined by unaltered minerals from CAIs in Young and Russell [130]. V-SMOW: Vienna standard mean ocean water. Note the different scales on x- and y-axis. **(B)** $\varepsilon^{54}Cr$ versus $\Delta^{17}O'$ in Chelyabinsk (red square), compared to the other major meteorite groups. Data sources for $\Delta^{17}O'$ and $\varepsilon^{54}Cr$ data of chondrites and achondrites are from [1, 20-21, 129-134].

A total of eleven interior chips of Chelaybinsk were analysed (Table S20 and Fig. S68). The TJI sample is from the light lithology. Samples 001-A and 002-A are from the light grey coloured host chondrite with abundant relict chondrules and recrystallized matrix; it also contains metal and sulfide, and is highly shocked and invaded with sulfide-rich impact melt veins. Sample 002-B is dark grey/black impact melt material, consisting of a matrix that is quenched silicate melt, including finely disseminated sulfides. Abundant partly resorbed grains

derived from the chondrite host are entrained in this melt material. Sample C3-3-3 is from a greyish lithology with small spots of light lithology, and is from the same stone (C3-3) that was analyzed for its Cr-isotopes in the previous section.

The results show that all eleven data fall in the oxygen 3-isotope space occupied by the equilibrated LL-group meteorites (≥ petrologic type 4) reported by Clayton *et al.* [20] (Fig. S68). The Chelyabinsk mean value of 1.18 ± 0.02‰ (1 sigma standard deviation) for $\Delta^{17}O$ also agrees well with literature data of LL chondrites that range from 0.97‰ to 1.44‰ with a mean $\Delta^{17}O$ = 1.24 ± 0.13‰ [20].

These results indicate that Chelyabinsk is heterogeneous both on a large (different stones) and a small (different C3-3-3 aliquots) scale in terms of oxygen isotopes. There are two possible reasons for this variation: (1) the oxygen isotopes are not fully equilibrated in spite of thermal metamorphism typical for LL5 meteorites, or (2) the oxygen isotopes are equilibrated, but the mineral abundances of the eight 1-3 mg chips analyzed are not the same. The variation seen in the Chelyabinsk data is common for ordinary L and LL chondrites with petrologic types 4 and 5.

4.8. U-Pb Age

(Contributed by: Q-Z. Yin, Q. Zhou, X-H. Li, Q-L. Li, Y. Liu, and G.-Q. Tang)

Prior to in-situ U-Pb analyses, a thin section of the Chelyabinsk meteorite was imaged with JEOL JXA-8100 electron probe at the Institute of Geology and Geophysics, Chinese Academy of Sciences (IGG-CAS) in Beijing. The electron microprobe was equipped with an energy dispersive spectrometer (EDS) to identify phosphate grains and select suitable analytical spots, i.e., to avoid micro-fractures, inclusions and other observed physical defects in the individual phosphate grains (Fig. S69). For more details see Section 4.4.

In-situ isotopic analysis of the U-Pb system was performed on a large radius magnetic sector multi-collector Cameca IMS-1280 ion microprobe at the Institute of Geology and Geophysics, Chinese Academy of Sciences (IGGCAS) in Beijing. Samples were carbon-coated prior to SIMS analysis. The detailed analytical procedure for U-Pb dating of phosphate grains can be found in Li *et al.* [135] and a brief introduction is given here. The O_2^- primary ion beam was accelerated at -13kV, with an intensity ranging between 7 and 9 nA. The aperture illumination mode (Kohler illumination) was used with a 200μm diameter aperture, resulting an ellipsoidal spot size of 20 × 30 μm. Positive secondary ions were extracted with a 10 kV potential. A single ion-counting

electron multiplier (EM) was used as the detection device to measure secondary ion beam intensities of $^{204}Pb^{+}$, $^{206}Pb^{+}$, $^{207}Pb^{+}$, $^{208}Pb^{+}$, $^{232}Th^{+}$, $^{238}U^{+}$, $^{232}Th^{16}O^{+}$, $^{238}U^{16}O^{+}$, $^{238}U^{16}O_2^{+}$ and a matrix reference peak of $^{40}Ca_2{}^{31}P^{16}O_3^{+}$ at a mass resolution of ~9,000 (defined at 50% height). The $^{40}Ca_2{}^{31}P^{16}O_3^{+}$ signal was used as reference peak for tuning the secondary ions, energy and mass adjustments.

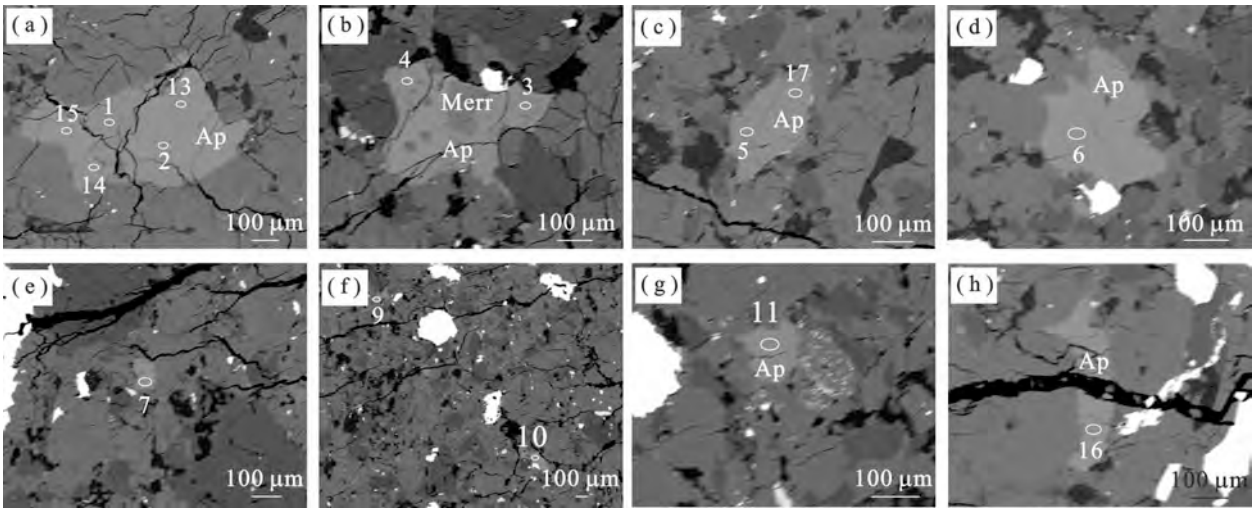

Fig. S69. Apatite grains found in Chelyabinsk (section C3-3-2). Ovals indicate analyzed spots by Cameca IMS-1280. Numbers indicate the corresponding data in Table S21.

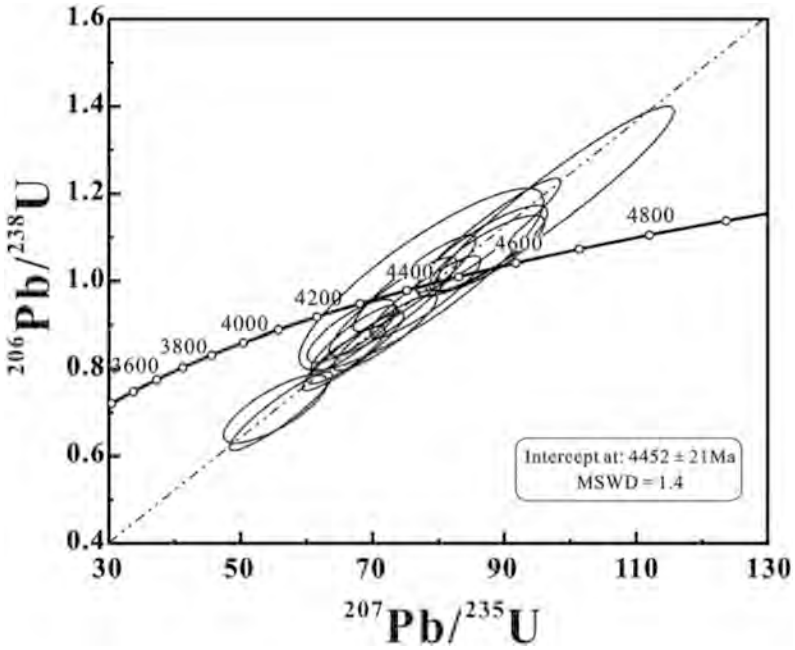

Fig. S70. U-Pb Concordia plot for Chelyabinsk apatite grains (Table S21). The upper intercept age is 4,452±21 Ma with a mean-square weighted deviates (MSWD)=1.4.

Pb/U ratios (Fig. S70) were calibrated with power law relationship between Pb/U and UO_2/U relative to an apatite standard of NW-1 (1,160 Ma) that comes from the same complex of Prairie Lake as that of the Sano *et al.* [136] apatite standard (PRAP). U concentration is calibrated relative to the Durango apatite which has U ~9 ppm [137]. The standard deviation of the measured $^{206}Pb/^{238}U$ ratios in the standard was propagated into the unknown samples, in this case the Chelyabinsk sample. Each measurement consisted of 10 cycles, with the total analytical time of about 12 minutes. Correction for common Pb was made by measuring the amount of ^{204}Pb and the CDT Pb isotopic compositions [138]. The uncertainties for individual analyses are reported as 1σ. The weighted average of $^{206}Pb^*/^{238}U$ and Pb-Pb ages, quoted at the 95% confidence level, was calculated using ISOPLOT 3.0 [139].

Table S21. SIMS U-Pb isotopic data of apatite from Chelyabinsk.

Spot	U (ppm)	Th (ppm)	Th/U	$^{207}Pb^*/^{206}Pb^*$	±1σ (%)	$^{207}Pb^*/^{235}U$	±1σ (%)	$^{206}Pb^*/^{238}U$	±1σ (%)	$t_{207/206}$ (Ma)	±1σ	$t_{207/235}$ (Ma)	±1σ	$t_{206/238}$ (Ma)	±1σ
1	5.4	5.6	1.03	0.5795	1.79	67.1	4.7	0.840	4.34	4457	26	4286	32	3930	77
2	6.9	6.9	1.00	0.5459	2.42	66.7	4.1	0.887	3.29	4370	35	4281	33	4092	65
3	5.6	4.6	0.82	0.5609	1.78	67.2	4.0	0.869	3.57	4410	26	4288	29	4033	68
4	6.2	5.2	0.84	0.5965	2.29	87.4	4.1	1.063	3.37	4499	33	4551	37	4669	92
5	7.0	9.0	1.29	0.5871	1.94	78.1	4.4	0.964	3.95	4476	28	4438	30	4353	71
6	5.6	4.5	0.81	0.5570	2.11	76.4	5.0	0.995	4.53	4400	30	4416	30	4453	66
7	4.4	3.2	0.73	0.5877	2.48	86.7	4.7	1.070	3.99	4478	36	4542	35	4689	77
9	4.7	5.6	1.21	0.5948	2.39	97.6	7.6	1.190	7.25	4495	34	4662	34	5053	79
10	3.9	3.2	0.83	0.5625	2.38	73.1	5.4	0.942	4.88	4414	34	4372	32	4280	64
11	5.2	4.9	0.95	0.5747	1.76	87.6	5.1	1.106	4.82	4445	25	4553	39	4800	114
13	6.7	6.5	0.97	0.5660	3.68	55.3	5.8	0.708	4.54	4423	53	4092	42	3452	52
14	7.2	7.2	1.00	0.5789	2.24	56.1	5.7	0.703	5.26	4456	32	4107	30	3432	51
15	8.3	7.9	0.94	0.5758	1.80	66.0	3.7	0.831	3.21	4448	26	4269	27	3900	59
16	1.7	2.3	1.35	0.5589	4.97	77.4	9.8	1.005	8.45	4405	71	4429	55	4484	63
17	7.6	10.1	1.32	0.5909	2.00	71.9	4.5	0.883	4.01	4486	29	4355	28	4079	59

* denotes radiogenic, using the modern terrestrial Pb as common-lead compositions ($^{206}Pb/^{204}Pb$ =18.703, $^{207}Pb/^{206}Pb$ = 0.836, Stacey and Kramers, 1975);

To test and verify the reliability of the developed phosphate dating technique, two additional meteorites, a primitive achondrite Acapulco obtained from Dr. K. Marti and angrite NWA 4590 provided by Dr. Y. Amelin, were also selected for this study as both have precisely known phosphate U-Pb ages by TIMS [23, 140]. Both meteorites are from very fast cooled parent bodies with no sign of resetting [23, 140], ideal for precise age dating.

Seventy-three measurements of Pb-Pb isotope composition were obtained on apatite grains in Acapulco. The weighted mean of $^{207}Pb/^{206}Pb$ ratios is 0.620 ± 0.002, translating to a Pb-Pb age of

4,555.4 ± 5.2 Ma (uncertainties are reported at 95% confidence level, with a student t-factor applied for the number of repeat analyses), assuming a primordial Pb composition for the initial Pb [138]. The results from our study are consistent with the TIMS results (4,556.5 ± 1.3 Ma, [23]).

Eighteen Pb-Pb isotope measurements were obtained on silico-apatite grains [140,141] and one on a merrillite grain in angrite NWA 4590. There is no significant difference between the age of silico-apatite and merrillite. The weighted mean of $^{207}Pb/^{206}Pb$ for silico-apatite and merrillite is 0.620 ± 0.002, translating to a Pb-Pb age of 4,556.6 ± 4.6 Ma (uncertainties are reported at 95% confidence level). The common lead of the phosphate in this sample is extremely low and $^{204}Pb/^{206}Pb$ ratio is nearly zero. The results from our study are consistent with the TIMS result (4,557.381 ± 0.066 Ma [140]).

After these vigorous tests of our methodology, exactly 17 apatite spots were analyzed from the Chelyabinsk section C3-3-2 for U-Pb isotope composition. The results are listed in Table S21, and the data are plotted in the classic Wetherill type U-Pb Concordia diagram (Fig. S70). The upper intercept age of Chelyabinsk apatite is found to be 4452±21 Ma, using ISOPLOT 3.0 [139]. There are a few smaller merrillite grains, however, the U contents were found to be too low to yield useful data. Results from individual spot measurements for Chelyabinsk apatites are summarized in Fig. S70.

The upper intercept age of 4,452±21 Ma is much younger than phosphate ages from other ordinary chondrites phosphate ages dated by conventional TIMS methods [22,23,142]. We note that no ordinary chondrites, including H, L and LL chondrites reported by these workers, have apatite U-Pb ages younger than 4.51 Ga. The only exception, to our knowledge, is a recent work by Tereda and Bischoff [24] who reported a Pb-Pb isochron age of 4.48±0.12 Ga Pb-Pb for phosphate in a granite-like fragment found in a LL3-6 ordinary chondrite regolith breccia Adzhi-Bogdo. This was performed using the SHRIMP ion probe technique, a similar SIMS technique to that used here for Chelyabinsk. We have no reason to believe the SIMS and TIMS technique would provide a systematic bias in the U-Pb ages. Our results suggest that the Chelyabinsk parent body must have experienced a significant thermal and/or collision resetting event 115±21 Ma after formation of the oldest Calcium Aluminum rich inclusions in meteorites [25]. This may indicate a prolonged thermal cooling history of the Chelyabinsk parent body or,

perhaps more likely, a more recent impact related disturbance on the LL parent body in a different area than sampled by most other LL ordinary chondrites.

4.9. Reflection Spectroscopy

(Contributed by: T. Hiroi)

Figure S71 shows the bidirectional visible-Near IR and biconical FT-IR reflectance spectra measured at the Reflectance Experiment Laboratory at Brown University. Spectra are shown for the exposed interior surfaces of two chips of C3 (a light lithology) and the shock darkened C6 [143]. From these same samples, powders of grain size < 125 μm were prepared after removing a surface layer. The resulting material looked fresh, but did show stronger atmospheric water bands due to a damper environment in the spectrograph. Those residual bands were removed.

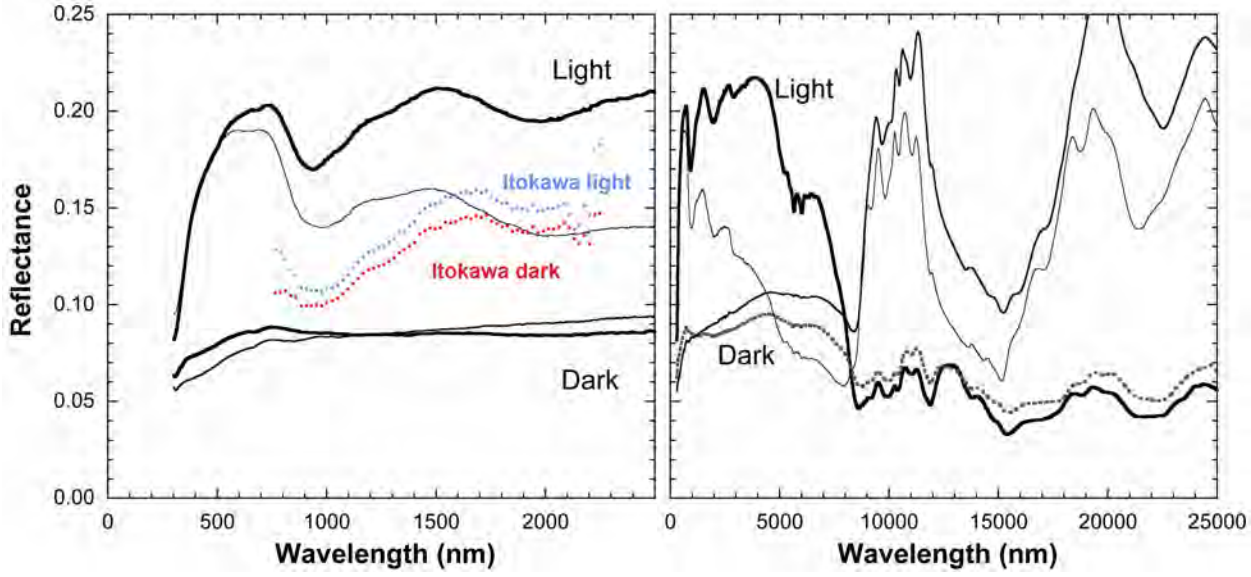

Fig. S71. Reflection spectra of powder (thick line) and exposed surfaces (thin line) measured over the 0.3 to 2.5 μm wavelength range (left) and the 0.3 to 25 μm range (right), for both light (C3, top two curves) and dark lithologies (C6, bottom two curves) of the Chelyabinsk meteorite. In color are shown the reflectance spectra of light and dark lithologies on Itokawa [144].

Fig. S72 shows the continuum-removed natural log spectral plot of the C3-1 powder sample, compared to powder samples of representative ordinary chondrites of H, L, and LL type. The chip shows a similar band shape, but not shown here as the comparison spectra are for powder samples. In detail, the light chip (C3-1) has a 0.8-1.2 micron reflectance shaped like that of H

chondrites, not LL chondrites. It is possible that this represents heterogeneity in the sample, C3-1 being richer in pyroxene than the bulk rock Chelyabinsk. The reflectance spectrum over this wavelength range is mostly dependent on the olivine/pyroxene ratio of this particular specimen. In detail, the band shape also depends on the Fe/Mg ratio and crystal size.

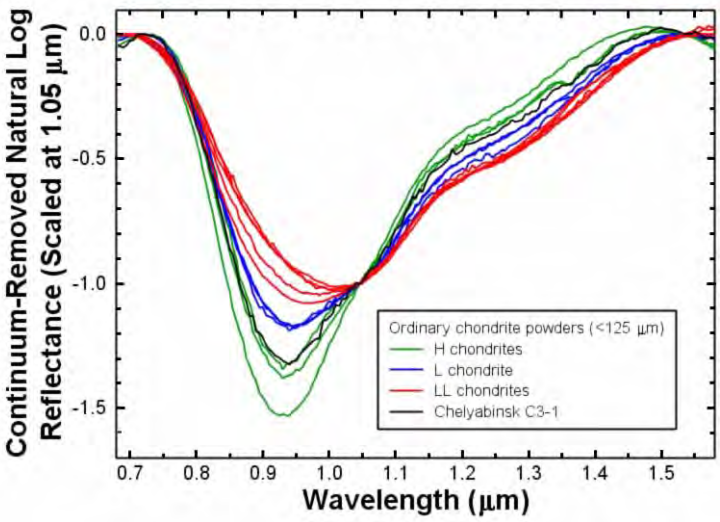

Fig. S72. Continuum-removed natural log spectral plot of C3-1 powder sample, compared to powder samples of typical H (green), L (blue) and LL (red) chondrites.

The optical spectrum of the darker (C6) chip is mostly featureless (Fig. S71), with a bit of terrestrial weathering at 0.5 microns. However, the 3-micron hydration bands are not strong, so these surfaces are relatively fresh.

The resulting spectrum for the pre-atmospheric body would depend on how those light and dark components are mixed. If they are occur in separate components like boulders or gravels, and no intimate mixing occurs, then the asteroid spectrum would be nearly a simple linear combination of those two. If fine grain regolith mixing occurs, then the dark component tends to affect the whole spectrum significantly, which can make the absorption bands shallower and the albedo lower. If the dark material is low in abundance, a Q-type spectrum can be the outcome, which can space-weather into an S-type spectrum. Even when the dark component is abundant, space weathering can make the whole spectrum redder, and the cause of weak absorption bands can be indistinguishable between dark matter mixing and space weathering.

Results are compared to in-situ measured reflectance spectra of the light and dark lthologies of Itokawa in Fig. S71. Itokawa had black boulders as isolated rocks as well as lower-albedo areas of regolith [144]. The near-infrared spectrometer (NIRS) onboard Hayabusa did not have enough spatial resolution to measure spectra of individual boulders, and thus the "dark" lithology spectrum in Fig. S71 is likely a combination of spectra of light and dark materials. The "dark" Itokawa spectrum may result from the "light" Itokawa spectrum adding linearly a small fraction of dark Chelyabinsk component.

4.10. Thermoluminescence

(Contributed by: D. Sears, I. A. Weinstein, A. S. Vokhmintsev, A. V. Ishchenko, and V. I. Grokhovsky)

Fragments of several Chelyabinsk meteorites were analyzed for thermoluminescence at the Ural Federal University. Samples consisted of slices of 1 mm thickness (Fig. S73A) and powders prepared by separating the core of some fragments from the fusion crust and then crushing this material into a ~100 μm grain size powder, which was treated in hydrochloric acid to remove metal particles (Fig. S73B).

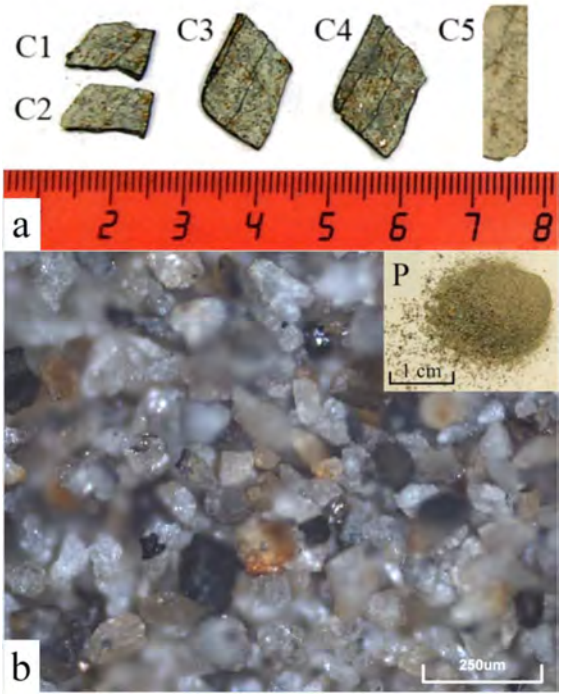

Fig. S73. Chelyabinsk meteorite slices and powder.

Measurements were carried out in phosphorescence mode using a LS55 Perkin Elmer spectrometer. A specially designed small heating appliance was used to measure the thermoluminescence (TL). The glow curves of the natural TL were registered at 440 nm wavelength over the range from room temperature to 873 K at a linear heating rate of r = 2 K/s. The natural TL spectra were measured at r = 1 K/s over the 300 - 650 nm wavelength range, scanned at 700 nm/min. The temperature of the sample varied by ~30 K during one scan.

Table S22. Spectral parameters of luminescence in Chelyabinsk meteorite

Technique	Sample	T, K	Component	E_{max}, ± 0.05 eV	FWHM, ± 0.05 eV	R^2
TL	slice C3	437	G1	2.74	0.73	0.996
			G2	2.40	0.35	
		481	G1	2.82	0.73	0.993
			G2	2.43	0.38	
	powder P	393	G1	2.81	0.68	0.995
			G2	2.43	0.40	
PL	powder P	300	G1	2.77	0.69	0.999
			G2	2.45	0.41	
			G3	6.28	0.96	
			G4	5.42	0.21	
			G5	5.17	0.40	
			G6	4.84	0.70	
	slice C5	300	G1	2.80	0.70	0.999
			G2	2.45	0.37	
			G3	6.23	0.92	
			G4	5.39	0.18	

Photoluminescence (PL) spectra were measured at room temperature, and scanned at a rate of 60 nm/min. Excitation spectra were recorded the sample excited at 440 nm, and measured at 200 - 360 nm, while the emission spectra were recorded for 200 nm excitation over the wavelength range of 300 - 650 nm.

TL spectra for samples C3 (Slice and Powder) are shown in Fig. S74A and S74B, peaking at T = 437 and 393 K, respectively. The band profiles were decomposed by superposition of two Gaussian shapes (satisfactory to $R^2 > 0.993$) and the maximum energy (E_{max}) and Full-Width-at-Half-Maximum (FWHM) of each component are listed in Table S22. The stronger band (G1) is 2-4 times higher than the weaker (G2).

The natural TL (Fig. S75) has a peak in the 400 - 520 K range, with a high-temperature shoulder at 520-750 K. These ranges are similar in shape and position to Dhajala's main TL peak

[145]. The Dhajala meteorite is commonly used as a normalization standard for induced TL measurements because it lies in the middle of the log-normal range for ordinary chondrites.

The intensity varies by a factor of 10 and the maximum temperature (T_{max}) of the TL peak from 427 to 487 K (Table S22) for different samples. This can be due to inhomogeneous mineral phases or mineral compositions, or differences in irradiation doses in space [29].

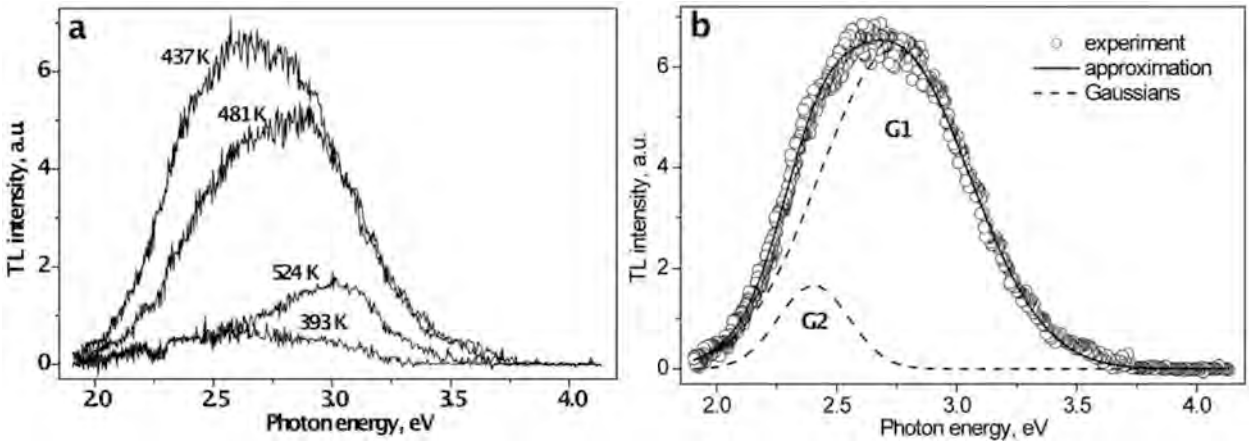

Fig. S74A. The natural TL spectra for the C3 slice measured at different temperatures (a) and approximation by independent Gaussian components for T = 437 K (b)

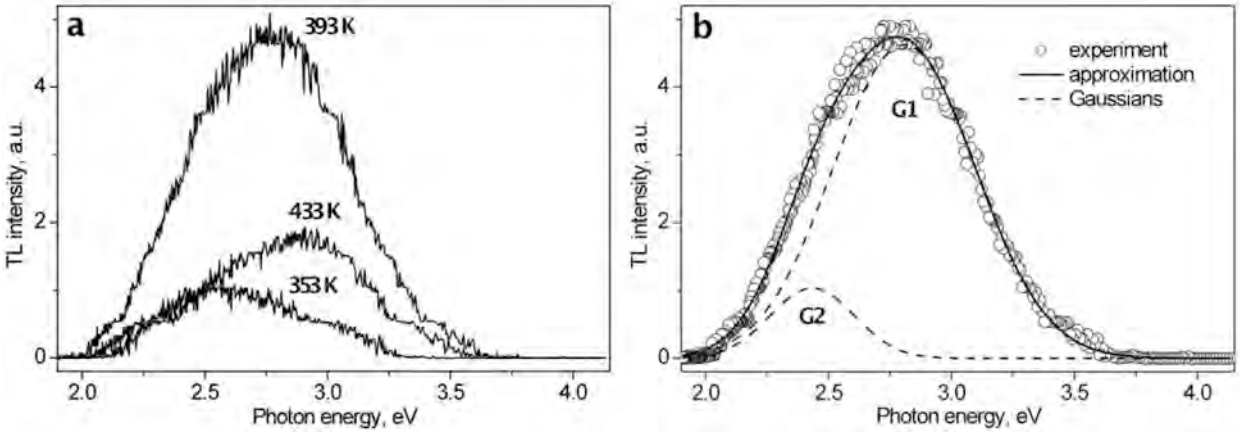

Fig. S74B. The natural TL spectra for the C3 powder sample measured at different temperatures (a) and approximation by independent Gaussian components for T = 393 K (b)

For a quantitative interpretation, the experimental curves of the 300-500 K range were described in terms of a general-order kinetics equation [146]:

$$I(T) = s'' n_0 \exp\left(-\frac{E_A}{kT}\right)\left[1 + (b-1)\frac{s''}{r}\int_{T_0}^{T}\exp\left(-\frac{E_A}{k\theta}\right)d\theta\right]^{-\frac{b}{b-1}}, \qquad \text{(Eq. S7)}$$

where E_A – activation energy, eV; r – linear heating rate, K/s; k – Boltzmann constant, eV/K; n_0 – initial concentration of occupied traps, cm^{-3}; s'' – effective frequency factor, s^{-1}; b – kinetic order, b > 1; T_0 – initial temperature, K. The values obtained for activation energy and frequency factor (Table S23) agree with those obtained by Biswas *et al.* [145].

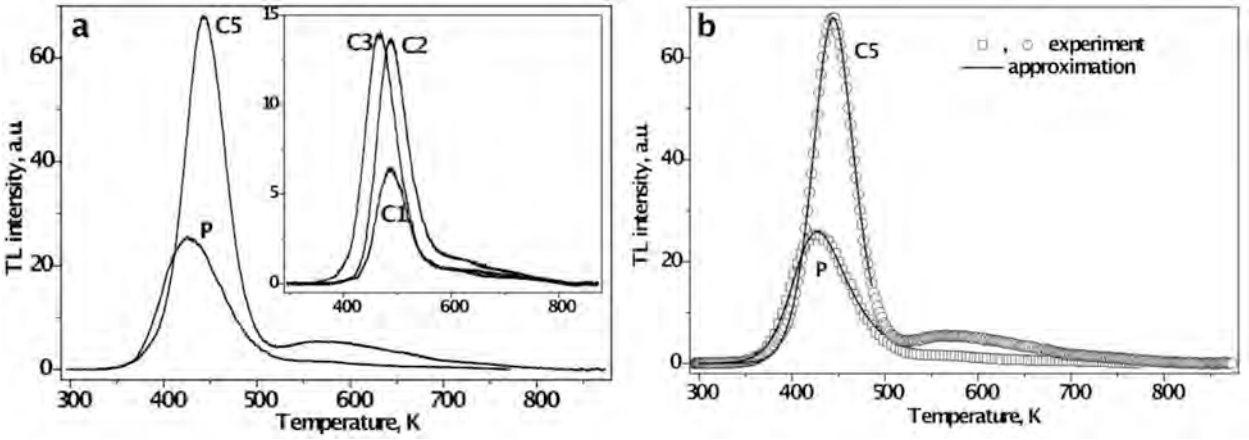

Fig. S75. The natural TL measured in the 440 nm band (2.82 eV) for the samples of Chelyabinsk meteorite (a) and approximation of the TL curves in terms of general order kinetics (b).

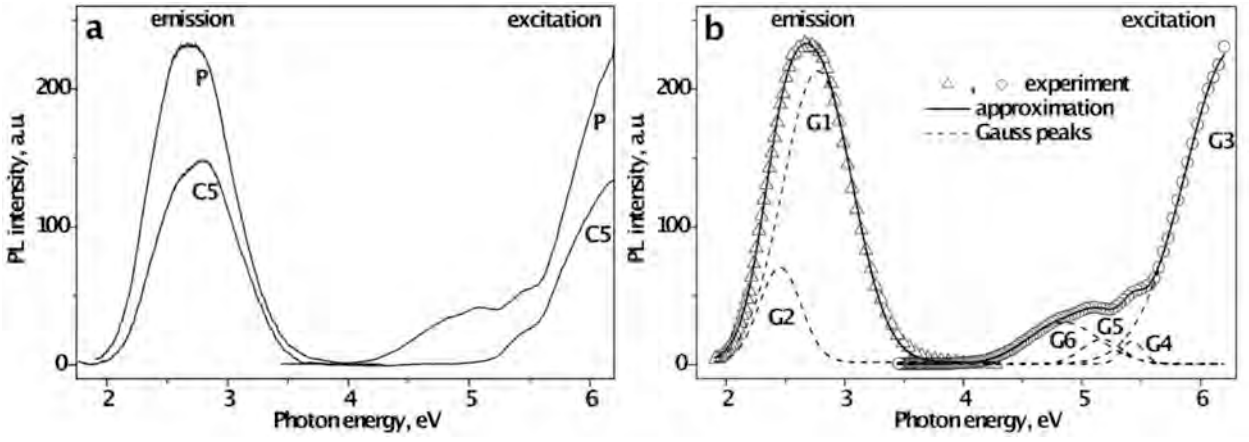

Fig. S76. The experimental excitation and emission PL spectra measured at room temperature for C5 powder and C5 slice (a) and spectra deconvolution into independent Gaussian components for C5 powder sample (b).

Biwas *et al.* [145] also found that the kinetics order varies between b = 2 - 3, indicating that charge carrier traps of different types may be active at the temperatures under study. This could mean that there are up to eight overlapping TL components so that a full theoretical analysis of the glow curve structure would require independent input of the kinetic parameters (activation

energy, Arrhenius factor, etc.) for each peak. Because of that, empirical methods are normally used to interpret induced TL data.

Table S23. Calculated TL kinetic parameters: T_{max} is temperature of maximum thermoluminescense, E_A is activation energy barrier in eV, s" is effective frequency factor, b is kinetic order, and R^2 is the correlation coefficient describing the accuracy of the fit [146].

Sample	T_{max}, ± 2 K	E_A, ± 0.06 eV	s″, s^{-1}	b, ± 0.3	R^2
C1	487	1.18	$1.7 \cdot 10^{11}$	2.7	–
C2	487	1.23	$5.4 \cdot 10^{11}$	2.9	0.999
C4	467	0.97	$2.8 \cdot 10^{9}$	2.3	0.999
C5	444	1.05	$1.0 \cdot 10^{11}$	1.9	–
P	427	0.83	$5.6 \cdot 10^{8}$	2.7	–

Figs. S76 show the emission and excitation spectra for the most PL active meteorite C5 and its powder. Again, the spectral dependences are a superposition of several independent Gaussian components, parameters of which are listed in Table S22. With varying energy, the shape of the PL peaks do not change while their intensity decreases with varying energy of excitation in the range 6.2 to 4.5 eV. The similar values for the two Gaussian components suggests that the PL and TL processes are due to similar recombination centers. The excitation spectra of the powder sample show two extra bands (G5 and G6 in Table S22), alongside the dominant G3 and less intensive G4 band that are typical for all studied samples.

At NASA Ames Research Center, two internal chips of light lithology taken 2-3 mm from the crust of sample C3 (left of line in Fig. S77) had a strong natural TL signal suggesting that temperatures ~200ºC did not penetrate that far into the meteorite and that the temperature gradient of this 1 cm meteorite were extremely steep. Consistent with this, the fusion crust is extremely thin (~0.2 mm). The average natural TL level, calculated in the way described by Sears *et al.*

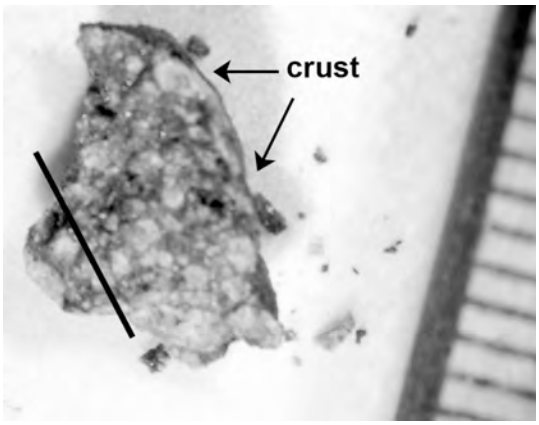

Fig. S77. Chelyabinsk C3 fragment for thermoluminescence. Scale is in mm.

[147], is 47+/-13 krad. This corresponds to an orbit with a perihelion of 0.6-0.8 AU, using the arguments and curves of Sears *et al.* [148] to relate natural TL to perihelion (Fig. S78). This is consistent with the estimates made on the basis of observed trajectory (Table S5B) and with exposure ages (SOM Sect. 4.12) and dynamic ages (Table S6) indicating that the natural TL levels were at their equilibrium at the time of fall. The TL properties of the dark vein material were not determined, but they might have resembled the shock blackened ordinary chondrites reported by Haq *et al.* [149].

The two chips had induced TL properties (TL sensitivity, TL peak temperature, and TL peak width) in reasonable agreement and the temperature and width are consistent with values expected for equilibrated ordinary chondrites [150].

The TL sensitivity (the level of TL induced by a standard laboratory test dose normalized to a standard meteorite, Dhajala) is 1.05+/-0.35. There is ambiguity in the significance of this number which is easily removed when it is realized that this is a shocked meteorite (scale S4 on the scheme described by Stöffler *et al.* [19]. If it was not shocked, the TL sensitivity of Chelyabinsk would suggest that it was a petrographic type 3.8 or 4 on the metamorphism scale described by Van Schmus and Wood [150] and Sears *et al.* [151]. This is inconsistent with the petrographic type assigned on the basis of mineral composition and petrography.

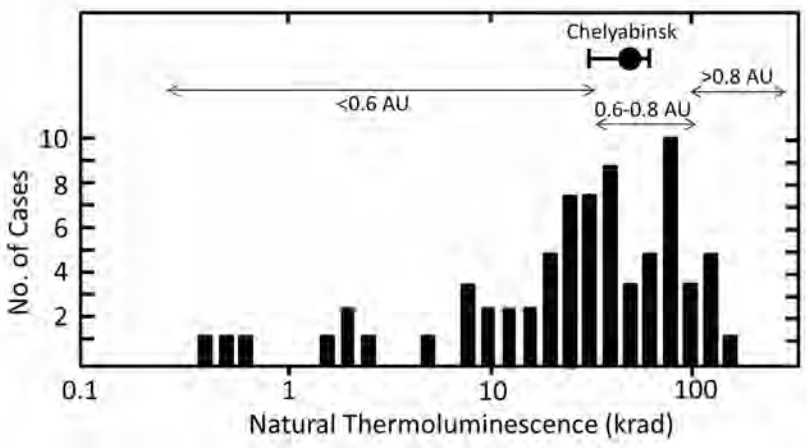

Fig. S78. Natural TL levels for observed ordinary chondrites falls from Benoit *et al.* [153] with the perihelia distances suggested by Sears *et al.* [148] and with the data for Chelyabinsk indicated.

Figure S79 shows the Thermoluminescence sensitivity (TL induced by a standard laboratory radiation dose normalized to a standard meteorite, Dhajala) as a function of petrographic type

(i.e., degree of metamorphism on the parent body). The figure is from Sears *et al.* [152] with data for Chelyabinsk superimposed with uncertainties reflected by the grey area. Using the TL sensitivity, petroraphic type 3 has been subdivided into types 3.0 to 3.9 where the three meteorites clustered around Dhalaja are type 3.8. On this basis, Chelyabinsk appears to be type 3.8 but this would be inconsistent with petrographic data (Sect. 4.4) that assigns it to petrographic type 5.

The TL sensitivity of Chelyabinsk compared with the TL sensitivity shocked ordinary chondrites suggests that the low TL sensitivity relative to types 5 and 6 is due to the meteorite having experienced shock metamorphism to the level of S4 (30-35 GPa) (Fig. S80). Shock to levels of S5 - S6 result in the complete destruction of feldspar, the mineral phase responsible for the thermoluminescence signal, which would reduce the TL sensitivity to levels of ~0.01 or lower [154].

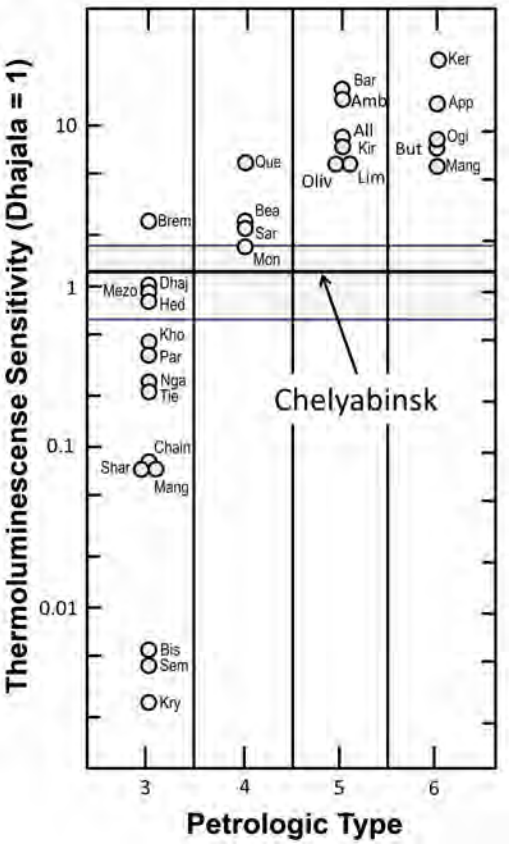

Fig. S79. TL induced by a standard laboratory radiation dose, normalized to a standard meteorite (Dhajala), as a function of petrographic type.

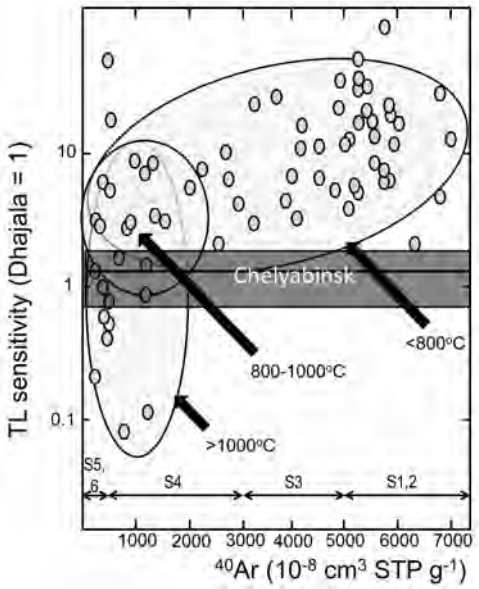

Fig. S80. Diagram from [149] showing the TL sensitivity of shocked meteorites as a function of ^{40}Ar content. Stepwise heating experiments shows that ^{40}Ar is lost at the temperatures indicated and this has been related to shock class using data in [19]. These data are consistent with a shock classification of S4.

4.11. Electrospray Ionization Ultra-High Resolution Mass Spectrometry

(Contributed by: P. Schmitt-Kopplin and N. Hertkorn)

The samples were surrounded by dense snow when found. After recovery, they were wrapped in porous paper to remove water. After drying, the samples were placed in plastic bags and stored at room temperature. No further actions to prevent terrestrial organic contamination were taken.

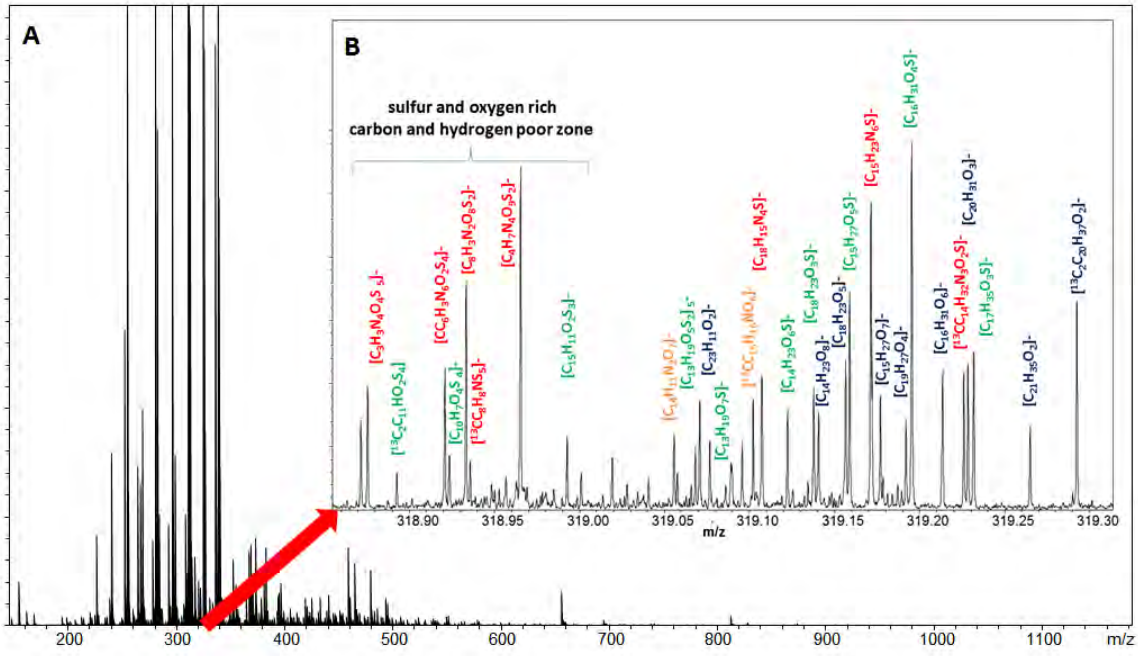

Fig. S81. (A) Negative ESI-ICR-FT/MS mass spectra in the range m/z 150 to m/z 1,200 of the chondritic methanol extract. **(B)** section of nominal mass 319 with corresponding assigned elemental compositions of mass peaks as singly charged negative ions.

Two samples were analyzed at Helmholtz Zentrum München, a 3.6 g whole rock with complete fusion crust and a pea-sized 2.8 g impact melt sample (Fig. S49D,E). They were cut in two with a diamond wire saw under minimal water cooling using water of Liquid Chromatography / Mass Spectroscopy (LC/MS) analytical grade, in order to qualitatively examine the interior of the sample and to choose the parts to be analyzed. One half of the respective samples are shown in Fig. S49D-E. The other half pieces were immediately crushed in an agate pillar, to avoid terrestrial contamination, and fragments from the core were isolated for further analysis.

An 80 mg fragment was selected and washed with methanol (500 µl LC/MS grade) prior of being further crushed in the agate pillar. Methanol, a polar protic solvent was shown previously to extract the maximum chemical diversity of polar compounds from organic chondrites as detected by Electrospray Ionization Mass Spectrometry (ESI-MS [30, 155]). The slurry was transferred into a 2 mL Eppendorf vial that was subjected to sonication for 60 seconds at room temperature and directly centrifuged. The supernatant was injected into the Ion Cyclotron Resonance Fourier-Transform (ICR/FT) mass spectrometer without further treatment.

Mass spectra were acquired using a Bruker SOLARIX 12 Tesla ion cyclotron resonance Fourier transform mass spectrometer. Singly charged and unfragmented negative ions were generated at atmospheric pressure within an Apollo II electrospray ionization (ESI) source at a flow rate of 2 µL min^{-1}. Detailed information about the Electronspray Ionization Ion Cyclotron Resonance Fourier-Transform Mass Spectroscopy (ESI-ICR-FT/MS) method applied in this study for complex materials is given elsewhere [30]. Negative Electrospray Ionization (negative ESI) was performed under conditions described earlier [155]; 3,000 scans were accumulated with 4 million data points resulting in more than 18,000 resolved mass peaks ranging from mass 150 to 700. The instrument´s performance was controlled by means of internal calibration on arginine clusters prior to any analysis. The average errors in mass values relative to internal standards (fatty acids) were usually < 100 ppb across a range of 150 < m/z < 1,500. The average mass resolution ranged near 400,000 at nominal mass 400. The same internal calibrants were used as in a previous study [30], resulting in a common absolute mass accuracy of 0.1 ppm. The conversion of the exact masses into elemental compositions was shown in Tziotis *et al.* [156]. Basically, the molecular formula calculations based on excellent mass accuracy and mass resolution were validated by network-based mass difference analysis from all initially assigned compositions, with up to 5 elements (CHNOS) and isotopes as follows: ^{1}H, ^{12}C, ^{16}O, ^{14}N, ^{32}S; the ^{13}C and ^{34}S isotopomers were included to validate the assigned molecular formulas with a precision of 0.15 ppm.

The ultrahigh resolution mass spectra showed a wealth of organic compounds (Fig. S81). Out of 18,000 mass signals in the chondritic sample extracts within the mass range m/z 150 to 700, 2,536 elemental compositions could be assigned with the elements C, H, N, O, S (involving isotopologues of ^{13}C and ^{34}S), of which 1,102 were identified as CHO compounds (shown in blue in the van Krevelen diagrams in Fig. S82A and S82B, 899 were identified as CHOS

compounds (shown in green), 391 were found CHNO compounds (orange), and 144 compounds contained both sulfur and nitrogen (CHNOS; red). The impact melt solvent extract showed almost identical counts of elemental formulas but with a shift in compositions towards higher molecular mass, a relatively larger proportion of released nitrogen and aromatic compounds. The van Krevelen diagrams (Fig. S82A,B) readily showed the rich chemical diversity as a projection of the H/C versus O/C elemental ratios derived from all assigned elemental compositions, whereas the H/C versus mass diagram (Fig. S82C,D) allowed visualizing many chemical homologous molecular series. In both diagrams, the size of the symbols was proportional to peak intensities, providing relative abundances of ions and a proxy of formation rate and stability of the respective ions.

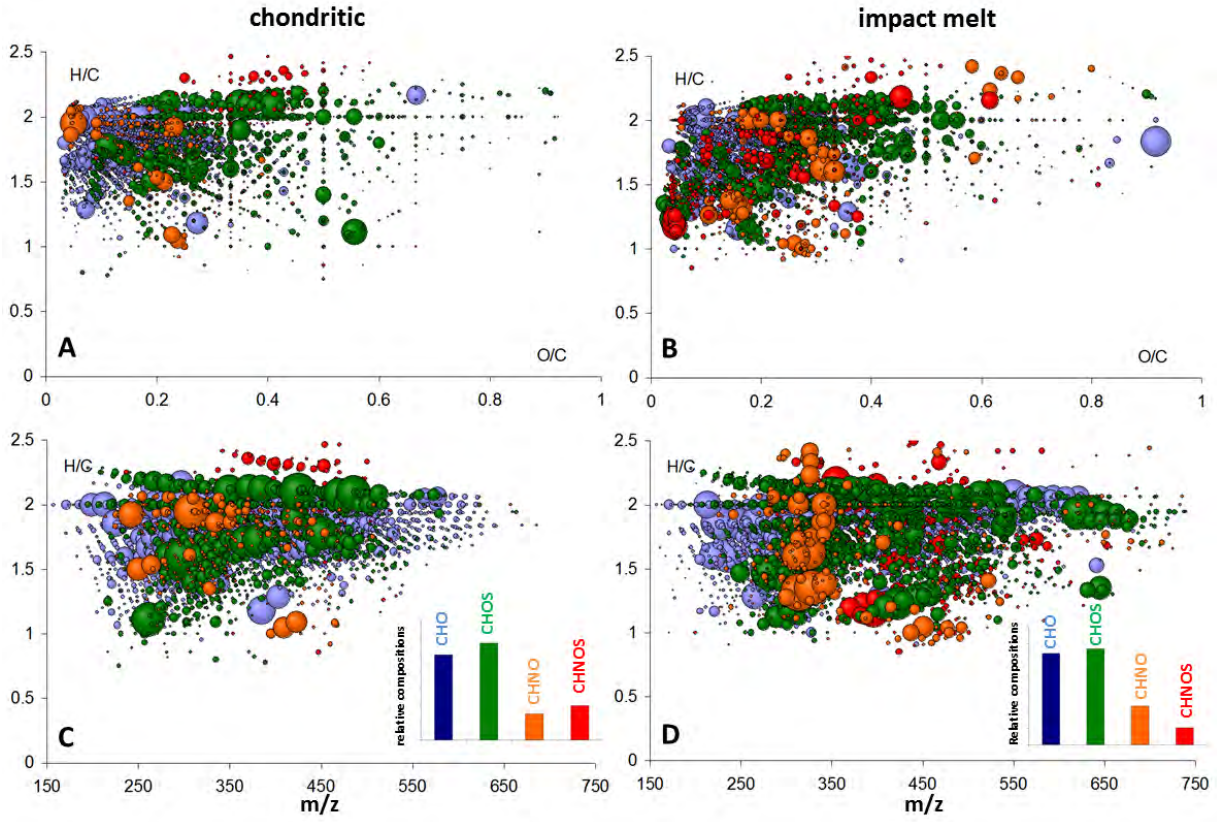

Fig. S82. van Krevelen diagram (H/C versus O/C elemental ratio) and H/C versus m/z plots of the negative ESI-ICR-FT/MS data from the chondritic (A, C) and impact melt (B, D) samples; relative abundance of assigned molecular compositions in four key molecular series (CHO (blue), CHOS (green), CHNO (orange) and CHNOS (red), respectively).

This chemical fingerprint and its distribution characteristics, with a high abundance of CHNO and CHOS homologous series, showed significant differences between chondritic and impact melt fractions in the Chelyabinsk meteorite. The similar distribution characteristics of all molecular series, however, ensured that most of these organic compounds were no biogenic contaminants from residence following the fall and subsequent handling. Terrestrial biological contamination commonly shows known discontinuous signatures typical of biomolecules (e.g. relative odd/even preferences for CHO molecules or clustering according to common classes of biomolecules). Conceivable terrestrial impurities, while possibly present in trace amounts, left no notable signature in the mass spectra of both meteorite extracts (Fig. S81).

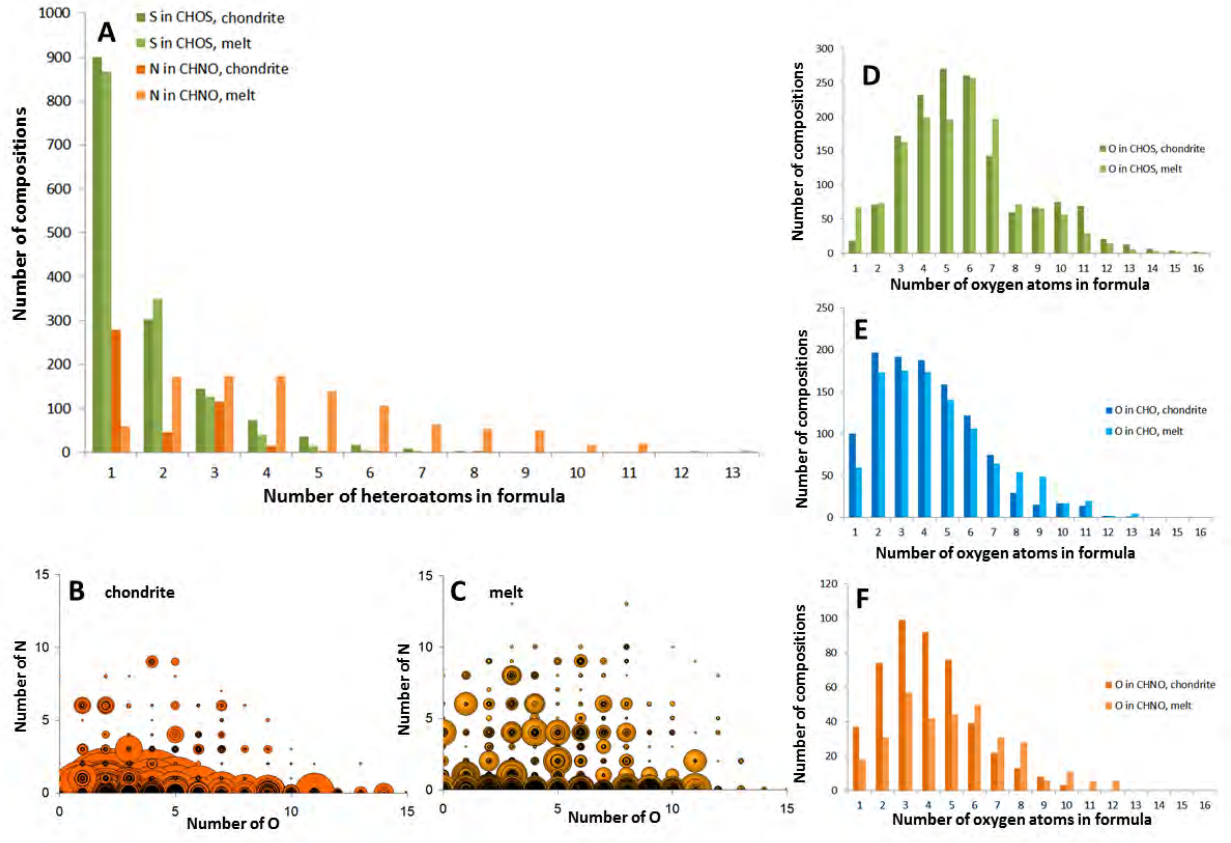

Fig. S83. Count and distribution of the O, N, S atoms within the different chemical classes, showing the peculiar changes of oxygen counts in soluble CHNO molecules when proceeding from the chondrite to the impact or melt phase. **(A)** Count of sulfur and nitrogen atoms within the CHOS and CHNO series, respectively, of the chondrite and impact melt extracts. Count of nitrogen versus oxygen atoms in chondrite **(B)** and melt fractions **(C)** in CHNO compounds. Count of oxygen atoms in CHOS **(D)**, CHO **(E)** and CHNO **(F)** molecular series; note the shift in oxygen distribution within CHNO molecules during processing of chondrite matter into melt phase.

The distribution of the elemental compositions of the two meteorite extracts is shown in Fig. S83. Most of the CHNO and many CHOS compounds in the chondritic material contained only a single heteroatom, i.e., one sulfur ($CHOS_1$) or, alternatively, one nitrogen atom (CHN_1O) per molecule. The fraction of compounds with (ever) more than one heteroatom decreased rapidly for both CHNO and less so for CHOS series (Fig. S83A), reflecting a lower tendency during chemosynthesis to form these respective *soluble* compounds. The count and distribution of sulfur within CHOS molecular series in the chondritic and the melt solvent extracts were almost identical (Fig. S83A,D). In contrast, the distribution of nitrogen atoms within CHNO molecular series showed a rather broad abundance maximum from $CHN_{2\text{-}4}O$ in the impact melt, reaching out to CHNO compounds with up to ten nitrogen atoms. Taking into account that in case of Negative ESI ion detection, nitrogen-rich molecules will also carry sizable numbers of oxygen (Fig. S83B,C), one anticipates remarkable differences in oxygen distribution for chondritic and impact melt CHNO molecules (cf. below).

When plotting the distribution of oxygen atoms according to molecular series (Fig. S83D-F), a rather close accordance is found for both CHO and CHOS series for both chondritic and melt materials, but not for CHNO molecules. The melt phase is depleted in oxygen-poor and enriched in oxygen-rich CHNO molecules (Fig. S83F). In addition, when compared with CHO and CHNO molecular series; CHOS compounds contain three more oxygen atoms on average in what seems a bimodal distribution, suggesting compositional and structural preferences for molecules with sulfur in elevated oxidation states. High temperatures affecting the extraterrestrial organic matter during the fall might have initiated a cascade of structural changes, including thermogenesis of functionalized N-heterocycles with selective loss of volatiles, leading to a relative higher methanol solubility of ionizable CHNO molecules in the melt relative to the chondritic phase.

The data show a high chemical diversity and abundance of soluble organic compounds in an ordinary (non-carbonaceous) chondrite, based on C, H, N, O, and S belonging to continuous homologous series reflecting their abiotic chemiosynthesis origin. In addition, the impact melt fraction shows a significant increase in oxygen-rich CHNO compounds, suggesting that (precursors of these) polar soluble compounds were already present when these impact melts were formed, and would have been accumulated during accretion and planetary formation. No appreciable difference of relative oxygenation is observed for CHO and CHOS compounds in the

chondrite phase and impact melt, suggesting a different evolution of CHNO and CHOS chemistry not only in Murchison [30] but also in the Chelyabinsk LL5 type meteorite.

4.12 Noble Gas Isotopes

(Contributed by: K. Nagao, M. K. Haba, M. Komatsu, and T. Mikouchi)

Noble gas isotopes were measured for four chips from meteorite C3-2 (Table S13, Fig. S47), and nine samples from seven commercially obtained Chelyabinsk meteorites (HR-1 to HR-7), using a modified-VG5400(MS-3) mass spectrometer at the University of Tokyo. The HR samples are from an unknown source and unknown location in the strewn field.

Table S24A. He and Ne isotopic ratios, and concentrations of noble gases in fragments C3-2 and HR-1 to HR-7 of meteorite Chelyabinsk (LL5).

Sample Mass	^{3}He 10^{-11} cc/g	^{4}He 10^{-9} cc/g	^{3}He/^{4}He	^{20}Ne 10^{-9} cc/g	^{21}Ne 10^{-9} cc/g	^{22}Ne 10^{-9} cc/g	^{20}Ne/^{22}Ne	^{21}Ne/^{22}Ne
C3-2 (Bulk-1)	4.3	116.4	0.00037	0.219	0.011	0.036	6.091	0.313
10.12mg ±	0.4	8.6	0.00003	0.018	0.001	0.002	0.588	0.024
C3-2 (Bulk-2)	5.8	131.1	0.00044	0.705	0.020	0.094	7.481	0.216
32.15 mg ±	0.4	9.3	0.00003	0.048	0.002	0.006	0.474	0.015
C3-2 (Light)	5.5	117.6	0.00047	0.570	0.009	0.072	7.942	0.132
3.20 mg ±	0.8	8.3	0.00006	0.046	0.001	0.005	0.591	0.017
C3-2 (Dark)	8.0	118.4	0.00068	3.187	0.025	0.383	8.328	0.067
2.54 mg ±	0.8	7.5	0.00006	0.221	0.002	0.024	0.559	0.007
HR-1 (Bulk)	311	353.7	0.0088	1.381	0.778	0.945	1.460	0.822
33.5 mg ±	20	24.2	0.0006	0.091	0.049	0.057	0.089	0.050
HR-2 (Bulk)	200	98.3	0.0204	0.560	0.548	0.608	0.922	0.901
30.0 mg ±	20	9.9	0.0001	0.057	0.055	0.061	0.013	0.009
HR-3 (Bulk)	902	1069.6	0.0084	1.911	2.037	2.244	0.852	0.908
28.5 mg ±	90	107.0	0.0001	0.192	0.205	0.225	0.006	0.010
HR-4 (Bulk)	1421	121.7	0.1168	0.948	1.028	1.146	0.827	0.897
27.2 mg ±	146	12.2	0.0025	0.103	0.104	0.115	0.034	0.012
HR-5 (Bulk)	554	796.0	0.0070	3.547	3.836	4.195	0.846	0.914
25.5 mg ±	55	79.7	0.0000	0.355	0.386	0.420	0.005	0.009
HR-6 (Bulk)	939	2216.1	0.0042	0.644	0.730	0.817	0.789	0.894
25.9 mg ±	120	221.7	0.0003	0.065	0.074	0.082	0.012	0.010
HR-7 (Light)	1254	402.2	0.0312	2.285	2.454	2.743	0.833	0.895
31.6 mg ±	83	26.7	0.0021	0.160	0.177	0.195	0.051	0.054
HR-7 (Black)	1309	312.5	0.0419	3.724	2.989	3.569	1.044	0.838
28.8 mg ±	93	19.2	0.0026	0.210	0.192	0.222	0.065	0.050
HR-7 (Bulk)*	1245	330.5	0.0377	2.883	2.763	3.033	0.951	0.911
501.8 mg ±	125	33.0	0.0002	0.289	0.277	0.303	0.004	0.008

* ^{81}Kr was measured

A stepwise-heating noble gas extraction method (T = 600, 1000, 1300 or 1400, and 1700°C) was applied to four C3-2 chips (2 bulk samples, one light and one dark color portion), HR-1 (bulk), HR-7 (light), and HR-7 (black). Noble gases were extracted from the bulk samples HR-2, 3, 4, 5, and 6 by total melting at 1700°C. Weights used for the noble gas analyses are listed in Table S24A. The concentration of ^{81}Kr was measured for the HR-7 (bulk), the sample weighing 501.8 mg.

Table S24B. Ar isotopic ratios, and concentrations of noble gases in meteorite Chelyabinsk (LL5).

Sample	^{36}Ar 10^{-9}cc/g	^{38}Ar 10^{-9}cc/g	^{40}Ar 10^{-9}cc/g	^{38}Ar/^{36}Ar	^{40}Ar/^{36}Ar	^{84}Kr 10^{-12}cc/g	^{132}Xe 10^{-12}cc/g
C3-2 (Bulk-1)	3.981	0.752	2228	0.1890	559.6	168.8	291.5
±	0.266	0.050	141	0.015 8	247.2	9.6	15.1
C3-2 (Bulk-2)	5.879	1.112	2587	0.1892	440.0	178.8	227.8
±	0.331	0.063	148	0.0107	131.1	10.0	12.1
C3-2 (Light)	6.365	1.193	1605	0.1874	252.1	275.7	249.0
±	0.368	0.069	86	0.0098	69.2	15.7	14.2
C3-2 (Dark)	10.185	1.924	4649	0.1889	456.4	279.2	205.6
±	0.610	0.038	280	0.0064	80.0	16.2	12.2
HR-1 (Bulk)	3.769	0.801	1304	0.2126	346.0	46.0	45.2
±	0.262	0.055	88	0.0148	113.1	2.4	2.2
HR-2 (Bulk)	3.495	0.701	674	0.2005	192.8	110.2	75.7
±	0.353	0.071	68	0.0010	0.4	11.0	7.6
HR-3 (Bulk)	4.309	0.979	4265	0.2271	989.6	65.5	135.4
±	0.434	0.099	431	0.0026	6.8	6.6	13.6
HR-4 (Bulk)	0.463	0.179	159	0.3875	342.4	11.8	15.3
±	0.050	0.020	17	0.0053	1.3	1.2	1.5
HR-5 (Bulk)	7.674	1.729	3944	0.2253	514.0	97.7	202.8
±	0.771	0.174	397	0.0010	3.3	9.8	20.3
HR-6 (Bulk)	0.794	0.199	7382	0.2509	9296.4	30.8	21.4
±	0.083	0.021	789	0.0043	200.8	3.1	2.2
HR-7 (Light)	3.661	0.921	861	0.2515	235.1	44.0	57.7
±	0.239	0.058	50	0.0175	61.5	2.4	3.0
HR-7 (Black)	6.100	1.401	26875	0.2296	4405.7	185.0	98.6
±	0.372	0.089	1973	0.0102	952.9	11.7	5.9
HR-7 (Bulk)	3.126	0.822	783	0.2628	250.6	49.0	87.2
±	0.313	0.082	78	0.0009	0.3	4.9	8.7

Tables S24A and S24B summarize the total concentrations and isotopic ratios of He, Ne, and Ar, and concentrations of ^{84}Ke and ^{132}Xe. Krypton isotopic ratios, including ^{81}Kr ($T_{1/2}$ = 0.23 My), for the sample HR-7(bulk) are presented in Table S24C. Isotopic ratios of Kr and Xe for other samples are not given here.

Cosmogenic He, Ne and ^{38}Ar were clearly observed in the HR samples. The samples from

C3-2, on the other hand show very low concentrations. This indicates that the C3-2 fragment was derived from inside the large meteoroid, while the HR samples were from shallower parts of the pre-atmospheric body. The HR-7 fragment had black portions larger than the typical scale of melt veins. Part of this black material, weighing about 30 mg, was used for noble gas analysis. This material showed the highest concentration of ^{40}Ar among the samples measured in this work, which indicates enrichment in K in the black material.

Table S24C. Kr isotopic ratios, and concentrations of ^{81}Kr and ^{84}Kr (10^{-12} ccSTP/g) in meteorite Chelyabinsk HR-7 (Bulk).

Sample	^{84}Kr	^{81}Kr	^{78}Kr/^{84}Kr	^{80}Kr/^{84}Kr	^{81}Kr/^{84}Kr	^{82}Kr/^{84}Kr	^{83}Kr/^{84}Kr	^{86}Kr/^{84}Kr
HR-7 (Bulk)	49.0	0.0158	0.00639	0.0406	0.000322	0.2044	0.2030	0.3045
±	4.9	0.0019	0.00019	0.0005	0.000022	0.0007	0.0007	0.0012

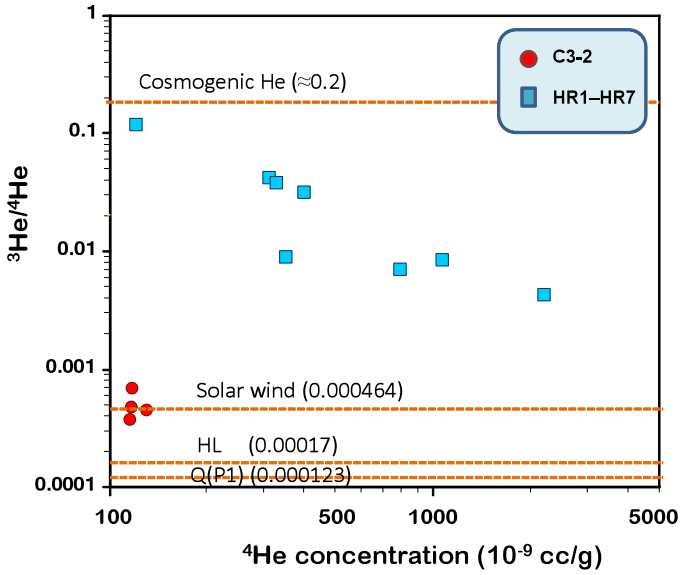

Fig. S84. Helium isotope ratios versus helium concentrations.

Fig. S84 is a plot of ^{3}He/^{4}He versus ^{4}He concentrations. The ^{3}He/^{4}He ratios of the C3-2 samples are in the range of primordial or solar wind He and relatively low concentrations of ^{4}He, suggesting negligible effect from cosmic-ray irradiation as well as loss of radiogenic ^{4}He. Presence of cosmogenic He in the HR samples is evident, but the concentrations are rather low compared with those of most ordinary chondrites. Neon and Ar isotopic ratios plotted in Figs. S85 and S86 also show a clear difference between the C3-2 and HR samples. Concentrations of

^{40}Ar in these meteorites are distinctly lower than those in unshocked ordinary chondrites. A rough estimation of the K-Ar age for the samples shows young ages of about 1,000 My or less, which may be the time of a violent shock event, possibly the one that left the numerous melt veins in the meteorites (Fig. 4A, main manuscript).

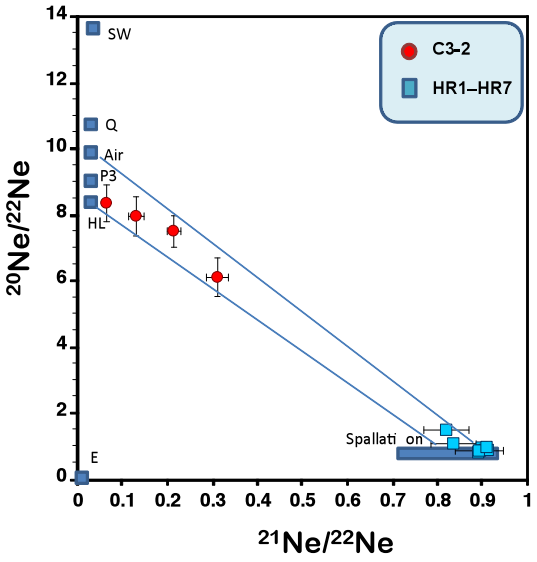

Fig. S85. Neon three isotope plot.

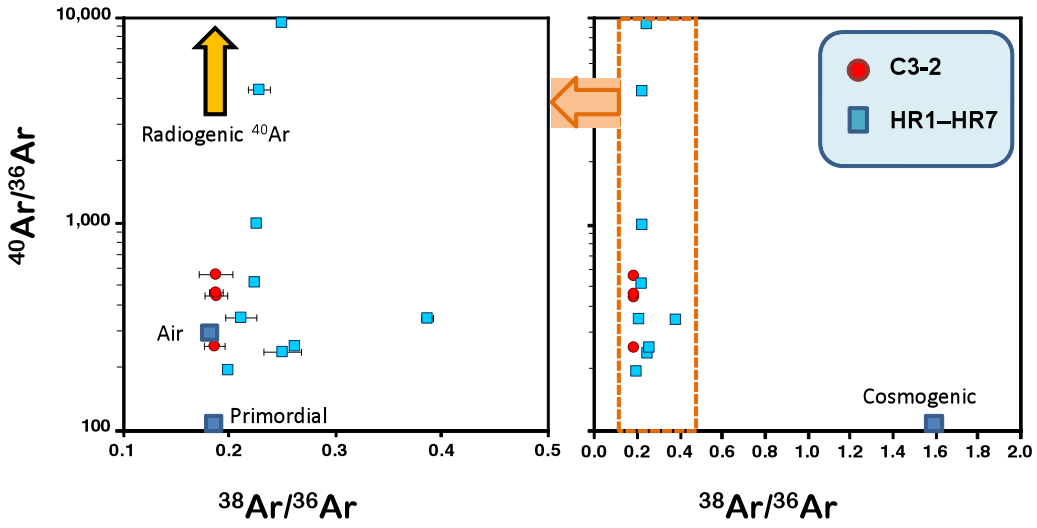

Fig. S86. Argon isotope ratios.

The shielding depth against cosmic-ray bombardment for each sample, and the cosmic-ray exposure age for the Chelyabinsk meteoroid are estimated based on the cosmogenic noble gas compositions measured in this work. Although the concentration of ^{81}Kr was measured for the

sample HR-7 (bulk), the usual Kr-Kr method could not be applied due to the low concentration of cosmogenic Kr in the sample. Because the concentration of ^{81}Kr, 1.6×10^{-14} ccSTP/g, is in the range of the equilibrium level for ordinary chondrites, this fragment should have been at a shallow depth in the preatmospheric body. Calculation of the depth profile of ^{81}Kr concentration under 2π-geometry irradiation, following the method in Hohenberg *et al.* [157], indicates that the observed concentration of ^{81}Kr corresponds to a shielding depth of about 1 g/cm^2. In the calculation, the average concentrations of Rb, Sr, Y and Zr for other LL-chondrites were adopted.

The expected production rate of cosmogenic ^{21}Ne under the same shielding condition of 1 g/cm^2 is calculated to be 2.29×10^{-9} ccSTP/g/My (2π-geometry) following Hohenberg et al. [157]. Combined with the measured concentration of cosmogenic ^{21}Ne, 2.76×10^{-9} ccSTP/g for sample HR-7 (bulk), the cosmic-ray exposure is calculated as 1.2 My. Measured concentrations of cosmogenic ^{21}Ne for other HR samples from the same fragment, HR-7 (light) and HR-7 (black), are 2.45 and 2.98×10^{-9} ccSTP/g, respectively, and give similar exposure ages.

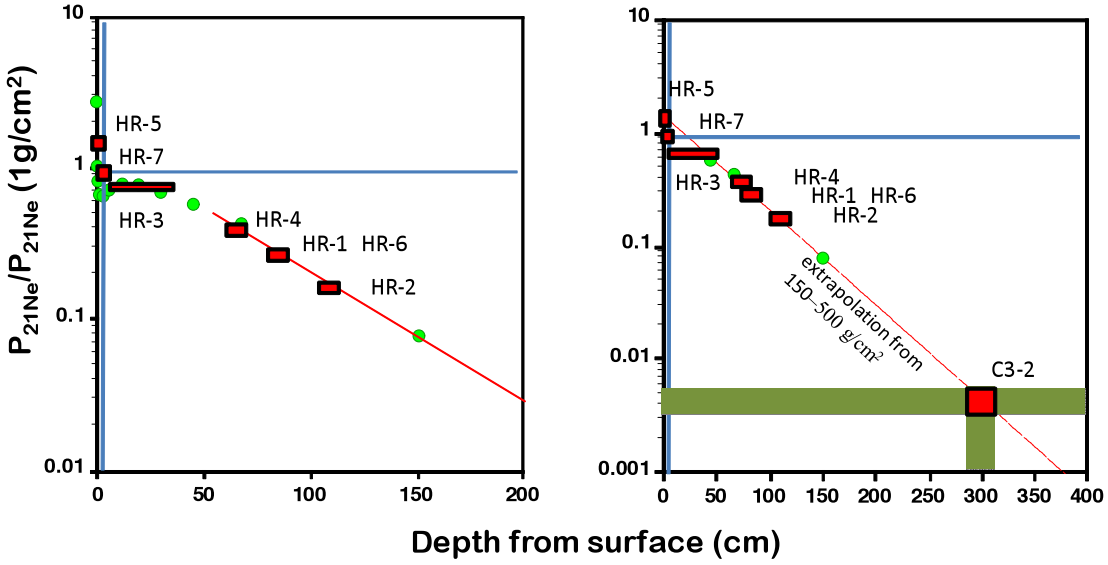

Fig. S87. Estimation of depth from the surface for each fragment in the preatmospheric body of the Chelyabinsk meteoroid.

The depth profile of the ^{21}Ne production rate, normalized to that at the shielding depth of 1 g/cm^2, is shown in Fig. S87, where the production rate was calculated in the range from surface to 500 g/cm^2, following Hohenberg *et al.* [157], and extrapolated to about 400 cm in depth. An average density of 3.3 g/cm^3 (see Sect. 4.2) was used in the calculation. The observed ^{21}Ne

production rate ratios for the measured samples, ranging from 1.39 for HR-5 (bulk) to 0.003 for C3-2 (light), may correspond to different depths, ranging from surface to ~300 cm beneath the surface of the Chelyabinsk meteoroid. These data show that the diameter of the Chelyabinsk meteoroid was larger than 6 m, which supports other estimates of about 20 m in diameter (see main text). If that is the case, however, we can expect that fragments will be recovered derived from deeper parts of the meteoroid that would have negligible effects from cosmic-ray bombardment.

References

1. P. Jenniskens, M. D. Fries, Q. Z. Yin, M. Zolensky, A. N. Krot, S. A. Sandford, D. Sears, R. Beauford, D. S. Ebel, J. M. Friedrich, K. Nagashima, J. Wimpenny, A. Yamakawa, K. Nishiizumi, Y. Hamajima, M. W. Caffee, K. C. Welten, M. Laubenstein, A. M. Davis, S. B. Simon, P. R. Heck, E. D. Young, I. E. Kohl, M. H. Thiemens, M. H. Nunn, T. Mikouchi, K. Hagiya, K. Ohsumi, T. A. Cahill, J. A. Lawton, D. Barnes, A. Steele, P. Rochette, K. L. Verosub, J. Gattacceca, G. Cooper, D. P. Glavin, A. S. Burton, J. P. Dworkin, J. E. Elsila, S. Pizzarello, R. Ogliore, P. Schmitt-Kopplin, M. Harir, N. Hertkorn, A. Verchovsky, M. Grady, K. Nagao, R. Okazaki, H. Takechi, T. Hiroi, K. Smith, E. A. Silber, P. G. Brown, J. Albers, D. Klotz, M. Hankey, R. Matson, J. A. Fries, R. J. Walker, I. Puchtel, C. T. Lee, M. E. Erdman, G. R. Eppich, S. Roeske, Z. Gabelica, M. Lerche, M. Nuevo, B. Girten, S. P. Worden; Sutter's Mill Meteorite Consortium, Radar-enabled recovery of the Sutter's Mill meteorite, a carbonaceous chondrite regolith breccia. *Science* **338**, 1583–1587 (2012). doi:10.1126/science.1227163 Medline

2. M. B. E. Boslough, D. A. Crawford, Shoemaker-Levy 9 and Plume-forming collisions on Earth. *Ann. N. Y. Acad. Sci.* **822**, 236–282 (1997). doi:10.1111/j.1749-6632.1997.tb48345.x

3. V. V. Svetsov, V. V. Shuvalov, in *Catastrophic events Caused by Cosmic Objects*, V. Adushkin, I. Nemtchinov, Eds. (Springer, Dordrecht, 2008), pp. 227−267.

4. D. R. Christie, P. Campus, in *Infrasound Monitoring for Atmospheric Studies*, A. Le Pichon, E. Blanc, A. Hauchecorne, Eds. (Springer, Dordrecht 2010), pp. 29−75.

5. D. Yeomans, P. Chodas, Additional Details on the Large Fireball Event over Russia on Feb. 15, 2013. *NASA NEO Program Office Announcement, March 1, 2013* (NASA, Washington, 2013).

6. Materials and methods are available as supporting material on *Science Online*.

7. E. Tagliaferri, R. Spalding, C. Jacobs, S. P. Worden, A. Erlich, in *Hazards Due to Comets and Asteroids, Space Science Series* (University of Arizona Press, Tucson, 1994), pp. 199.

8. T. A. Ens, P. G. Brown, W. N. Edwards, E. A. Silber, Infrasound production of bolides: A global statistical study. *J. Atmos. Sol. Terr. Phys.* **80**, 208–229 (2012). doi:10.1016/j.jastp.2012.01.018

9. I. V. Nemtchinov, V. V. Svetsov, I. B. Kosarev, A. P. Golub', O. P. Popova, V. V. Shuvalov, R. E. Spalding, C. Jacobs, E. Tagliaferri, Assessment of kinetic energy of meteoroids detected by satellites-based light sensors. *Icarus* **130**, 259–274 (1997). doi:10.1006/icar.1997.5821

10. D. O. Revelle, Z. Ceplecha, Bolide physical theory with application to PN and EN fireballs. *ESA Special Publ.* **495**, 507–512 (2001).

11. J. Borovicka, P. Spurny, L. Shrbeny, Trajectory and orbit of the Chelyabinsk superbolide. CBET 3423, Central Bureau for Astronomical Telegrams, International Astronomical Union (2013); www.icq.eps.harvard.edu/CBET3423.html.

12. J. Zinn, J. Drummond, Observations of persistent Leonid meteor trails: 4. Buoyant rise/vortex formation as mechanism for creation of parallel meteor train pairs. *JGR Space Physics* **110**, (A4), A04306 (2005). doi:10.1029/2004JA010575

13. S. Glasstone, P. J. Dolan, *The Effects of Nuclear Weapons, Third edition* (U.S. Government Printing Office, Washington, D.C. (1977).

14. M.-W. Huang, P.-Y. Lo, K.-S. Cheng, Objective assessment of sunburn and minimal erythema doses: Comparison of noninvasive in vitro measuring techniques after UVB irradiation. *EURASIP J. Adv. Signal Process.* **2010**, 483562 (2010). doi:10.1155/2010/483562

15. O. Popova, J. Borovicka, W. K. Hartmann, P. Spurny, E. Gnos, I. Nemtchinov, J. M. Trigo-Rodríguez, Very low strengths of interplanetary meteoroids and small asteroids. *Meteorit. Planet. Sci.* **46**, 1525–1550 (2011). doi:10.1111/j.1945-5100.2011.01247.x

16. G. J. Consolmagno, D. T. Britt, R. J. Macke, The significance of meteorite density and porosity. *Chem. Erde* **68**, 1–29 (2008). doi:10.1016/j.chemer.2008.01.003

17. A. Bischoff, E. R. D. Scott, K. Metzler, C. A. Goodrich, in *Meteorites and the Early Solar System II*, D. S. Lauretta, H. Y. McSween Jr., Eds. (University of Arizona Press, Tucson, AZ, 2006), pp. 679−712.

18. M. A. Nazarov, D. D. Badyukov, N. N. Kononkova, I. V. Kubrakova, Chelyabinsk Meteoritical Bulletin: Entry for Chelyabinsk; http://www.lpi.usra.edu/meteor/metbull.php?code=57165 (2013).

19. D. Stöffler, K. Keil, E. R. D. Scott, Shock metamorphism of ordinary chondrites. *Geochim. Cosmochim. Acta* **55**, 3845–3867 (1991). doi:10.1016/0016-7037(91)90078-J

20. R. N. Clayton, T. K. Mayeda, J. N. Goswami, E. J. Olsen, Oxygen isotope studies of ordinary chondrites. *Geochim. Cosmochim. Acta* **55**, 2317–2337 (1991). doi:10.1016/0016-7037(91)90107-G

21. A. Trinquier, J.-L. Birck, C. J. Allègre, Widespread ^{54}Cr Heterogeneity in the inner solar system. *Astrophys. J.* **655**, 1179–1185 (2007). doi:10.1086/510360

22. C. Göpel, G. Manhès, C. J. Allègre, U-Pb systematics of phosphates from equilibrated ordinary chondrites. *Earth Planet. Sci. Lett.* **121**, 153–171 (1994). doi:10.1016/0012-821X(94)90038-8

23. Y. Amelin, Meteorite phosphates show constant ^{176}Lu decay rate since 4557 million years ago. *Science* **310**, 839–841 (2005). doi:10.1126/science.1117919 Medline

24. K. Terada, A. Bischoff, Asteroidal granite-like magmatism 4.53 Gyr ago. *Astrophys. J.* **699**, L68–L71 (2009). doi:10.1088/0004-637X/699/2/L68

25. J. N. Connelly, M. Bizzarro, A. N. Krot, Å. Nordlund, D. Wielandt, M. A. Ivanova, The absolute chronology and thermal processing of solids in the solar protoplanetary disk. *Science* **338**, 651–655 (2012). doi:10.1126/science.1226919 Medline

26. J. M. Friedrich, J. C. Bridges, M.-S. Wang, M. E. Lipschutz, Chemical studies of L chondrites. VI: Variations with petrographic type and shock-loading among equilibrated falls. *Geochim. Cosmochim. Acta* **68**, 2889–2904 (2004). doi:10.1016/j.gca.2004.01.010

27. P. Rochette, L. Sagnotti, M. Bourout-Denise, G. Consolmagno, L. Folco, J. Gattacceca, M. L. Osete, L. Pesonen, Magnetic classification of stony meteorites: 1. Ordinary chondrites. *Meteorit. Planet. Sci.* **38**, 251–268 (2003). doi:10.1111/j.1945-5100.2003.tb00263.x

28. C. P. Hartmetz, D. W. G. Sears, Thermoluminescence properties of shocked and annealed plagioclases with implications for meteorites. *Meteoritics* **22**, 400–401 (1988).

29. D. W. Sears, A. A. Mills, Temperature gradients and atmospheric ablation rates for the Barwell meteorite. *Nat. Phys. Sci (Lond.)* **242**, 25–26 (1973). doi:10.1038/physci242025a0

30. P. Schmitt-Kopplin, Z. Gabelica, R. D. Gougeon, A. Fekete, B. Kanawati, M. Harir, I. Gebefuegi, G. Eckel, N. Hertkorn, High molecular diversity of extraterrestrial organic matter in Murchison meteorite revealed 40 years after its fall. *Proc. Natl. Acad. Sci. U.S.A.* **107**, 2763–2768 (2010). doi:10.1073/pnas.0912157107 Medline

31. T. L. Dunn, T. H. Burbine, W. F. Bottke, Jr., J. P. Clark, Mineralogies and source regions of near Earth asteroids. *Icarus* **222**, 273–282 (2013). doi:10.1016/j.icarus.2012.11.007

32. T. Nakamura, T. Noguchi, M. Tanaka, M. E. Zolensky, M. Kimura, A. Tsuchiyama, A. Nakato, T. Ogami, H. Ishida, M. Uesugi, T. Yada, K. Shirai, A. Fujimura, R. Okazaki, S. A. Sandford, Y. Ishibashi, M. Abe, T. Okada, M. Ueno, T. Mukai, M. Yoshikawa, J. Kawaguchi, Itokawa dust particles: A direct link between S-type asteroids and ordinary chondrites. *Science* **333**, 1113–1116 (2011). doi:10.1126/science.1207758 Medline

33. W. F. Bottke, A. Morbidelli, R. Jedicke, J.-M. Petit, H. F. Levison, P. Michel, T. S. Metcalfe, De-biased orbital and absolute magnitude distributions of near earth objects. *Icarus* **156**, 339–433 (2000).

34. P. Michel, M. Yoshikawa, Dynamical origin of the asteroid (25143) Itokawa: The target of the sample-return Hayabusa space mission. *Astron. Astrophys.* **449**, 817–820 (2006). doi:10.1051/0004-6361:20054319

35. V. Reddy, J. M. Carvano, D. Lazzaro, T. A. Michtchenko, M. J. Gaffey, M. S. Kelley, T. Mothé-Diniz, A. Alvarez-Candal, N. A. Moskovitz, E. A. Cloutis, E. L. Ryan, Mineralogical characterization of Baptistina Asteroid Family: Implications for K/T impactor source. *Icarus* **216**, 184–197 (2011). doi:10.1016/j.icarus.2011.08.027

36. D. Nesvorny, A. Morbidelli, D. Vokrouhlicky, W. F. Bottke, M. Broz, The Flora family: A case of the dynamically dispersed collisional swarm? *Icarus* **157**, 155–172 (2002). doi:10.1006/icar.2002.6830

37. E. Schunová, M. Granvik, R. Jedicke, G. Gronchi, R. Wainscoat, S. Abe, Searching for the first near-Earth object family. *Icarus* **220**, 1050–1063 (2012). doi:10.1016/j.icarus.2012.06.042

38. J. Troiano, D. Rumble, III, M. L. Rivers, J. M. Friedrich, Compositions of three low-FeO ordinary chondrites: indications of a common origin with the H chondrites. *Geochim. Cosmochim. Acta* **75**, 6511–6519 (2011). doi:10.1016/j.gca.2011.08.033

39. W. F. McDonough, in *The Mantle and Core, Vol. 2. Treatise on Geochemistry*, R. W. Carlson, Ed. (Elsevier-Pergamon, Oxford, 2003), pp. 547–568.

40. J. T. Wasson, G. W. Kallemeyn, Compositions of chondrites. *Phil. Trans. Roy. Soc. London A* **325**, 535–544 (1988). doi:10.1098/rsta.1988.0066

41. J. M. Friedrich, M.-S. Wang, M. E. Lipschutz, Chemical studies of L chondrites. V: Compositional patterns for 49 trace elements in 14 L4-6 and 7 LL4-6 Falls. *Geochim. Cosmochim. Acta* **67**, 2467–2479 (2003). doi:10.1016/S0016-7037(03)00024-3

42. J. I. Zuluaga, I. Ferrin, A preliminary reconstruction of the orbit of the Chelyabinsk meteoroid. 21 Feb 2013, arXiv:1302.5377v1 [astro-ph.ED] (2013).

43. P. Jenniskens, P. S. Gural, L. Dynneson, B. J. Grigsby, K. E. Newman, M. Borden, M. Koop, D. Holman, CAMS: Cameras for allsky meteor surveillance to establish minor meteor showers. *Icarus* **216**, 40–61 (2011). doi:10.1016/j.icarus.2011.08.012

44. P. S. Gural, A new method of meteor trajectory determination applied to mulitple unsynchronized video cameras. *Meteorit. Planet. Sci.* **47**, 1405–1418 (2012). doi:10.1111/j.1945-5100.2012.01402.x

45. F. L. Whipple, L. G. Jacchia, Reduction methods for photographic meteor trails. *Smiths. Contr. Astrophysics* **1**, 183–206 (1957). doi:10.5479/si.00810231.1-2.183

46. J. Borovicka, P. Spurny, L. Shrbeny, Trajectory and orbit of the Chelyabinsk superbolide. CBET 3423, D. W. E. Green, Ed., Central Bureau for Astronomical Telegrams, International Astronomical Union, p. 1–1 (2013); www.icq.eps.harvard.edu/CBET3423.html.

47. D. Yeomans, P. Chodas, Additional details on the large fireball event over Russia on Feb. 15, 2013. NASA/JPL Near-Earth Object Program Office, March 1, 2013; http://neo.jpl.nasa.gov/news/fireball_130301.html (2013).

48. B. J. Gladman, F. Migliorini, A. Morbidelli, V. Zappala, P. Michel, A. Cellino, C. Froschle, H. F. Levison, M. Bailey, M. Duncan, Dynamical lifetimes of objects injected into asteroid belt. *Science* **277**, 197–201 (1997). doi:10.1126/science.277.5323.197

49. P. Jenniskens, Observations of the Stardust Sample Return Capsule entry with a slitless echelle spectrograph. *J. Spacecr. Rockets* **47**, 718–735 (2010). doi:10.2514/1.37518

50. O. Popova, Meteoroid ablation models. *Earth Moon Planets* **95**, 303–319 (2004). doi:10.1007/s11038-005-9026-x

51. V. V. Svetsov, I. V. Nemtchinov, A. V. Teterev, Disintegration of large meteoroids in Earth's atmosphere: Theoretical models. *Icarus* **116**, 131–153 (1995). doi:10.1006/icar.1995.1116

52. A. P. Golub', I. B. Kosarev, I. V. Nemtchinov, O. P. Popova, Emission spectra of bright bolides. *Sol. Syst. Res.* **31**, 85–98 (1997).

53. M. Boslough, D. Crawford, A. Robinson, T. Trucano, Mass and penetration depth of Shoemaker-Levy 9 fragments from time-resolved photometry. *Geophys. Res. Lett.* **21**, 1555–1558 (1994). doi:10.1029/94GL01582

54. V. V. Shuvalov, N. A. Artemieva, Numerical modeling of Tunguska-like impacts. *Planet. Space Sci.* **50**, 181–192 (2002). doi:10.1016/S0032-0633(01)00079-4

55. B. Baldwin, Y. Sheaffer, Ablation and breakup of large meteoroids during atmospheric entry. *J. Geophys. Res.* **76**, 4653–4668 (1971). doi:10.1029/JA076i019p04653

56. J. Borovička, O. P. Popova, I. V. Nemtchinov, P. Spurný, Z. Ceplecha, Bolides produced by impacts of large meteoroids into the Earth's atmosphere: Comparison of theory with observations. I. Benesov bolide dynamics and fragmentation. *Astron. Astrophys.* **334**, 713–728 (1998).

57. P. A. Bland, N. A. Artemieva, The rate of small impacts on Earth. *Meteorit. Planet. Sci.* **41**, 607–631 (2006). doi:10.1111/j.1945-5100.2006.tb00485.x

58. Z. Ceplecha, P. Spurny, J. Borovička, J. Keclikova, Atmospheric fragmentation of meteoroids. *Astron. Astrophys.* **279**, 615–626 (1993).

59. Z. Ceplecha, D. O. Revelle, Fragmentation model of meteoroid motion, mass loss, and radiation in the atmosphere. *Meteorit. Planet. Sci.* **40**, 35–54 (2005). doi:10.1111/j.1945-5100.2005.tb00363.x

60. O. P. Popova, Passage of Bolides Through the Atmosphere. Meteoroids: The Smallest Solar System Bodies, Proc. Meteoroids Conference, Breckenridge, Colorado, USA, May 24–28, 2010, W. J. Cooke, D. E. Moser, B. F. Hardin, D. Janches, Eds. NASA/CP-2011-216469, p. 232 (2011).

61. V. I. Tsvetkov, A. Ya. Skripnik, Atmospheric fragmentation of meteorites according to strength theory. *Sol. Syst. Res.* **25**, 273–279 (1991).

62. O. Popova, J. Borovička, W. K. Hartmann, P. Spurný, E. Gnos, I. Nemtchinov, J. M. Trigo-Rodríguez, Very low strength of interplanetary meteoroids and small asteroids. *Meteorit. Planet. Sci.* **46**, 1525–1550 (2011). doi:10.1111/j.1945-5100.2011.01247.x

63. Z. Ceplecha, J. Borovička, W. G. Elford, D. O. ReVelle, R. L. Hawkes, V. Í. Porubčan, M. Šimek, Meteor phenomena and bodies. *Space Sci. Rev.* **84**, 327–471 (1998). doi:10.1023/A:1005069928850

64. A. P. Golub', I. B. Kosarev, I. V. Nemtchinov, V. V. Shuvalov, Emission and ablation of a large meteoroid in the course of its motion through the Earth's atmosphere. *Sol. Syst. Res.* **30**, 183–197 (1996).

65. I. V. Nemtchinov, V. V. Svetsov *et al*., Assessment of kinetic energy of meteoroids detected by satellite-based light sensors. *Icarus* **130**, 259–274 (1997). doi:10.1006/icar.1997.5821

66. A. R. Klekociuk, P. G. Brown, D. W. Pack, D. O. ReVelle, W. N. Edwards, R. E. Spalding, E. Tagliaferri, B. B. Yoo, J. Zagari, Meteoritic dust from the atmospheric disintegration of a large meteoroid. *Nature* **436**, 1132–1135 (2005). doi:10.1038/nature03881 Medline

67. J. Borovička, Z. Charavat, Meteosat observation of the atmospheric entry of 2008 TC3 over Sudan and associated dust cloud. *Astron. Astrophys.* **507**, 1015–1022 (2009). doi:10.1051/0004-6361/200912639

68. J. Zinn, J. Drummond, Observations of persistent Leonid meteor trails: 4. Buoyant model rise/vortex formation as mechanism for creation of parallel meteor train pairs. *JGR Space Physics* **110**, (A4), A04306 (2005). doi:10.1029/2004JA010575

69. Comprehensive Nuclear-Test-Ban Treaty organization (CTBTO) press release, 18.02.2013; http://www.ctbto.org/press-centre/press-releases/2013/russian-fireball-largest-ever-detected-by-ctbtos-infrasound-sensors/ (2013).

70. Y. Cansi, An automatic seismic event processing for detection and location: The P.M.C.C. method. *Geophys. Res. Lett.* **22**, 1021–1024 (1995). doi:10.1029/95GL00468

71. Yu. S. Rybnov, V. A. Kharlamov, V. F. Evmenov, in *Dynamic Processes in a System of Inner and Outer Interacting Geospheres*, V. V. Adushkin, Ed., pp. 29–34 (2005).

72. M. A. Tsikulin, Shock waves during the movement of large meteorites in the atmosphere. Moscow, Nauka, 86 p. (1969). (English Translation: AD 715-537, National Technical Information Service, Springfield, Virginia, 1970)

73. D. O. ReVelle, Historical detection of atmospheric impacts by large bolides using acoustic-gravity waves, in Annals of the New York Academy of Sciences, Near- Earth Objects: The United Nations International Conference, J. L. Remo, Ed., New York Academy of Sciences, 822, 284–302 (1997).

74. W. N. Edwards, P. G. Brown, D. O. ReVelle, Estimates of meteoroid kinetic energies from observations of infrasonic airwaves. *J. Atmos. Sol. Terr. Phys.* **68**, 1136–1160 (2006). doi:10.1016/j.jastp.2006.02.010

75. W. N. Edwards, in *Infrasound Monitoring for Atmospheric Studies*, A. Le Pichon, E. Blanc, A. Hauchecorne, Eds., (Springer, Dordrecht, Netherlands, 2010), pp. 361–414.

76. E. Silber, D. O. ReVelle, P. G. Brown, W. N. Edwards, An estimate of the terrestrial influx of large meteoroids from infrasonic measurements. *J. Geophys. Res.* **114**, (E8), E08006 (2009). doi:10.1029/2009JE003334

77. J. L. Stevens, D. A. Adams, G. E. Baker, H. Xu, J. R. Murphy, I. Divnov, V. N. Bourchik, Infrasound Modeling Using Soviet Explosion Data and Instrument Design Criteria from Experiments and Simulations. Technical Report ADA446517S (2006).

78. P. Brown, A preliminary report on the Chelyabinsk fireball/airburst. *J. Int. Meteor Org.* **41**, 22–25 (2013).

79. J. P. Mutschlecner, R. W. Whitaker, L. H. Auer, An empirical study of infrasonic propagation, Los Alamos National Laboratory Technical Report, LA-13620-MS, Los Alamos, NM (1999).

80. J. P. Mutschlecner, R. W. Whitaker, in *Infrasound Monitoring for Atmospheric Studies*, A. Le Pichon, E. Blanc, A. Hauchecorne, Eds. (Springer, Dordrecht, Netherlands, 2010), pp. 455–474.

81. K. E. Gubkin, About similarity of explosions. *Физ. Земли Fizika Zemli* **N10**, 49–60 (1978).

82. J. Reed, Airblast overpressure decay at long ranges. *J. Geophys. Res.* **77**, 1623–1629 (1972). doi:10.1029/JC077i009p01623

83. V. N. Arkhipov *et al.*, *Mechanical Action of Nuclear Explosions* (Fizmatlit, Moscow, (2003).

84. S. Glasstone, P. J. Dolan, *The Effects of Nuclear Weapons* (U.S. Department of Defense, U.S. Department of Energy, Washington, 1977).

85. J. Reed, Climatology of Airblast Propagations from Nevada Test Site Nuclear Airbursts. Sandia Laboratories Report SC-RR-69-572 (1969).

86. M. Lutzky, D. Lechto, Shock propagation in spherically symmetric exponential atmosphere. *Phys. Fluids* **11**, 1466–1472 (1968). doi:10.1063/1.1692129

87. S. Mannan, F. P. Lees, *Lees' Loss Prevention in the Process Industries: Hazard Identification, Assessment and Control*, vol. 1, 3rd edition (Elsevier Butterworth-Heinemann, 2005).

88. M. D. Brown, A. S. Loewe, Reference manual to mitigate potential terrorist attacks against buildings. USA, FEMA, pp. 4–19 (2003).

89. V. V. Shuvalov, Multi-dimensional hydrodynamic code SOVA for interfacial flows: Application to thermal layer effect. *Shock Waves* **9**, 381–390 (1999). doi:10.1007/s001930050168

90. N. M. Kuznetsov, *Thermodynamic Functions and Shock Adiabats for Air at High Temperatures* (Mashinostroyenie, Moscow, 1965).

91. C. E. Needham, *Blast Waves: Shock Wave and High Pressure Phenomena* (Springer-Verlag, Berlin, 2010), 339 pp..

92. J. R. Blackford, Sintering and microstructure of ice: A review. *J. Phys. D.* **40**, R355–R385 (2007). doi:10.1088/0022-3727/40/21/R02

93. A. van Herwijnen, D. A. Miller, Experimental and numerical investigation of the sintering of snow. *J. Glaciol.* **59**, 269–274 (2013). doi:10.3189/2013JoG12J094

94. A. N. Kolmogorov, *Selected Proceedings: Probability Theory and Mathematical Statistics*, M. Nauka, Ed. (1986).

95. I. T. Zotkin, Stony meteorite shower Tsarev. *Meteoritika* **41**, 3–12 (1982).

96. P. Jenniskens, M. H. Shaddad, D. Numan, S. Elsir, A. M. Kudoda, M. E. Zolensky, L. Le, G. A. Robinson, J. M. Friedrich, D. Rumble, A. Steele, S. R. Chesley, A. Fitzsimmons, S. Duddy, H. H. Hsieh, G. Ramsay, P. G. Brown, W. N. Edwards, E. Tagliaferri, M. B. Boslough, R. E. Spalding, R. Dantowitz, M. Kozubal, P. Pravec, J. Borovicka, Z. Charvat, J. Vaubaillon, J. Kuiper, J. Albers, J. L. Bishop, R. L. Mancinelli, S. A. Sandford, S. N. Milam, M. Nuevo, S. P. Worden, The impact and recovery of asteroid 2008 TC(3). *Nature* **458**, 485–488 (2009). doi:10.1038/nature07920 Medline

97. Q. R. Passey, H. J. Melosh; Q. R. Passey H. J. Melosh, Effects of atmospheric breakup on crater field formation. *Icarus* **42**, 211–233 (1980). doi:10.1016/0019-1035(80)90072-X

98. E. D. Narkhov, V. A. Sapunov, A. Yu. Denisov, D. V. Savelyev, D. A. Galkin, D. S. Yakovenko, A. L. Fedorov, Magnetic prospecting and data interpretation of the Chebarkul meteorite, in Proceedings of the International Workshop Asteroids and Comets: The Chelyabinsk event and the Chebarkul lake meteorite fall, Chebarkul, June 21–22, 2013, (Kray Ra, Chelyabinsk, 2013), pp. 72–75.

99. M. L. Gittings *et al*., The RAGE radiation-hydrodynamic code, Los Alamos National Laboratory Report LA-UR- 06-0027, Los Alamos, New Mexico. Published in: Computational Science and Discovery 1, 015005 (2008).

100. J. Kimberley, K. T. Ramesh, The dynamic strength of an ordinary chondrite. Meteoritics and Plan. *Sci.* **46**, 1653–1669 (2011).

101. R. V. Medvedev, F. Gorbachevich, I. Zotkin, Determination of physical properties of stone meteorites from the point of view of their disruption. *Meteoritika* **44**, 105–110 (1985).

102. I. T. Zotkin, P. V. Medvedev, F. F. Gorbatsevich, Strength properties of the Tsarev meteorite. *Meteoritika* **46**, 86–93 (1987).

103. E. N. Slyuta, S. M. Nikitin, A. V. Korochantsev, C. A. Lorents, A. Ya. Skripnik, Strong physical and mechanical anisotropy of ordinary chondrites. 40th Lunar and Planetary Science Conference, Abstr.1051 (2010).

104. J. M. Friedrich, Quantitative methods for three-dimensional comparison and petrographic description of chondrites. *Comput. Geosci.* **34**, 1926–1935 (2008). doi:10.1016/j.cageo.2008.05.001

105. J. M. Friedrich, D. P. Wignarajah, S. Chaudhary, M. L. Rivers, C. E. Nehru, D. S. Ebel, Three-dimensional petrography of metal phases in equilibrated L chondrites: Effects of shock loading and dynamic compaction. *Earth Planet. Sci. Lett.* **275**, 172–180 (2008). doi:10.1016/j.epsl.2008.08.024

106. E. Jarosewich, Chemical analyses of meteorites: A compilation of stony and iron meteorite analyses. *Meteoritics* **25**, 323–337 (1990). doi:10.1111/j.1945-5100.1990.tb00717.x

107. H. C. Urey, H. Craig, The composition of the stone meteorites and the origin of the meteorites. *Geochim. Cosmochim. Acta* **4**, 36–82 (1953). doi:10.1016/0016-7037(53)90064-7

108. A. J. Brearley, R. H. Jones, Chondritic meteorites, in *Planetary Materials*, J. J. Papike, Ed., Mineralogical Society of America, Reviews in Mineralogy 36, pp. 3-1–3-398 (1998).

109. A. N. Krot, K. Keil, E. R. D. Scott, C. A. Goodrich, M. K. Weisberg, in *Meteorites, Comets and Planets*, A. M. Davis, Ed., Vol. 1, Treatise on Geochemistry (K. K. Turekian, H. D. Holland, Eds.) (Elsevier, Oxford, 2013).

110. J. M. Friedrich, A. Ruzicka, M. L. Rivers, D. S. Ebel, J. O. Thostenson, R. A. Rudolph, Metal veins in the Kernouve (H6 S1) chondrite: Evidence for pre- or syn-metamorphic shear deformation. *Geochim. Cosmochim. Acta* **116**, 71–83 (2013). doi:10.1016/j.gca.2013.01.009

111. N. H. Woodcock, Specification of fabric shapes using an eigenvalue method. *Geol. Soc. Am. Bull.* **88**, 1231–1236 (1977). doi:10.1130/0016-7606(1977)88<1231:SOFSUA>2.0.CO;2

112. N. H. Woodcock, M. A. Naylor, Randomness testing in three-dimensional orientation data. *J. Struct. Geol.* **5**, 539–548 (1983). doi:10.1016/0191-8141(83)90058-5

113. P. Rochette, L. Sagnotti, G. Consolmagno, L. Folco, A. Maras, F. Panzarino, L. Pesonen, R. Serra, M. Terho, A magnetic susceptibility database for stony meteorites. *Quaderni di Geofisica* **18**, 1–31 (2001).

114. S. J. Morden, The anomalous demagnetization behaviour of chondritic meteorites. *Phys. Earth Planet. Interiors* **71**, 189–204 (1992).

115. J. Gattacceca, P. Rochette, Toward a robust normalized magnetic paleointensity method applied to meteorites. *Earth Planet. Sci. Lett.* **227**, 377–393 (2004). doi:10.1016/j.epsl.2004.09.013

116. E. Jarosewich, R. S. Clarke, Jr., J. N. Barrows, Eds., The Allende meteorite reference sample. *Smithson. Contrib. Earth Sci.* **27**, 1–49 (1986).

117. P. G. Brown, A. R. Hildebrand, M. E. Zolensky, M. Grady, R. N. Clayton, T. K. Mayeda, E. Tagliaferri, R. Spalding, N. D. MacRae, E. L. Hoffman, D. W. Mittlefehldt, J. F. Wacker, J. A. Bird, M. D. Campbell, R. Carpenter, H. Gingerich, M. Glatiotis, E. Greiner, M. J. Mazur, P. J. McCausland, H. Plotkin, T. Rubak Mazur, The fall, recovery, orbit, and composition of the Tagish Lake meteorite: A new type of carbonaceous chondrite. *Science* **290**, 320–325 (2000). doi:10.1126/science.290.5490.320 Medline

118. J. M. Friedrich, M.-S. Wang, M. E. Lipschutz, Comparison of the trace element composition of Tagish Lake with other primitive carbonaceous chondrites. *Meteorit. Planet. Sci.* **37**, 677–686 (2002). doi:10.1111/j.1945-5100.2002.tb00847.x

119. K. Lodders, Solar system abundances and condensation temperatures of the elements. *Astrophys. J.* **591**, 1220–1247 (2003). doi:10.1086/375492

120. Metbase homepage; http://www.metbase.de/home.html (2013).

121. A. Yamakawa, K. Yamashita, A. Makishima, E. Nakamura, Chemical separation and mass spectrometry of Cr, Fe, Ni, Zn, and Cu in terrestrial and extraterrestrial materials using thermal ionization mass spectrometry. *Anal. Chem.* **81**, 9787–9794 (2009). doi:10.1021/ac901762a Medline

122. W. R. Shields, T. J. Murphy, E. J. Catanzaro, E. L. Garner, Absolute isotopic abundance ratios and the atomic weight of a reference sample of chromium. *J. Res. Natl. Bur. Stand.* **70A**, 193–197 (1966). doi:10.6028/jres.070A.016

123. A. Trinquier, J.-L. Birck, C. J. Allègre, C. Göpel, D. Ulfbeck, 53Mn–53Cr systematics of the early solar system revisited. *Geochim. Cosmochim. Acta* **72**, 5146–5163 (2008). doi:10.1016/j.gca.2008.03.023

124. P. H. Warren, Stable-isotopic anomalies and the accretionary assemblage of the Earth and Mars: A subordinate role for carbonaceous chondrites. *Earth Planet. Sci. Lett.* **311**, 93–100 (2011). doi:10.1016/j.epsl.2011.08.047

125. L. Qin, C. M. O. D. Alexander, R. W. Carlson, M. F. Horan, T. Yokoyama, Contributors to chromium isotope variation of meteorites. *Geochim. Cosmochim. Acta* **74**, 1122–1145 (2010). doi:10.1016/j.gca.2009.11.005

126. A. Yamakawa, K. Yamashita, A. Makishima, E. Nakamura, Chromium isotope systematics of achondrites: Chronology and isotopic heterogeneity of the inner solar system bodies. *Astrophys. J.* **720**, 150–154 (2010). doi:10.1088/0004-637X/720/1/150

127. I. Ahn, J. Lee, M. Kusakabe, B. Choi, Oxygen isotope measurements of terrestrial silicates using a CO2-laser BrF5 fluorination technique and the slope of terrestrial fractionation line. *Geosci. J.* **16**, 7–16 (2012). doi:10.1007/s12303-012-0011-x

128. Z. D. Sharp, A laser-based microanalytical method for the in situ determination of oxygen isotope ratios of silicates and oxides. *Geochim. Cosmochim. Acta* **54**, 1353–1357 (1990). doi:10.1016/0016-7037(90)90160-M

129. R. N. Clayton, T. K. Mayeda, Oxygen isotope studies of carbonaceous chondrites. *Geochim. Cosmochim. Acta* **63**, 2089–2104 (1999). doi:10.1016/S0016-7037(99)00090-3

130. E. D. Young, S. S. Russell, Oxygen reservoirs in the early solar nebula inferred from an Allende CAI. *Science* **282**, 452–455 (1998). doi:10.1126/science.282.5388.452

131. R. N. Clayton, T. K. Mayeda, A. E. Rubin, Oxygen isotopic compositions of enstatite chondrites and aubrites. *J. Geophys. Res.* **89**, (S01), C245–C249 (1984). doi:10.1029/JB089iS01p0C245

132. R. N. Clayton, T. K. Mayeda, Oxygen isotope studies of achondrites. *Geochim. Cosmochim. Acta* **60**, 1999–2017 (1996). doi:10.1016/0016-7037(96)00074-9

133. C. Gopel, J.-L. Birck, Mn/Cr systematics: A tool to discriminate the origin of primitive meteorites? Goldschmidt Conference Abstracts, A348 (2010).

134. A. J. Irving, R. Tanaka, A. Steele, S. M. Kuehner, T. E. Bunch, J. H. Wittke, G. M. Hupe, Northwest Africa 6704: A unique cumulate permafic achondrite containing sodic feldspar, awaruite and “fluid” inclusions, with an oxygen isotopic composition in the Acapulcoite-Lodranite field. Annual Meteoritical Society Meeting, #5231 (2011).

135. Q. L. Li, X. H. Li, F. Y. Wu, Q. Z. Yin, H. M. Ye, Y. Liu, G. Q. Tang, C. L. Zhang, In-situ SIMS U-Pb dating of phanerzoic apatite with low U and high common Pb. *Gondwana Res.* **21**, 745–756 (2012). doi:10.1016/j.gr.2011.07.008

136. T. Sano, S. M. Miyama, Magnetorotational instability in protoplanetary disks. I. On the global stability of weakly ionized disks with ohmic dissipiation. *Astrophys. J.* **515**, 776–786 (1999). doi:10.1086/307063

137. J. A. Trotter, S. M. Eggins, Chemical systematics of conodont apatite determined by laser ablation ICPMS. *Chem. Geol.* **233**, 196–216 (2006). doi:10.1016/j.chemgeo.2006.03.004

138. M. Tatsumoto, R. J. Knight, C. J. Allegre, Time differences in the formation of meteorites as determined from the ratio of lead-207 to lead-206. *Science* **180**, 1279–1283 (1973). doi:10.1126/science.180.4092.1279 Medline

139. K. R. Ludwig, User’s manual for Isoplot, v. 3.0, a geochronological toolkit for Microsoft Excel. Berkeley Geochronological Center, Special Publication 4 (2003).

140. Y. Amelin, A. Kaltenbach, C. H. Stirling, The U-Pb systematics and cooling rate of plutonic angrite NWA 4590. 42nd Lunar and Planetary Science Conference 2011, Abstract 1682 (2011).

141. T. Mikouchi, K. Sugiyama, W. Satake, Y. Amelin, Mineralogy and Crystallography of Calcium Silico-Phosphate in Northwest Africa 4590 Angrite. 42nd Lunar and Planetary Science Conference 2011, Abstract 2026 (2011).

142. Y. Amelin, A. Ghosh, E. Rotenberg, Unraveling the evolution of chondrite parent asteroids by precise U-Pb dating and thermal modeling. *Geochim. Cosmochim. Acta* **69**, 505–518 (2005). doi:10.1016/j.gca.2004.05.047

143. T. Hiroi, S. Sasaki, S. K. Noble, C. M. Pieters, Space weathering of ordinary chondrite parent bodies, its impact on the method of distinguishing H, L, and LL types and implications for Itokawa samples returned by the Hayabusa mission. 42nd Lunar and Planetary Science Conference 2011, Abstract 1264 (2011).

144. T. Hiroi, M. Abe, K. Kitazato, S. Abe, B. E. Clark, S. Sasaki, M. Ishiguro, O. S. Barnouin-Jha, Developing space weathering on the asteroid 25143 Itokawa. *Nature* **443**, 56–58 (2006). doi:10.1038/nature05073 Medline

145. R. H. Biswas, P. Morthekai, R. K. Gartia, S. Chawla, A. K. Singhvi, Thermoluminescence of the meteorite interior: A possible tool for the estimation of cosmic ray exposure ages. *Earth Planet. Sci. Lett.* **304**, 36–44 (2011). doi:10.1016/j.epsl.2011.01.012

146. D. W. G. Sears, A. A. Mills, Temperature gradients and atmospheric ablation rates for the Barwell meteorite. *Nat. Phys. Sci (Lond.)* **242**, 25–26 (1973). doi:10.1038/physci242025a0

147. R. Chen, S. W. S. McKeever, *Theory of Thermoluminescence and Related Phenomena* (World Scientific, Singapore, 1997).

148. D. W. G. Sears, K. Ninagawa, A. Signhvi, Luminescence studies of extraterrestrial materials: Insights into their recent radiation and thermal histories and into their metamorphic history. *Chemie Erde Geochemistry* **73**, 1–37 (2013). http://dx.doi.org/10.1016/j.chemer.2012.12.001

149. M. Haq, F. A. Hasan, D. W. G. Sears, Thermoluminescence and the shock and reheating history of meteorites: IV. The induced TL properties of type 4-6 ordinary chondrites. *Geochim. Cosmochim. Acta* **52**, 1679–1689 (1988). doi:10.1016/0016-7037(88)90236-0

150. R. K. Guimon, K. S. Weeks, B. D. Keck, D. W. G. Sears, Thermoluminescence as a palaeothermometer. *Nature* **311**, 363–365 (1984). doi:10.1038/311363a0

151. W. R. Van Schmus, J. A. Wood, A chemical-petrologic classification for the chondritic meteorites. *Geochim. Cosmochim. Acta* **31**, 747–765 (1967). doi:10.1016/S0016-7037(67)80030-9

152. D. W. G. Sears, J. N. Grossman, C. L. Melcher, L. M. Ross, A. A. Mills, Measuring the metamorphic history of unequilibrated ordinary chondrites. *Nature* **287**, 791–795 (1980). doi:10.1038/287791a0

153. C. P. Hartmetz, R. Ostertag, D. W. G. Sears, A thermoluminescence study of experimentally shock-loaded oligoclase and bytownite. *J. Geophys. Res.* **91**, (B13), E263–E274 (1986). doi:10.1029/JB091iB13p0E263

154. P. H. Benoit, H. Sears, D. W. G. Sears, The natural thermoluminescence of meteorites: IV. Ordinary chondrites at the Lewis Cliff ice field. *J. Geophys. Res.* **97**, (B4), 4629–4647 (1992). doi:10.1029/91JB02982

155. P. Schmitt-Kopplin, Z. Gabelica, R. D. Gougeon, A. Fekete, B. Kanawati, M. Harir, I. Gebefuegi, G. Eckel, N. Hertkorn, High molecular diversity of extraterrestrial organic matter in Murchison meteorite revealed 40 years after its fall. *Proc. Natl. Acad. Sci. U.S.A.* **107**, 2763–2768 (2010). doi:10.1073/pnas.0912157107 Medline

156. D. Tziotis, N. Hertkorn, P. Schmitt-Kopplin, Kendrick-analogous network visualisation of ion cyclotron resonance Fourier transform mass spectra: Improved options for the assignment of elemental compositions and the classification of organic molecular complexity. *Eur. J. Mass Spectrom. (Chichester, Eng.)* **17**, 415–421 (2011). doi:10.1255/ejms.1135 Medline

157. C. M. Hohenberg, F. A. Podosek, J. R. Shirck, K. Arti, R. C. Reedy, Comparisons between observed and predicted cosmogenic noble gases in lunar samples, in Proceedings 9th Lunar and Planetary Science Conference, Houston, TX, March 13–17, 1978, Vol. 2, New York, Pergamon Press, Inc., pp. 2311–2344 (1978).